Quantum Diamond Microscopes for Biological Systems and Integrated Circuits

A thesis presented

by

Matthew James Turner

to

The Physics Department

in partial fulfillment of the requirements

for the degree of

Doctor of Philosophy

in the subject of

Physics

Harvard University

Cambridge, Massachusetts

August 2020

Dissertation Advisor

Adam Cohen and Ron Walsworth

Author

Matthew James Turner

Quantum Diamond Microscopes for Biological Systems and Integrated Circuits

Abstract

Nitrogen-Vacancy (NV) centers are atom-like point defects in diamond that have been utilized for applications in biological systems, integrated circuits, materials science, geoscience, positioning and navigation, quantum information, and other areas due to their robust performance at room temperature. The optical initialization and readout of the NV electronic spin state has been utilized to parallelize measurements and create simultaneous widefield maps of several parameters, including vector magnetic fields, in a modality known as a Quantum Diamond Microscope (QDM). The robustness and small intrinsic size of the NV centers allow for them to be placed within close proximity of samples of interest, enabling high spatial resolution magnetic field measurements in regimes previously unattainable.

We present an introduction to the methods, applications, and performance of QDMs in different scenarios to provide an overview of the technique and motivate what measurements are possible. Next, we give a background to magnetic field analysis and provide intuition for the magnetic inverse problems and challenges associated with it. Neural network techniques are utilized to carry out the magnetic inversion for various current source distributions, and we demonstrate improved robustness to high frequency spatial noise for simulated datasets. In an initial experimental demonstration, we achieve state-of-the-art magnetic sensitivity to measure the bio-magnetic field associated with the propagation of an action potential along axonal structures. This initial result motivated efforts to improve

the quality of the diamond sensors through improved characterization of the diamond strain and charge state environments. We demonstrate that our current magnetic imaging sensitivity when combined with machine learning classification methods is sufficient for measuring the unique magnetic fingerprints of the functional state in integrated circuits, enabling further applications in fault detection, quality control, and device security. Finally, we combine our imaging capabilities with lock-in methods to enable fast magnetic imaging applications. Through this effort, we demonstrate a biocompatible, real-time widefield magnetic imager with state-of-the-art magnetic field imaging sensitivity while showing long term viability of cardiomyocyte cell cultures under measurement conditions. Recent Ramsey imaging results have shown that we are on the cusp of the volume normalized sensitivity needed for QDM imaging of bio-magnetic fields.

Contents

List of Figures

List of Tables

Citations to previously published work

Parts of this dissertation cover research reported in the following articles:

1. *Principles and Techniques of the Quantum Diamond Microscope.* E. V. Levine*, **M. J. Turner***, P. Kehayias, C. A. Hart, N. Langellier, R. Trubko, D. R. Glenn, R. R. Fu, R. L. Walsworth. Nanophotonics 8(11): 1945–1973. (2019) [1]

2. *Optical magnetic detection of single-neuron action potentials using quantum defects in diamond.* J. F. Barry, **M. J. Turner**, J. M. Schloss, D. R. Glenn, Y. Song, M. D. Lukin, H. Park, and R. L. Walsworth. PNAS vol.113 no.49. (2016)

3. *Imaging crystal stress in diamond using ensembles of nitrogen-vacancy centers.* P. Kehayias, **M. J. Turner**, R. Trubko, J. M. Schloss, C. A. Hart, M. Wesson, D. R. Glenn, R. L. Walsworth. Phys. Rev. B 100, 174103. (2019) [2]

4. *Microwave-Assisted Spectroscopy Technique for Studying Charge State in Nitrogen-Vacancy Ensembles in Diamond.* D.P.L. Aude Craik, P. Kehayias, A.S. Greenspon, X. Zhang, **M.J. Turner**, J.M. Schloss, E. Bauch, C.A. Hart, E.L. Hu, and R.L. Walsworth. Physical Review Applied, 14(1): 014009. (2020) [3]

5. *Generation of nitrogen-vacancy ensembles in diamond for quantum sensors: Optimization and scalability of CVD processes.* A. M. Edmonds, C. A. Hart, **M. J. Turner**, P. Colard, J. M. Schloss, K. Olsson, R. Trubko, M. L. Markham, A. Rathmill, B. Horne-Smith, W. Lew, A. Manickam, S. Bruce, P. G. Kaup, J. C. Russo, M. J. DiMario, J. T. South, J. T. Hansen, D. J. Twitchen, R. L. Walsworth. arXiv:2004.01746. (2020)

[1] ©2019 Edlyn V. Levine et al., published by De Gruyter, Berlin/Boston. This work is licensed under the Creative Commons Attribution 4.0 Public License. BY 4.0

[2] © 2019 American Physical Society

[3] © 2020 American Physical Society

6. *Magnetic Field Fingerprinting of Integrated Circuit Activity with a Quantum Diamond Microscope.* **M. J. Turner**, N. Langellier, R. Bainbridge, D. Walters, S. Meesala, T. M. Babinec, P. Kehayias, A. Yacoby, E. Hu, M. Lončar, R. L. Walsworth, E. V. Levine. Phys. Rev. Applied 14, 014097. (2020) [4]

7. *NV-Diamond Magnetic Microscopy using a Double Quantum 4-Ramsey Protocol.* C. A. Hart, J. M. Schloss, **M. J Turner**, P. J. Scheidegger, E. Bauch, R. L. Walsworth. arXiv:2009.02371. (2020)

8. *Simultaneous Broadband Vector Magnetometry Using Solid-State Spins.* J. M. Schloss, J. F. Barry, **M. J. Turner**, and R. L. Walsworth. Physical Review Applied, 10(3): 034044. (2018) [5]

[4] © 2020 American Physical Society
[5] © 2018 American Physical Society

Acknowledgments

Graduate school has been a transformative experience where I have been able to grow as a person and as a scientist. Throughout this journey there have been a large number of people that have supported me and enabled a lot of the progress and success I was able to achieve. Below I want to acknowledge these people and the roles they have played in my graduate school career and building up foundations for me to reach graduate school and achieve success.

I want to acknowledge the contributions and support of current and former members of the Walsworth Group for all the assistance and guidance they have provided me throughout the years. John Barry, David Le Sage, Linh Pham, and David Glenn provided tremendous guidance throughout my early graduate years including on the necessary skills for NV center research and applications. In these early years, other students and post docs, Chinmay Belthangady, Keigo Arai, Huiliang Zhang, Stephen DeVience, Francesco Casola, and Junghyun Lee, provided a welcoming and collaborative environment and were always available for discussions and feedback on the ongoing projects. Throughout the majority of my graduate career, I worked closest with Connor Hart, Jennifer Schloss, Erik Bauch, John Barry, Linh Pham, and Patrick Scheidegger on improving measurement protocols and enabling applications. I am grateful for the collaborative environment created by this team and all that we were able to accomplish through our focused efforts. Later on in my graduate career I was fortunate to be able to work closely and collaborate with a large number of post docs on a variety of different topics: Dominik Bucher, Nithya Arunkumar, Pauli Kehayias, Mark Ku, Mikael Backlund, Raisa Trubko, Diana Prado Lopes Aude Craik, and Oren Ben Dor. These projects and collaborations were useful in expanding the scope of possible applications and for making me aware of new techniques and methods to advance my studies. Recently, I have been fortunate to work with a new batch of graduate students and post docs through the efforts at University of Maryland: Kevin Olsson, JJ Oon, Emma Huck-

estein, Jiashen Tang, Shantam Revan, and Zechuan Yin. I am excited and motivated by their enthusiasm and desire to continue improving the NV technology and always interested in their new ideas and perspectives. I would also like to thank members of the astrophysics team Nick Langellier (especially for collaborative work on the IC Project), Aakash Ravi, and Tim Milbourne for listening to all of our talks at group meetings and providing valuable insight and feedback.

I would especially like to thank David Phillips for all the mentoring and support he has provided over the years. Whenever I have a question, whether it be technical, bureaucratic, or about life in general, David has always had his door open and been happy to provide insightful guidance.

A lot of the research in the thesis has been enabled through rich collaborations. I want to acknowledge their contributions and the role they have played in my thesis here. I want to provide special thanks to George Augustine and Yuyu Song for their assistance on the giant axon results. Yuyu was vital to the experimental efforts and helped teach me basic neuroscience and electrophysiology from scratch to be able to pursue this direction. I want to provide special thanks to Ed Soucy, Brett Graham, Joel Greenwood, Stan Contreau, and Stephen Turney for all of their assistance regarding machining and experimental fabrication, which enabled many of the applications. I want to thank Luke MacQueen, John Zimmerman, Kit Parker, and Harry McNamara for their assistance with regards to culturing cardiac and HEK cells. Edlyn Levine provided guidance and great leadership on the IC Project to provide an environment that enabled it to succeed. Maitreyi Ashok, Rachel Bainbridge, Dan Walters, Srujan Meesela, and Thomas Babinec have provided great assistance in the use and characterization of a variety of integrated circuits used throughout the project. Roger Fu has provided siginificant support with regards to the use and applications of quantum diamond microscopes. Andy Edmonds, Piere Colard, Matthew Markham, and Dan Twitchen

have been tremendously important with regards to providing diamond samples and for our collaborative efforts to improve quantum diamond material protocols.

I would like to thank my dissertation committee Adam Cohen, Amir Yacoby, and Marko Lončar for your support and advising during my graduate career. Adam Cohen has provided tremendous support and feedback with regards to my interest in addressing biological questions and has ensured that I stay focused on building tools to solve specific problems. Amir Yacoby has provided great feedback on a variety of projects throughout my graduate career, including mentoring on the IC Project results. Furthermore, I have had the pleasure of teaching lab classes with Amir and he has provided great insight in methodologies to efficiently teach physics students and lab courses. Also, Amir provided me with one of my first formal introductions to NVs through a colloquium he gave at UC Berkeley while I was an undergraduate student. Mark Lončar has provided tremendous support over the past couple of years, through providing lab space for the IC project and mentoring on applications and extensions to the project.

Thank you to Lisa Cacciabaudo and Jacob Barandes for all the support and guidance they have provided with the physics department and especially for making sure I have been on top of things during the dissertation submission process.

To my research advisor Ron Walsworth, I want to thank you for providing a vibrant research environment where I have been able to explore a wide variety of topics and have been setup to do so. When I first got accepted to Harvard for graduate school, I knew I immediately wanted to start working for Ron because of the wide range of high quality applications within his group and the opportunities it would provide in terms expanding my scientific interests and toolsets. I am grateful to the collaborative environment that Ron has fostered within his group, which makes our diverse experimental applications possible.

I want to thank my friends who have always been supportive of me and my endeavors

at different levels of education. I want to thank my high school friends, Keith Harvey, James Green, Johnnel Fajardo, Elizabeth Ly, and Kayla Spawton, for their continued support after all these years. My college friends from UC Berkeley, Elizabeth Ly, Phoebe Yu, Frank Yu, Michael Suey, Erik Bertelli, Crystal Li, Kenny Wilson, Stephanie Chamberlain, and many others for being there for me and providing reasons to leave lab every once in a while. I want to thank my graduate school friends, Loic Anderegg, Urmila Powale, Anjalike Nande, Anne Hebert, Lucas Orona, and Elana Urbach for being supportive and encouraging during graduate school.

A very special thank you to my family for enabling all of this to happen. Even though they did not always know what I was doing or the nature of my research, they always took the time to try to understand and were supportive of whatever direction I wanted to pursue. Thank you to my sisters Megan and Shannon for all the adventures we shared growing up and for the support you have continued to show as we have become adults. I would like to thank my extended family including uncles, aunts, cousins, and grandparents for showing continued interest and support in my endeavors. Lastly, I want to thank my parents for making this all possible and providing a nurturing environment where I was able to develop and refine my interests.

Finally, I want to thank my significant other, Stephanie Cheng, for all the support she has provided throughout my graduate career. Through giving me reasons to come out of lab once in a while to encouraging us to go on amazing adventures, such as a trip to the Galapagos. I am in grateful for all the support she has provided (especially during the dissertation writing process).

Matthew Turner

August 27, 2020

To my family

Chapter 1

Introduction

1.1 Organization of Thesis

Chapter 1 introduces the underlying properties of diamonds and NV defects in diamond that make them useful sensors. Information will be given on the different measurement modalities commonly utilized in NV experiments. Generalized discussion regarding equipment considerations for imaging experiments is given. Finally, we discuss achievable levels of performance for sensitivity, temporal resolution, and spatial resolution and what methods can be used to improve these metrics.

Chapter 2 focuses on the magnetic inverse problem and methods to interpret magnetic field maps. We specifically focus on the Fourier Filter formalism of the magnetic inverse problem to provide intuition on the nature of magnetic fields. Some example reconstructions in different regimes and a gradiometry example is given. In order to improve the quality of source reconstruction, we trained a deep neural network based on the AUTOMAP framework to learn the constrained magnetic inverse problem for current sources. We show initial results along these lines on comment on the value of going further in this direction.

Chapter 3 describes an experimental realization of using quantum diamond sensors

for the detection of neuronal magnetic fields from a giant axon. We comment on the measurement modality needed to detect these fields and sensitivity optimization. We utilized these measurements to demonstrate the added information of vector magnetometry on signal propagation, especially in non-uniform axonal structures. Finally, we comment on the improvements needed to extend these results to mammalian cells.

Chapter 4 discusses improvement of the NV diamond sensing material and steps toward optimizing the growth protocols. Specifically, we develop tools to better characterize and understand strain inhomogeneities in the diamond lattice and the instability of the NV charge state at high laser excitation intensities. With this better understanding of these processes, we collaborated with diamond growers to iterative upon and improve diamond strain homogeneity and charge state robustness. Finally, we explore the use of confocal microscopy to build an efficient tool for non-destructively characterizing the layer thickness of diamond.

Chapter 5 highlights the use of a Quantum Diamond Microscope (QDM) to image quasi-static magnetic fields with an application to fingerprinting magnetic activity and machine learning based automatic state classification. Here we show proof of principle measurements for QDMs augmented with machine learning methods to be used for integrated circuit quality control, failure analysis, and device security.

Chapter 6 presents the development of real time magnetic imaging with Lock-In CW ODMR and the development of a platform for experimental development and biocompatible studies. We demonstrate the ability to collect real time magnetic images of an oscillating current distribution. Finally, we briefly discuss more sensitive methods for imaging over smaller fields of view and the sensitivities needed for various biological applications and reasonable sensitives for near term measurements.

Chapter 7 introduces some promising directions and next steps for improving mea-

surements and for extended applications.

1.2 Co-author Contributions

All of the work conducted under this thesis was performed under the supervision of Ron Walsworth.

Chapter 1

Edlyn Levine and I researched and conducted most of the review into and writing of the techniques and principles of the NVs and Quantum Diamond Microscopes (QDMs). Pauli Kehayias assisted on sections regarding equipment considerations for QDMs and for reviewing the manuscript. Connor Hart assisted in the performance characterization and AC magnetometry descriptions along with editing the manuscript. Nicholas Langellier assisted in creation of figures. Raisa Trubko, David Glenn, and Roger Fu provided comments and assisted with editing of the manuscript.

Chapter 2

The work in this section originated from efforts I led to interpret data-sets from wide-field magnetic imaging measurements with assistance and input from Edlyn Levine for theoretical insights and Nick Langellier for machine learning insights. Mark Ku and I independently conceived of the idea to utilize neural networks to improve the magnetic inverse problem analysis for current source distribution reconstructions. Bo Zhu, Matt Rosen, and Danyal Bhutto assisted with applying the AUTOMAP framework to the magnetic inverse problem. I led the generation and curation of the training dataset of magnetic field images and current distributions. Danyal Bhutto led the initial neural network training process.

Chapter 3

Ron Walsworth, David Glenn, Mikhail Lukin, and Hongkun Park originally conceived

of the idea of using nitrogen vacancy centers in diamond for the study of neuronal systems. John Barry and I led the conception and construction of the initial experimental efforts. I led the biological efforts with great assistance from Yuyu Song and George Augustine. John Barry led the sensitivity optimization efforts of the experiment with assistance from Jennifer Schloss and me on sensitivity calibration and calculation. John Barry, Jennifer Schloss, and I conducted the experiments and took the data presented in the section. I led the interpretation of the biological results and electrophysiology results. Ed Soucy, Brett Graham, and Joel Greenwood assisted with experimental construction and machining.

Chapter 4

Strain Measurements:

The measurements were motivated through work being done by Pauli Kehayias and me simultaneously on different setups where strain inhomogeneity would lead to degradation of experimental performance. I designed and built the experimental apparatus for simultaneous birefringence and NV strain measurements. I conducted the NV strain measurements utilized in Chapter 4 and Pauli Kehayias and David Glenn collected most of the strain maps in Appendix C. Raisa Trubko, Connor Hart, and Jennifer Schloss assisted with writing and editing the relevant manuscript and with making figures. Patrick Scheidegger developed the GPU-based fitting protocols needed for fitting the wide-field imaging data and Raisa Trubko followed up on this work for specialized protocols for QDM fitting. Marie Wesson assisted on developing the initial birefringence imaging measurements. Pauli Kehayias led in the interpretation of the strain and stress terms for the different NV axes. I led the measurements and analysis for characterizing the impact of strain inhomogeneity on sensing parameters.

Charge State Measurements:

The original technique for using microwave PL differences for measure charge state was

developed by Diana Aude-Craik and Pauli Kehayias. I led the integration of the technique into several different experiments for *in-situ* charge state characterization under realistic measurement conditions. Kevin Olsson and Connor Hart led the development, construction, and calibration of the optical system for well-defined measurements of the charge state for small beam spots. Andrew Edmonds, Pierre Colard, Matthew Markham, and Dan Twitchen led the diamond growth and process improvement for increased charge state in diamond samples. Jonathan Hoffman and Don Fahey have provided insights and discussions on next steps for understanding and characterizing the diamond charge state.

Confocal Layer Scan Measurements:

I led the development of this technique with initial assistance and guidance from John Barry. Theoretical assistance in modelling the index mismatch interface and optical propagation was provided by Toeno van der Sar and Mikael Backlund. The confocal microscope utilized for these studies was provided by Steve Turney and the Harvard Center for Brain Science Imaging Core Facility. I led the data acquisition and the analysis and interpretation of the data. Matthew Markham and Element Six provided the diamond samples used in this study.

Chapter 5

Edlyn Levine and Ron Walsworth conceived of the original idea to use QDMs for integrated circuit activity monitoring and security. Marko Lončar, Amir Yacoby, and Evelyn Hu provided technical feedback on the project. Marko Lončar provided lab space for the experiments. Linbo Shao initially worked on exploring the feasibility of measuring high frequency fields in integrated circuits utilizing the ODMR contrast. I led the efforts to explore using the current QDM infrastructure for monitoring DC magnetic fields associated with localized current delivery. Rachel Bainbridge and Dan Walters provided useful information regarding the structure and control of the FPGA used for the study. Srujan Meesala and

Thomas Babinec led the efforts on FPGA characterization with x-ray and SEM images and on decapping the FPGA. I built the QDM, took all the data, and performed the analysis to extract the magnetic field images. Nick Langellier led to the machine learning analysis efforts to predict the IC functional state. Edlyn Levine, Nick Langellier, Pauli Kehayias, and I wrote the manuscript with input from other authors.

Chapter 6

CW ODMR Lock-In Imaging:

I conceived of the idea of performing real-time CW ODMR Lock-In Imaging. Jennifer Schloss and John Barry provided technical input regarding use of the heliotis lock-in camera. Alex Chortos and Jennifer Lewis fabricated the 3D printed silver phantoms used in this study. Luke MacQueen and Kit Parker led and supervised the efforts on using neonatal rat ventricular myocytes (NRVMs) for culturing on the surface of the diamond. I built the experimental apparatus, took the data, and analyzed the data.

Ramsey Imaging:

Connor Hart, Patrick Sheidegger, and Jennifer Schloss led initial efforts in developing Double Quantum and 4-Ramsey Imaging. I led in the fabrication of the phantom for these measurements and the experiment layout for the Ramsey Phantom Imaging work was based off the setup I built and designed in Chapter 6.

Chapter 7

This chapter provides updates on ongoing efforts to both improve the performance of measurements, extend existing applications, and expand the application space in new directions. There is a large number of people contributing to this ongoing work and I will describe the relevant contributions below.

Improved Diamond Properties

Connor Hart, Kevin Olsson, Andrew Edmonds, Piere Colard, Matthew Markham, and

I are actively working on the development and improvement of diamond samples.

Integrated Circuits

I am actively leading the extension of the integrated circuit measurements from Chapter 5 to a wider range of circuit architectures, functions, and measurement protocols. These efforts are being assisted by Nick Langellier and Maitreyi Ashok with regards to extended machine learning analysis. Maitreyi Ashok is also leading the investigation of further security applications and the development of different circuit functions and control. The work is being supervised by Edlyn Levine and Ron Walsworth.

Biological Measurements

I am leading the investigation into near term biological measurements and applications.

NV NMR

Nithya Arunkumar, Dominik Bucher, and David Glenn have been leading the efforts on the expansion of NV NMR capabilities.

Diamond-Based Dark Matter Detector

Efforts along this direction were originally proposed by Surjeet Rajendran, Nicholas Zobrist, Alex Sushkov, Ron Walsworth, and Mikhail Lukin. Mason Marshall has led recent experimental efforts to realize these ideas by quantifying the small-scale strain distribution in diamond and further methodologies to characterize strain on different length scales. David Phillips, Mark Ku, and I have assisted with these efforts.

Appendix

Jennifer Schloss and John Barry led the experimental work described in Appendix B. I developed the data analysis and robustness tests described in Appendix B.

Editing

I want to also acknowledge Emma Huckestein, JJ Oon, Mark Ku, Connor Hart, Nithya Arunkumar, Kevin Olsson, Shantam Ravan, and Jiashen Tang for providing comments and

feedback on this dissertation.

1.3 Nitrogen Vacancy (NV) Center Defect in Diamond

Nitrogen-vacancy (NV) centers in diamond are a leading modality for sensitive, high-spatial-resolution, wide field of view imaging of microscopic magnetic fields. NV-diamond sensors operate in a wide range of conditions, from cryogenic to well above room temperature, and can serve as broadband detectors of slowly-varying magnetic fields, or as narrow-band detectors of magnetic fields over a wide range of frequencies from near DC to GHz. Full vector magnetic field sensing is possible using the distribution of NV orientations along the four crystallographic directions in diamond.

NV centers function at ambient conditions, and have magnetically, electrically, and thermally sensitive electronic spin ground states with long coherence lifetimes. The NV spin state can be initialized, and the evolution of the spin states can be detected optically, thus allowing precision sensing of magnetic fields and other effects. Magnetic field sensitivity and spatial resolution are determined by the number of NVs in the sensing volume, the resonance linewidth, the resonance spin-state fluorescence contrast, the collected NV fluorescence intensity, and the NV-to-sample separation.

Variation of the experimental setup and measurement protocol allows NV-diamond magnetic imaging to be adapted for a wide range of applications in different fields of research. Although the desired capabilities for each magnetic imaging application vary widely, common requirements include good field sensitivity within a defined frequency range, fine spatial resolution, large field of view, quantitative vector magnetometry, wide field and frequency dynamic range, and flexibility in the bias field and temperature during measurement. For example, imaging for geoscience [1] and cell biology [2] applications generally require high

sensitivity to DC magnetic fields, spatial resolution at the optical diffraction limit, and room temperature operation. In contrast, microelectronics magnetic field imaging [3] can require magnetic field frequency sensitivity up to the GHz range. Applications that do not require simultaneous imaging over a wide-field of view can also leverage scanning magnetometry using single NV centers at the tips of monolithic diamond nanopillars, or in nanodiamonds at the ends of atomic force microscopy cantilevers [4–6].

With proper optimization, NV diamond magnetometry can offer combinations of the above capabilities unattainable using alternative magnetic imaging techniques. The Magnetic Force Microscope (MFM) [7], while offering higher spatial resolution, is limited by small (<100 μm) fields of view, worse DC field resolution (>10 μT), and potential complications due to sensor-sample interactions. Meanwhile, the SQUID microscope, if measuring a room-temperature sample, can only achieve spatial resolution of >150 μm, although with excellent DC sensitivity (<500 fT/$\sqrt{\text{Hz}}$) [8]. Atomic vapor and Hall probe magnetometers have typical spatial resolution >100 μm [9–12]. Finally, other techniques such as Magneto-Optical Kerr Effect (MOKE) [13,14] and other Faraday Effect-based magneto-optical imaging cannot produce reliable, quantitative maps of the vector magnetic field.

This chapter provides an overview of the Quantum Diamond Microscope (QDM), a common approach to ensemble NV wide-field magnetic imaging, and describes specific optimization of the QDM for several applications [1,15]. Schematics of typical QDM setups are shown in Fig. 1.1. The QDM uses an optical microscope and a camera (or photodiode for single point measurements) to measure the fluorescence from an NV layer at the surface of the diamond sensor chip, with the sample placed near to or in contact with the diamond. The local magnetic field of the sample is extracted from each pixel measured, with spatial resolution set by the larger of the NV layer thickness or the diffraction limit, and a map of the magnetic field is thereby constructed. We present the methods needed to image static

and dynamic magnetic fields with the QDM, and briefly discuss imaging of temperature and electric fields. For each type of sample field – narrow-band, broadband, etc. – we describe the quantum control procedures and hardware choices that are necessary for ideal imaging, and emphasize the design trade-offs in optimal sensitivity and resolution limits that can be achieved.

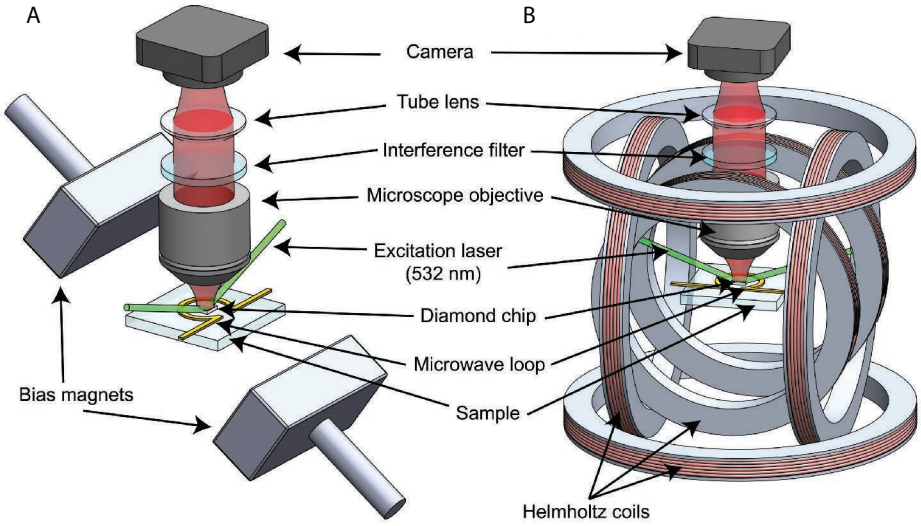

Figure 1.1: Quantum Diamond Microscope (QDM). Examples with (A) permanent magnets and (B) Helmholtz coils to apply a bias magnetic field. In both configurations, 532 nm excitation laser light illuminates the diamond chip and optics collect NV fluorescence onto a camera. The interference filter is chosen to transmit NV fluorescence and, in particular, block scattered excitation light. A planar, gold omega-loop, fabricated onto a substrate, is depicted delivering microwaves to the diamond chip for NV control.

.

1.3.1 NV Ground Electronic States and Bare Hamiltonian

High resolution and sensitive magnetic imaging with the QDM is possible due to the NV electronic and spin level structure [16, 17] and interaction Hamiltonian. An NV center consists of a substitutional nitrogen and an adjacent lattice vacancy defect in a diamond

crystal. A negatively-charged NV has six electrons, with two electrons from nitrogen, one electron from each of the three carbon atoms, and an additional electron from the lattice. These electrons occupy four sp^3 atomic orbitals with electronic spin quantum number $S = 1$. These sp^3 orbitals linearly combine to form four molecular orbitals [18] comprising the ground electronic configuration. The lowest energy state of the ground configuration is the orbital singlet, spin triplet state, $^3A_2$, which has fine, Zeeman, and hyperfine structures as shown in Figure 1.2. The four molecular orbitals also give rise to electronic excited states: orbital-doublet spin-triplet ^3E, and spin-singlet orbital-singlet $^1A_1$ shown in Figure 1.3.

NV magnetometry uses spin-state-dependent fluorescence from electronic state transitions to detect changes to the $^3A_2$ ground state configuration that result from coupling to a sample magnetic field. Therefore, focus is placed on the physics of the $^3A_2$ Hamiltonian. NV centers have C_{3v} point-group symmetry, and are spatially invariant under the C_{3v} symmetry transformations (the identity, two 120° rotations about the N-V axis, and three vertical reflection planes). NV centers also have a quantization axis along the NV axis (called the NV z-axis, or the crystallographic [*111*] direction). The $^3A_2$ electronic ground state is an orbital singlet and spin triplet manifold, with bare ground-state Hamiltonian [19]

$$\frac{\hat{H}_{gs}}{h} = \hat{S} \cdot \mathbf{D} \cdot \hat{S} + \hat{S} \cdot \mathbf{A} \cdot \hat{I} + \hat{I} \cdot \mathbf{Q} \cdot \hat{I}, \tag{1.1}$$

where h is Planck's constant and $\hat{S} = (\hat{S}_x, \hat{S}_y, \hat{S}_x)$ and $\hat{I} = (\hat{I}_x, \hat{I}_y, \hat{I}_x)$ are the dimensionless electron and nitrogen nuclear spin operators, respectively. The first term is the fine structure splitting due to the electronic spin-spin interaction, with the fine structure tensor $\mathbf{D}$ [20]. The second term is the hyperfine interaction between NV electrons and the nitrogen nucleus with the hyperfine tensor $\mathbf{A}$. The third term is the nuclear electric quadrupole interaction, with electric quadrupole tensor $\mathbf{Q}$. Under the C_{3v} symmetry of the NV center, $\mathbf{D}$, $\mathbf{A}$, and

Q, are diagonal in the NV coordinate system [21, 22], and $\hat{H}_{gs}$ can be written as [16]

$$\frac{\hat{H}_{gs}}{h} = D(T)\left[\hat{S}_z^2 - \hat{S}^2/3\right] + A^{\parallel}\hat{S}_z\hat{I}_z + A^{\perp}\left[\hat{S}_x\hat{I}_x + \hat{S}_y\hat{I}_y\right] + P\left[\hat{I}_z^2 - \hat{I}^2/3\right]. \tag{1.2}$$

Here, $D(T)$ is the fine structure term called the zero-field splitting (ZFS), $A^{\parallel}$ and $A^{\perp}$ are the axial and transverse hyperfine terms, and P is the nuclear electric quadrupole component. Two important features of the ground state are evident from the Hamiltonian. First, the $^3A_2$ $m_s = \pm 1$ magnetic sublevels and the $m_s = 0$ have $D(T)$ difference in energy. $D(T)$ is temperature dependent due to spin-spin interaction changes with the lattice spacing [23, 24], with $D \sim 2.87$ GHz and $dD/dT \approx -74.2$ kHz/K [25] at room temperature. Second, the $^3A_2$ electronic states have an additional hyperfine energy splitting $A_{gs}^{\parallel}\hat{S}_z\hat{I}_z$ due to the nitrogen nucleus. $I = 1$ for a ^{14}N nucleus while $I = 1/2$ for a ^{15}N nucleus. The energy level diagrams for ^{14}N and ^{15}N are shown in Figure 1.2. Hyperfine parameters are $A_{14N}^{\parallel} \approx -2.14$ MHz, $A_{14N}^{\perp} \approx -2.70$ MHz, $P_{14N}^{\parallel} \approx -5.01$ MHz, $A_{15N}^{\parallel} \approx 3.03$ MHz, $A_{15N}^{\perp} \approx 3.65$ MHz [26].

Crystal stress in the diamond also contributes to the $^3A_2$ Hamiltonian. This is expressed as [27–29],

$$\frac{\hat{H}_{str}}{h} = M_z\hat{S}_z^2 + M_x(\hat{S}_x^2 - \hat{S}_y^2) + M_y(\hat{S}_x\hat{S}_y + \hat{S}_y\hat{S}_x) + N_x(\hat{S}_x\hat{S}_z + \hat{S}_z\hat{S}_x) + N_y(\hat{S}_y\hat{S}_z + \hat{S}_z\hat{S}_y). \tag{1.3}$$

Here M_x, M_y, M_z, N_x, and N_y are stress-dependent amplitudes. The M_z term contributes to the zero-field splitting, while the other terms may be negligible or suppressed depending on the experimental conditions (such as applied magnetic field [30]). The NV spin sensitivity to this spin-stress induced interaction can be used to image internal or external diamond stress [31], which is important for diamond material characterization. However, for imaging external magnetic fields, we consider NV stress sensitivity as a potential limitation.

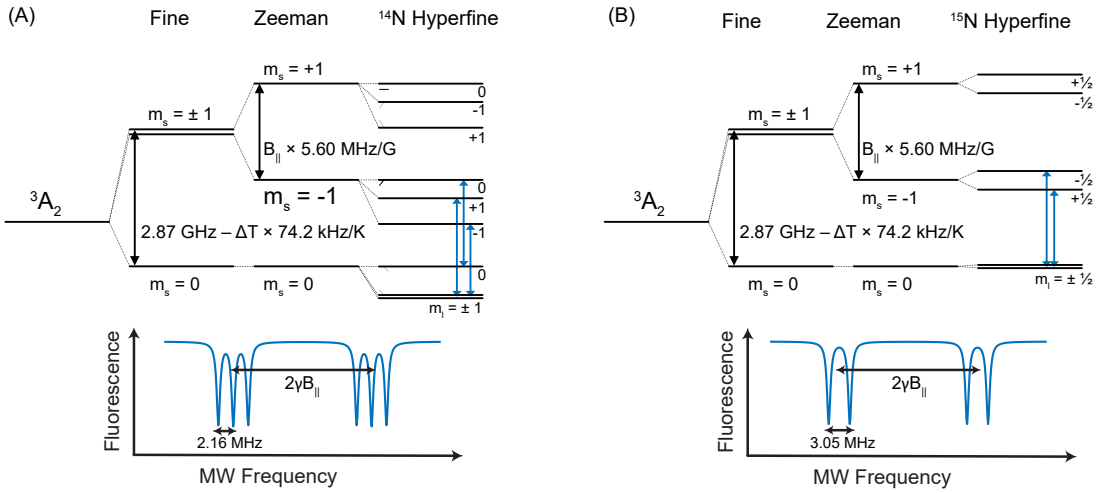

Figure 1.2: NV Ground State Configurations and ODMR Spectra. (A) ^{14}N hyperfine states and (B) ^{15}N hyperfine states. Schematic optically-detected magnetic resonance (ODMR) spectra are shown with Zeeman splitting and hyperfine splitting for ^{14}N and ^{15}N. The hyperfine energy levels for ^{14}N are further shifted by quadrupolar interactions.

1.3.2 NV Electronic Transitions

The NV first excited electronic configuration has an orbital-doublet, spin-triplet state, ^3E shown in Figure 1.3. The two orbital states and three spin states of ^3E combine to form six fine structure states that reduce to three states at room temperature [32], resembling the $^3A_2$ state. ^3E is coupled to the $^3A_2$ ground state by an optical 637 nm zero-phonon line (ZPL). The $^3E \leftrightarrow {}^3A_2$ is a radiative transition that generally conserves the electron spin state m_s as a result of weak spin-orbit interaction [33]. The $^3E \rightarrow {}^3A_2$ ($^3A_2 \rightarrow {}^3E$) transition works for longer [shorter] wavelengths in fluorescence [absorption] as a result of the phonon sideband (PSB). This behavior is similar to Stokes and anti-Stokes shifted transitions [34]. Figure 1.3 also shows the radiative, spin conserving $^1E \leftrightarrow {}^1A_1$ transition which has an infrared 1042 nm ZPL and its own sideband structure.

Nonradiative transitions between states of different spin multiplicity exist between

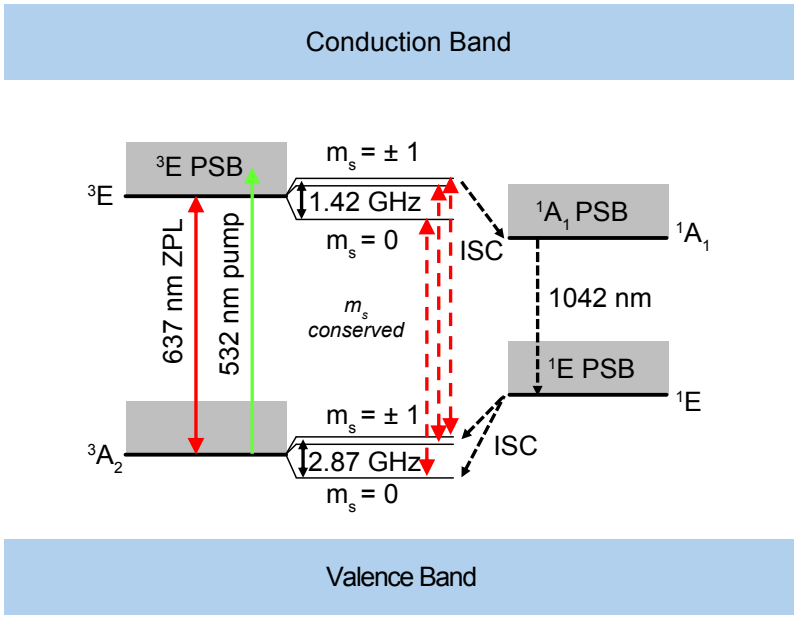

Figure 1.3: NV Radiative and Non-radiative State Transitions. Radiative $^3E \leftrightarrow ^3A_2$ transition with optical 637nm zero-phonon line (ZPL), and $^1E \leftrightarrow {}^1A_1$ transition with non-optical 1042 nm ZPL. Phonon sidebands (PSBs) can shift the transition frequencies. Non-radiative intersystem crossing (ISC) mediated transitions exist between ^3E and $^1A_1$, and ^1E and $^3A_2$.

^3E and $^1A_1$, and between ^1E and $^3A_2$. These nonradiative transitions are caused by an electron-phonon mediated intersystem crossing (ISC) mechanism, and do not conserve spin. The probability of the ISC transition occurring for the ^3E to $^1A_1$ is only non-negligible for $m_s = \pm 1$ states of ^3E and is characterized by the ISC rate of transition [18]. Similarly, the ISC transition probability from ^1E to the $m_s = 0$ state of $^3A_2$ is approximately 1.1 to 2 times that of the ISC transition from ^1E to the $m_s = \pm 1$ states of $^3A_2$ [35, 36]. These state-selective differences in the ISC transition rate allow for spin polarization of the NV under optical excitation, typically from 532 nm laser illumination.

1.3.3 Optical Pumping and Spin Polarization

An optical driving field from a pump laser is applied in order to spin polarize the NV electronic state at the start of a QDM measurement. This pump laser is also used at the end of a measurement to read out the final NV spin state through the fluorescence intensity. NV optical pumping takes advantage of the m_s-selective nonradiative ISC decay pathway [35,36]. An NV that is optically excited from $^3A_2$ to ^3E state by a 532 nm photon, decays along either the optically radiative $^3E \rightarrow {}^3A_2$ pathway or the non-optical, ISC mediated $^3E \rightarrow^1 A_1 \rightarrow^1 E \rightarrow {}^3A_2$ pathway. The m_s-selectivity of the ISC will preferentially depopulate the $m_s = \pm 1$ spin projection states. NVs starting in the $^3A_2$ $m_s = \pm 1$ sublevel are eventually pumped (on average, after a few pump photon absorption cycles) into the $^3A_2$ $m_s = 0$ sublevel. Typically only $\sim 80\%$ of NVs in an ensemble can be initialized into the $m_s = 0$ state [37], where they remain in a cycling transition. The ^1E state is metastable with a $\sim$200 ns lifetime at room temperature [38–40]. The ^3E upper state has a $t_{3E} \approx 13$ ns lifetime [35, 36], and the $^3A_2 \rightarrow {}^3E$ absorption cross section at $\lambda = 532$ nm [41] is $\sigma = 3.1 \times 10^{-17}$ cm^2 (although there is disparity in the reported 532 nm absorption cross section value and saturation intensity [42]). These corresponds to a $(hc)/(\lambda\sigma t_{3E}) \approx 0.9$ MW/cm^2 saturation intensity, where c is the speed of light.

The ISC is also responsible for the reduced fluorescence intensities of NVs in the $m_s = \pm 1$ sublevels, since they emit fewer optical photons when returning to the $^3A_2$ state through the ISC mediated pathway. The fractional fluorescence difference between NVs in the $m_s = \pm 1$ sublevels and NVs in the $m_s = 0$ sublevel is called the fluorescence contrast, and can be as large as $\sim$20% for a single NV [43]. The fluorescence intensity from an optically pumped NV diamond chip therefore indicates the percentage of the NVs in the $m_s = 0$ state, or in the $m_s = \pm 1$ states. A transition of NVs from the $m_s = 0$ to the $m_s = \pm 1$ state, e.g., induced by a resonant MW field, drops the fluorescence as more NVs

follow the ISC mediated decay transition. This is the mechanism underlying optical readout for QDM imaging.

1.3.4 Microwave Driving Field

A MW driving field resonant with the $m_s = 0$ to $+1$ or -1 transitions induces Rabi oscillations, transferring the NV population from one sublevel to the other, and creating superpositions of m_s states. Either a continuous-wave (CW) or a pulsed MW field can be used. The length of the MW pulse determines its impact on the NV population: π pulses are of sufficient duration to transfer the NV population from the $m_s = 0$ to $m_s = 1$ when the NVs are initialized in the $m_s = 0$ state; $\pi/2$ pulses are of duration to create an equal superposition of m_s states.

Applying resonant CW MWs simultaneously while optically pumping of the NVs to the $m_s = 0$ sublevel results in MW-induced transfer of the NV population out of the $m_s = 0$ sublevel, spoiling the optical spin polarization and decreasing the emitted fluorescence intensity. Measuring the NV fluorescence intensity as a function of the probing MW frequency is called Optically-Detected Magnetic Resonance (ODMR) spectroscopy [44]. Simulations of ensemble NV ODMR spectra for NVs with ^{14}N and ^{15}N isotopes are shown in Figure 1.2. The known dependencies of the $^3A_2$ sublevel energy on external fields allow conversion of these ODMR spectra into magnetic field, electric field, temperature, and crystal stress information.

1.3.5 Static Magnetic Bias Field and Zeeman Splitting

A static magnetic field $\mathbf{B}_0$ causes a Zeeman interaction in the $^3A_2$ state, written as

$$\frac{\hat{H}_{mag}}{h} = \frac{\mu_B}{h}\mathbf{B}_0 \cdot \mathbf{g} \cdot \hat{S} = \frac{g_e \mu_B}{h}(B_{0x}\hat{S}_x + B_{0y}\hat{S}_y + B_{0z}\hat{S}_z). \tag{1.4}$$

Here, $\mu_B = 9.27 \times 10^{-24}$ J/T is the Bohr magneton, $\mathbf{g}$ is the electronic g-factor tensor (which is nearly diagonal), $g_e \approx 2.003$ equal to the NV center's electronic g-factor [16], and $\gamma = g_e \mu_B / h \approx 28.7$ GHz/T is the NV gyromagnetic ratio. The Zeeman interaction lifts the degeneracy between the $m_s = \pm 1$ sublevels, and for $|\mathbf{B}_0|$ along the N-V axis, the $m_s = \pm 1$ sublevel energies split linearly with $|\mathbf{B}_0|$ while the $m_s = 0$ sublevel is unaffected. The nuclear Zeeman terms are considered negligible and have been excluded.

A sufficiently large bias magnetic field makes the Zeeman term dominant in the Hamiltonian. Otherwise, terms including stress and electric field would dominate with the Zeeman term acting as a perturbation, reducing magnetic field sensitivity and complicating the data analysis. For magnetic imaging, both the static bias fields, which are part of the QDM, and the sample magnetic fields, contribute to the Zeeman interaction.

1.3.6 Sensing Fields and Parameters

QDM experiments create a two dimensional image of the magnetic fields from a sample containing a distribution of magnetic field sources. It is also possible to image a sample's temperature distribution and electric fields.

The sample magnetic field is generated by field sources, such as current densities or magnetic dipoles, with either known or unknown distributions. Measurement of the sample magnetic field can be used for the inverse problem of estimating an unknown source distribution under certain conditions [45–47]. The form of the sample magnetic field in terms of its sources is:

$$\mathbf{B_s}(\mathbf{r}, \mathbf{t}) = \frac{\mu_0}{4\pi} \int d^3 r' \frac{\mathbf{J}(\mathbf{r}', \mathbf{t}) \times (\mathbf{r} - \mathbf{r}')}{|\mathbf{r} - \mathbf{r}'|^3} \tag{1.5}$$

where $\mathbf{J}$ is the current density of the sample, $\mathbf{r} - \mathbf{r}'$ is the distance from a magnetic source at $\mathbf{r}'$ to an observation point at $\mathbf{r}$. Eqn. 1.5 is the Biot-Savart Law for static fields,

and applies to fields in the quasistatic regime for which the characteristic system size is small compared to the electromagnetic wavelength. Furthermore, the current oscillations considered are slow enough ($\frac{\omega R}{c} << 1$, where ω is the characteristic oscillator frequency of the magnetic field, R is the length scale of the separation between the source and sensor, and c is the speed of light) to be considered stationary, so the Jefimenko generalization can be neglected.

A sample consisting of small magnetic particles will have a magnetic field composed of single dipole fields of the form

$$\mathbf{B}_s(\mathbf{r}) = \frac{\mu_0}{4\pi}\left[\frac{3\mathbf{n}(\mathbf{n}\cdot\mathbf{m}) - \mathbf{m}}{r^3} + \frac{8\pi}{3}\mathbf{m}\,\delta(\mathbf{r})\right] \tag{1.6}$$

Here $\mathbf{m}$ is the magnetic moment, $\mathbf{n} = \mathbf{r}/r$, and the delta function only contributes to the field at the site of the dipole $\mathbf{r} = 0$. Other typical sample fields, such as the narrowband magnetic field from the Larmor precession of protons can also be derived [48]. Figure 1.4 shows examples of the magnetic fields for a current distribution and a distribution of magnetic dipoles.

The time dependence of the sample magnetic field will determine the QDM measurement protocol. Static and quasi-static sample fields will contribute to the NV Hamiltonian by an additional term in Eqn. 1.4

$$\frac{\hat{H}_{mag}}{h} = \frac{g_e\mu_B}{h}(\mathbf{B}_0 + \mathbf{B}_s)\cdot\hat{S} \tag{1.7}$$

were $\mathbf{B}_s$ is the magnetic field of the sample, which can take the forms given in Eqns. 1.5 and 1.6. The magnitude of the sample field along the NV axis is therefore determined by changes in separation in the ODMR resonance features that result from $\mathbf{B}_s$ in addition to the effect of the bias field. ODMR measurements, with and without the sample, then allow

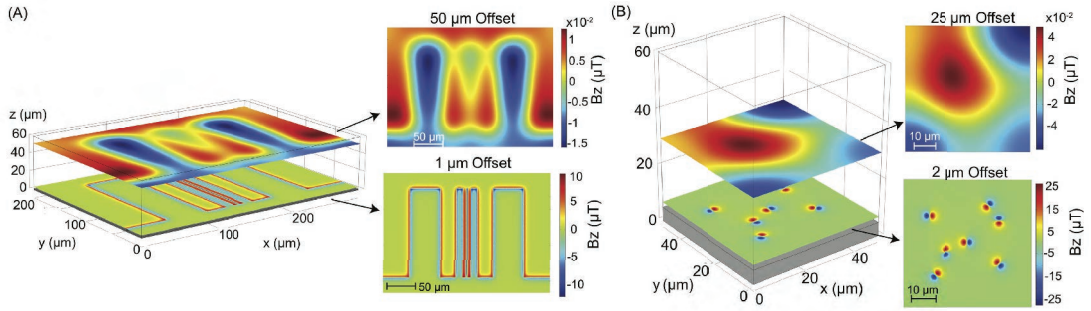

Figure 1.4: Simulated QDM Measurement Planes above Magnetic Samples. Magnetic field distributions from (A) current distributions and (B) magnetic dipole distributions simulated in COMSOL. The NV layer in the QDM measures the sample magnetic field in the x-y plane a distance z above the sample. Two measurement planes at different values of z are shown for each simulation. A smaller stand-off distance between the measurement plane and the sample gives a magnetic field image with higher spatial resolution.

determination of the unknown $\mathbf{B}_s$ field. Reasonable assumptions can be made to determine $\mathbf{B}_s$ without having to take multiple measurements [1]. A time-varying sample magnetic field with frequency components near the 2.87 GHz ZFS will in turn induce NV spin transitions if the $\mathbf{B}_0$ bias field has been tuned to the appropriate Zeeman splitting. Sweeping the $\mathbf{B}_0$ field will then locate the frequency of the sample fields, with magnitude determined by the ODMR contrast depth and line width.

Electric field and temperature distributions from the sample will also change the NV spin states. The external sample electric field $\mathbf{E}_s = (E_{sx}, E_{sy}, E_{sz})$ adds to the internal local electric fields [49], $\mathbf{E}_{loc} = (E_{loc,x}, E_{loc,y}, E_{loc,z})$ in the diamond, e.g., induced by a high density of P1 (Nitrogen) centers, such that $\mathbf{E}_{tot} = \mathbf{E}_s + \mathbf{E}_{loc}$ contribute to the Hamiltonian in Eqn. 1.2 [20]

$$\frac{\hat{H}_{el}}{h} = d_{\parallel} E_{tot,z} \hat{S}_z^2 - d_{\perp} E_{tot,x} (\hat{S}_x^2 - \hat{S}_y^2) + d_{\perp} E_{tot,y} (\hat{S}_x \hat{S}_y + \hat{S}_y \hat{S}_x) \tag{1.8}$$

Here, $d_{\parallel}$ and $d_{\perp}$ are coupling constants related to the NV electric dipole moment; $d_{\parallel} \ll d_{\perp}$

with $d_{\parallel} = 3.5 \times 10^{-3}$ Hz/(V/m) and $d_{\perp} = 0.17$ Hz/(V/m) [50, 51]. For the typical scale of sample electric fields, coupling to the NVs is small compared to sample magnetic fields of interest. Hence electric fields do not cause noticeable shifts in ODMR resonances for typical QDM magnetic imaging experiments. External temperature variations, e.g., from the sample, couple to the NV by the temperature dependence, $D(T)$, of the ZFS [23]. Changes in temperature of the diamond due to the sample temperature field will therefore result in a common mode shift ($dD/dT = -74.2$ kHz/K [23]) of the ODMR resonance, which is distinct from the effect of magnetic fields.

1.4 NV Control and Sensing

The large toolbox of QDM sensing protocols allows for imaging magnetic fields over a wide range of characteristic timescales. Figure 1.5 shows a schematic of the most commonly used sensing protocols. The interplay and timing of the laser pulses and MW pulses determines the basic properties of the techniques introduced in this section.

1.4.1 DC Magnetometry: Static and Low-Frequency Fields

Three established QDM sensing protocols exist for measuring static (DC) and slowly-varying magnetic fields: continuous-wave (CW) ODMR, pulsed ODMR, and Ramsey magnetometry. These protocols have been used to sample time-varying magnetic fields up to ∼1 MHz in a single-pixel experiment [52].

CW ODMR

CW ODMR is a robust and simple method that can image the vector components of a magnetic field in the QDM modality. Due to easy implementation, CW ODMR is the most common technique used for QDM applications. Continuous laser pumping, MW driving, and

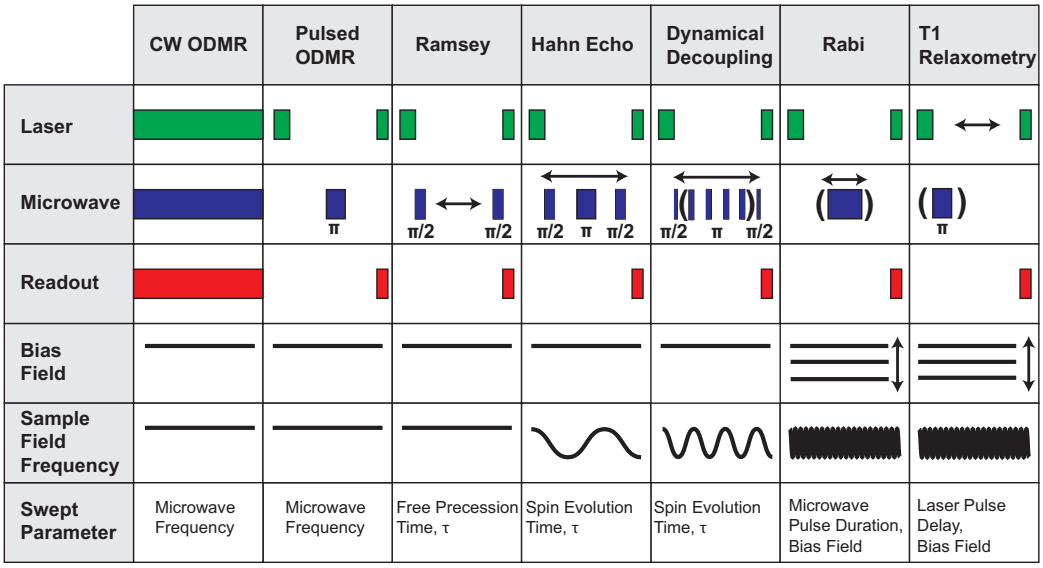

Figure 1.5: NV Measurement Protocols. Schematic of timing and duration of laser pulses, MW pulses, and readout sequences relative to the field being sensed for common NV diamond protocols. Swept parameters are indicated by arrows. Straight lines for the bias and sample fields indicate static magnetic fields, including the swept static bias field for Rabi and T_1 Relaxometry; sinusoidal curves represent time dependent sample fields, which are very high frequency for Rabi and T_1 Relaxometry.

fluorescence readout are performed simultaneously, as shown in Figure 1.5. The laser is used to both pump the NVs into the $m_s = 0$ spin state and to probe spin states of the population via the NV fluorescence. The frequency of the MW drive is swept in time and synchronized with the readout. A decrease in fluorescence occurs when the MW frequency matches the NV resonance due to the spin state dependence of NV photon emission described previously.

Figure 1.6(A) shows an example where a change in $\mathbf{B}_0$ shifts the line center of the resonance feature. For an NV ensemble, the resonance lineshape – often modeled as a Lorentzian or Gaussian – is parametrized by the center frequency, linewidth, and fluorescence contrast. The center frequencies of every NV resonance feature are fit to the appropriate Hamiltonian to extract the desired magnetic field, strain, temperature, and electric field. In

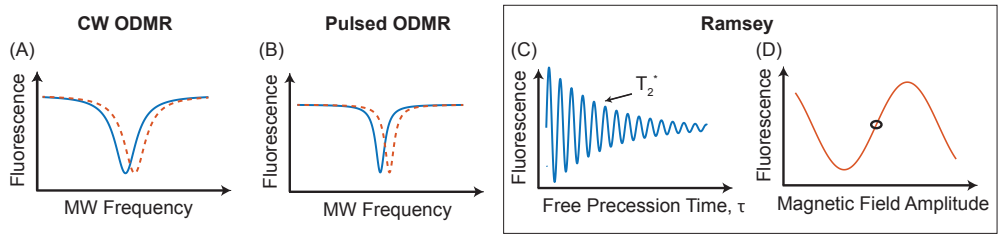

Figure 1.6: DC Magnetometry Protocols. (A) Example CW ODMR lineshape before (blue) and after (red) change in magnetic field. (B) Example pulsed ODMR lineshape before (blue) and after (red) change in sample magnetic field. (C) Schematic Ramsey Free Induction Decay (FID) to determine dephasing time (T_2^*) and optimal sensing time, τ_{sense}. (D) Schematic Ramsey Magnetometry Curve. Free precession time is fixed to be the point of maximum slope of the FID curve closest to T_2^*, indicated by a black circle. Accumulated phase from sample field results in an oscillatory response of fluorescence with changing amplitude.

a magnetic imaging experiment, this analysis yields $\mathbf{B}_0 + \mathbf{B}_s$, from which the magnetic field of the sample can be determined [15, 52, 53].

Measuring the entire resonance spectrum in CW ODMR limits the sensitivity and the temporal resolution of the measurements, due to the significant fraction of experiment time spent interrogating with probe frequencies that yield no signal contrast. Sparse sampling of the resonance spectrum can improve the sensitivity of the measurement by minimizing dead time. An extreme version of sparse sampling can be achieved using a lock-in modality where the probe frequency is modulated between the points of maximum slope of an ODMR resonance feature [54]. This technique has been extended to monitor multiple ODMR features simultaneously to extract the vector magnetic field by modulating at different frequencies [55]. Frequency-modulated (or Lock-in ODMR) has been performed with bandwidths up to 2 MHz [52], but was demonstrated on a small volume and required high laser and MW intensity beyond that typically employed with QDMs [56].

Pulsed ODMR

CW ODMR suffers from laser repumping of the NV spins through the entire measurement. This simultaneous laser pumping and MW drive spoils the measurement sensitivity as a result of the competing processes of initializing the spin state (laser) and driving transitions (MW drive) [43]. In order to mitigate this power broadening, a pulsed ODMR protocol uses a temporally separated laser initialization, a MW control π pulse, and a laser readout pulse as demonstrated in Figure 1.5. This leads to the decreased linewidths shown in Figure 1.6(B) as compared to CW ODMR. Alteration of the MW power changes the necessary duration of a π pulse, and must be optimized to balance linewidth and contrast of ODMR resonance features [43].

Ramsey

Ramsey spectroscopy [57] determines the magnitude of a DC magnetic field by measuring the relative phase accumulation between the different electronic spin states prepared in a superposition with a $\pi/2$ pulse [58, 59]. A green laser pulse initializes the spin state into the $m_s = 0$ state to begin the sequence. Next, a resonant MW $\pi/2$ pulse prepares the spin into a superposition of the $m_s = 0$ and $m_s = +1$ spin states (or $m_s = -1$ depending on the drive frequency). The system is allowed to evolve under the relevant Hamiltonian for a free precession time, τ. In the simplified scenario where the dynamics are dominated by the magnetic field, the NV superposition state accumulates a phase $\phi = 2\pi\gamma(|\mathbf{B}_0 + \mathbf{B}_s|)\tau$. A second MW $\pi/2$ pulse is applied to project the accumulated phase information onto the relative population of $m_s = 0$ and $m_s = +1$ spin states. A second laser pulse is applied to measure the spin state population through the spin dependent fluorescence of the NV.

To obtain information about the magnetic field, $|\mathbf{B}_0 + \mathbf{B}_s|$, a Ramsey pulse sequence is repeated several times, sweeping the free precession interval such that each measurement is

taken for different τ. The resultant fluorescence contrast signal as a function of τ is known as the Ramsey fringes, illustrated in Figure 1.6(C). By taking a Fourier transform of these fringes, one can locate the position of the dominant frequencies and determine deviations from those set by the bias magnetic field that result from the sample field.

Mapping out the Ramsey fringes is inefficient with respect to speed of the measurement, similar to the inefficiency of the frequency sweep for ODMR. Instead of mapping out the full fringe and taking the Fourier transform, the free precession time, τ_{sense}, is fixed to sample the Ramsey fringe at the point of maximum sensitivity, the point of maximum slope closest to T_2^*. This process maps out a magnetometry curve illustrated in Figure 1.6(D). The steeper the slope of the magnetometry curve, the more sensitive the protocol.

A key feature of Ramsey magnetometry is having both the laser and MWs switched off when the NV electronic spin is accumulating phase via interaction with the magnetic field. The Ramsey protocol is consequently not vulnerable to the power broadening that impacts CW ODMR, and allows use of high MW and laser power to increase the sensitivity [56]. Other benefits of Ramsey magnetometry over CW and pulsed ODMR is that it more efficiently leverages protocols that mitigate dephasing such as spin bath driving and is compatible with sensing in the double quantum basis [21].

1.4.2 AC Magnetometry: Narrowband Fields

A QDM can measure narrowband oscillating magnetic fields using AC magnetometry sequences, including Hahn Echo and Dynamical Decoupling. These pulse sequence protocols act as frequency filters and allow the QDM to operate as sensitive lock-in detector [59] of these AC fields. The frequency range of narrowband signals that are detectable with NV AC magnetometry is ~ 1 kHz to ~ 10 MHz, limited at the low end by NV decoherence and at the high-end by the amplitude of fast MW pulses that can be realistically applied to an

NV ensemble.

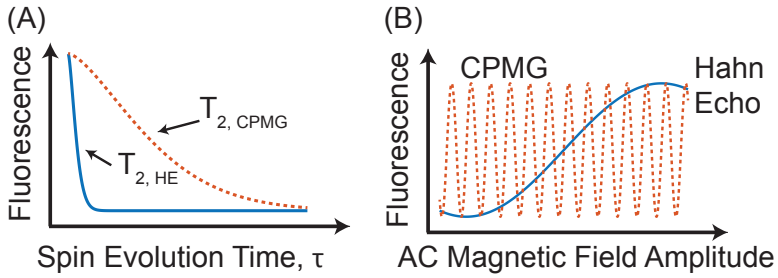

Figure 1.7: AC Magnetometry Protocols. (A) Schematic T_2 decoherence curves for Hahn Echo and CPMG sequences. Improved decoupling from interactions with the spin bath environment results in an extended CPMG T_2 decoherence time compared to the Hahn Echo T_2 (B) Schematic magnetometry curves. Longer T_2 for CPMG leads to increased magnetic field sensitivity, as indicated by the slope of the CPMG magnetometry curve. Hahn Echo is much less sensitive, exhibiting a similar oscillation to CPMG over a much larger magnetic field amplitude range.

Hahn Echo

The addition of a π pulse into the middle of a Ramsey sequence mitigates environmental perturbations that are slow compared to the free precession interval between pulses [59]. This pulse sequence is known as the Hahn Echo sequence [58,60], and results in the refocusing of NV ensemble dephasing such that the limiting measurement timescale becomes the decoherence time T_2 rather than the dephasing time T_2^*. The consequence is improved magnetic field sensitivity, especially for lower frequency signals, because T_2 typically exceeds T_2^* by over an order of magnitude [61]. Figure 1.7(A) demonstrates a decoherence curve when using a Hahn Echo pulse protocol. The spacing between MW pulses acts as a narrowband filter in frequency space. The width of this filter is given by the filter response function [62]. Hahn Echo uses only one π pulse and therefore has a fairly broad filter allowing for sensing of a wide bandwidth of magnetic field frequencies.

To optimally sense external oscillating fields, the spin evolution time, τ, is set to be

$\sim T_2$; however, the frequency of the sensed magnetic field can lead to operation with a non-optimal τ. [59] For a fixed spin evolution time, a change in magnetic field will lead to a difference in phase accumulation that maps onto the total fluorescence, Figure 1.7(B).

Dynamical Decoupling

Building upon the Hahn Echo sequence, dynamical decoupling techniques commonly apply multiple refocusing pulses with spacing determined by the period of the sample field. [59, 63] These additional refocusing pulses result in an advantageous extension of the decoherence time by narrowing the width of the filter response function and reducing sensitivity to magnetic noise outside the bandwidth. In particular, decoupling of the NV from spin-bath-induced magnetic noise improves with additional pulses at the trade-off of making the technique sensitive to a narrower range of frequencies [62, 64]. The extension in the decoherence time, Figure 1.7(A), can lead to a dramatic improvement in magnetic field sensitivity Figure 1.7(B).

The Carr-Purcell-Meiboom-Gill (CPMG) pulse sequence is a dynamical decoupling sequence employing π pulses that rotate the NV about the same axis as it is polarized by the initial $\pi/2$ pulse. Another common sequence, XY8, extends this by choosing the rotation axis for each π pulse in order to suppress the effects of pulse errors. A large family of similar sequences exist, many well known in NMR, to improve NV sensing through more efficient robust control of the NV electronic spin state [65].

1.4.3 Resonant Coupling to External GHz Fields

Applications that require measurement of GHz scale oscillations can leverage interactions between the NV and magnetic signals near the NV resonance as a probe [66–68]. CW ODMR constitutes a simple protocol that can be used in this manner. Measurements of the

contrast and linewidth enable the determination of the optical power and MW power that power broaden the lines, Figure 1.8(A), in addition to other mechanisms that contribute to the ensemble inhomogeneous dephasing [43]. However, this method is not very sensitive and difficult to quantify due to the various ways the contrast and linewidth can vary over a field of view [1]. Alternative methods to CW ODMR include Rabi Driving and T_1 Relaxometry.

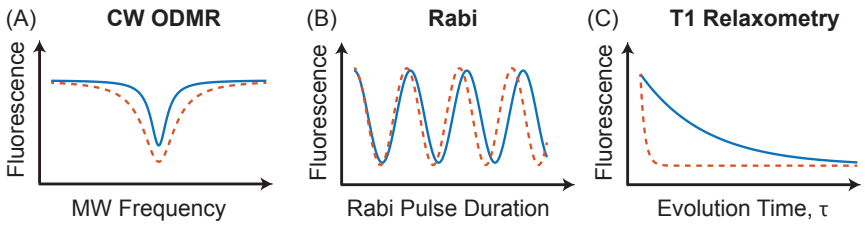

Figure 1.8: GHz Magnetometry Protocols. (A) CW ODMR broadening: increased MW power will increase ODMR fluorescence contrast and linewidth (red). (B) Rabi Oscillation: increased amplitude of the MW field will increase the Rabi frequency (red). (C) T_1 relaxometry: phonon limited T_1 decay rate (blue) is increased (red) by high frequency magnetic noise near the NV resonance frequency.

Rabi Driving

Use of a Rabi sequence provides a more direct way to determine local magnetic fields oscillating at or near GHz frequencies as compared to CW ODMR [67]. Similar to previously discussed protocols, the NV spin state is initiated to the $m_s = 0$ state with a green laser light. A MW drive is left on for a varying amount of time. If the MW drive is on resonance with the NV spin state transitions, for example between $m_s = 0$ and $m_s = +1$ states, the population will be driven back and forth between the spin states. The strength of this GHz drive determines the rate at which the transition is driven. This rate is called the Rabi frequency, and scales with the square root of the input microwave power. Figure 1.8(B) illustrates the increase in Rabi frequency as a function of increasing amplitude of the MW driving field.

T_1 Relaxometry

When the NV is initially polarized into the $m_s = 0$ state with green illumination, there is a characteristic timescale over which the spin population decays back to a thermally mixed state. This timescale is the longitudinal (spin-lattice) relaxation time T_1 and can be up to 6 ms when dominated by phonon interactions at room temperature [69]. However, T_1 can be spoiled by the presence of magnetic frequency noise or other paramagnetic spins at the NV resonance frequency, as shown in Figure 1.8(C) [70]. The local bias field can be swept to change the characteristic noise frequency the measurement is sensitive to.

1.5 General Equipment Considerations for Magnetometry Experiments

This section will provide an introduction to the major components used is most NV diamond ensemble experiments and considerations for choosing components. Special notice will be given on components whose characteristics are currently limiting the achievable performance of NV diamond sensors.

1.5.1 General Design Considerations

Table 1.1 summarizes equipment parameters that optimize QDM operation. While some of the above specifications are technique- or application-specific, this table describes general design choices that affect all QDM instruments.

1.5.2 Diamond

Properties of the diamond chip that impact QDM performance include NV layer thickness, NV concentration, isotope and impurity concentration, and diamond cut. These properties

Design choice	**Diamond**	**Laser**	**Microwaves**	**$\mathbf{B}_0$ field**
Considerations	- NV density affects the sensitivity - Inhomogeneity in strain, density, and magnetic environment spoils the sensitivity - Match the NV layer thickness and sample thickness	- field of view sets laser intensity - Laser intensity noise can limit sensitivity - Laser polarization addresses different NV orientations - Homogeneous illumination is desirable	- Amplitude and phase instability affect sensitivity. - Amplitude homogeneity is desirable	- A $\mathbf{B}_0$ gradient can cause varying sensitivity uniformity
Design choice	**Optics**	**Camera**	**Diamond mount**	**Magnetic environment**
Considerations	- Microscope objective sets the collection efficiency and optical diffraction limit - Microscope components set the magnification and field of view size	- Pixel size should oversample other resolution limitations (e.g., optical diffraction) - Frame rate x well depth x number of pixels set the best-possible sensitivity - Transfer rate and buffer size can limit the maximum experiment rate - Camera efficiency is worse than photodiode efficiency	- Aim for high thermal and mechanical stability during an experiment	- Control background field (e.g., Earth's field, electronics, ...)

Table 1.1: General QDM hardware considerations that apply to all measurement techniques

are controlled for in the diamond fabrication process. Single-crystal diamond substrates used for QDM imaging are grown in one of two ways. One technique, high-pressure high-temperature (HPHT) growth, resembles natural diamond formation, requires an anvil press at ∼1700 K and 5 GPa, and produces diamond samples with ∼100 ppm nitrogen density (known as Type Ib diamonds). The second technique, chemical vapor deposition (CVD), grows diamond substrates layer-by-layer from a plasma and yields diamond samples with nitrogen concentration (∼ppb, known as Type IIa diamonds).

On top of these single crystal diamond substrates, a thin layer of N-doped diamond is grown. Imaging a thin two-dimensional magnetic sample is optimal when the NV layer

thickness is comparable to the magnetic source separation. The typical NV layer thickness for QDMs ranges from ∼10 nm to ∼100 µm. There are several methods available to make NV layers of varying thickness:

1. N^+ or N_2^+ is implanted in a type IIa diamond with ppb impurity density to create a ∼10-100 nm shallow layer. Annealing the diamond improves the NV yield and NV density [71].

2. A ppm-density nitrogen-rich layer is grown on top of a type IIa diamond substrate using CVD. After growth, electron-irradiation of the diamond introduces vacancies and annealing improves the NV yield by converting substitutional nitrogen atoms (P1 centers) into NVs with a ∼10% conversion rate [72]. The nitrogen rich layer can be several microns down to several nanometers in thickness [73].

3. Instead of irradiating in #2, the small fraction of naturally occurring NVs [56] are used and can be preferentially oriented along one of the crystallographic directions (instead of equal NV fractions along all four orientations). Removing three of the NV orientations can improve the magnetic field sensitivity by $\sim 2\times$, but can come at the expense of reduced NV density and fluorescence [74] along with high background Nitrogen concentrations.

4. Similar to #2, nitrogen is temporarily introduced during CVD diamond growth to create a few-nm nitrogen-rich layer, followed by a nitrogen-free diamond capping layer to separate the N from the surface. NV centers are then created by electron-irradiating and annealing. This technique is called delta doping [75]. The cap layer adds to the standoff distance, so the surface-layer version in #2 is often preferred, or the cap layer is etched away [76].

5. An HPHT diamond with uniform NV volume density can be cut into ∼35 µm thin slice. Alternatively, an HPHT diamond can be implanted with helium ions to form a shallow NV layer [77–79].

The NV density in the NV layer is optimized to achieve a desired magnetic field sensitivity. High NV density yields more fluorescence intensity and good photon shot noise. However, the greater density of P1 paramagnetic impurities – required for high NV yield – contributes to magnetic inhomogeneity, thereby broadening ODMR resonances and spoiling magnetic field sensitivity. Optimal sensitivity therefore requires balancing the ODMR linewidth and contrast with the NV density in Eq. 1.9. Conditions for a favorable ratio of the two NV charge states, NV^- / NV^0, are also needed to minimize the NV^0 contribution to background fluorescence, which spoils the NV^- contrast used for imaging [80], discussed further in Chapter 4.

The performance of diamonds with different C and N isotopes is an important consideration. The ^{15}NV (spin-1/2 nucleus) is more optimal for QDM imaging because it gives greater ODMR contrast and requires a narrower range of MW probe frequencies than the more common ^{14}NV (spin-1 nucleus). However, because ^{15}N is the less abundant isotope, diamonds fabricated without special procedures for isotopic control will typically be dominated by ^{14}N.

Magnetic inhomogeneity from ^{13}C (spin-1/2) and paramagentic P1 defect centers limits the NV T_2^*; thus, isotopically-purified ^{12}C ($I = 0$) diamonds are ideal [21, 58]. For diamonds with a 1.1% natural abundance of ^{13}C present, it is advantageous to increase the P1 density resulting in larger NV density without contributing too much to the P1-limited T_2^* [79]. An NV layer fabricated in an isotopically-enriched ^{12}C layer can reduce the ODMR linewidth. However, this may be irrelevant for NVs shallower than ~ 10 nm, due to magnetic inhomogeneity introduced by electrons on the diamond surface [81].

Synthetic diamond chips used in QDMs are available in several cuts. The most common are diamonds with the top face along the [*100*] plane and the sides along the [*100*] or [*110*] planes (Figure 1.9A). The NVs in these diamonds point roughly 35° out of the plane. Less common diamond cuts include [*110*] and [*111*] top faces. The former has two NV orientations in-plane, while the latter has one NV orientation pointing normal to the face. Other more exotic diamond cuts exist, for instance Ref. [67] used a diamond with a [*113*] NV layer. The choice of diamond cut does not usually impact the QDM performance. However, different cuts of diamond have different availability and pricing due to the challenge of producing crystals that are not grown along diamond's preferential growth axis. Surface termination effects can be of impact [82].

The impact of diamond characteristics on specific QDM techniques is summarized as follows:

1. For CW ODMR imaging, the laser and microwave linewidth broadening should match the diamond T_2^* (1.10).

2. For Ramsey imaging, the diamond T_2^* limits the phase accumulation time.

3. For dynamical decoupling imaging, the diamond T_2 limits the phase accumulation time (depending on the magnetic noise spectrum and pulse sequence).

4. For Rabi and T_1 imaging, the diamond T_2^* sets the spectral filter function. The intrinsic NV T_1 depends on the NV density and depth.

1.5.3 Laser

A QDM typically uses a 532 nm solid-state laser for optical pumping due to availability and performance. The green pump laser intensity is weak, typically ∼10 - 1,000 W/cm^2, when illuminating a few-mm field of view, which can be a limitation for pulsed-readout

techniques. The NV $^3A_2 \rightarrow {}^3E$ optical transition is $\sim$ hundreds of nanometers wide due to the phonon sideband, which allows for laser excitation wavelengths ranging from $\sim$470 nm to 637 nm [83]. Past experiments have pumped the NVs with 532 nm frequency-doubled Nd:YAG and Nd:YVO_4 lasers, 637 nm and 520 nm diode lasers and LEDs, 594 nm HeNe lasers, argon-ion laser lines (457, 476, 488, 496, and 514 nm), and supercontinuum lasers with an acousto-optic tunable filter [84–86]. There have been attempts to find the illumination wavelength with the most favorable cross-section and NV^-/NV^0 charge-state ratio, but this is still an active area of research for ensembles [87] (see Chapter 4. Since the NV readout measures a fluorescence intensity, fluorescence intensity instability from the laser or the optics must be minimized for the QDM magnetic sensitivity to reach the photon shot-noise limit.

The $^3A_2 \rightarrow {}^3E$ optical transition is dipole-allowed when illuminating with light polarized in the xy plane of the NV [39]. Thus, in a projection magnetic microscopy experiment (Figure 1.9C) a laser polarization is chosen that favors the optical absorption selection rules for the selected NV orientation. If all NV orientations are interrogated, a laser polarization is selected that addresses all NV orientations with comparable strength. Increasing the laser illumination power increases the diamond and sample heating on approximately linear scaling, while the photon-shot-noise limit only increases as the square root of the laser power. Furthermore, as the fractional photon shot noise improves, the analog-to-digital conversion bit depth must also improve to avoid being quantization-noise-limited.

Increasing the illumination intensity improves the NV fluorescence intensity, the photon shot noise, and sometimes the ODMR lineshape. The available laser intensity affects the various QDM techniques in the following ways:

1. For CW ODMR imaging, varying the laser intensity affects the ODMR linewidth (Figure 1.10).

2. For pulsed imaging experiments, ideally the laser intensity should be close to optical saturation. Weaker laser intensity, longer t_I, and longer t_R will worsen the experimental temporal resolution.

1.5.4 Optical Sensor

QDM camera selection for a targeted application requires consideration of the expected photon collection rate from the NV layer, camera read-noise and dark-current noise, well depth, global/rolling shutter capability, software and external triggering, frame rate, data transfer rate, pixel size, and quantum efficiency [88]. For experiments with a high photon count rate, the camera must handle enough (10^{13} to 10^{15}) photoelectrons per second without saturating. Here, the pixel well depth, number of pixels, quantum efficiency, and frame rate are the important quantities to consider, because they determine the maximum photon count rate for fluorescence detection.

The camera frame rate can limit the experimentally-realizable temporal resolution. Increasing the camera frame rate is possible by using only a fraction of the sensor. However, the trade-off between frame rate and number of pixels is generally not favorable with regards to maximizing total photoelectrons/s. Alternatively, if the photon count rate is low, parameters like the read noise and dark-current noise should be minimized while the quantum efficiency is maximized. For pulsed experiments, a slow camera frame rate can limit the experiment repetition rate and sensitivity.

The camera sensor size determines the microscope magnification for a desired field of view. The microscope spatial resolution can be set by the camera pixel size (rather than the optical diffraction limit) if the camera pixels are too widely spaced for the microscope magnification. The diffraction-limited spatial resolution should be oversampled by at least $2\times$ to avoid having the pixel size spoil the diffraction-limited spatial resolution.

As previously mentioned, the optical readout time, t_R, must be balanced with the minimum camera exposure time, and the maximum camera frame rate for pulsed QDM experiments. Specifically:

1. Sensitivity is lost for experiments with a measurement time, t_{meas}, faster than the camera frame rate, because the camera is too slow to acquire a new frame at the rate it takes to do each experiment.

2. Experiments for which the minimum camera exposure time is longer than t_R require the readout laser to be off for the duration of the time difference.

1.5.5 Static Magnetic Field

The QDM bias magnetic field $\mathbf{B}_0$ can be provided by electromagnets (Helmholtz coil sets, solenoids, and C-frame/H-frame electromagnets) or permanent magnets [1, 48, 89] as shown in Figure 1.1. Electromagnets allow us to select arbitrary $|\mathbf{B}_0|$ up to a few tesla. However, they require a stable current supply, may need water cooling for the magnet, and can add to sample and system heating. Permanent magnets allow higher $\mathbf{B}_0$ in a more compact instrument, though the applied $\mathbf{B}_0$ can drift with temperature.

The choice of bias field amplitude $|\mathbf{B}_0|$ depends on the samples being measured. Soft magnetic samples that might have their magnetization changed by an applied magnetic field require $|\mathbf{B}_0|$ to be minimized. This has the added benefit that small $|\mathbf{B}_0|$ typically implies a small $|\mathbf{B}_0|$ gradient across the field of view. A large $|\mathbf{B}_0|$ can be beneficial when imaging paramagnetic minerals, since the magnetization from paramagnetic particles scales with $|\mathbf{B}_0|$ until saturation [90]. For Rabi imaging or T_1 magnetometry, $|\mathbf{B}_0|$ is chosen such that the NV spin transition frequency matches the AC sample frequency being interrogated [67, 89]. Due to nitrogen nuclear polarization, operating a bias magnetic field $|\mathbf{B}_0|$, ~30-50 mT can

improve the NV fluorescence contrast [91, 92]. Finally, $|\mathbf{B}_0| = 0$ is an intuitive choice for NV thermometry or electrometry experiments (Figure 1.9B) due to favorability of the Hamiltonian response. [30]

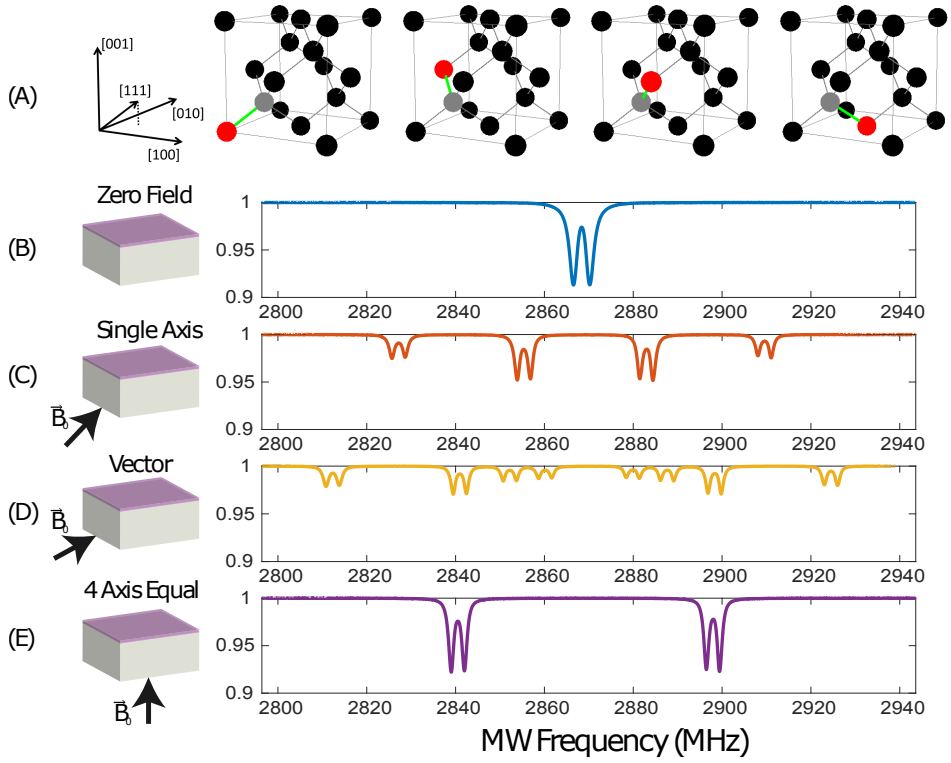

Figure 1.9: Experimental ODMR Spectra for Different Bias Magnetic Field Magnitudes and Orientations. (A) Example of four possible NV orientations in the diamond lattice, and the crystallographic directions. (B) Example ensemble NV ODMR spectrum with $|\mathbf{B}_0| = 0$. The resonance is centered at ~2.87 GHz, but splits into two peaks around this resonance frequency due to the ^{15}N hyperfine coupling. Strain and electric field also contribute to the ODMR lineshape and broadening, and can cause a variety of lineshapes at $|\mathbf{B}_0| = 0$ for different samples. (C) Ensemble NV ODMR spectrum with $|\mathbf{B}_0|$ pointing along one axis. The frequency separation between the outer resonance peaks is proportional to the applied field. The inner peaks are from the three other NV orientations overlapping with each other due to equal Zeeman interactions for each. The ^{15}N hyperfine interaction again splits each resonance into a doublet. (D) Ensemble NV ODMR spectrum with $|\mathbf{B}_0|$ orientation such that each axis has different projection of bias field. (E) Ensemble NV ODMR spectrum with $|\mathbf{B}_0|$ along the [001] direction, such that each NV orientation has the same Zeeman interaction. The peak separation is proportional to the $|\mathbf{B}_0|$ field projection along the NV axes.

The direction of $\mathbf{B}_0$ also factors into the specific QDM application [1]. Alignment of $\mathbf{B}_0$ along the N-V axis ([*111*] crystallographic direction) allows for interrogating the NVs along this crystallographic direction, Figure 1.9C. This approach allows optimization of the other measurement parameters, e.g., the optical polarization, which maximizes the fluorescence and contrast from the selected NV orientation.

Alternatively the $\mathbf{B}_0$ magnitude and direction can be chosen such that each NV orientation has different resonance frequencies and non-overlapping spectra, Figure 1.9D. This approach allows reconstruction of vector magnetic field information from the eight NV resonance frequencies. $\mathbf{B}_0$ can also be aligned with the crystallographic [100] or [110] directions, such that the resonance frequencies for different NV orientations are degenerate, leading to improved contrast. If $\mathbf{B}_0$ is aligned along the [100] direction with a diamond cut along [100], the magnetic field projection direction is normal to the chip, though the Zeeman shift is $\sqrt{3}$ times weaker than for $\mathbf{B}_0$ along the [111] direction (Figure 1.9E). Finally, there may be some experiments where the choice of $\mathbf{B}_0$ is forced by the sample being tested. This could cause the NV ODMR lines to overlap, making it difficult to resolve the resonance frequencies and extract vector magnetic field information. This difficulty can be ameliorated using the ${}^3A_2 \leftrightarrow {}^3E$ optical polarization selection rules to distinguish the light contributions from each NV orientation [93].

The $\mathbf{B}_0$ field is ideally as uniform as possible. $\mathbf{B}_0$ inhomogeneity can cause the following problems:

1. In pulsed NV experiments, $\mathbf{B}_0$ inhomogeneity will cause spatially-dependent pulse errors, which limit the NV contrast and sensitivity.

2. For most experiments, we are interested in just the sample field $\mathbf{B}_s$. If there is a large non-uniform bias field $\mathbf{B}_0$, then isolating the sample field from the bias field can be

challenging.

3. In an extreme case, $\mathbf{B}_0$ inhomogeneity can contribute to NV linewidth broadening within each pixel.

1.5.6 Microwave Delivery

The simplest way to apply a MW field to the NVs is with a piece of wire connected to a coaxial cable. The QDM MW field is ideally uniform across the NV layer field of view, and there are a variety of alternative engineered MW antennas that aim to optimize the MW field homogeneity, efficiency, or bandwidth [94–100]. By the transition selection rules, the transitions between $^3A_2$ sublevels require left-circularly or right-circularly polarized microwaves [101]. One QDM MW antenna option is a pair MW loop as shown in Figure 1.1; another option is a crossed MW stripline resonators [1]. The striplines are excited in-phase (or 90 degrees out-of-phase) to produce a linearly (or circularly) polarized MW field as needed for a given sensing protocol.

Increasing the MW power improves the contrast in a CW ODMR measurement, but also broadens the linewidth between $^3A_2$ resonances. Figure 1.10 demonstrates for simulated CW ODMR measurements that optimizing QDM magnetic sensitivity implies tradeoffs of laser and MW power [43]. Choosing an optical pumping rate much greater than the MW transition rate results in weak contrast, since the laser quickly repumps any NV population fraction removed by resonant MWs. Increasing the MW field amplitude improves the fluorescence contrast but also broadens the ODMR linewidth. The MW intensity noise also affects the QDM sensitivity by influencing the ODMR contrast and linewidth in a manner similar to fluorescence intensity noise.

Selecting an appropriate MW frequency sweep rate is critical in CW ODMR measurements where we sweep the probe MW frequency across the NV resonance. The NV reaction

time depends on the NV optical pumping rate and MW transition rate, and a sufficient response time is needed for the NVs to re-equilibrate to the updated conditions after moving to the next microwave frequency. This also applies to experiments using lock-in detection to combat fluorescence intensity noise: the MW modulation rate must be slower than the NV reaction time, typically set by the optically pumping rate [52].

When deciding how to apply the microwave field, the different measurement modalities have drastically different considerations and optimizations.

1. For CW ODMR imaging, increasing the MW power broadens the ODMR linewidth but also improves the contrast.

2. For Ramsey, Hahn Echo, and dynamical decoupling imaging, spatial MW inhomogeneity and pulse errors can reduce the NV contrast and worsen the sensitivity.

1.5.7 Optics

QDMs employ various ways to illuminate the NV layer with pump-laser light, depending on other experimental constraints. Side illumination of the diamond chip [1] is a good method for QDMs using a low-magnification (long working distance) objective with a large field of view since the beam will have enough space to avoid clipping the objective while illuminating a large area. Another approach is to illuminate through the objective by focusing the pump laser at the back aperture to get parallel rays out of the objective [102]. This method works better for QDMs operating with high-magnification microscopes. The laser polarization is easier to control, but focusing the laser at the objective back aperture can lead to burns. Techniques to avoid illuminating the sample as well as the NVs include illumination via total internal reflection in the diamond, shaping the pump laser beam into a light sheet using cylindrical lenses, or coating the NV surface with a reflective layer to reduce the

optical intensity through the diamond chip [15, 54, 67].

Optimal photon collection efficiency requires the largest achievable numerical aperture (NA) for the microscope objective. In practice the NA for a given magnification is limited, and high-NA objectives are often also high-magnification objectives with a short working distance (sometimes shorter than the diamond thickness). Imaging NV fluorescence through the diamond chip may cause optical aberrations that can also spoil the image quality. As with other optical microscopes, a QDM images a broadband NV fluorescence (∼637-900 nm), so chromatic aberration in the microscope optics is also important to mitigate. Pulsed NV experiments commonly use an acousto-optic modulator (AOM) as an optical switch. For the AOM, the rise-time, extinction ratio, and efficiency are the parameters to consider for a given application.

1.6 QDM Performance

QDM performance characteristics include magnetic field sensitivity, temporal resolution, frequency bandwidth, spatial resolution, and field of view of the sample. These characteristics depend on the sensing protocol of the QDM, which in turn are determined by the spectral and spatial qualities of the sample fields to be imaged. This section focuses on the physical limits affecting measurement performance.

1.6.1 Magnetic Field Sensitivity

The minimum detectable field difference is defined as the change in magnetic field magnitude, δB for which the resulting change in a given measurement of the field equals the standard deviation of a series of identical measurements. However, for meaningful determination of sensor performance characterizations of the minimum detectable field must consider the total measurement duration, as well as the total number of NVs that contributed to the

Diamond [N]	n_N	NV^-/N	$n_{NV^-,SA}$	Single Axis Counts/s	Photon Rate (Counts/s)	Counts Per Readout	Contrast	T_2^* (μs)	T_2 (μs)
1 ppm	1.76×10^5	0.1	4.4×10^3	10^5	4.4×10^8	132	5%	10.0	160
20 ppm	3.52×10^6	0.1	8.8×10^4	10^5	8.8×10^9	2640	5%	0.50	8.0

Table 1.2: Simulated diamond properties. Properties of two notional diamonds used for performance simulations for a 1 μm^3 QDM voxel. [N] is the concentration of nitrogen in the diamond. n_N is the number of nitrogen atoms per 1 μm^3 voxel, $NV^-/N = 10\%$ of the N atoms are NV centers. A single NV axis is considered, giving $n_{NV^-,SA}$ with 10^5 fluorescence counts/s for each NV in a 1 μm^3 QDM voxel. More NV centers per voxel increases magnetic field sensitivity because the rate of photons emitted scales with n_{NV^-}. Counts per readout are for an assumed readout time of 300 ns. Assumed scaling of T_2^* and T_2 are from Ref [61].

measurement. The magnetic field sensitivity scales as the square root of the number of detected photons. The number of photons collected over a unit time from a unit volume of NVs increases proportionally with time and volume. To account for measurement time, sensitivity is represented as $\eta = \delta B\sqrt{t_{meas}}$ with units of T $Hz^{-1/2}$, where t_{meas} is the total measurement time. To account for the number of NV spins required to reach a given sensitivity, a sensor volume-normalized sensitivity is defined as $\eta_{vol} = \eta\sqrt{V}$ with units T $\mu m^{3/2}$ $Hz^{-1/2}$, where V is volume for a fixed density of NVs [9, 103].

DC (Broadband) Sensitivity

CW ODMR magnetometry is the most widely used QDM measurement technique due to its simplicity. The sensitivity of a CW ODMR magnetometry sequence is characterized by the rate of photon detection from a cubic micron of NVs, R, and the slope of the resonance line, $\partial I/\partial\nu_0$ with fluorescence intensity I and frequency ν_0. The CW ODMR, shot-noise-limited sensitivity is:

$$\eta_{\text{CW ODMR}} \approx 2\pi\frac{\hbar}{g_e\mu_B}\frac{\sqrt{R}}{\max|\partial I/\partial\nu_0|} = \frac{8\pi}{3\sqrt{3}}\frac{\hbar}{g_e\mu_B}\frac{\Delta\nu}{C\sqrt{R}} \tag{1.9}$$

where C is the contrast and $\Delta\nu$ is the linewidth of the ODMR resonance. The resonance line shape is typically fit by a Lorentzian, giving the $4/(3\sqrt{3})$ factor for the maximum slope. The relationship between the ODMR linewidth and the previously defined dephasing time is $T_2^* = \frac{1}{\pi\Delta\nu}$ [21, 56, 61, 104, 105].

The sensitivity of CW ODMR magnetometry is limited by laser and MW ODMR lineshape power broadening. Solving the Bloch equation for a simplified two-level model yields the contrast, linewidth, and volume-normalized magnetic sensitivity, shown in Figure 1.10. The calculations are based on [43] for CW ODMR using parameters from Table 1.2. Figure 1.10 displays a broad range of laser and MW powers to indicate how these affect the sensitivity. The trade-off between laser and MW power will limit the achievable volume normalized-sensitivity of CW ODMR, precluding simultaneous optimal contrast and narrow linewidth. Generally speaking, applications that require higher temporal and spatial resolution should use techniques more sensitive than CW ODMR.

Ramsey magnetometry achieves the best DC magnetic field sensitivity of the QDM protocols due to its pulse scheme: the NV spins interrogate the sample fields during an interval without simultaneous interaction of the optical and MW driving fields. The shot-noise-limited sensitivity for DC magnetic fields using a Ramsey pulse is [56]:

$$\eta_{\text{Ramsey}} \approx \underbrace{\frac{\hbar}{g_e\mu_B}\left(\frac{1}{\Delta m_s\sqrt{N\tau}}\right)}_{\text{Spin Projection Noise}}\underbrace{\left(\frac{1}{e^{-(\tau/T_2^*)^p}}\right)}_{\text{Spin Dephasing}}\underbrace{\sqrt{1+\frac{1}{C^2 n_{avg}}}}_{\text{Readout}}\underbrace{\sqrt{\frac{t_I+\tau+t_R}{\tau}}}_{\text{Overhead Time}} \tag{1.10}$$

where N is the number of non-interacting NVs contributing to the measurement, Δm_s is the generalization to greater-than-one spin state difference used for measurement (e.g., $\Delta m_s = 2$ for the NV $m_s = -1$ to $m_s = 1$ transition when operating with a double-quantum coherence [21] and $\Delta m_s = 1$ is for operating in the single-quantum basis), C is the resonance contrast, n is the average number of photons collected per NV per measurement, τ is the spin

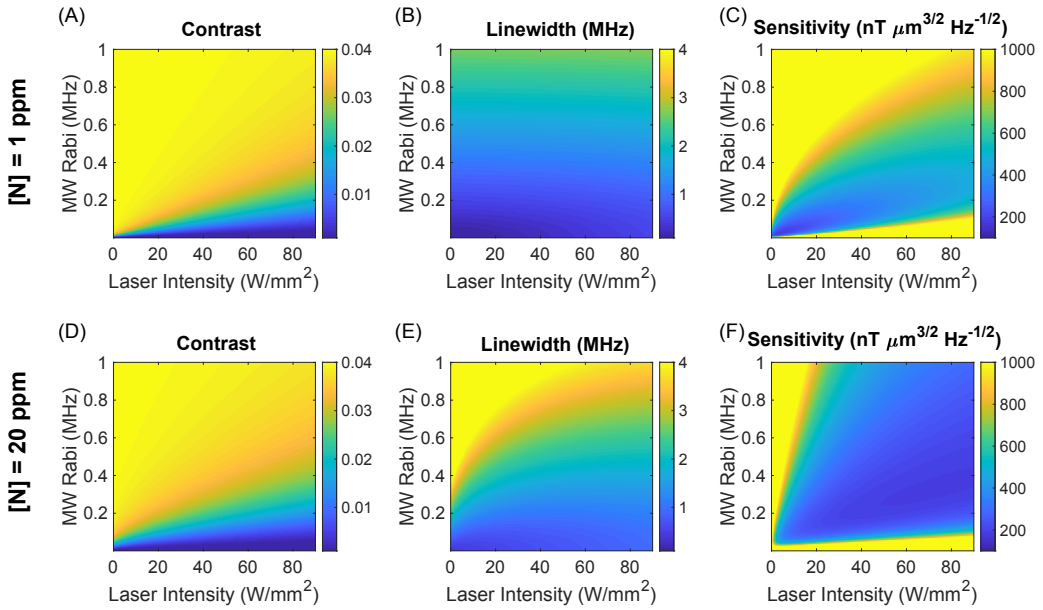

Figure 1.10: Ensemble CW ODMR Sensitivity Analysis. Simplified simulations of CW ODMR contrast, linewidth, and volume-normalized magnetic field sensitivity η_{vol} as a function of laser intensity and MW Rabi (which scales as the square root of the input MW power) with parameters from Table 1.2 for a diamond with 1 ppm of nitrogen (Top Row), and a diamond with 20 ppm nitrogen (Bottom Row). Laser intensity scale assumes saturation intensity of 0.9 MW/cm^2.

interrogation time, and t_I and t_R are the optical spin-state initialization and readout times respectively, ($t_{meas} = t_I + \tau + t_R$). The spin-projection-noise-limited sensitivity is given by the first two terms of Eqn. 1.10. It is evident that longer interrogation time, τ and larger number of spins, N allow for better sensitivity to small magnetic fields. However, several factors cause Ramsey magnetometry to fall short of this limit: a decrease in sensitivity due to spin dephasing with characteristic time T_2^* is accounted for in the exponential term with parameter p depending on the origin of dephasing; imperfect readout contributes the first square root term; and the reduced fraction of total measurement time allocated for spin interrogation due to the overhead time from t_I and t_R is accounted for in the last term. Optimal DC sensitivity is achieved for $\tau \sim T_2^*$ [56]. Figure 1.11 compares the sensitivity of

Technique	CW ODMR and Lock-In ODMR	Ramsey
Diamond Homogeneity Improvement (Strain, NV Distribution, etc)	Strain inhomogeneity is detrimental for ODMR slope.	Compatible with Double Quantum techniques, which minimizes detrimental effects of strain inhomogeneity.
Ensemble NV^- Charge State Stability	Low optical intensity utilized minimizes intensity-dependent charge state stability issues.	High optical intensity utilized needed for fast initialization and readout is detrimental to charge state and contrast.
Diamond Growth Optimization	Improved diamond growth and processing (unwanted defect control, surface control, NV density, irradiation, annealing, etc) is always beneficial.	
Double Quantum Coherence	Not compatible.	Increased effective gyromagnetic ratio, improved robustness to crystal strain variations and temperature instabilities.
Spin Bath Driving and Quantum Control	Generally not useful. (Laser and microwave power will predominantly impact slope.)	Minimizes detrimental impact of nitrogen spins, unwanted spin defects and NV-NV interactions on T_2^*.
Photon Collection Maximization	Always maximize collection of available NV fluorescence, when possible.	
Exotic Techniques (NV-NV Interactions, etc)	Likely not compatible	Rather than mitigating interactions, attempt to utilize them. Active area of research.

Table 1.3: Overview of general methods to improve DC sensitivity and measurement performance. The relevance for each method on the different NV control schemes utilized later on in this work in Chapters 5 and 6 is discussed.

Ramsey magnetometry as a function of the frequency of the field being measured for the two diamonds in Table 1.2.

Techniques to Improve DC Broadband Magnetic Sensitivity

Table 1.3 provides a brief overview of the techniques identified [56] that can provide increased sensitivity for DC magnetometry. More in depth information on the proposed techniques can be found in Refs. [56, 106, 107]. More information on the experimental realization of a subset of these techniques can be found in Refs. [21, 108]. A subset of these techniques will be later discussed in this work in Chapters 4 and 6.

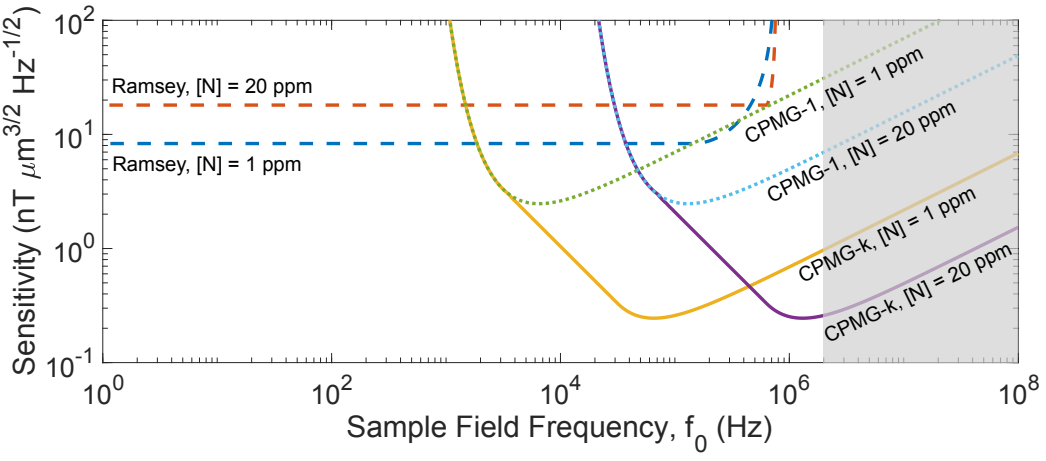

Figure 1.11: Frequency Dependence of QDM Volume-Normalized Sensitivity. Achievable volume-normalized magnetic field sensitivity as a function of the sample field frequency for DC broadband and AC narrowband QDM protocols. Calculations use parameters from Table 1.2. Ramsey is broadband, and is sensitive to magnetic fields of differing frequencies without requiring changes in the pulse sequence. CPMG is narrowband and requires a change in the pulse sequence based on the field frequency being sensed in order to maintain optimal sensitivity. The grey region indicates high sample frequencies where experimental requirements on MW pulses and power become technically challenging. Dotted lines are for a single pulse, which achieves the same sensitivity as a Hahn Echo sequence. Solid lines are for CPMG-k protocols limited up to 1024 pulses.

AC (Narrowband) Sensitivity

The sensitivity for measurement of AC magnetic fields using the Hahn echo protocol is

$$\eta_{\text{Hahn Echo}} \approx \underbrace{\frac{\pi}{2}\frac{\hbar}{g_e\mu_B}\left(\frac{1}{\Delta m_s\sqrt{N\tau}}\right)}_{\text{Spin Projection Noise}} \underbrace{\left(\frac{1}{e^{-(\tau/T_2)^p}}\right)}_{\text{Spin Decoherence}} \underbrace{\sqrt{1+\frac{1}{C^2 n_{avg}}}}_{\text{Readout}} \underbrace{\sqrt{\frac{t_I+\tau+t_R}{\tau}}}_{\text{Overhead Time}} \tag{1.11}$$

Hahn echo magnetometry builds on the Ramsey protocol, resulting in similar physics underlying the AC magnetic field sensitivity to that of DC fields. The additional MW π pulse in the Hahn Echo sequence refocuses the dephasing NV ensemble such that the sensing duration, τ approaches the spin decoherence time T_2. Because T_2 is at least an order of magnitude longer than the spin dephasing time, T_2^*, the sensing duration increases translating to an improvement in sensitivity. AC sensing protocols are thus limited by T_2,

whereas DC sensing protocols are limited by T_2^*; because $T_2 \gg T_2^*$, the AC protocols can generally achieve better sensitivity than DC protocols. However, the benefit of being T_2 limited can be degraded by coherent interactions between the NV spin ensemble and other spin impurities that decrease the T_2 coherence time. The optimal spin interrogation time τ for Hahn echo magnetometry is $\tau \sim T_2$; additionally, τ should match the period of the AC magnetic field, T_{AC}. Consequently, maximal sensitivity is achieved for AC magnetic fields with $T_{AC} \sim T_2$ of the diamond.

CPMG pulse sequences improve the sensitivity by extending T_2 even further [56, 63]:

$$\eta_{\mathrm{CPMG}} \approx \frac{\pi}{2}\frac{\hbar}{g_e \mu_B}\left(\frac{1}{\Delta m_s \sqrt{N\tau}}\right)\left(\frac{1}{e^{-(k^{-s}\tau/T_2)^p}}\right)\sqrt{1+\frac{1}{C^2 n_{avg}}}\sqrt{\frac{t_I+\tau+t_R}{\tau}} \tag{1.12}$$

where k is the number of pulses, and $\tau = k/(2f_0)$ is the full spin evolution time, and f_0 is the frequency of the sample field. The optimal number of pulses for a given frequency is given by $k_{opt} = \left(\frac{1}{2p(1-s)}(2T_2 f_0)^p\right)^{1/(p(1-s))}$, with s $\sim$ 2/3 and p $\sim$ 3/2, which are set predominantly by the spin bath dynamics [63, 106]. The measurement time increases linearly with increased number of pulses, whereas the decoherence time T_2 increases sublinearly; the optimal number of pulses balances these effects [56]. Extensions of Eqn. 1.12 exist to take into account multi-pulse dynamical decoupling protocols.

1.6.2 Temporal Resolution and Frequency Bandwidth

For broadband QDM measurements, temporal resolution is defined as the time between subsequent measurements of the sample field. The physical limitation determining the fastest temporal resolution is set by the time it takes for the NVs to react to a change in the sample field. The temporal resolution can never be faster than the inverse of ~5 MHz (the maximum optical pumping rate), which is limited by the ^1E metastable state lifetime. The same is true for pulsed measurements, since NVs are optically reinitialized to the $m_s = 0$ state

before each measurement. For a measurement with continuous laser illumination and MW field, the QDM temporal resolution is set by the optical pumping rate and the MW Rabi frequency. There is also a practical limit to the temporal resolution, set by signal-to-noise ratio (SNR) tolerance: faster temporal resolution gives worse SNR per measurement.

QDM frequency bandwidth is the range of sample frequencies that can be interrogated with the same experimental protocol. A broadband magnetometry experiment has a frequency resolution spanning from static DC fields to ∼100s of kHz. A dynamical decoupling AC magnetometry experiment has an approximate frequency bandwidth that is roughly equal to $1/T_{tot}$ (the Fourier limit), where T_{tot} is the duration of the dynamical decoupling pulse sequence. An AC magnetometry measurement based on driving the spin population between m_s sublevels (Rabi) or spoiling of the initialized spin state (T_1 relaxometry) has a frequency bandwidth corresponding to the NV resonance linewidth; i.e, the frequency span over which the NVs are on resonance with the MW field, which is $> 1/(\pi T_2^*)$.

AC magnetometry sequences that are based on pulse control of the NV spin state have a frequency bandwidth dictated by the filter function, $S(f)$, for the specific pulse sequence being used. The center frequency and bandwidth are defined by the number of pulses, k, and the spacing between π pulses, τ [62]. The center frequency of the filter is given by $f_0 = 1/2\tau$. For a sequence of k pulses, with total measurement time $T = k\tau$, the width of the filter function is given by $\Delta f = 1/T = 1/k\tau$. The filter function $S(f)$ depends upon a protocol-specific response $F(fT)$

$$S(f) = 2F(fT)/(2\pi f)^2, \tag{1.13}$$

where an example response function for the CPMG protocol is [62]

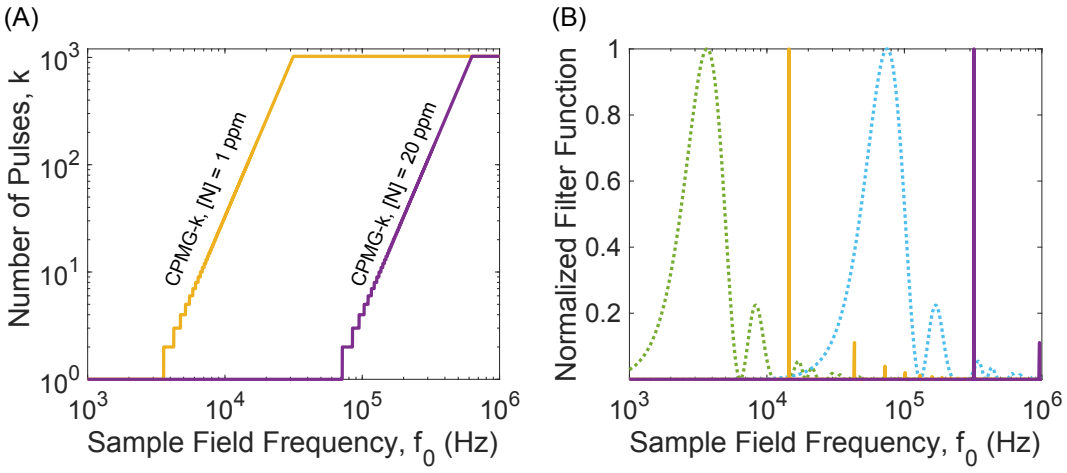

Figure 1.12: CPMG Protocol Bandwidth. (A) The optimal number of pulses for the CPMG protocol changes with the sample field frequency. (B) Example filter functions $S(f)$, at the most sensitive sample frequencies for each of the CPMG curves in Figure 1.11. Dotted lines represent the response for a 1 pulse CPMG. Solid lines are for the most sensitive center sample field frequencies for CPMG limited to 1024 pulses. The solid lines are ∼1000 times narrower than the dotted lines due to having ∼1000 times more pulses.

$$F_{\text{CPMG-k}}(fT) = 8\sin^4\left(\frac{2\pi fT}{4k}\right)\sin^2\left(\frac{2\pi fT}{2}\right)/\cos^2\left(\frac{2\pi fT}{2k}\right). \tag{1.14}$$

Figure 1.12(A) demonstrates the need to change the number of pulses in order to operate at the sensitivity limit shown in the CPMG curves in Figure 1.11. Figure 1.12(B) gives filter functions for the most sensitive points along the curves presented in Figure 1.11.

It is tempting to conflate temporal resolution and frequency bandwidth, but they in fact represent different characteristics. For example, an NV T_1 measurement can detect magnetic noise across a few MHz frequency bandwidth around a central frequency ranging from near zero to many GHz (depending on the applied $\mathbf{B}_0$), but measurements may only be repeatable at < 1 kHz (temporal resolution). Only in the case of broadband DC magnetometry protocols do the temporal resolution and frequency bandwidth correspond to the

same sensor property.

1.6.3 Spatial Resolution and Field of View

QDM imaging seeks to resolve magnetic fields with sufficiently high spatial variation and wide-field of view to probe the sample properties of interest; and to successfully invert the magnetic field measurements to generate a map of closely-separated magnetic sources. Both goals have fundamental and sensor-specific limitations. It is ideal to operate at the limit of magnetic field inversion and not to be limited by the sensor properties such as resolution and field of view.

The magnetic inversion problem does not generally have a unique solution. Only if the current distribution is limited to two dimensions (2D) can the inverse problem be solved uniquely from a planar measurement of the magnetic field. A magnetometer must sample the field at discrete points in a 2D plane with a sufficient sampling density to recover the continuous magnetic field created by the sample sources. The spatial resolution that can be obtained from this 2D map of the field is then limited by the offset distance between the measurement plane and the sources, and by noise in the data [45, 109]. In general, the offset distance should be as small, or smaller than the characteristic length scale of the magnetic field sources, as shown in Figure 1.4, for reliable inversion of the magnetic image to the source distribution. In an analog to the Nyquist sampling theorem, the pixel size sets the maximum spatial (k-space) frequency. The field of view size sets the spatial frequency resolution (again by a Fourier transform argument). Both of these effects impact the ability to perform magnetic field inversions and map the underlying sources [45].

If the in-plane pixel size is made too small, then the noise level could preclude detection of magnetic fields of interest. This is similar to the negative impact to δB that can result from pushing the temporal resolution. On the other hand, if the pixel size is too large, then

small length scale signals of interest will be blurred out and the fidelity of the magnetic field amplitude will be degraded. Figure 1.13 illustrates an example of this trade-off for magnetic fields simulated in Figure 1.4.

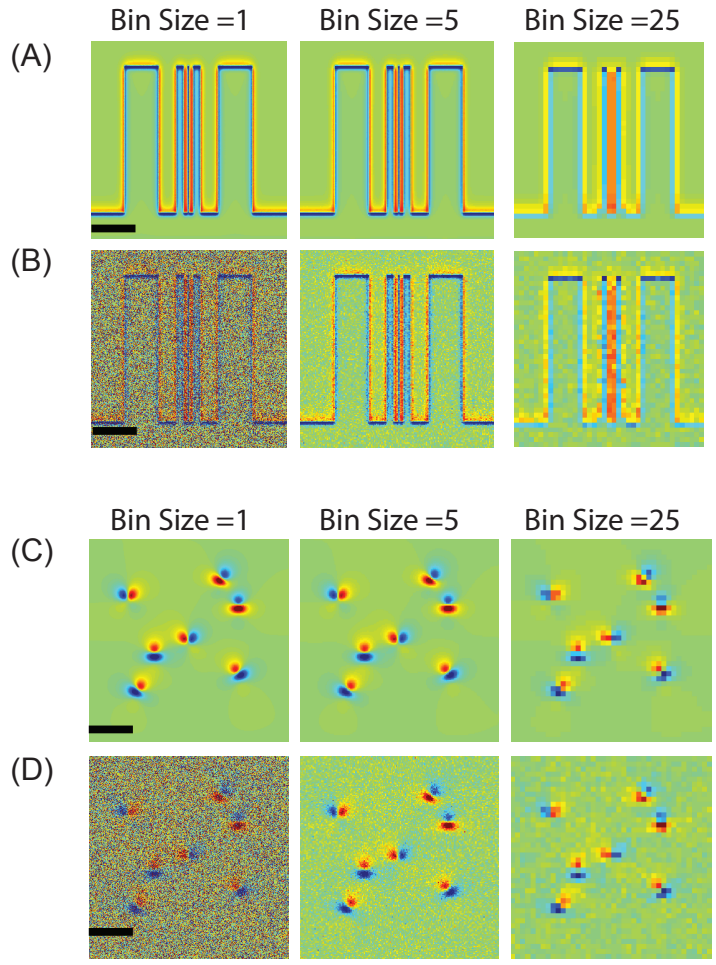

Figure 1.13: QDM Spatial Resolution and SNR Trade-off. (A) Magnetic field from the current distribution in Figure 1.4(A) for different planar binning sizes. No additional noise is applied. Scale bar is 50 μm (B) Binning with fractional noise leading to SNR of 1 for a bin size of 1. C) Magnetic field from magnetic dipole sources in Figure 1.4(B). No additional noise is applied. Scale bar is 10 μm

QDM spatial resolution is set by the following:

1. NV-sample standoff distance. As the standoff distance Δz increases, the 2D magnetic map is convolved with a Lorentzian of width Δz, reducing the ability to resolve closely-separated magnetic sources [110]. Reducing the standoff distance improves the field strength and often the spatial resolution.

2. NV layer thickness. An sample with an NV layer much larger than the sample standoff distance will degrade the spatial resolution. An infinitesimally thin NV layer will ensure the imaging resolution is not limited by the diamond properties. However, thicker NV layers can increase sensitivity through increasing the amount of photons produced for a given optical excitation intensity. Therefore, the optimal NV layer needs to be tuned to balance needed imaging resolution with measurement sensitivity.

3. Optical diffraction limit. Set by the numerical aperture (NA) of the microscope objective ($\lambda/(2\text{NA})$ for a typical fluorescence wavelength of $\lambda \approx 700$ nm. This assumes that the camera pixel size is small compared to the diffraction-limited spot size in the image plane. The spherical aberration from the diamond chip or other optics can also degrade the resolution so the optical diffraction limit would need to be modified.

In general, QDM magnetic field imaging is best used for applications that need both high spatial resolution and wide-field of view, and can also afford small NV-sample separation. The intuitive rule-of-thumb is to have NV layer thickness, standoff distance, and sample thickness of comparable sizes.

Chapter 2

The Magnetic Inverse Problem and Magnetic Field Interpretation

2.1 Magnetic Fields and the Inverse Problem

For a wide range of applications including medical [109, 111–116], integrated circuits [117], condensed matter systems [118–122], geosciences [46], manufacturing and quality control [123–131] and many others it is important to be able to determine the source distribution that caused the measured magnetic field, in what is known as the magnetic inverse problem [109, 132]. In the applications above, the source distribution can be well described by either current distributions [45], effective current dipoles [109] (or higher expansions), and/or magnetic dipoles [129] (or higher expansions.)

This chapter will focus on the magnetic inverse problem for current distributions in a homogeneously conducting source region. For discussions on magnetization sources and the relevant inverse problem, see Reference [118]. In general, the magnetic inversion process is not unique due to the presence of "magnetically silent" current sources [109, 132], current

sources that do not lead to a net magnetic field in the measurement plane. An arbitrarily large number of these sources can be added to a current distribution and all would be valid solutions for the same measured magnetic field profile. This non-uniqueness of the problem precludes the development of a direct analytical formalism for solving the general inverse problem. Therefore, constrained versions of the problem need to be considered and mathematical (regularization) or geometrical features of the specific problem being studied need to be utilized to solve the constrained problem through the addition of prior knowledge

Many different methods and protocols have been developed in order to attempt to tackle a constrained, ill-posed inverse problem including Tikhonov regularization [133], Fourier Filters [45, 134], estimation theory [135], probabilistic multi-source reconstructions [136], least square fitting [109, 112], Bayesian methods [137], genetic algorithms [138], and direct mapping and fitting in low dimensionality systems [121, 139, 140]. Each method and approach have their own strength with regards to computational complexity, accuracy, robustness to noise, flexibility, ability to incorporate prior information, matching the specific application, and achievable source resolution.

This chapter focuses on the Fourier Filter formalism [45], which matches well with the 2D widefield imaging of NV experiments, enables intuition for general trends of the inverse problem, and provides an efficient platform for the generation of large amounts of test data to be later used in the chapter. However, this Fourier-based method is exponentially sensitive to experimental noise, which precludes the practical application of this method in many circumstances.

As a first step, it is generally useful to begin with an investigation of the relevant equations governing the magnetic forward problem (source current distribution to magnetic field) to look for natural assumptions or simplifications that can be made to generate the structure for the solution. The forward problem for calculating the magnetic field from a

given current distribution is described by Biot-Savart's Law:

$$\mathbf{B}(\mathbf{r},\mathbf{t}) = \frac{\mu_0}{4\pi}\int_{V_{Source}} d^3r' \frac{\mathbf{J}(\mathbf{r}',\mathbf{t}) \times (\mathbf{r}-\mathbf{r}')}{|\mathbf{r}-\mathbf{r}'|^3} \tag{2.1}$$

An assumption that will be made for most of this chapter is that currents are confined to 2D and this assumption dramatically simplifies the problem and enables an analytical solution to this constrained inverse problem. [45] For most approaches to solve the inverse problem, similar kinds of assumptions are made about the source distribution and possible functional forms to make the problem better posed [109, 132]. Following these needed simplifications, the next step is finding the functional form, search algorithm, or optimization process to find the specific source configuration that minimizes the error with the measured magnetic field [141].

2.1.1 Fourier Filter Formalism

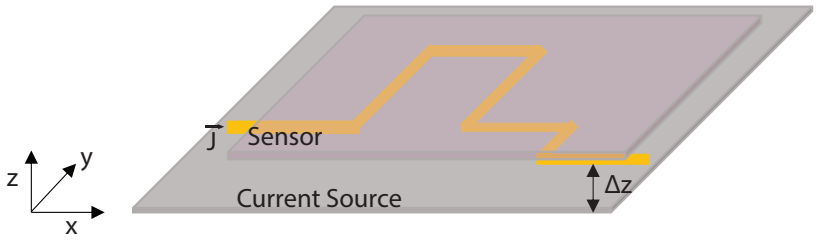

Figure 2.1: Diagram showing the geometry of the problem and definition of the Cartesian axes. For this purely 2D current distribution geometry, the current source is located at z=0 and the sensor plane is located at $z = \Delta z$. The current is given by $\vec{J} = J_x(x,y,0)\hat{x} + J_y(x,y,0)\hat{y}$.

The goal of this section is to present the formalism for calculating the magnetic field from an arbitrary current distribution using the common Fourier filter method [45].

Fundamentally, the Biot-Savart Law acts as a low pass filter on the current distribution, where the larger the stand-off distance between the current source and the magnetic

measurement plane, the more significant the loss in high spatial frequency components, which can be clearly seen in the Fourier Transform treatment of Biot-Savart for 2D current sources [45, 117]. Viewing the law of Biot-Savart as a low pass filter highlights the value of using the Fourier transformed version of forward problem.

In the Fourier Transform formalism, knowledge of kernel functions and their Fourier Transforms are utilized to create a computationally efficient way of calculating the magnetic field from a 2D (J_x and J_y) current distribution.

2.1.2 Inverse Problem in 2D

While the computation in real space (denoted by the uppercase **J** and **B** for the current and magnetic fields) of the Biot Savart Law in Eq. 2.1 is a complicated integral that requires breaking the problem up into discrete current segments, the Fourier formalism (denoted by the lowercase **j** and **b** for the 2D Fourier transform of the current and magnetic fields) and the assumption of current conservation combined with utilization of the Convolution Theorem allows for the problem to be greatly simplified in Fourier space and become simple multiplication [45].

$$\begin{aligned} b_x(k_x, k_y) &= g_{j_y \to b_x} j_y(k_x, k_y) \\ b_y(k_x, k_y) &= g_{j_x \to b_y} j_x(k_x, k_y) \\ b_z(k_x, k_y) &= g_{j_x \to b_z} j_x(k_x, k_y) \\ b_z(k_x, k_y) &= g_{j_y \to b_z} j_y(k_x, k_y) \end{aligned} \tag{2.2}$$

Where the last two equations utilize current conservation to write b_z in terms of just j_x or j_y.

An explicit calculation for one of these transformations is presented below. Starting from Equation 2.1, and integrating over a small slice in z.

$$B_x(x,y,\Delta z) = \frac{\mu_0 d}{4\pi}\int_{-\infty}^{\infty}\int_{-\infty}^{\infty}\frac{J_y(x',y')\Delta z}{[(x-x')^2+(y-y')^2+\Delta z^2]^{3/2}}dx'dy' \tag{2.3}$$

Defining $G_{j_y\to b_x}(x,y,\Delta z) = \frac{\mu_0 d\Delta z}{4\pi}\frac{1}{[(x-x')^2+(y-y')^2+\Delta z^2]^{3/2}}$ as being a Greens-like kernel function. The Fourier transform of $G_{j_x\to b_y}(x,y,\Delta z)$ is defined as:

$$\begin{aligned} g_{j_y\to b_x}(k_x,k_y,\Delta z) &= \int_{-\infty}^{\infty}\int_{-\infty}^{\infty} G_{j_y\to b_x}(x,y,\Delta z)\mathrm{e}^{i(k_x x+k_y y)}dxdy \\ g_{j_y\to b_x}(k_x,k_y,\Delta z) &= \frac{\mu_0 d\Delta z}{4\pi}\int_{-\infty}^{\infty}\int_{-\infty}^{\infty}\frac{1}{[(x-x')^2+(y-y')^2+\Delta z^2]^{3/2}}\mathrm{e}^{i(k_x x+k_y y)}dxdy \end{aligned} \tag{2.4}$$

This integral can be solved through a transformation to polar coordinates ($x = r\cos\theta,\ y = r\sin\theta,\ k_x = k\cos\phi,\ k_y = k\sin\phi$).

$$g_{j_y\to b_x}(k_x,k_y,\Delta z) = \frac{\mu_0 d\Delta z}{4\pi}\int_0^{\infty}\int_0^{2\pi}\frac{1}{[r^2+\Delta z^2]^{3/2}}\mathrm{e}^{ikr\cos(\theta-\phi)}rd\theta dr \tag{2.5}$$

Evaluating the integral over θ:

$$g_{j_y\to b_x}(k_x,k_y,\Delta z) = \frac{\mu_0 d\Delta z}{4\pi}\int_0^{\infty}\frac{rJ_0(kr)}{[r^2+\Delta z^2]^{3/2}}dr \tag{2.6}$$

The solution to this integral can be found in Ref [142]:

$$g_{j_y\to b_x}(k_x,k_y,\Delta z) = \frac{\mu_0 d}{2}\mathrm{e}^{-\Delta z\sqrt{k_x^2+k_y^2}} \tag{2.7}$$

Equation 2.7 agrees with the results from Reference [45]. The relevant filter functions, g, for the forward problem for the other magnetic field vector directions and current sources are given by [45, 117]:

$$
\begin{aligned}
g_{j_x \to b_y} &= -\frac{\mu_0 d}{2} \mathrm{e}^{-\Delta z \sqrt{k_x^2 + k_y^2}} \\
g_{j_y \to b_x} &= \frac{\mu_0 d}{2} \mathrm{e}^{-\Delta z \sqrt{k_x^2 + k_y^2}} \\
g_{j_x \to b_z} &= i \frac{\mu_0 d}{2} \frac{\sqrt{k_x^2 + k_y^2}}{k_y} \mathrm{e}^{-\Delta z \sqrt{k_x^2 + k_y^2}} \\
g_{j_y \to b_z} &= -i \frac{\mu_0 d}{2} \frac{\sqrt{k_x^2 + k_y^2}}{k_x} \mathrm{e}^{-\Delta z \sqrt{k_x^2 + k_y^2}}
\end{aligned}
\tag{2.8}
$$

where d is a parameter that encompasses the finite thickness of the current source in an experimental apparatus [45].

The 2D constrained magnetic inverse problem can be analytically solved by inverting the functions above.

$$
\begin{aligned}
j_x(k_x, k_y) &= g^{-1}_{j_x \to b_y} b_y(k_x, k_y) \\
j_y(k_x, k_y) &= g^{-1}_{j_y \to b_x} b_x(k_x, k_y) \\
j_x(k_x, k_y) &= g^{-1}_{j_x \to b_z} b_z(k_x, k_y) \\
j_y(k_x, k_y) &= g^{-1}_{j_y \to b_z} b_z(k_x, k_y)
\end{aligned}
\tag{2.9}
$$

This transformation yields the inverse filter functions that can be used to reconstruct current sources from magnetic field measurements.

$$
\begin{aligned}
g^{-1}_{j_x \to b_y} &= -\frac{2}{\mu_0 d} \mathrm{e}^{\Delta z \sqrt{k_x^2 + k_y^2}} \\
g^{-1}_{j_y \to b_x} &= \frac{2}{\mu_0 d} \mathrm{e}^{\Delta z \sqrt{k_x^2 + k_y^2}} \\
g^{-1}_{j_x \to b_z} &= -i \frac{2}{\mu_0 d} \frac{k_y}{\sqrt{k_x^2 + k_y^2}} \mathrm{e}^{\Delta z \sqrt{k_x^2 + k_y^2}} \\
g^{-1}_{j_y \to b_z} &= i \frac{2}{\mu_0 d} \frac{k_x}{\sqrt{k_x^2 + k_y^2}} \mathrm{e}^{\Delta z \sqrt{k_x^2 + k_y^2}}
\end{aligned}
\tag{2.10}
$$

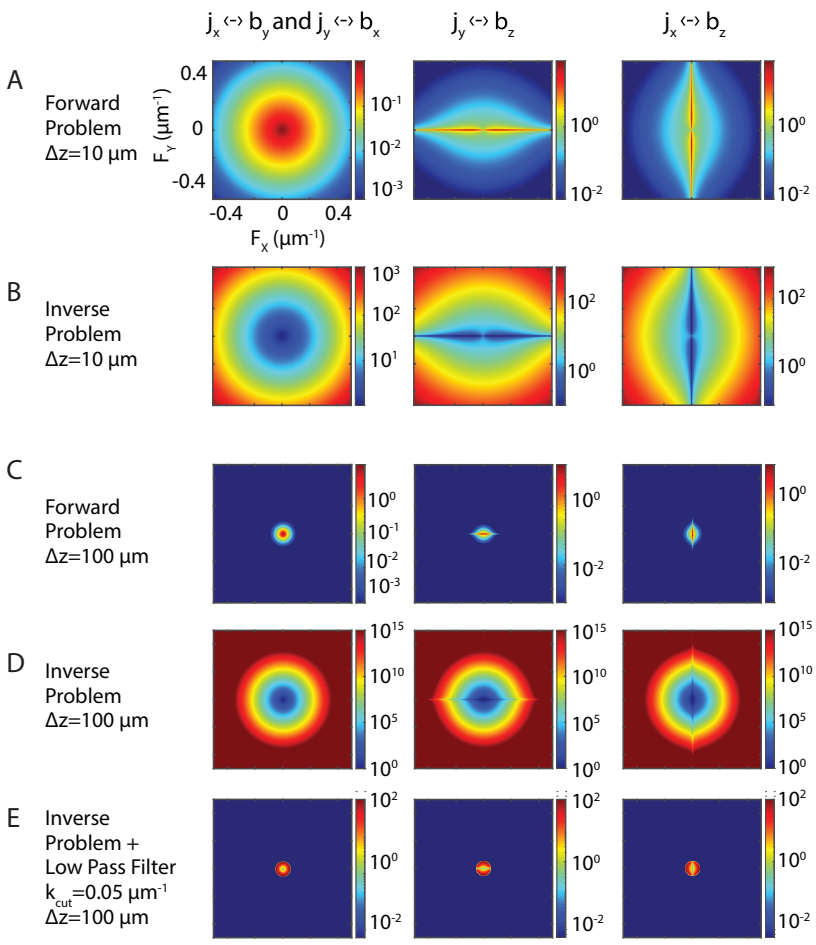

Figure 2.2: The stability of the inverse filter functions is explored for different standoff distances. (A) The magnitude of the forward problem filter functions (Equation 2.8 are displayed for a stand-off distance of $\Delta z = 10$ μm. The filter functions for the b_x and b_y components are symmetric in the spatial frequencies (F_x and F_y), whereas the b_z filter functions are stretched along either the x or y spatial frequency axis. (B) The inverse of the functions in (A) are plotted (see Equation 2.10. At the small stand-off distances, the values of the function are relatively small demonstrating relative stability for small stand-off distances. (C) The forward problem filter functions are plotted for a stand-off distance of $\Delta z = 100$ μm. Much more of the higher frequency spatial components are suppressed by the filter function. (D) The inverse of the functions in (C) are shown. The large values of the functions ($>10^{15}$) illustrate the instability of the inversion process. (E) Windowing (or application of a low-pass filter) is needed to ensure a stable reconstruction of the current source in the presence of experimental spatial noise.

One clear feature of the inverse filter functions in Equation 2.10 and in Figure 2.2, is the positive exponential scaling with stand-off distance and high spatial frequencies. Even though the 2D magnetic inverse problem has a unique solution, the inversion process is not stable to spatial noise (as seen in realistic experiments) due to the exponential in the filter function [45]. As seen in Figure 2.2, the further a measurement plane is away (large Δz), the problem becomes exponentially more unstable. One common way to overcome this instability is through the application of a low pass filter or windowing function in spatial frequency space to suppress high frequency noise components as shown in the bottom row of Figure 2.2. This method stabilizes the problem, but at the cost of spatial resolution and the introduction of spurious ringing and other spatial features depending on the windowing function applied.

2.1.3 Validation of Current Reconstruction Process

This section explores how standoff distance, spatial noise levels, cutoff frequencies for windowing functions, and current source geometry influence the achievable reconstruction of current source distributions from magnetic field images and reveals general trends on ways to maximize reconstruction fidelity. The general procedure for how these parameters are characterizes is given in Figure 2.3. Initially, an arrangement of wires is generated to create positions where the current magnitude is non-zero. For this example, a procedurally generated Hilbert Curve is used as a model system to utilize the structure's many different length scales and the dense sampling of the different vector components. Following the generation of the current profile, we calculate the J_x and J_y components based on the geometry of the problem and the coordinate axes defined in Figure 2.1. We use MATLAB [144] to calculate the 2D Fourier Transform of the J_x and J_y profiles, generating j_x and j_y. Equations 2.2 and 2.8 are used to calculate b_x, b_y, and b_z. The 2D inverse Fourier Transform is calculated to

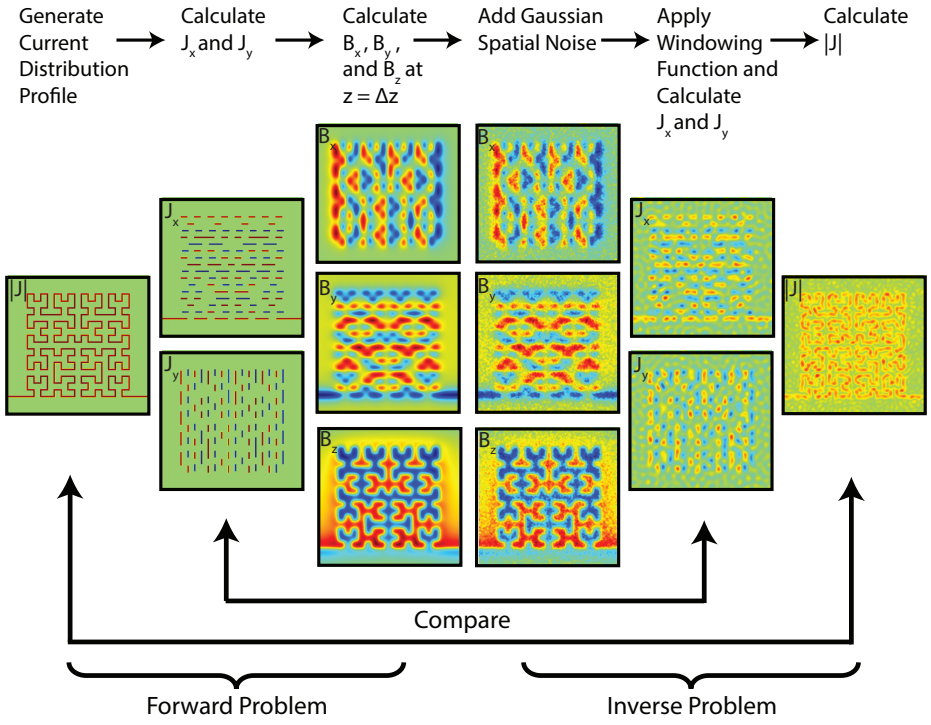

Figure 2.3: General process for characterizing stability of the magnetic inverse problem, based on the method in Reference [143]. First, a current distribution profile is generated, either through an analytical function for a particular profile or a procedurally generated profile (utilized more later.) The x and y components of the current profile are determined through the local slope of the current profile. The Fourier Method for Biot Savart is utilized to calculate B_x, B_y, and B_z. Before noise is added, the process can be reversed with high fidelity and without the need for extra filtering. Gaussian noise is added to the magnetic field maps to simulate experimental conditions. For the current reconstruction, a windowing function is applied to suppress high frequency noise and instabilities. The current profiles are calculated from the magnetic inversion and the magnitude of the current distribution is determined. The initial and final distributions for the magnitude and vector components are compared to determine the stability and fidelity of the inversion. (Color scales are normalized to highlight the characteristic spatial features.)

give the real space magnetic field, B_x, B_y, and B_z seen in Figure 2.3.

Depending on the test being performed, a varying amount of Gaussian spatial noise (often spatially filtered noise so the added noise frequency profile matches reasonable experimental noise) is added to the real space magnetic field image. The 2D Fourier Transform is

calculated to find $b_{x,noise}, b_{y,noise}$ and $b_{z,noise}$. A windowing function (could be a simple low pass filter or a Hanning window [45] to reduce oscillating artifacts in the final reconstruction) is applied to minimize the effect of high spatial frequency noise on the reconstruction and improve the stability. Applying the Inverse Problem Filter Functions (Equations 2.9 and 2.10) allows for the calculation of $J_{x,noise}$ and $J_{y,noise}$. Finally the magnitude of the current is calculated to determine $|J_{noise}|$, which localizes the position of the current. From Figure 2.3, the detrimental effect of a small amount of spatial noise is apparent. Even with the magnetic field being well resolved visually, stringent filtering is needed to stabilize the process which degrades the resolution of the reconstructed current sources. Even with the carefully tuned filtering parameters, the final data is noisy and blurred.

To fully map out the robustness and performance of the method the standoff distance (Δz), amount of spatial noise, the type and amount of windowing, the measurement field of view, and the pixel size of the image can all be varied. However, the top two priorities for experimental optimization are minimization of the stand-off distance and the amount of noise. Minimizing the stand-off distance has an exponential effect on reconstruction stability, and this is one of the key benefits of NV magnetic imaging for many applications. The NVs can be brought significantly closer to the sources of interest while maintaining favorable sensitivity, making source interpretation a much less daunting task.

2.1.4 Simple Channel Geometries

The simplest 2D current source geometry is one that reduces the current dimensionality to $\sim 1D$, i.e., a wire going in a single direction (J_x for this example), with some finite width. Despite the apparent simplicity of the current distribution, this geometry has great significance toward condensed matter experiments involving the hydrodynamic flow of electrons in graphene [145]. In these experiments, the cross section profile of the current flow was

a primary metric for determination and direct observation of the hydrodynamic (parabolic profile) versus ballistic (rectangular profile) flow of electrons [145]. Careful analysis with a procedure that involves cost-function minimization and a least-squares parameterized functional model is needed in [145] to ensure a sufficient solution to the inverse problem, even with modest stand-off distances (< 100 nm).

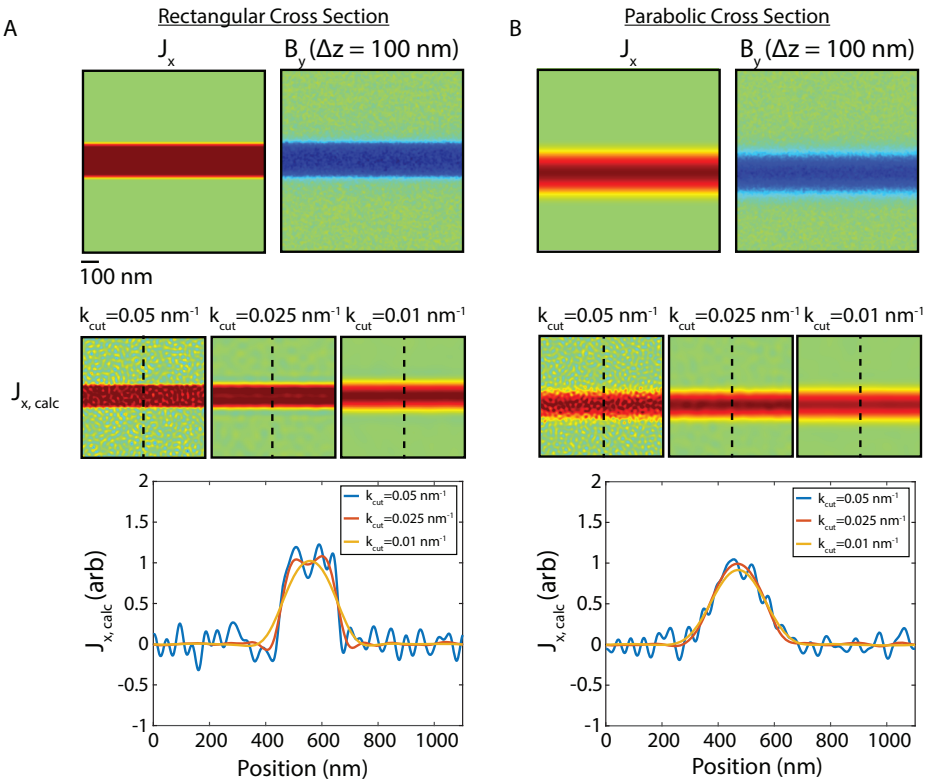

Figure 2.4: Optimization of the proper cut-off frequency to balance signal to noise resolution with preservation of cross section for a (A) rectangular current cross section and (B) parabolic current cross section. In general, this needs to be optimized as the wire properties, measurement standoff, and noise level vary. Even for modest noise levels where the SNR of the magnetic image is large, the propagation of the noise is significant enough to dramatically influence the results.

Fitting a parameterized model of the current source (with a least-squares search or a min-norm estimate) is a common technique to overcome the inherent instabilities of the inversion in the presence of experimental noise. [132] However, this method becomes compu-

tationally intense rapidly as the possible source space size and dimensionality increases. For a 1D cross section of a current profile, the problem is tractable and stable solutions can be found [145]. For 2D and even some 3D current sources in well constrained geometries (known as a Manhattan Grid), fitting procedures can provide robust inversions when the parameter search space is sufficiently constrained and the initial guesses for the current location are sufficiently close [117].

2.1.5 Interpretation of Magnetic Fields with Large Standoff Distance

To provide further intuition behind the capabilities (and limitations) of the Fourier filter formalism and inverse problem methods in general, in Figure 2.5 we generate an example where the measurement plane standoff distance is large, compared to the spatial extent of the current features. Through this example we show that in the presence of no added noise, even when the measured magnetic field is a blob with no obvious sign of the underlying current (see Figure 2.5), a high resolution current map can be resolved. This ability to resolve detailed current information from a blurred magnetic field map highlights the fundamental challenge and goal of inverse problem studies. All the information we need to reconstruct high resolution current maps is encoded in the magnetic field profile, we just need to be able to find proper methods to handle experimental noise which obfuscate the useful information and necessitate detrimental trade-offs between signal fidelity and spatial resolution.

However, even for the case above with no additional noise added (see Figure 2.5), some windowing had to be applied to ensure the problem was numerically stable (for a standoff distance of $\Delta z = 800\ \mu m$, maximum values of the inverse filter function are of the order 10^{258}, so numerical rounding errors become significant) and to account for the finite field of view and the size of the pixels. This use of windowing results in a slight degradation of the current amplitude and spatial resolution. When a significant amount of simulated noise

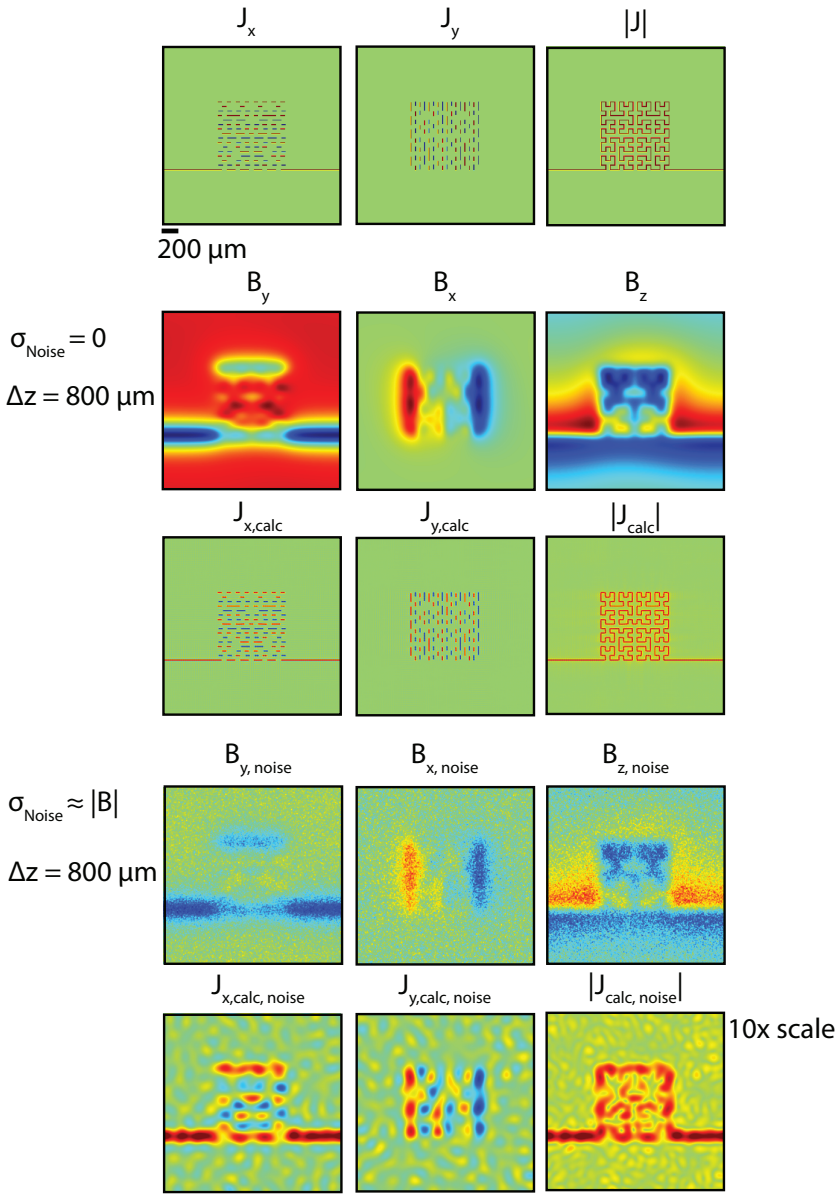

Figure 2.5: Example analysis of the ability to reconstruct current distributions for measurements planes far away from the source distribution. The same current distribution as in Figure 2.3 is generated here, but a larger field of view is used for the larger standoff simulations. Initially, the large stand-off distance magnetic field is simulated with no noise is added. The inverse calculation is then performed. In the bottom two rows of the figure, noise is introduced and a windowing function is utilized for the reconstruction.

($\sigma_{noise} = |B|$) is added to the magnetic field profile, further fine tuning is needed to extract any realistic current distribution. Extensive filtering is utilized to avoid instabilities of the reconstruction and this results in a dramatic degradation of the signal size (the color scale in Figure 2.5 needed to be magnified by 10× for the noisy current distributions to make the structure visible) and spatial resolution.

2.1.6 Inverse Problem Considerations in 2.5D

Allowing for multiple planes of current flow better approximates the different metal layers seen in structures like integrated circuits [117, 146] while still being compatible with the inverse problem formalism presented in Equation 2.10.

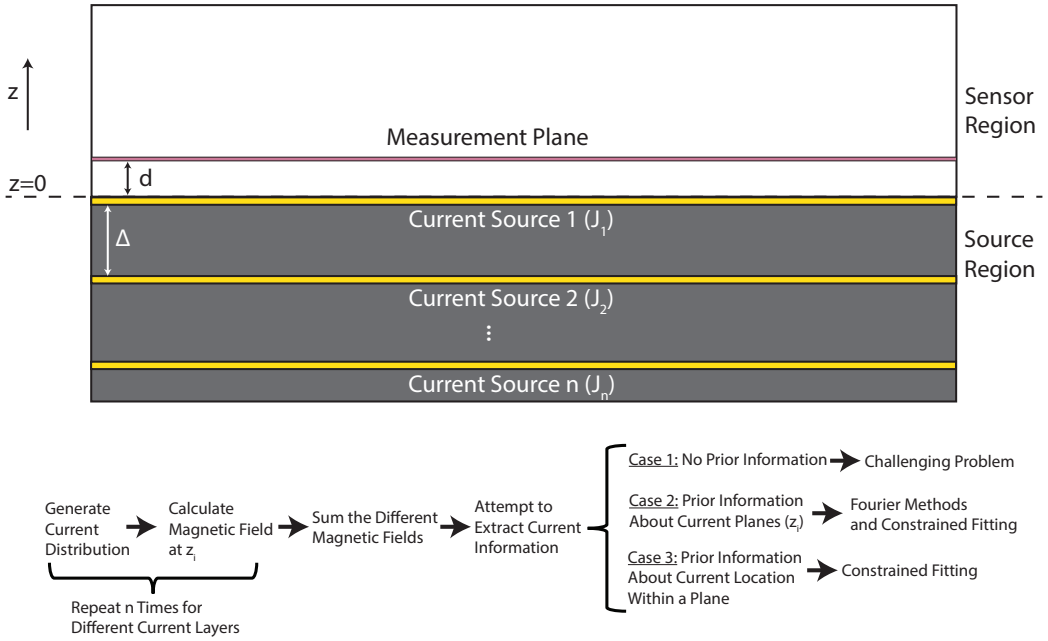

Figure 2.6: Cartoon of the geometry for 2.5D Current sources.

The linearity of Maxwell's Equations [147] (see Equation 2.11) is utilized here to analyze (so-called) 2.5D current source geometries (i.e., currents are restricted to only contain J_x or J_y components, but there can be multiple planes of current.)

$$\begin{aligned} \nabla \times \mathbf{B_1} &= \mu_0 \mathbf{J_1} \\ \nabla \times \mathbf{B_2} &= \mu_0 \mathbf{J_2} \\ \nabla \times (\mathbf{B_1} + \mathbf{B_2}) &= \mu_0 (\mathbf{J_1} + \mathbf{J_2}) \end{aligned} \tag{2.11}$$

For this situation the magnetic field for each plane is calculated independently and the magnetic fields profiles are superimposed on top of each other. Ideally, we would want to do the inverse of this process and determine the contribution from each layer and subtract them out from the measured magnetic field to differentiate the contribution from each layer in Figure 2.6. However, especially for geometries where the magnetic fields from different layers are overlapping and fields are canceling, it is not always straightforward to separate the contributions of different layers.

This section seeks to explore how the Fourier Filter methods used above begins to break down for these more complex source geometries. In general, current sources are not necessarily confined to a regular (or Manhattan grid), so previous inverse problem fitting methods [117] would not apply.

In Figure 2.7, a situation where current sources on two planes is considered. For this first example, the problem is simplified by considering straight wire segments with currents flowing in the opposite directions. The choice of opposing current directions makes the interpretation of the magnetic field images more straight-forward by visual inspection. In the summed magnetic field image in Figure 2.7, the layers are apparent in the B_y image, but not the B_x or B_z image due to the cancellation and superposition of neighboring fields. Since there are two different measurements planes, the conventional Fourier inverse solution can only work for one at a time. The bottom rows of Figure 2.7 illustrate the effect of assuming a given stand-off distance on the other current source. For example, if $\Delta z = 150$ μm is used in the calculation, then J_1 will appear in focus and J_2 will appear slightly blurred

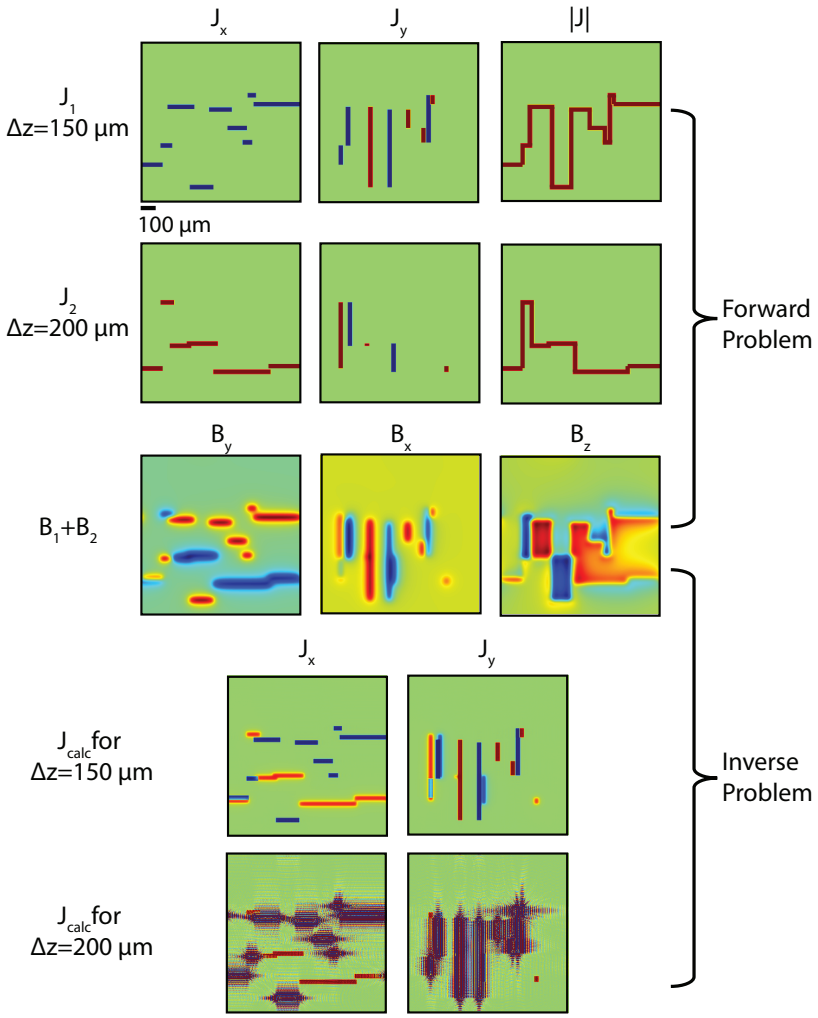

Figure 2.7: Example procedure for interpretation of current sources in two different planes in a 2.5D geometry from a magnetic field measured in a single plane. The current sources are generated in fixed planes (with standoff distances of $\Delta z = 150\ \mu m$ and $\Delta z = 200\ \mu m$. The profile of the current distributions are wire-like sources with right angles where the number of segments and length of each segment is randomly generated.

and out of focus (for the J_x component where there is no cancellation.) However, if $\Delta z = 200\ \mu m$ is used as is done in the bottom row of Figure 2.7, then the problem breaks down because the assumptions of propagating through a source free region are not met. Downward continuation [45] of a measurement plane to a lower one only works in a source-free region,

so J_1 is exponentially amplified to nonphysical values.

In order to accurately interpret the current sources under this framework, an iterative process would be needed using thresholding and fitting to isolate the effect of the closest layer, calculate the magnetic field from that layer, subtract the calculated magnetic field from the measured one, and repeat for all the current source layers. As seen in Figure 2.7, overlapping of current sources in different layers can lead to cancellation or addition of magnetic fields. If the current distribution is assumed to be uniform and prior knowledge was known about the source ($|J|$ is an approximation of a physical wire trace), then constrained fitting methods [132] could be utilized to isolate the layers.

Below, we present two sections that seek to provide extra information in alternative ways. In the first section, we explore the capabilities of vertical gradiometry (measurements of the magnetic field in different planes) and its ability to differentiate close sources from far away ones. In the last section, we explore the usage of machine learning methods, specifically deep neural networks, to provide a general method for solving magnetic inverse problems for current distributions without the need for specialized fine tuning for each specific geometry, source distribution, noise environment, and dimensionality.

2.2 Magnetic Imaging Gradiometry

Magnetic gradiometry (specifically vertical gradiometry here) is a commonly used technique in geophysical [148], medical [149], anomaly detection [150], and mineral exploration [151] due to its ability to differentiate the signal magnetic field from unwanted stray background fields. At least two (larger arrays can be used) magnetic sensors are placed such that one of the sensors is maximally sensitive to the signal of interest, whereas the other sensor is placed at a distance away such that it is primarily sensitive to an assumed uniform background

magnetic field (can be Earth's field or other magnetic sources.) Through taking the difference between the measurements on the two sensors, the signal magnetic field can be isolated under ideal circumstances. More complicated arrays of sensors can be arranged to extract the full magnetic gradient tensor [151–154].

Magnetic gradiometry has found significant use primarily because of the dipole characteristic of the fields of interest and operating in the presence of a uniform background. The dipole characteristic of the magnetic field leads to a faster fall-off of the signal magnetic field ensuring that the signal magnetic field does not influence the background sensor. Operating in the presence of a uniform magnetic field ensures that the placement of the background sensor does not significantly influence the results and fidelity of the noise correction.

These dipole-like and uniform background assumptions are not fully valid for the wide-field imaging examples explored in the works presented in this thesis, which are described Chapters 5 and 6. The NV sensor utilized is within close proximity of the current sources being studied, so the fall-off of the magnetic field is wire-like ($1/r$ to $1/r^2$ scaling compared to the $\sim 1/r^3$ scaling for dipoles.) The slow fall-off of the magnetic field with distance requires the background sensor to be sufficiently far away. For the applications of interest, the background field of interest is not Earth's field or other large fields from instrumentation near the experiment (however, the gradiometry experiments would help correct for those). The background field of interest is other deeper current sources (such as J_2 in Figure 2.7) and we want to try to isolate the contribution of nearby current sources (J_1 in Figure 2.7). These two differences from the usual assumptions of gradiometry complicate the usage of vertical gradient imaging for NVs, but below we show instances where it can provide value.

Fundamentally, no new information is gained from the use of a second measurement plane (if both are in a source free region, illustrated in Figure 2.8). The magnetic field measurement in one plane can be upward continued [45] to the second plane. However, in

the presence of noise and technical constraints and given the need to differentiate one source from another, there is technical value and robustness gained from the measurement at a second plane. For measurements where fidelity of the signal of interest is critical, careful analysis and calibration is needed to correct for the spatial response of gradiometry [155,156].

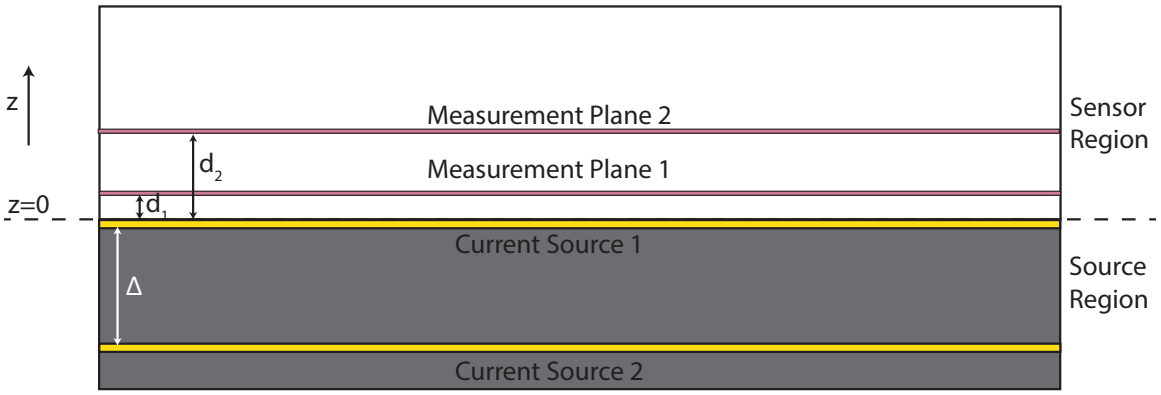

Figure 2.8: Cartoon of the geometry for the gradiometry measurements. The central goal of this problem is to determine what range of parameters are optimal for isolating the contribution of Current Source 1 in the presence of a large background, Current Source 2.

2.2.1 Analytical Approach in 1D

The situation above will be first analytically characterized for a simple 1D current system to understand scaling laws of interest. Specifically, what separation between measurement planes ($d_2 - d_1$) is required to differentiate source currents in different layers for a given separation of sources (Δ)? Simplifying assumptions are made to assist with analytical expressions and numerical simulations are shown for more complicated source geometries in the following section. The wire sources are assumed to be infinite wire-like sources (1D), the measurement tool is assumed to be sufficiently small to ignore finite-thickness effects, a single point directly above the wire is considered, and only the magnitude of the magnetic field at this point is explored.

Given these assumptions, the magnetic fields in Measurement Plane 1 (B_1) and Measurement Plane 2 (B_2) due to Current Source 1 (I_1) and Current Source 2 (I_2) are given by:

$$\begin{aligned} B_1 &= \frac{\mu_0 I_1}{2\pi d_1} + \frac{\mu_0 I_2}{2\pi(d_1+\Delta)} \\ B_2 &= \frac{\mu_0 I_1}{2\pi d_2} + \frac{\mu_0 I_2}{2\pi(d_2+\Delta)} \end{aligned} \tag{2.12}$$

The local vertical gradient of the magnetic field is proportional to $(B_1 - B_2)$.

$$B_1 - B_2 = \left[\frac{\mu_0 I_1}{2\pi d_1} + \frac{\mu_0 I_2}{2\pi(d_1+\Delta)} - \frac{\mu_0 I_1}{2\pi d_2} - \frac{\mu_0 I_2}{2\pi(d_2+\Delta)}\right] \tag{2.13}$$

The goal is to find the combination of d_1, d_2, and Δ that is maximally sensitive to the current source in layer 1 while canceling out the contribution from layer 2.

$$B_1 - B_2 = \left[\frac{\mu_0 I_1}{2\pi d_1} - \frac{\mu_0 I_1}{2\pi d_2}\right] + \left[\frac{\mu_0 I_2}{2\pi(d_1+\Delta)} - \frac{\mu_0 I_2}{2\pi(d_2+\Delta)}\right] \tag{2.14}$$

The equation is broken up into two terms; the first term is dependent on the current I_1 and this term should be as close to $\frac{\mu_0 I_1}{2\pi d_1}$ as possible, motivating $d_2 \gg d_1$. The second term contains information about the magnetic field due to the current in the unwanted layer, I_2. This term should be minimized, motivating the assumption $\Delta \gg d_1, d_2$. Putting together these constraints gives the ordering $\Delta \gg d_2 \gg d_1$, which matches the intuition that separating information from the different current source layers works best if the current layers are well separated from one another and if the first measurement plane is much closer to the first current layer than the second measurement layer.

The expression above can be rearranged into a simpler expression that allows for the identification of the relevant scaling terms.

$$B_1 - B_2 = \frac{\mu_0 I_1}{2\pi d_1}\left(1 - \frac{d_1}{d_2}\right) + \frac{\mu_0 I_2}{2\pi(d_1+\Delta)}\left(1 - \frac{d_1+\Delta}{d_2+\Delta}\right) \tag{2.15}$$

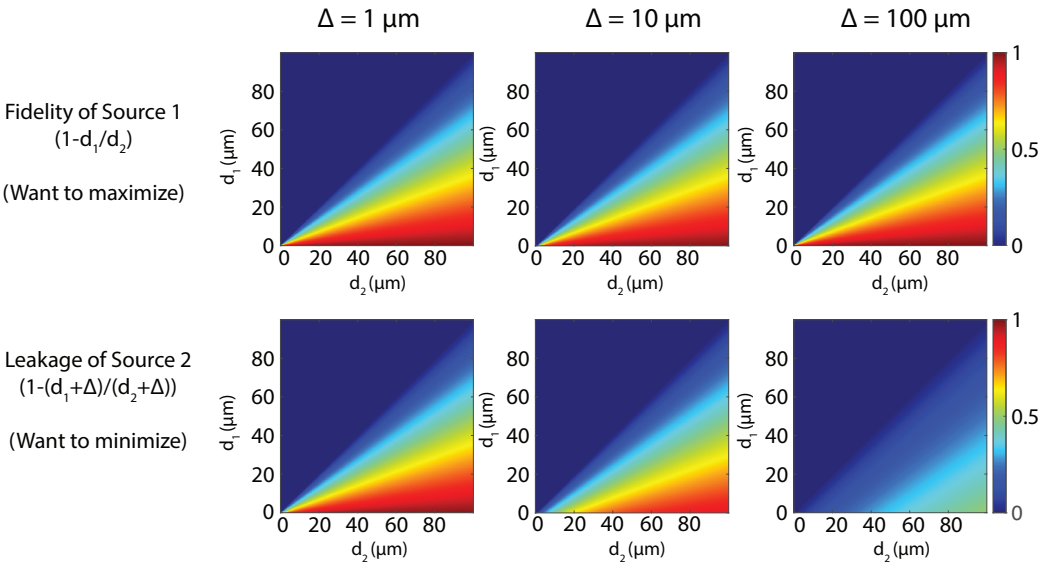

Figure 2.9: Scalings of correction factors for vertical gradient imaging as a function of current source layer separation Δ.

The first term in Equation 2.15 represents the purity of the signal of interest and the second term is how much the deeper current source contributes to the measured magnetic field. Gradiometry introduces two correction factors: (1) $\left(1 - \frac{d_1}{d_2}\right)$, which encodes how much the wanted signal is distorted by the subtraction of the magnetic field at the second plane and (2) $\left(1 - \frac{d_1+\Delta}{d_2+\Delta}\right)$, which shows the scaling of how much the second layer is suppressed by the gradiometry measurement. As a sanity check, in the limit of $d_2 \to \infty$ this expression becomes the magnetic field from a single measurement plane.

2.2.2 Analysis for More Complex Current Sources

Fourier Formalism

Transforming the problem to Fourier Space and looking back at the relevant filter functions (Equation 2.16) allows for a similar procedure to the 1D case. For all of the filter functions, the z-dependence of the function is only contained in the first term $e^{-\Delta z\sqrt{k_x^2+k_y^2}}$, so we can consider just one component of the magnetic field, B_x (and the Fourier transform (b_x) and the same general trends will apply to all components of the magnetic field.

$$\begin{aligned} b_x(k_x,k_y) &= \frac{\mu_0 d}{2} e^{-\Delta z\sqrt{k_x^2+k_y^2}} j_y(k_x,k_y) \\ b_y(k_x,k_y) &= \frac{\mu_0 d}{2} e^{-\Delta z\sqrt{k_x^2+k_y^2}} j_x(k_x,k_y) \\ b_z(k_x,k_y) &= -i\frac{\mu_0 d}{2} e^{-\Delta z\sqrt{k_x^2+k_y^2}} \left[\frac{k_y}{\sqrt{k_x^2+k_y^2}} j_x(k_x,k_y) - \frac{k_x}{\sqrt{k_x^2+k_y^2}} j_y(k_x,k_y) \right] \end{aligned} \tag{2.16}$$

With the same definitions from Figure 2.8 and defining $k_\perp = \sqrt{k_x^2+k_y^2}$ for clarity:

$$\begin{aligned} b_{1,x} &= \frac{\mu_0 d}{2} \left[e^{-d_1 k_\perp} j_{y,1} + e^{-(d_1+\Delta)k_\perp} j_{y,2} \right] \\ b_{2,x} &= \frac{\mu_0 d}{2} \left[e^{-d_2 k_\perp} j_{y,1} + e^{-(d_2+\Delta)k_\perp} j_{y,2} \right] \\ b_{1,x} - b_{2,x} &= \frac{\mu_0 d}{2} \left[e^{-d_1 k_\perp}(1 - e^{-(d_2-d_1)k_\perp}) j_{y,1} + e^{-(d_1+\Delta)k_\perp}(1 - e^{-(d_2-d_1)k_\perp}) j_{y,2} \right] \end{aligned} \tag{2.17}$$

This expression leads to similar conclusions as Equation 2.15, with a slight difference. In this case, the Δ terms cancel out in the second correction factor due to the behavior of the exponential function compared to the inverse function in Equation 2.15. This makes the trade-off between isolating the source term of interest while minimizing distortion. So the term to be minimized $(1 - e^{-(d_2-d_1)k_\perp})$ is the same term to be maximized. This forces a choice to be made in the more general case for how much the fidelity of the current source

of interest should be preserved versus how much the contribution from second source should be canceled.

Trivial Cases

When applying this analysis to currents of greater complexity, there is a large distribution of 3D current sources that are easily distinguishable from one another through the spatial configuration of currents and not necessarily through gradiometry. For example, cases where the current sources are well separated in space (relative to the stand-off distance of the measurement) allows for the separation of current sources at different layers. Another example of this is if there are wires that are spatially overlapping, but are flowing in orthogonal directions, such that they show up in different vector components of the magnetic. Such a geometry is often utilized in the different top layers of integrated circuits [146] to minimize couplings between the metal traces. In this scenario, the vector magnetic imaging of NV diamond provides [146] an advantage over techniques that would just be sensitive to one component of the magnetic field, for example B_z, which is common in scanning probes. Another class of current sources that allow for easy determination of the source layer, are ones where each layer can be independently controlled and a situation can be engineered where only one layer is active at a given time, thereby using temporal or frequency characteristics of the signals to isolate the layers. Both of these situations are using prior information or inferred information about the structure to assist in the differentiation of current sources.

Nontrivial Geometries

Magnetic gradiometry of wire-like current sources is less advantageous compared to the traditional use-case of surveying magnetic dipoles due to the different scaling laws for the magnetic fields. Due to the slower $1/r$ fall off of the magnetic field with distance for wire-like

current sources, large separation between the layers and measurements planes is needed to sufficiently distinguish the layers from one another.

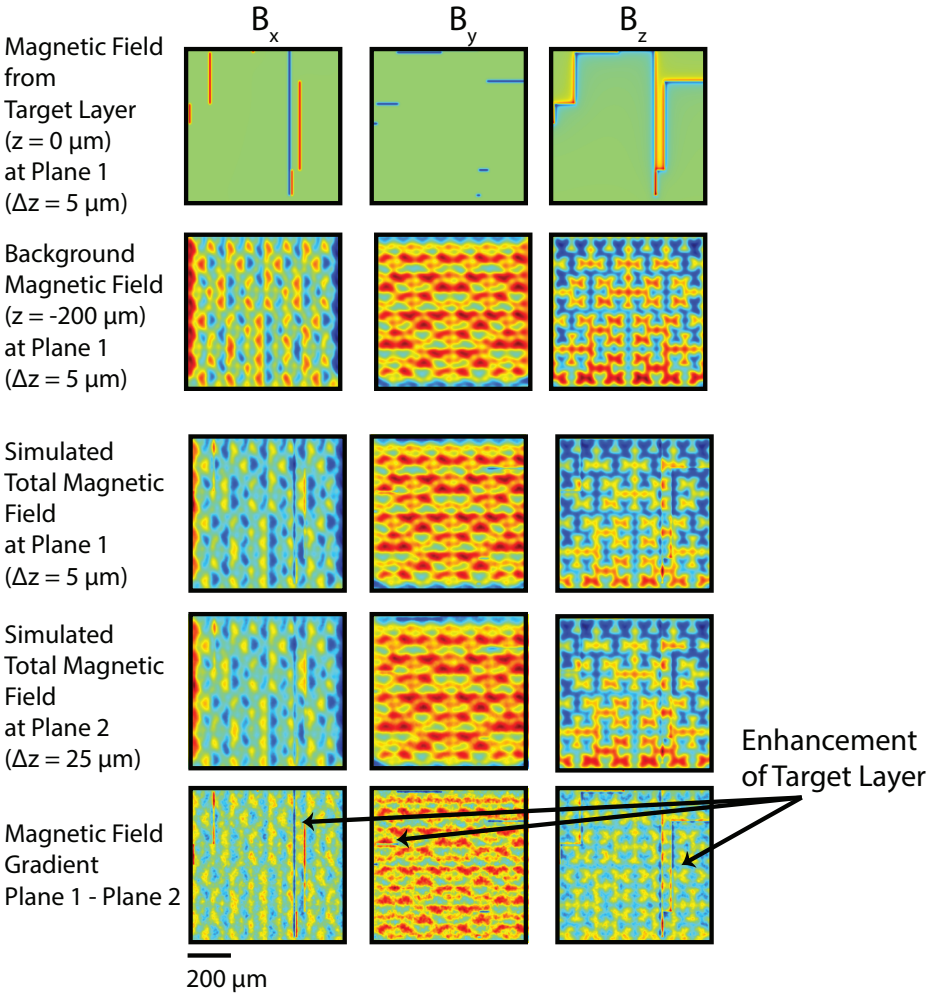

Figure 2.10: Utility of imaging the magnetic field at multiple measurement planes to enhance the distinguishability of a nearby target current source layer in the presence of a larger spatially varying background.

Figure 2.10 illustrates an example where there is a relatively weak, sparse target current source that needs to be differentiated from a strong, spatially complex background. Operating in a favorable measurement regime where the separation between the current sources is greater than the separation between the measurement planes, illustrates that

gradiometry has the ability to enhance nearby current sources of interest, but it is often challenging to completely eliminate the influence of the spatially varying background from gradiometry alone (in this regime).

Imaging the magnetic field at multiple planes can improve measurement performance under a set of certain conditions: (i) the different layers cannot be independently controlled or modulated (ii) the different layers cover roughly the same regions with similar vector components (iii) the nearby layer (the target layer) has a much lower magnitude of current than the background layer (otherwise differentiating the layers is feasible with only a single measurement plane) and (iv) the target plane and background plane are well separated from one another. Further improvements can be made if the background field or the source field was dipole-like (for example trying to distinguish a current distribution from a background field of magnetic materials or vice versa).

2.3 Teaching a Neural Network Biot-Savart's Law

Neural networks are increasingly becoming a useful tool for analysis and interpretation of complex, multi-dimensional datasets and even ill-posed inverse problems in medical sciences [157–160], microscopy [161–163], imaging [164], nondestructive evaluation [165], tokamak diagnostics [166], and magnetic anomaly detection [167] among many other fields and applications. As discussed in Reference [160], neural network-based supervised learning methods are a natural solution for problems that are conventionally solved by complex reconstructions with multiple steps that need to be fine tuned dependent on the experimental situation and desired performance. Rather than having an experimenter finely tune the cut-off frequency and the methods to constrain the fits and hyperparameters to ensure optimal performance for each implementation of the inverse problem, a neural network can be uti-

lized given there is sufficient training data. One benefit of trying to solve inverse problems, is that the forward problem is often well described. For the situation of the magnetic inverse problem where the sources are current distributions, the forward problem is given by Biot-Savart's Law (Equation 2.1). Coupled with the Fourier Filter Formalism [45], which makes the forward problem computationally efficient, large amount of datasets spanning a wide range of conditions can be generated. This section discusses recent efforts to combine the data generation capability of the magnetic forward problem with the demonstrated success of the AUTOMAP framework [160] and deep neural networks in image reconstruction.

In this section, we will focus on validation of the usage of deep neural networks for 2D current distributions to allow for comparisons to earlier chapters. Furthermore, we are actively working on scaling up the framework to 2.5D and 3D current distributions and overcoming the intensive data needs for these scenarios. Since we are utilizing the neural network to solve an inverse problem, nominal solutions can always be checked and confirmed efficiently through calculation of the forward problem. At the very least, the output of these models can be used to inform weights or starting guesses in conventional inverse problem regularization and fitting methodologies.

2.3.1 Training Data Generation

The quality of the results of deep neural networks is largely dependent on the quality and amount of training data. Through the training data, prior information can be added by choosing what types of sources and distributions are included in the dataset. Training the neural network is an iterative process; through the training and validation procedure, the choice of training data can be modified to focus on classes of current sources, noise levels, or stand-off distances with the lowest reconstruction accuracy to constantly improve performance. To enable this process, we have developed a pipeline that can generate a

sufficiently large amount of data for the intended magnetic field images.

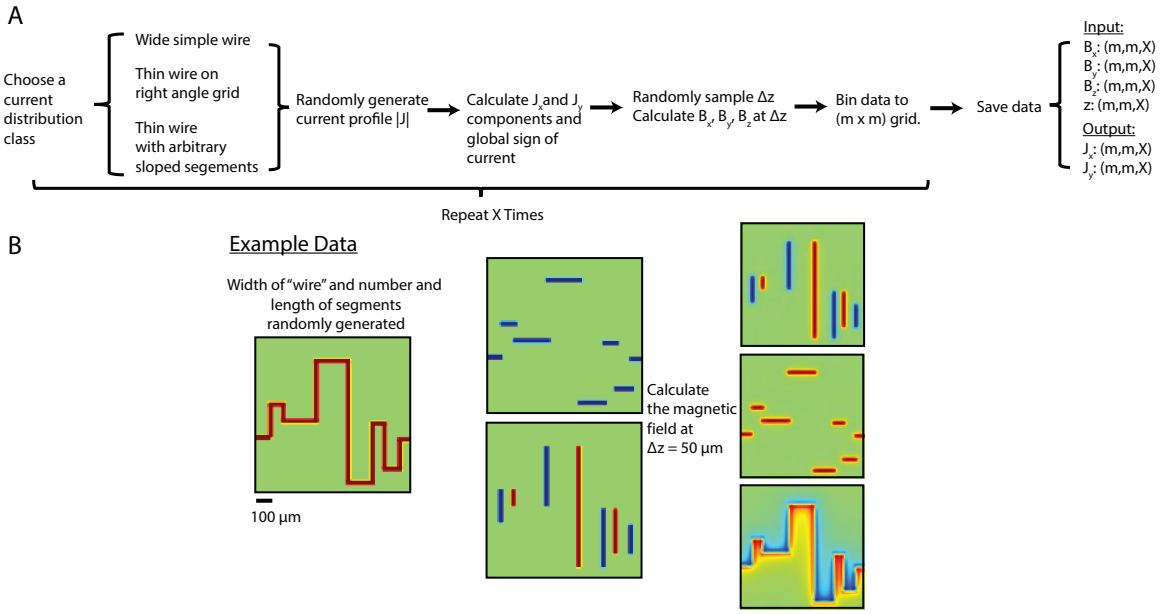

Figure 2.11: (A) Overview of the process for generating training data (B) An example dataset showing the narrow right angle class of wire and the calculated magnetic field.

Generation of all the parameters and distributions manually would drastically slow down the data generation process, so we developed a process to automatically generate a large set of diverse datasets. We chose four different classes of 2D current distributions that are representative of different classes of experiments and situations. Furthermore, given the nature of the calculation of the inverse problem with the Fourier Filter method, many different length scales can be represented with one simulation. For example, a magnetic field simulation with a field of view of 1 mm with a 100 μm stand-off distance is equivalent to a simulation with a field of view of 1 μm with a 100 nm stand-off distance.

1. A wide wire (relative to the field of view) with a single segment that travels in only one Cartesian coordinate (J_x, J_y) and projects onto only two components of the magnetic field. This situation is representative of many condensed matter applications such as

electron flow in graphene and other conductors [145].

2. A wide wire with a single segment at an arbitrary angle that has projections on all three components of the magnetic field, which mathematically is equivalent to a rotated version of the first case, but influences the training process differently.

3. A narrow wire that can have many different segments, but each segment is connected to the previous by a 90° turn. This situation is most comparable to the Manhattan Grid configuration [117] and is an approximation of some of the structures in integrated circuits.

4. A narrow wire with many segments that are connected to one another at arbitrary angles. This class of wires shows the capability of resolving currents that are not confined to a grid and assists in the training process where the many slopes effectively sample many different values of the current and magnetic field in a given image.

One piece of prior information built into these structures is the conservation of current. There is always one continuous current segment flowing through the field of view in a given simulation. (In later sections, the linearity of Maxwell's Equations and superposition of fields is used to generate more complex 2D distributions from the summation of several different profiles.) We are actively working on expanding this list of classes to include more complex phenomena like non-uniform cross sections of current profiles due to propagation around a defect or the splitting of current into different paths.

Following the generation of a given current distribution class and calculation of J_x and J_y for a given field of view and grid size, the magnetic field is calculated. A higher resolution and larger field of view is used to calculate the magnetic field than is eventually used in the training of the neural network to limit the binning artifacts and edge effects. The stand-off distance (Δz) is randomly generated and the magnetic field is calculated at this

plane. The magnetic field and original current profiles are binned to the final grid size (100 × 100) for the present work and the process is repeated until sufficient data is generated. This protocols allows for the generation of 100, 000 datasets in ten minutes without much computational optimization.

2.3.2 Model architecture and Training

The specific model architecture utilized for the neural network is based off previous work from Reference [160]. The generated data in Figure 2.11 was vectorized from (m, m, X) to (m^2, X) where m is 100, the number of pixels in the field of view and X is 50,000, the size of the first training set used. The magnetic field values were normalized between 0 and 1 and the z values where normalized by the maximum stand-off distance in the dataset ($\Delta z_{max} = 710$). A 100×100 matrix of the z-values was used to better incorporate the z-information into the existing data structure, rather than a single value. This data structure enables using other prior information like the extent of the physical structure carrying the current to be integrated in the training process in a natural way. The data was vectorized in the format $[B_{x,1},\ B_{y,1},\ B_{z,1},\ z_1,\ B_{x,2},\ B_{y,2},\ B_{z,2},\ z_2\ \ldots\ B_{x,m^2},\ B_{y,m^2},\ B_{x,m^2},\ z_{m^2}]$, where the exact ordering of the individual components does not influence the result [160] due to the use of a fully connected layer at the first layer. The input layer denoted, FC1, is connected to the first fully connected hidden layer, FC2, of size 20000 × 1 and activated by the hyperbolic tangent function. The FC2 is fully connected to the second hidden layer, FC3, which also utilizes hyperbolic tangent activation. FC3 is reshaped to a matrix of size 100 × 200 to enable the use of convolution layers. The first convolution layer, C1, convolves 200 filters of size 5 × 5 with stride 1 (moves one pixel at a time). This is followed by a rectifier non-linearity (ReLU). The second convolution, C2, repeats this process with 200 filters of size 5 × 5 with stride 1 followed by another rectifier non-linearity. The final output layer

deconvolves the C2 layer with 1 filter of size 7×7 and stride 1. Finally, this is output to a vector of size 1×20000. This output is a prediction of the J_x and J_y current profiles with a similar format to the magnetic field, $[J_{x,1},\ J_{y,1},\ J_{x,2},\ J_{y,2}\ \ldots\ J_{x,m^2},\ J_{y,m^2}]$. This model architecture was previously optimized for calculating the Fourier transform of images and for the analysis of MRI datasets [160] and the exact structure (filter size, etc) likely requires some tuning to further optimize for current distribution reconstruction.

Proper curation of the training dataset is vital to the performance of the learning process and this is where prior informed and physics-informed choices are introduced [160]. The initial training image set consisted of 50,000 sets of magnetic field and current images, tested on a held out set of size 1,838 images. The RMSProp algorithm [168] was used with minibatch sizes of 100, trained for 100 epochs, and learning rate of 0.000001. The loss function minimized during training was the mean squared loss between the network output and ground truth values. An additional L1-norm penalty ($\lambda = 0.0001$) was applied to the feature map activations of the final hidden layer C2 to promote sparse convolutional representations given that the network was being trained on a small fraction of all the possible 2D current distributions. Three separate networks were trained on datasets with varying amounts of spatially distributed Gaussian noise (i) 0 (noiseless) (ii) 0.025*randn([100,100]) (iii) 0.25*randn([100,100]) added to the normalized magnetic field mages to probe the robustness of the neural network to noise on the reconstruction. The superior noise handling of neural networks [160] for image reconstruction is one of the key potential benefits of using a neural network for inverse problem. This avoids the trade-off between stability and spatial resolution found in the Fourier Filter method and other inverse problem protocols.

2.3.3 Simple Current Profiles

Following the training, we tested the performance of the neural network and compared the results to previous reconstructions performed with the Fourier method (Figure 2.4). The neural network demonstrates remarkable robustness to high frequency spatial noise (Figure 2.12(A)) without degrading the sharp rise of the current profile (Figure 2.12(B)). Furthermore in regions far away from the current source where there is still significant spatial noise, the current profile is almost entirely flat without any ringings or artifacts present in traditional reconstruction methods.

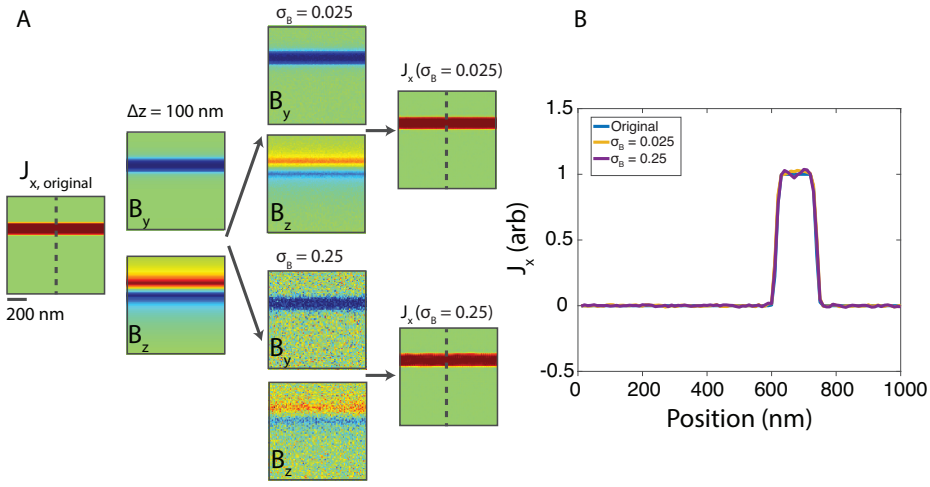

Figure 2.12: Channel reconstruction with AUTOMAP framework (A) We generate a J_x current distribution of a simple channel like-source and calculate the expected magnetic field at a standoff plane Δz above the surface. Varying amounts of Gaussian spatial noise with fractional amplitudes $\sigma_B = 0.025$ and $\sigma_B = 0.25$ are added to the normalized magnetic field profiles. Neural network reconstruction of the original current profile demonstrates robustness to spatial noise, especially compared to Figure 2.4. (B) The cross sectional profile is taken along the center of the field of view. These cross sections demonstrate that the neural network reconstruction is robust to spatial noise without having to degrade spatial resolution.

This result shows great promise for the potential use of neural networks for the magnetic inverse problem from complex current distributions, and we explore the present results

and limitations with regards to more complex distributions below in Figure 2.13.

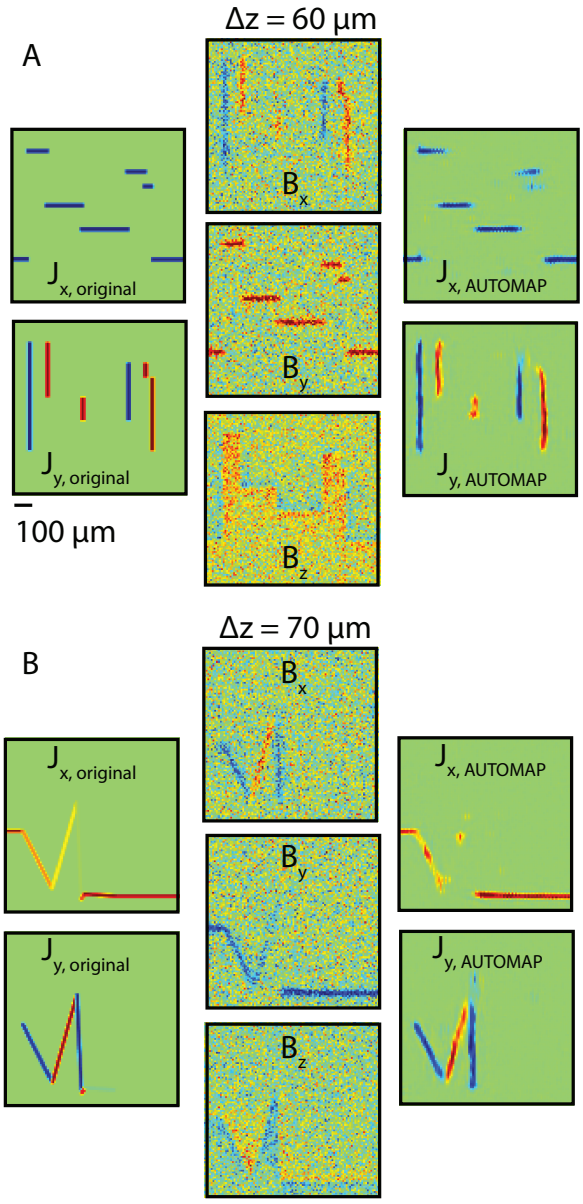

Figure 2.13: Robustness of AUTOMAP framework to high spatial noise. (A) A current source distribution of thin wire segments connecting to each other at right angles was generated. Compared to Figure 2.12, the width of the wires is much narrower, which likely explains the slight degradation in reconstruction performance compared to the wide wire example. (B) A sloped current was generated and tested to demonstrate another limitation of the reconstruction. Cancellation of magnetic fields near the tip of the point leads to decreased reconstruction accuracy and the introduction of some anomalous currents in the J_x to compensate.

In the presence of a large amount of high frequency noise, the reconstruction of the narrower and more complex features in Figure 2.13 begins to suffer, but is still overall significantly more robust to high frequency spatial noise compared to the Fourier method and others. Noticing areas where the reconstruction accuracy is suffering allows for feedback into the training process. More training data can be generated with sharp peaks and areas of current cancellation, the structure of the model can be modified to change the filter size, or datasets with more pixels in the field of view can be generated (at the cost of significant training time) to attempt to minimize the edge effects of the reconstruction and blurring.

2.3.4 Initial Large Stand-off Distance Reconstruction

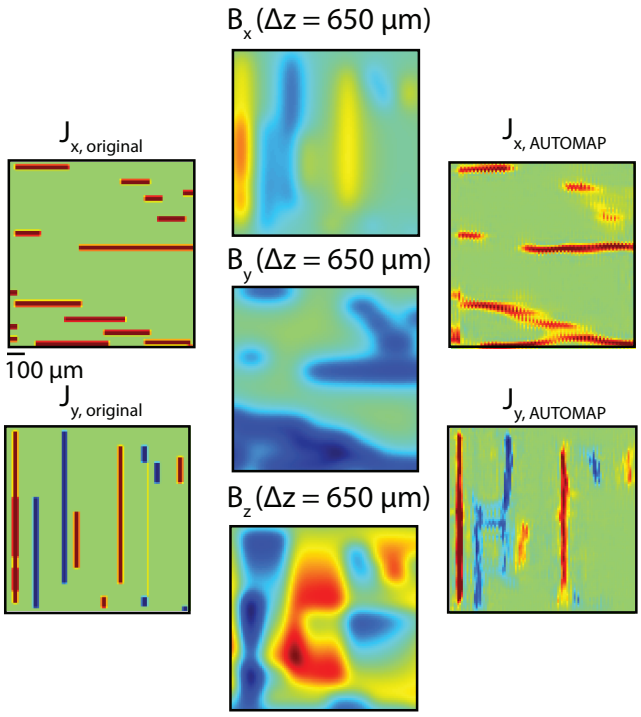

Figure 2.14: Reconstruction of complex current sources from a large stand-off distance with no additional noise. The reconstructed current distribution shows reasonable agreement with the initial distribution, but more work is needed to further train the neural network on datasets with larger stand-off distances and with added noise.

Another region of parameter space that helps to illustrate the limitations and capabilities of the neural network method is the reconstruction of a current source from a measurement plane with a large stand-off distance as shown in Figure 2.14. The general agreement between the initial and reconstructed current distributions shows promise in terms of the generalizability of the method to more complex distributions. Furthermore, this reconstruction is trained with a relatively sparse set of data like it because this is on the far end of the Δz distribution in the dataset. Training with more images with large stand-off distances is likely to increase the performance.

2.3.5 Outlook

These initial results demonstrating the capability of neural networks to solve the magnetic inverse problem for current sources even in the presence of high amounts of spatial noise are encouraging for the development of future applications in this direction. Specifically, we are exploring the potential use case of neural networks to solve many of the examples shown previously in this chapter:

- Differentiating between rectangular, parabolic, and even more complex cross sectional profiles of current flow.
- Exploration of the benefit of full vector magnetic imaging is and under what circumstances fewer components can be used.
- Reconstruction of non-uniform current flow around defects in conductors.
- Precise inversion of current sources for magnetic fields with large stand-off distances and low signal to noise ratio magnetic field measurements.
- Localizing current sources in 2.5D and 3D structures and differentiating the nearest layer from the deeper ones.

- Combining multi-plane magnetic field measurements to further evaluate the value of vertical imaging gradiometry.
- Integration of prior information and multi-modal measurements.
- Applications to biological structures and systems where there aren't regularly ordered or aligned wire-like structures.

Training datasets for all of these tasks can be generated with the current capabilities. Going forward, some of the main limitations are going to be data management, training time, and the limitations of hardware. For these datasets taken above, training took on average 1 day with the hardware described in Reference [160] and the training images were limited to 100 by 100 because of limitations of the hardware used for training and the drastic increase in training time larger images would demand. These obstacles need to be overcome to advance further in this direction.

Chapter 3

Optical Detection of Biomagnetic Fields from Giant Axons

Magnetic fields from neuronal action potentials (APs) pass largely unperturbed through biological tissue, allowing magnetic measurements of AP dynamics to be performed extracellularly or even outside intact organisms. To date, however, magnetic techniques for sensing neuronal activity have either operated at the macroscale with coarse spatial and/or temporal resolution—e.g., magnetic resonance imaging methods and magnetoencephalography—or been restricted to biophysics studies of excised neurons probed with cryogenic or bulky detectors that do not provide single-neuron spatial resolution and are not scalable to functional networks or intact organisms. Here, we show that AP magnetic sensing can be realized with both single-neuron sensitivity and intact organism applicability using optically probed nitrogen-vacancy (NV) quantum defects in diamond, operated under ambient conditions and with the NV diamond sensor in close proximity ($\sim 10\ \mu m$) to the biological sample. We demonstrate this method for excised single neurons from marine worm and squid, and then exterior to intact, optically opaque marine worms for extended periods and with no observed

adverse effect on the animal. NV diamond magnetometry is noninvasive and label-free and does not cause photodamage. The method provides precise measurement of AP waveforms from individual neurons and directly determines the AP propagation direction through the inherent sensitivity of NVs to the associated AP magnetic field vector.

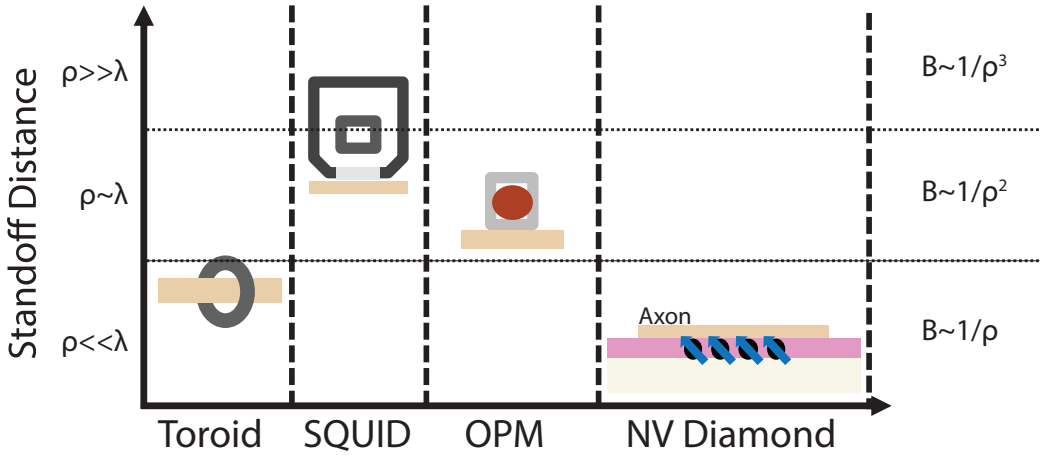

Figure 3.1: Cartoon of minimum standoff distance for different sensors. Schematic of different sensors, a Toroid pickup loop, a Superconducting Quantum Interference Device (SQUID), Optically Pumped (or Atomic) Magnetometer (OPM), and an NV Diamond magnetometer used for magnetic sensing. The characteristic stand-off distance ρ is displayed relative to the characteristic wavelength of the action potential ($\lambda = v_c \Delta t$), where v_c is the conduction velocity of the axon and Δt is the rise time of the action potential. Three different scaling regimes are presented. For stand-off distances much larger than characteristic length scales of the action potential, for example those seen in MEG, the current acts like a current dipole and scale as $\sim \frac{1}{\rho^3}$ [109]. NV Diamond sensors allow for close proximity of the axon and operate in a much more favorable scaling regime of $\sim \frac{1}{\rho}$.

3.1 Simple Magnetic Field Model for the Giant Axon

The magnetic field produced by an axon AP (see Figure 3.2 for details), here denoted as $B_{axon}(z, \rho, t)$, can be derived from the intracellular AP voltage $\Phi(z, \rho, t)$, where z and ρ denote the axial and radial coordinates respectively, using a simple model that agrees with more complex cable theory calculations [169,170]. The axon is modeled as a conducting wire;

hence the magnetic field is $B_{wire} = (\mu_0 I)/(2\pi\rho)$, with axial current I due to the propagating AP.

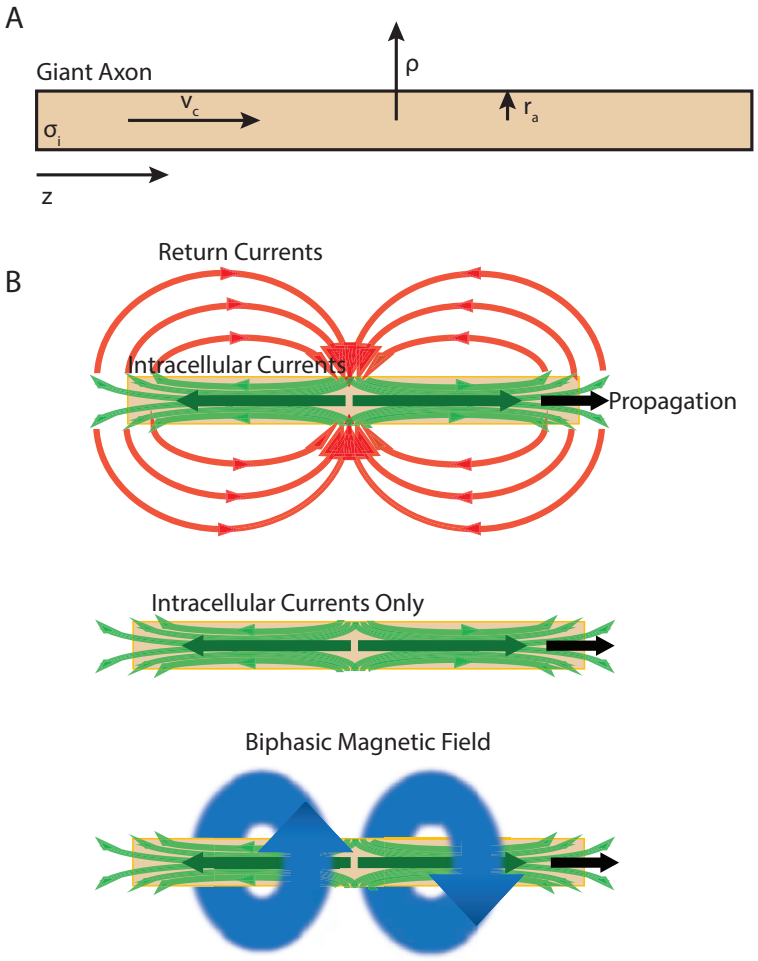

Figure 3.2: (A) Schematic showing relevant parameters used in the simple model for calculating the expected magnetic field associated with a giant axon action potential. (B) Relevant currents associated with action potential propagation. For stand-off distances much closer than the characteristic length scale of the action potential, return currents can be neglected and the model dramatically simplifies.

From Ohm's Law, the wire's current density is $J = -\sigma\Delta\Phi(z, \rho, t)$, where σ is the electrical conductivity. For a uniform cylindrical wire of radius r_a, the axial current may be expressed as:

$$I = \pi r_a^2 J_z = -\pi r_a^2 \sigma \frac{\partial \Phi}{\partial z} \tag{3.1}$$

For constant (or near constant) values of conduction velocity v_c, the equality $\frac{\partial \Phi(z,\rho,t)}{\partial t} = -v_c \frac{\partial \Phi(z,\rho,t)}{\partial z}$ holds, where v_c is defined by convention to be positive [169]. Substitution then yields $I = \frac{\pi r_a^2 \sigma}{v_c} \frac{\partial \Phi(z,\rho,t)}{\partial t}$. At distances close to the axon surface where $\rho \sim r_a$, return currents outside the axon are minimal [169] (Figure 3.2(B)), and fringing effects from the finite axon length can be ignored, yielding:

$$B_{axon}(z,\rho,t) = \frac{\mu_0 r_a^2 \sigma}{2 v_c \rho} \frac{\partial \Phi(z,\rho,t)}{\partial t}. \tag{3.2}$$

Defining $s \equiv (\mu_0 r_a^2 \sigma)/(2 v_c \rho)$ gives $B_{axon}(z,\rho,t) = s \frac{\partial \Phi(z,\rho,t)}{\partial t}$, where s depends only on geometric and electrophysiological quantities. In order to maximize both the amplitude of the magnetic field and the sensing volume of NVs that can be effectively utilized, organisms with large axons and fast action potential rise times are ideal.

3.2 Specimen Selection and Electrophysiology Protocols

3.2.1 *Myxicola infundibulum*

M. infundibulum specimens are marine invertebrates that possess a large giant axon [171], are readily available year-round, and can be kept for long periods of time in laboratory environments, making them an ideal organism for these experiments. The giant axon mediates a rapid escape reflex; electrical or physical stimulus elicits a violent muscular contraction, which can shorten the worm by 50% or more compared to the relaxed state. Specimens are obtained from a commercial supplier (Gulf of Maine Inc., Bay of Fundy, Maine, USA) or a research laboratory (UC Davis Bodega Bay Marine Biology Laboratory, California, USA). Worms are housed in a 200 L aquarium filled with artificial seawater (ASW) from a

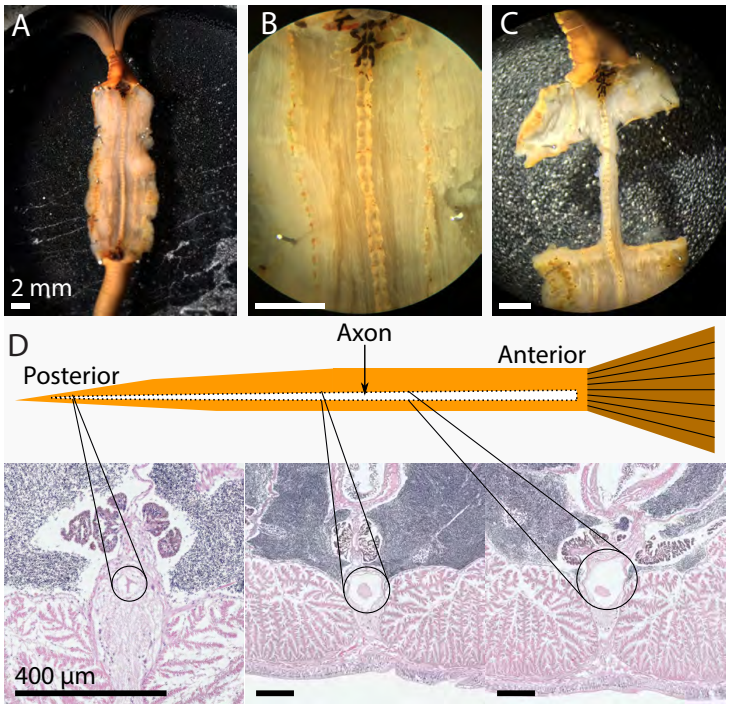

Figure 3.3: *Myxicola infundibulum* preparation. (A) Photo of worm with nerve cord containing giant axon exposed. (B) Close-up view of same specimen. The nerve cord is ~ 400 μm across near the anterior (top) end. (C) Same specimen with muscle tissue removed. At this stage the dissection protocol is complete. All white scale bars correspond to 2 mm. (D) Cartoon drawing of worm and transverse sections. Leftmost section is from near the tip of the posterior end of the specimen, demonstrating the significant tapering of the giant axon. All black scale bars correspond to ~ 400 μm.

commercial supplier (Instant Ocean Sea Salt) and temperature stabilized to 7.5 ± 0.5 $^{\circ}C$. Worms are fed a plankton-based food source (Sera Marin Coraliquid) every 14 days. Large specimens of length ~ 60 mm and diameter > 5 mm (both measured when fully contracted) are used in the magnetic measurements. Electrophysiology measurements [172] use worms of length > 30 mm and diameter ~ 3.5 mm.

For studies of the excised giant axon of *M. infundibulum*, a modified version of the Binstock and Goldman method is followed [173]: (i) The ventral side of *M. infundibulum* is

identified by a triangular structure on the thorax [174]. (ii) The worm is pinned ventral side down in a glass dish spray-painted flat black (Krylon Ultra Flat Black 1602) and filled with PDMS (Dow Corning Sylgard 184). The specimen is illuminated with broadband white light at a shallow grazing angle. The painted dish and shallow lighting increased contrast between the axon and the surrounding tissue for better visibility. The preparation is submerged in chilled ASW throughout. (iii) A median dorsal incision of length ~ 2 cm is made through the body wall at the mid-section of the animal. Further cuts sever connective tissue between the body wall and the gut. (iv) The freed body wall is pinned to the PDMS away from the axon with substantial tension (see Reference [173]). (v) The gut is partially lifted (vertically up) from the body wall, allowing fine vanassas scissors to cut the connective tissue connecting the gut to the body wall. The gut is excised from the specimen, revealing the dorsal side of the ventral nerve cord containing the giant axon. (vi) The ventral blood vessels and additional tissue close to the axon are carefully stripped away with fine forceps, further exposing the nerve cord as shown in Figure 3.3(A,B). (vii) Additional cuts through the body wall remove tissue around the nerve cord as shown in Figure 3.3(C). (viii) The excised nerve cord (still connected to the undissected worm anterior and posterior) is then placed dorsal-side-down on the diamond sensor chip. In this configuration the worm is alive, and action potential (AP) firing can continue for 72 hours or longer. A flexible acrylic clamp holds the nerve cord fixed against the diamond chip to restrain the worm's muscle contractions [175]. Axon viability is checked periodically through physical or electrical stimulus at the worm posterior and confirmation of muscle response at the worm anterior. For studies of intact specimens of *M. infundibulum*, the worm is cleaned of accumulated mucus and placed in an acrylic jig to fix the dorsal side of the animal closest to the NV layer of the diamond. For both excised axons and live, intact worms, the specimen preparation is continuously perfused with 10°C ASW with a gaseous solute of 99.5% O_2 and 0.5% CO_2.

3.2.2 *Loligo pealeii*

Specimens of *L. pealeii* are acquired seasonally from the Marine Biological Laboratory in Woods Hole, Massachusetts, USA, with medium to large squid (0.3 m to 0.5 m in overall length) chosen for the present studies. Following decapitation of the squid, the post-synaptic giant axons are isolated following the protocol described in Reference [176]. The axons are placed in vials containing calcium-free saline solution and stored on ice. The iced vials are transported from Woods Hole to our laboratory at Harvard University (90-minute drive). The isolated axons maintain viability for up to 12 hours after initial excision. For studies of the excised giant axon of *L. pealeii*, a squid buffer solution (475 mM NaCl, 115 mM $MgCl_2$, 10 mM $CaCl_2$, 10 mM KCl, 3 mM $NaHCO_3$, 10 mM HEPES) chilled to 10°C perfuses the axon.

3.2.3 Electrophysiology Methods

Determination of $B^{calc}(t)$ requires recording the intracellular AP voltage $\Phi_{in}(t)$. Intracellular microelectrodes are pulled from commercial glass (World Precision Instruments 1B150-4) to a resistance of 20 – 40 M on a pipette puller (Dagan DMZ Universal Puller), filled with 3M KCl, and fitted into a headstage (Axon Instruments HS-2A) connected to an amplifier (Axon Instruments AxoProbe 1B). The microelectrode is mounted to a micro-manipulator for precise insertion into the axon. *M. infundibulum* specimens are dissected but remain pinned in the dissection dish during this measurement so that the microelectrode remains sealed to the axon despite the worm's contractions. The time trace $\Phi_{in}^{meas}(t)$ is digitized (Tektronix TDS2004B), and subsequently low-pass-filtered at 2 kHz. Axon resting potential values Φ_0 of -60 mV to -85 mV and peak AP amplitudes of 100 mV to 110 mV are observed for *M. infundibulum*, consistent with typical values in the literature [173].

AP stimulation and extracellular voltage detection for *L. pealeii* is accomplished

through the same methods used for *M. infundibulum*, except for an increase in the stimulation repetition rate f_{stim}. The squid giant axon can be fired as often as 100 Hz without reducing detected AP signal quality. For increased longevity of squid axons, stimulation is applied at $f_{stim} = 25$ Hz for 15 s followed by a rest period of 15 s.

For *M. infundibulum*, APs are found to be abolished for values of $f_{stim} \geq 5Hz$, and maximal AP amplitudes are realized for $f_{stim} \leq 1Hz$, both in agreement with previous reports in the literature [172]. For *L. pealeii*, consistent AP stimulation is observed up to $f_{stim} = 300Hz$, although eventual axon degradation is observed over ≈ 15 minutes at such high rates. *L. pealeii* exhibits a refractory period following the AP, wherein the potential experiences an overshoot below the resting voltage. The overshoot is not present in *M. infundibulum*.

APs are evoked by a current pulse of duration Δt_{stim} by a suction electrode engaging either the specimen posterior or anterior and driven by an isolated pulse stimulator (A-M Systems Model 2100) producing biphasic pulses (positive polarity first) with 10 mA amplitude. Posterior stimulation is used unless otherwise noted. The value of Δt_{stim} is typically set to twice the stimulation threshold and ranges from 100 μs to 1 ms depending on the size and health of the organism and the degree of contact between the worm body and the suction electrode. Stimulation pulses are applied at repetition rate f_{stim}=0.4 Hz. Successful AP stimulation and propagation are verified with a pair of bipolar platinum recording microelectrodes (World Precision Instruments PTM23B10 or PTM23B05) connected to a differential amplifier (A-M Systems Model 1800 Headstage), which is further amplified (A-M systems Model 1800) and then digitized (National Instruments USB-6259) at 250 kHz. For the intact worm studies, the same recording electrodes are gently positioned in contact with the worm skin near the axon, allowing verification of AP propagation. Care is taken to not puncture the skin to avoid damaging the specimen.

Diamond Details and Mounting Configuration

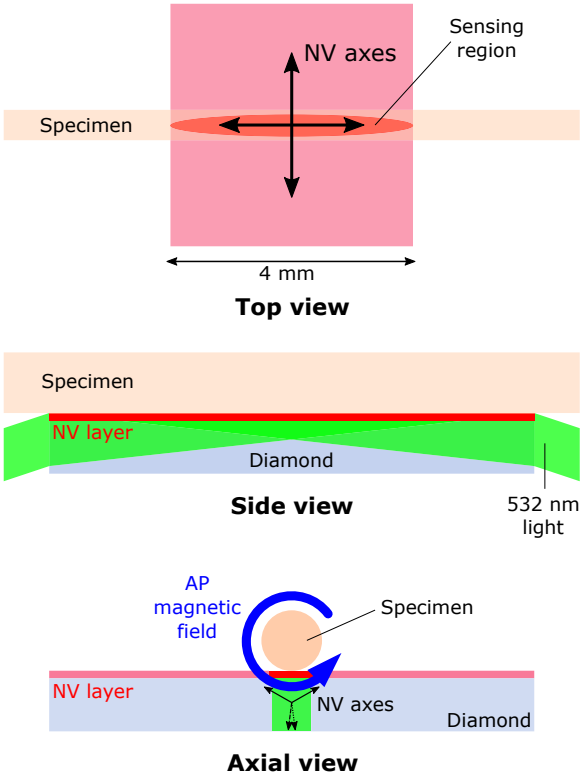

Figure 3.4: Diamond. Top, side, and axial views of NV diamond sensor and specimen. Top view shows sensing region from which fluorescence is collected, as well as top-down projection of the four crystallographic NV axes. AP magnetic field projects onto two NV axes perpendicular to specimen axis. Side view shows 532-nm laser light entering diamond at grazing angle and exciting NV layer. Blue arrow in axial view depicts AP magnetic field; black arrows depict NV axes in sensing region.

The diamond used in this work is an electronic grade (N $<$ 5 ppb) single crystal chip, with rectangular dimensions 4 mm $\times$ 4 mm $\times$ 500 µm, grown using chemical vapor deposition (CVD) by Element Six. The 13 µm thick top-surface NV sensing layer consists of 99.999% ^{12}C with 27 ppm ^{14}N as evaluated by secondary ion mass spectroscopy, which is irradiated with 4.6 MeV electrons with 1.3×10^{14} $cm^{-2}s^{-1}$ flux for 5 hours and subsequently annealed in vacuum at 800°C for 12 hours. The measured nitrogen-to-NV$^-$ conversion efficiency is

6%.

The diamond is cut so that the 500 µm × 4 mm faces are perpendicular to the [110] crystal axis. The sides are mechanically ground to an optical-quality polish. The diamond is mounted to a 50.8 mm diameter, 330 µm thick silicon carbide (SiC) heat spreader via thermal epoxy (Epotek H20E) as shown in Figure 3.5. A 2 mm × 25 mm slot in the SiC provides access to the diamond surface for the dissected axon studies.

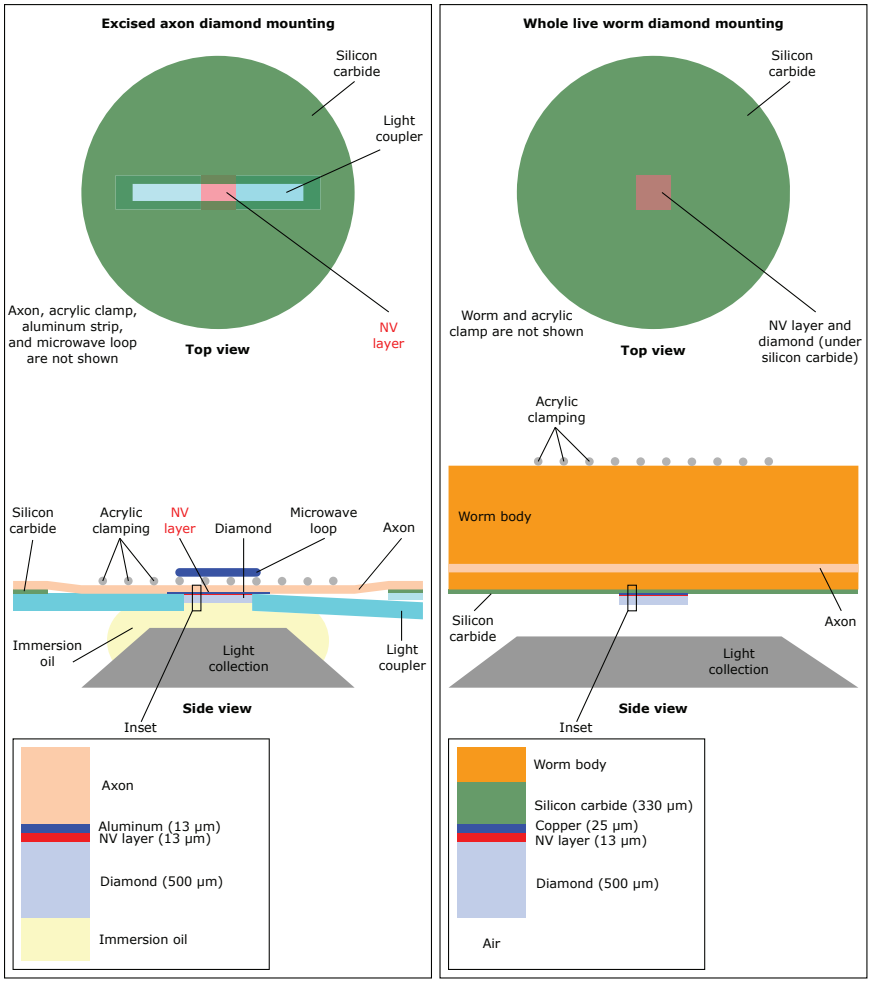

Figure 3.5: Schematic of Diamond Mounting. (Left) Diamond mounting for excised axon experiments. (Right) Diamond mounting for live, intact worm experiments.

For the intact worm studies, several changes are made to the experimental apparatus

(see Figure 3.5). An upgraded aluminum mount (larger than the mount for excised axons) is used to fit the large intact specimens. A SiC wafer with no slot is used as a heat spreader. The NV-diamond sensor is therefore offset from the worm exterior by a spacer of thickness 330 μm. MWs are delivered to a 25 μm thick copper foil layer directly on top of the diamond. The Olympus oil aspheric condensor is exchanged for a 0.79 NA air aspheric condensor (Thorlabs ACL25416U-B). Stained transverse sections in Figure 3.3 show a typical tissue thickness of $\sim$ 900 μm from the center of the axon to the worm exterior, consistent with the literature [171, 177], although this distance is also noted [171] to be highly variable among different specimens and along a single organism's length. The overall typical distance from the axon center to the diamond sensor is $\sim$ 1.2 mm, consistent with the measured roughly four-fold magnetic signal reduction compared to excised worm axons, where the distance from axon center to NV detector layer is typically $\sim$ 300 μm.

Excitation-laser-induced heating of the diamond is measured via NV ODMR frequency shifts to be 2.4°C/Watt. For the data presented in this chapter with dissected axons, the diamond temperature is 21±3 °C. Because the excised axons are placed directly against the diamond and thin aluminum layer, we estimate the temperature of both the worm and squid axons to be $\sim$ 21 °C. The live intact organisms are separated from the diamond by the SiC heat spreader and are thus at $\sim$ 10°C during sensing.

Magnet and Microwave Setup

A rare earth magnet (1" × 1" × 1" N42 K&J Magnetics) with south pole facing the diamond creates a bias magnetic field B_0 with equal projections of 7 gauss (0.7 mT) along the two NV axes perpendicular to the axon axis, shifting the MW resonance between the $m_s = 0$ and $m_s = 1$ sublevels to $\sim$ 2.89 GHz.

Figure 3.6 shows a schematic of the MW setup. A commercial MW source (Agilent

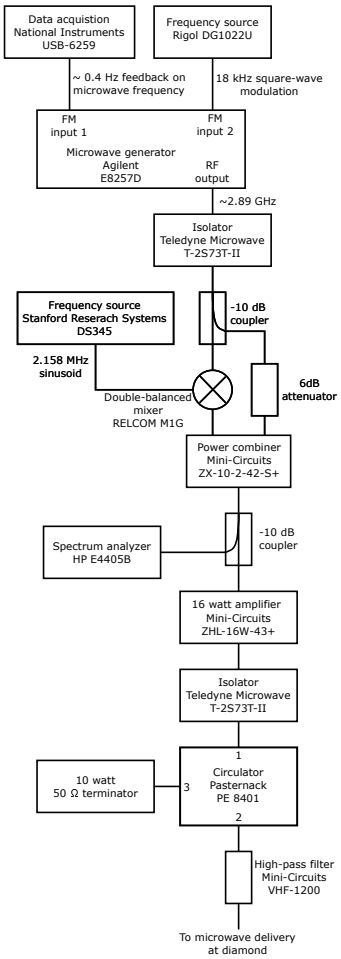

Figure 3.6: Microwave Setup. MW generation, modulation, and delivery setup as described in the text.

E8257D) outputs a single near-resonant frequency, which is square-wave modulated with frequency deviation $\omega_{dev} = 2\pi \times 360$ kHz at frequency $f_{mod} = 18$ kHz (Rigol DG1022U). The modulated MWs pass through an isolator (Teledyne Microwave T-2S73T-II) and a -10 dB coupler before mixing via a double balanced mixer (RELCOM M1G) with a 2.16 MHz sinusoid waveform (Stanford Research Systems DS345). The coupled port of the -10 dB coupler is further attenuated by 6 dB and combined (Mini-Circuits ZX-10-2-42-S+) with the mixer output and then sent through a second -10 dB coupler. The coupled output is sent

to a spectrum analyzer (Agilent E4405B) while the transmitted output is amplified (Mini-Circuits ZHL-16W-43+), passed through another isolator (Teledyne Microwave T-2S73T-II), a circulator (Pasternack, PE 8401), and a high-pass filter (Mini-Circuits VHF-1200), before delivery to a square 5 mm × 5 mm loop located ∼ 2 mm above the diamond sensor. Slow variations in the NV ODMR resonances, e.g., due to diamond temperature drift, are compensated with ∼ 0.4 Hz feedback to the MW frequency f_{MW}. The ODMR features can also be used to continuously monitor the diamond substrate temperature in real time [25].

Laser Excitation and Optical Collection

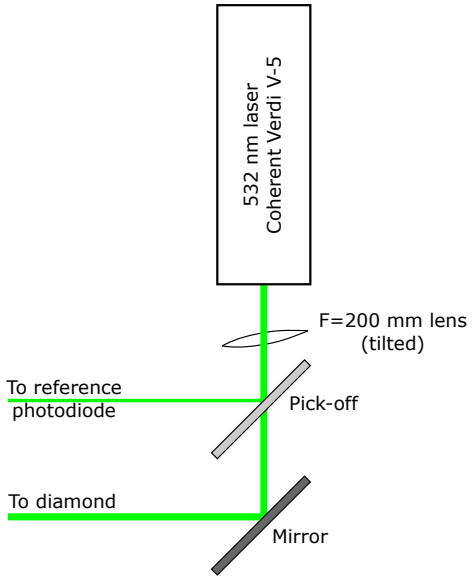

Figure 3.7: Laser Setup. Laser setup as described in the text.

For NV magnetometry, the diamond sensor is illuminated by 2.75 – 4.5 W of 532 nm laser light (Coherent Verdi V-5) as shown in Figure 3.7. Laser light is guided into the diamond via an in-house fabricated UV fused silica coupler, making a ≈ 3° angle to the NV layer. A 13 μm thick and 1 mm wide reflective aluminum layer on the diamond surface blocks both excitation light scattered by surface defects and fluorescence from impinging

upon the specimen.

Typically 17 mW (and up to 28 mW) of fluorescence from the NV-diamond is collected by a 1.4 numerical aperture (NA) aspheric aplanatic oil condenser (Olympus), passed through a 633 nm long-pass filter (Semrock LP02-633RU-25), and imaged onto a biased photodiode (Thorlabs DET100A). A photodiode is used in these experiments instead of a camera due to the better control, temporal response, and ability to collect enough fluorescence to reach the necessary shot noise limited sensitivity. The photodiode (PD) is powered by a 12 V lithium ion rechargable battery and is terminated into the RF + DC port of a bias tee (Universial Microwave Component Corporation BT-1000-LS) with bandwidth 10 kHz to 1 GHz. The bias tee DC port is terminated by 50 Ω during experiments; whereas during optical alignment the port is monitored on an oscilloscope to optimize fluorescence collection.

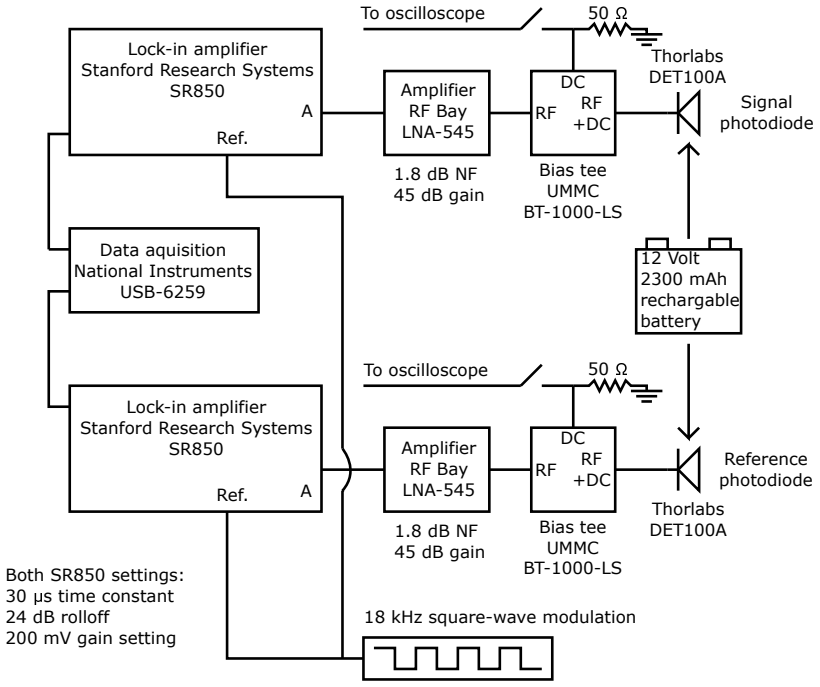

Figure 3.8: Light collection. Signal photodiode, reference photodiode, and downstream electronics and LIAs as described in the text.

The RF output of the bias tee is amplified by a low noise amplifier (RF Bay LNA-545) and then sent into a LIA (Stanford Research Systems SR850). The LIA gain setting is 200 mV and the nominal time constant is 30 μs with a 24 dB/octave roll-off, yielding a measured 3 dB cutoff frequency of f_c=3.6 kHz and a measured equivalent noise bandwidth (ENBW) of f_{ENBW}=4.0 kHz. The LIA voltage output is expanded by 5× using the LIA expand function, digitized (National Instruments USB-6259) at 250 kHz, and then subsequently divided by 5. The temporary LIA signal expansion is employed to mitigate digitization noise. A $\sim$ 1 nT magnetic field corresponds to a fractional change in the NV fluorescence of $\frac{\Delta F}{F} \sim 10^{-6}$.

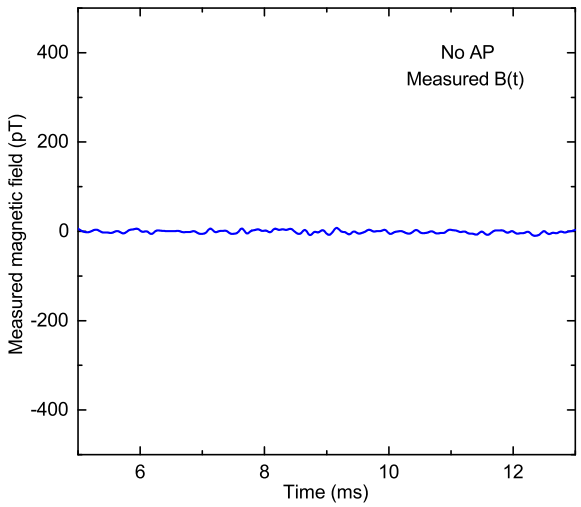

Figure 3.9: Measurement Noise Floor. Magnetometer signal $B(t)$ under experimental running conditions in the absence of a specimen, averaged for $N_{avg} = 75000$ traces. No discernable pattern in the noise is present, suggesting that the magnetometer is free from correlated noise.

To mitigate correlated magnetic noise from the lab environment, the following procedure is adopted. A lock-in amplifier (Stanford Research Systems, SR830) generates a 60 Hz transistor-transistor logic (TTL) signal phase-locked to the 60 Hz, 120 V facility supply power. Each pair of AP stimulations consists of one AP stimulation triggered after a fixed

delay T_{delay} relative to a TTL rising edge (following the nominally desired trigger time) and another AP stimulation triggered after the same fixed delay T_{delay} relative to a TTL falling edge (following the nominally desired trigger time). The value of T_{delay} for each pair of AP stimulations is randomly chosen without replacement from an even distribution from 0 to 1/60 seconds. Using this procedure, the magnetic noise is monitored and found to produce no discernable pattern after averaging for 75,000 stimulations under nominal experimental conditions and no magnetic sources, as shown in Figure 3.9. Allan variance measurements of $B(t)$ taken up to a total measurement time of 100 seconds (with all $B(t)$ filtering off) are consistent with uncorrelated noise.

To suppress laser intensity noise near f_{mod}, the 532 nm laser light is sampled and focused on a separate, reference PD (see Figure 3.7 and Figure 3.8). This PD and all electronics (bias-tee, low-noise amplifier, LIA, input into data acquisition system) exactly duplicate the setup of the signal PD and accompanying electronics. The phase of the reference LIA is aligned with the phase of the signal LIA. We find that subtraction (rather than division) of the correlated noise is sufficient to reach the photon shot noise sensitivity limit in the absence of the MWs, in agreement with Reference [178]. The detected signal is digitally filtered with an 80 Hz FFT high-pass filte, and with 1-Hz-wide notch stop filters at all 60 Hz harmonics through 660 Hz and at 30 other frequencies above 2 kHz.

3.2.4 Magnetometry Method

Lock-In CW ODMR Magnetometry

Here we go into more detail with regard to the Lock-In CW ODMR Magnetometry scheme first described in Chapter 1. Further details can be found in Appendix A. A modified CW-ODMR technique is employed for NV-diamond ODMR, wherein optical NV spin polarization, MW drive, and spin-state readout via fluorescence occur simultaneously. Continuous

green laser excitation at 532 nm polarizes the NV center into the $m_s = 0$ ground state. Applied MWs, when tuned to resonance with the transition between the optically bright $m_s = 0$ spin state and one of the less bright $m_s = +1$ or -1 states, cause NV spin precession into a mixed state and a detectable reduction in fluorescence. A change in the local magnetic field shifts the ODMR feature which, for near-resonant MW drive, is detected as a change in the fluorescence rate.

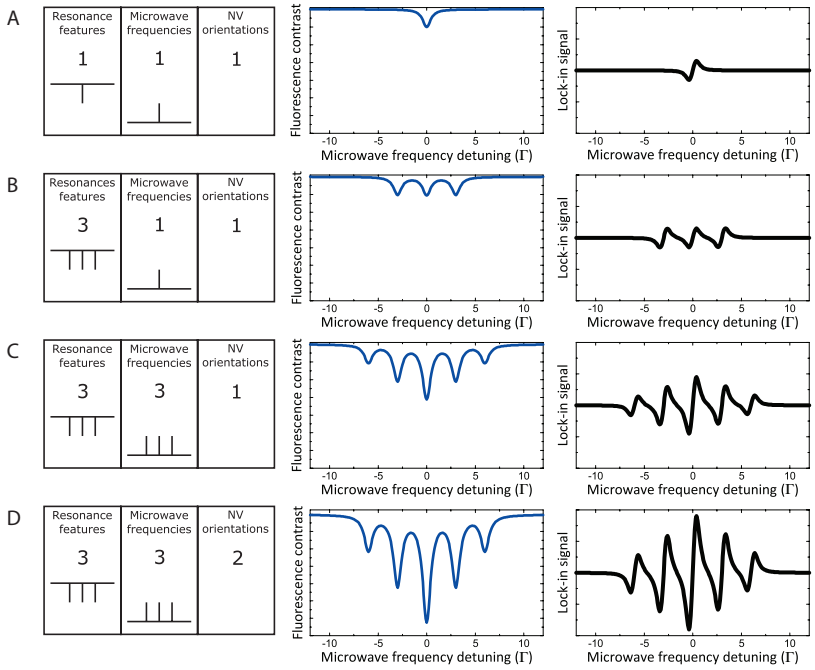

Figure 3.10: (A) Diagram, fluorescence signal, and LIA signal for a single ODMR feature addressed by a single (modulated) MW frequency, sensed along a single NV axis. (B) Diagram, fluorescence signal, and LIA signal for three ODMR features addressed by a single (modulated) MW frequency, sensed along a single NV axis. (C) Diagram, fluorescence signal, and LIA signal for three ODMR features addressed by three (modulated) MW frequencies with equivalent spacing, sensed along a single NV axis. The central feature corresponds to all three applied frequencies resonantly addressing ODMR features. (D) Diagram, fluorescence signal, and LIA signal for same scenario as in (C) but with B_0 oriented to have equal projection along two NV axes, overlapping their ODMR features.

A single ODMR feature of Lorentzian lineshape with angular frequency ω_0 (where

$\omega \equiv 2\pi f$), linewidth Γ, and contrast C is detected in fluorescence as:

$$F(\omega) = F_0 \left(1 - \frac{C(\Gamma/2)^2}{(\Gamma/2)^2 + (\omega - \omega_0)^2}\right) \tag{3.3}$$

(see Figure 3.10(A)), where F_0 is the fluorescence detected in the absence of MWs, and optical and MW broadening are ignored for simplicity. As the majority of noise in the system has 1/f character, greater SNR is achieved by shifting the measurement bandwidth to higher frequency via a lock-in technique, which generates a dispersion-like signal with a characteristic zero-crossing feature: i.e., a rapid change of the lock-in amplifier (LIA) voltage with frequency. The applied MWs are square-wave frequency modulated at f_{mod} (typically 18 kHz) about the center frequency ω_c with frequency deviation ω_{dev}: i.e., $\omega_{MW}(t) = \omega_c + \omega_{dev}\text{square}(2\pi f_{mod} t)$. The collected fluorescence is then $F(\omega_{MW})$. After demodulation by the LIA with a reference signal $V_{ref}\sin(2\pi f_{mod} t)$, the DC output is a dispersion-type signal with a zero-crossing at ω_0:

$$\begin{aligned} V_{LIA}(\omega_c, \omega_{dev}) \sim \frac{F(\omega_c + \omega_{dev}) - F(\omega_c - \omega_{dev})}{2} = \\ \frac{V_0 C}{2}\left(-\frac{(\Gamma/2)^2}{(\Gamma/2)^2 + (\omega_c + \omega_{dev} - \omega_0)^2} + \frac{(\Gamma/2)^2}{(\Gamma/2)^2 + (\omega_c - \omega_{dev} - \omega_0)^2}\right) \end{aligned} \tag{3.4}$$

where V_0 is a prefactor voltage determined by the output settings of the LIA. Setting $\omega_{dev} = \Gamma/(2\sqrt{3})$ theoretically maximizes the slope, $\frac{dV_{LIA}}{d\omega_c}$, of the zero-crossing for a Lorentzian lineshape [56]. Time-varying magnetic fields $B(t)$ are sensed for small values ($\frac{g_e \mu_B}{\hbar} B(t) \ll \Gamma$) of the external magnetic field deviation by setting $\omega_c = \omega_0$ and detecting resonance frequency shifts $\omega_0(t) = \omega_0 + \delta\omega(t)$, where $\delta\omega(t) = -\frac{g_e \mu_B}{\hbar} B(t)$, as:

$$V_{LIA}(t) = V_{LIA}\left(\omega_0 - \frac{g_e\mu_B}{\hbar}B(t)\right) = \frac{V_0 C}{2}\left(-\frac{(\Gamma/2)^2}{(\Gamma/2)^2 + (\frac{\Gamma}{2\sqrt{3}} - \frac{g_e\mu_B}{\hbar}B(t))^2} + \frac{(\Gamma/2)^2}{(\Gamma/2)^2 + (\frac{\Gamma}{2\sqrt{3}} + \frac{g_e\mu_B}{\hbar}B(t))^2}\right) \approx -\frac{3\sqrt{3}}{4}\frac{V_0 C}{\Gamma}\frac{g_e\mu_B}{\hbar}B(t) \tag{3.5}$$

The problem is further complicated by the fact that the 14N isotope of the NV spin resonance has three features separated by the hyperfine (HF) splitting of $\Delta\omega_{HF} = 2\pi \times 2.16$ MHz, as shown in Figure 3.10(B). For a single MW frequency sweeping across the features, and again ignoring MW power broadening, we find:

$$F(\omega) = F_0\left(1 - \sum_{k=-1}^{1} C\frac{(\Gamma/2)^2}{(\Gamma/2)^2 + (\omega - \omega_0 - k\Delta\omega_{HF})^2}\right) \tag{3.6}$$

Addressing all three NV HF features simultaneously with three MW frequencies also separated by $\Delta\omega_{HF}$ yields:

$$F(\omega, \Delta\omega_{HF}) = F_0\left(1 - \sum_{l=-1}^{1}\sum_{k=-1}^{1} C\frac{(\Gamma/2)^2}{(\Gamma/2)^2 + (\omega + l\Delta\omega_{HF} - \omega_0 - k\Delta\omega_{HF})^2}\right) \tag{3.7}$$

As displayed in Figure 3.10(C), the observed NV fluorescence signal shows five ODMR peaks. The outer two peaks correspond to one of the three MW frequencies on resonance; the second and fourth peaks correspond to two of the three frequencies tuned to resonance; and the innermost peak corresponds to all three MW frequencies resonantly addressing the HF features. The dispersion signal is then:

$$V_{LIA}(\omega, \Delta\omega_{HF}, \omega_{dev}) = \sum_{l=-1}^{1}\sum_{k=-1}^{1} -CV_0\frac{(\Gamma/2)^2}{(\Gamma/2)^2 + (\omega + l\Delta\omega_{HF} - \omega_{dev} - \omega_0 - k\Delta\omega_{HF})^2} + CV_0\frac{(\Gamma/2)^2}{(\Gamma/2)^2 + (\omega + l\Delta\omega_{HF} + \omega_{dev} - \omega_0 - k\Delta\omega_{HF})^2} \tag{3.8}$$

In this simple treatment in which MW power broadening is ignored, our measurement technique increases the contrast of the central NV HF feature by a factor of 3.

The overall measurement contrast is further improved by orienting the bias field B_0 to have equal projection along two NV axes. Projecting along two NV axes doubles the contrast as shown by comparing Figure 3.10(C) and Figure 3.10(D), although the angle between the NV axes and B(t) causes the sensitivity improvement to be $2\sin[\theta_{tet}/2] = 2\sqrt{2/3}$ where $\theta_{tet} = 109.4712°$ is the tetrahedral bond angle in the diamond lattice.

Temporal Resolution

Temporal resolution of the NV-diamond magnetometer is tested by applying a test magnetic field $B_{test}(t) = B_{test,0}$ square$(2\pi f_{test}t)$ with $B_{test,0} = 57\ nT$ and $f_{test} = 1\ kHz$, and measuring the 10% – 90% rise time of $B^{meas}(t)$, denoted by $\tau_{10/90}$. Using $f_{mod} = 60\ kHz$, $\tau_{LIA} = 10\ \mu s$, and 6 dB/octave roll-off (yielding a measured $f_{ENBW} = 33\ kHz$), $\tau_{10/90} = 32\ \mu s$ is observed as shown in Figure 3.11(A), which displays both real-time and averaged $B^{meas}(t)$ traces that are FFT low-pass filtered at 45 kHz. All AP data presented in this chapter are acquired using $f_{mod} = 18\ kHz$, $\tau_{LIA} = 30\ \mu s$, and 24 dB/octave roll-off, which gives $\tau_{10/90} \sim 100\ \mu s$ to increase measurement contrast (see Figure 3.11(B)). Higher values of f_{mod} reduce NV spin-state contrast, an effect previously observed in References [52, 179, 180] and shown here in Figure 3.11(B).

When operating with a temporal resolution better than 40 μs, the magnetic field sensitivity of the present instrument is reduced by a factor of ~ 1.6 with respect to standard running conditions. With pulsed Ramsey-type schemes [56, 181], to be employed in a next-generation NV-diamond magnetic imaging system (i.e. QDM), the time resolution is expected to be significantly enhanced without loss of NV contrast. The temporal resolution of a Ramsey scheme is in practice limited by the repetition rate of the pulse sequence. For

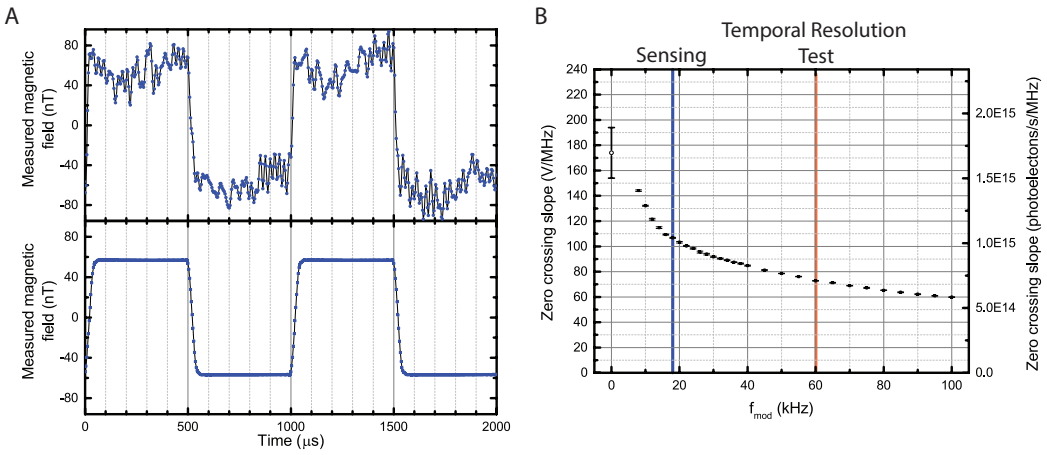

Figure 3.11: (A) Loss of contrast with high frequency modulation. Data showing the impact of the finite response on the NV ODMR contrast. (B) Characterization of temporal response

optimistic ensemble initialization and readout times of 1 μs and 300 ns respectively, and for a $\sim$ 500 ns T_2^*-limited spin precession time, we anticipate a maximum temporal resolution of $\sim$ 2 μs, if not limited by the detection electronics. Temporal resolution can be further increased at the expense of sensitivity by reducing the initialization and spin precession times, down to the theoretical limit given by the $\sim$ 200 ns NV singlet state lifetime [182].

3.3 Experimental Results

3.3.1 Magnetic Field Detection and Comparison with the Simple Model

We first performed magnetic sensing of single-neuron propagating APs from excised invertebrate giant axons, together with simultaneous electrophysiology measurements on the axons as a comparison and check on the magnetic data. We studied the two species, with consistent results: the marine fanworm *Myxicola infundibulum*; and the North Atlantic longfin inshore squid *Loligo pealeii*, a model organism for neuroscience. Figure 3.12 shows a representative measured intracellular axonal AP voltage time trace $\Phi_{in}^{meas}(t)$ from *M. infundibulum*.

From the simple model presented earlier of the electromagnetic dynamics of axonal propagating APs [143, 170, 183], the magnetic field $B(t)$ is proportional to the temporal derivative of the intracellular voltage $\Phi_{in}(t) : B(t) = s\frac{\partial \Phi_{in}}{\partial t}$, where s is the scaling constant dependent on geometrical parameters (axon radius r_a, radial distance of the field point to the axon center ρ) and electrophysiological axon parameters (AP conduction velocity v_c, axoplasm electrical conductivity σ).

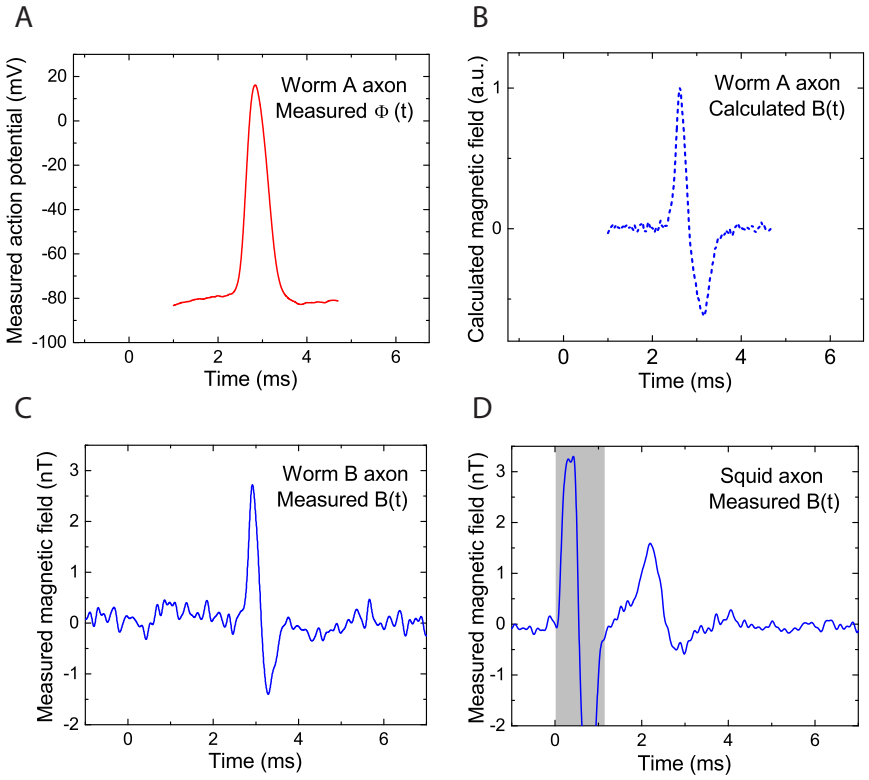

Figure 3.12: Validation of Magnetic Model. (A) Measured AP voltage and magnetic field from excised single neurons. Measured time trace of AP voltage $\Phi_{in}^{meas}(t)$ for giant axon from *M. infundibulum*. (B) Calculated time trace of AP magnetic field $B^{calc}(t)$ for *M. infundibulum* extracted from data in the first panel. (C) Measured time trace of AP magnetic field $B^{meas}(t)$ for *M. infundibulum* giant axon with $N_{avg} = 600$. (D) Measured time trace of AP magnetic field $B^{meas}(t)$ for *L. pealeii* (squid) giant axon with $N_{avg} = 375$. Gray box indicates magnetic artifact from stimulation current.

As shown in Figure 3.12(A,B,C), we find good agreement between (i) $B^{calc}(t)$, the AP

magnetic field calculated from $\Phi_{in}^{meas}(t)$ for a typical value of s for *M. infundibulum*, and (ii) a representative measured AP magnetic field time trace $B^{meas(t)}$. This correspondence demonstrates the consistency of NV-diamond magnetic AP measurements with standard electrophysiology techniques and theory. Note that the example $B^{meas}(t)$ in Figure 3.12(C) has a peak-to-peak amplitude of 4.1 ± 0.2 nT (mean $\pm$ standard deviation (s.d.)) for four measurements on the same specimen each with $N_{avg} = 150$, corresponding to an SNR of 1.2 ± 0.1 for a single AP firing, i.e., $N_{avg} = 1$. Here SNR is defined as the ratio of the mean signal peak-to-peak amplitude to the root mean square (RMS) noise after matched filtering is applied. Furthermore, we demonstrated that our method has multi-species capability via magnetic sensing of axonal APs from the squid *L. pealeii* (Figure 3.12(D)). No change to the apparatus or magnetic sensing protocol is required upon switching organisms, and good reproducibility is found for both the excised worm and squid axon AP magnetic field measurements, on the same and different specimens.

Accurate calculation of s from first principles is nontrivial [143], since r_a, ρ, σ, and v_c have substantial uncertainties. $r_a = 200 \pm 75$ μm is determined from stained transverse sections of *M. infundibulum* (see Figure 3.14), with large variations observed in axon size (up to 50%) among otherwise similarly sized specimens, as also noted in References [172,173]. For the excised axon studies, only the ventral nerve cord containing the giant axon is isolated, and there is also residual connective tissue around the axon: hence an estimate of $\rho = (r_a + 100\ \mu m) \pm 100\ \mu m$ is used (the large standard deviation is due to sample to sample variability). We take $\sigma = 1.47 \pm 0.5\ \Omega^{-1} m^{-1}$ for *M. infundibulum* [184], given the significant variation (50%) in axoplasm conductivity previously report in other giant axon [143]; and $v_c = 9 \pm 4 m/s$ (mean $\pm$ s.d. of 105 AP measurements taken on 7 worms, with 15 AP stimulations per worm) based on two-point electrophysiology measurements of v_c for similar representative-sized worms under posterior stimulation. With these values for r_a, ρ, σ, and

v_c, we extract $s^{calc} = 13 \pm 10\ pT/(V/s)$, which is in agreement with the experimentally derived value of $s^{meas} = 7.6 \pm 1\ pT/(V/s)$ given the larger uncertainty in the axon radius.

3.3.2 *In-Vivo* Experimental Results

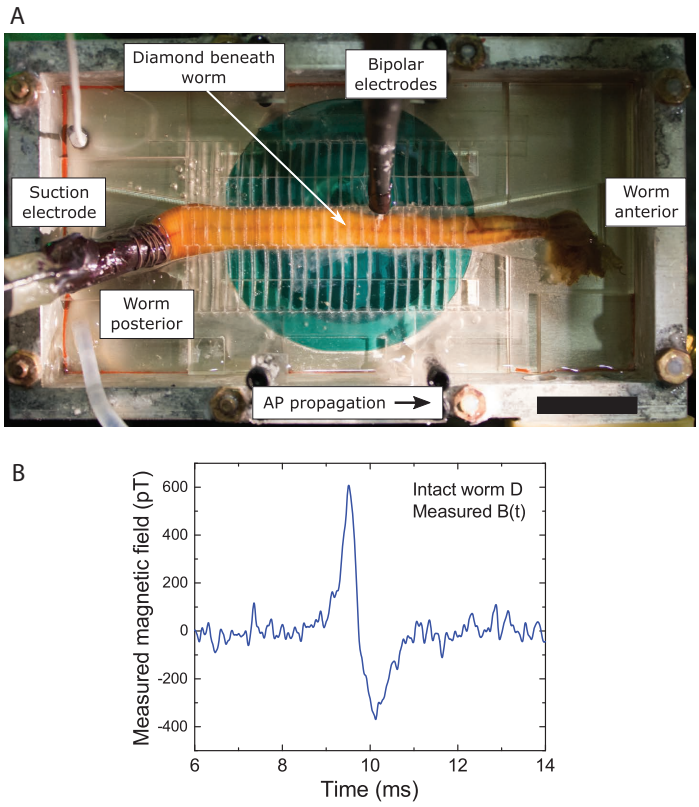

Figure 3.13: Intact Data. Single-neuron AP magnetic sensing exterior to live, intact organism. (A) Overhead view of intact living specimen of *M. infundibulum* on top of NV diamond sensor. In configuration shown, animal is stimulated from posterior end by suction electrode, APs propagate toward worm's anterior end, and bipolar electrodes confirm AP stimulation and propagation. (Scale bar, 20 mm.) (B) Recorded time trace of single-neuron AP magnetic field $B^{meas}(t)$ from live intact specimen of *M. infundibulum* for $N_{avg} = 1650$ events.

We next demonstrated single-neuron AP magnetic sensing exterior to a live, intact, opaque organism an undissected specimen of *M. infundibulum* (Figure 3.13(A)) for extended periods, with minimal adverse effect on the animal. Figure 3.13(B) shows an example

measured axonal AP magnetic field time trace $B^{meas}(t)$ for a live intact specimen, which is to the best of our knowledge the first demonstration of 'single-neuron MEG' from the exterior of an intact animal.

The measured AP waveform in Figure 3.13 is similar to that of an excised axon (Figure 3.12(B)), with roughly four times smaller peak-to-peak amplitude ($\sim$1 nT), which is consistent with the separation of $\sim$1.2 mm from the center of the axon inside the animal to the NV sensing layer (see transverse sections and diagrams in Figure 3.14). In addition, we recorded $B^{meas}(t)$ from a live intact worm after >24 hours of continuous exposure to the experimental conditions, including applied MWs and optical illumination of the diamond sensor. We observed little to no change in the magnetic AP signal or in the animal behavior.

3.3.3 Initiation and Propagation Asymmetry Due to a Conical Axon

We also used live intact worms to demonstrate the capability of NV-diamond magnetic sensing to determine the AP propagation direction and sense magnetic signal amplitude differences correlated with differences in conduction velocity v_c, all from a single-channel measurement. NV-diamond allows for vector magnetometry [9] by sensing the magnetic field projection along one or more of the four NV center orientations within the diamond crystal lattice. An axonal AP produces a bipolar azimuthal magnetic field waveform, with the time-varying field orientation set by the direction of AP propagation. Thus, the measured AP magnetic field time trace $B^{meas}(t)$ from an intact worm has an inverted waveform for anterior versus posterior AP stimulation. This demonstrates the clear distinguishability between oppositely-propagating APs, as shown in Figure 3.14, for three intact specimens (denoted worms F, G, and H) with both posterior and anterior stimulation, each with $N_{avg} = 1650$ trials.

In addition to inversion of the $B^{meas}(t)$ waveform upon reversal of the AP propaga-

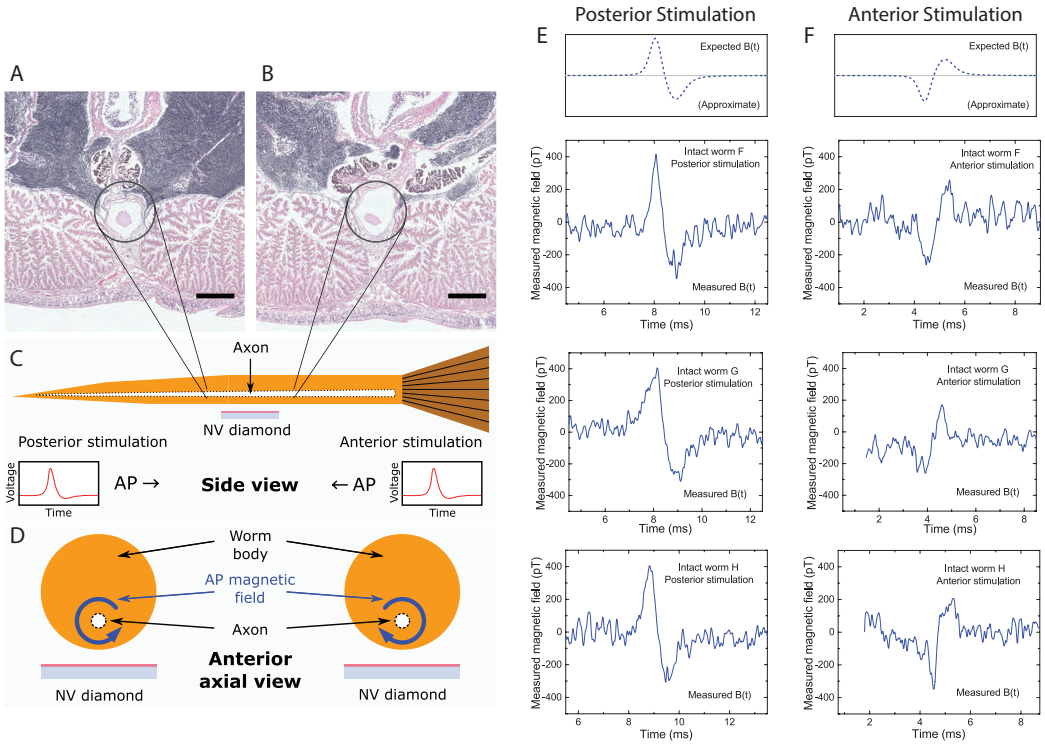

Figure 3.14: Single-channel magnetic sensing of AP propagation exterior to live, intact organism. Transverse sections of *M. infundibulum* near midpoint of worm illustrate giant axon radius tapering from (A) smaller near posterior to (B) larger near anterior. Sections were taken 1 cm apart. Encircled white structure is giant axon. (Scale bars, 400 µm.) (C) Cartoon cross-section side view of live, intact worm and NV diamond sensor. Black dashed lines indicate tapered giant axon. Cartoon time traces of AP voltage indicate they are typically qualitatively indistinguishable for posterior stimulation (right-propagating AP) and anterior stimulation (left-propagating AP). (D) Cartoon cross-section axial view looking from anterior end. Blue arrows encircling axon indicate opposite azimuthal AP magnetic field vectors for oppositely propagating APs. (E) Recorded time trace of AP magnetic field $B^{meas}(t)$ from three live intact specimens of *M. infundibulum* for posterior stimulation and $N_{avg} = 1,650$ events each. (F) Recorded time trace of AP magnetic field $B^{meas}(t)$ from same three intact live specimens of *M. infundibulum* as in E for anterior stimulation and $N_{avg} = 1,650$ events each. Note that the observed sign of $B^{meas}(t)$ is reversed depending on AP propagation direction, and the decreased magnetic field amplitude for anterior stimulation, consistent with two-point electrophysiology measurements of lower AP conduction velocity for posterior stimulation.

tion direction, an asymmetry is observed in the peak-to-peak amplitude of the magnetic signal in agreement with other studies on inhomogenous giant axon regions. [185] As shown in Figure 3.14, larger peak-to-peak values of $B^{meas}(t)$ are found for posterior stimulation (denoted B_p) than for anterior stimulation (B_a) for each of the three worms tested: for worm F, $B_p/B_a = 1.66 \pm 0.12$ for worm F, 1.28 ± 0.09 for worm G, and 1.27 ± 0.10 for worm H (mean $\pm$ s.d. for 1650 trials yielding one for each sample). The average asymmetry is $B_p/B_a = 1.41 \pm 0.22$ (mean $\pm$ s.d. for three samples). The asymmetry is independent of which point of stimulation (posterior or anterior) is tested first, and the effect is robust under multiple switches of stimulation (e.g., posterior, anterior, then posterior again).

3.3.4 Electrophysiology Validation of Asymmetry Experiments

	$v_{c,p}/v_{c,a}$	$(\partial\Phi_p/\partial t)/(\partial\Phi_a/\partial t)$	B_p/B_a
Magnetic Field Measurements	n/a	n/a	1.66 ±0.12 (Worm F) 1.28 ±0.09 (Worm G) 1.27 ±0.10 (Worm H) 1.41 ±0.22 (Mean 3 Worms)
Electrophysiology	0.72 ±0.11 (Mean 15 Worms)	0.97 ±0.11 (Mean 3 worms)	1.35 ±0.25 (Calculated)
NEURON Simulation	0.63	0.87	1.38 (Calculated)

Table 3.1: Summary of different methods used to test the origin of the asymmetric magnetic field amplitude for different propagation initiation sites.

To understand the origin of the observed asymmetry of $B^{meas}(t)$ with AP propagation direction, we (i) performed electrophysiology measurements of $\Phi_{in}(t)$ and v_c with both posterior and anterior stimulation; (ii) related the magnetic and electrophysiology data via the simple magnetic model, which predicts:

$$B_p/B_a = \frac{v_{c,a}}{v_{c,p}} \frac{\partial\Phi_p/\partial t}{\partial\Phi_a/\partial t} \tag{3.9}$$

for measurements taken at a fixed location along the axon z_0; and (iii) performed numerical simulations of APs using a model of the *M. infundibulum* giant axon.

For AP stimulation in tapered giant axon studies employing both intracellular and extracellular voltage detection, bipolar platinum microelectrodes (World Precision Instruments PTM23B10) deliver current pulses from an isolated pulse stimulator (A-M Systems Model 2100), to precisely control the location of initiation of APs. For posterior (anterior) stimulation, the bipolar electrode pair is placed within 2 mm of the end of the worm's tail (head). A schematic of the setup is shown in Figure 3.15.

For conduction velocity measurements, two pairs of platinum iridium bipolar recording electrodes (World Precision Instruments PTM123B20KT) are placed 2 mm apart about the mid-point of the worm. One electrode of each pair is placed on the surface of the worm above the axon while the other is displaced laterally 5 mm from the worm to perform a differential measurement. The electrode pairs are attached to a headstage (A-M Systems Model 1800 headstage). The signals are amplified by 100× by a differential amplifier (A-M Systems Model 1800) and digitized (National Instruments USB-6259) at 100 kHz. The signals are then high-pass filtered at 0.1 Hz, low-pass filtered at 20 kHz, and smoothed in software using a rectangular 7-point moving average. Measurements are taken after ensuring the electrodes are positioned well enough that the coupling to the axon allows a clearly defined peak upon AP stimulation for both channels. The measured conduction velocity is taken as the spatial distance between the pairs of electrodes along the axon (2 mm) divided by the recorded time delay between peaks in the two differential voltage measurements (see Figure 3.15.) We find $v_{c,p}/v_{c,a} = 0.72 \pm 0.11$ (mean $\pm$ s.d. of 1500 pairs of measurements of v_c taken on 15 worms, each with 100 AP trials stimulated from the posterior and 100 from the anterior, see Figure 3.15D.)

Intracellular AP measurements utilize microelectrodes described previously. The in-

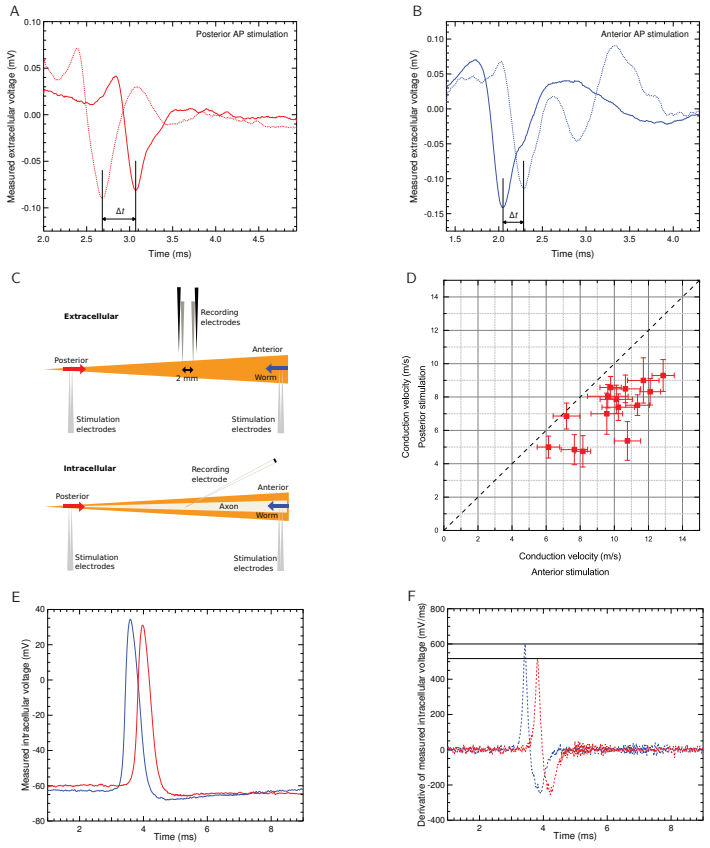

Figure 3.15: Representative pair of extracellular recordings of $\Phi_{ex}^{meas}(t)$ stimulated from (A) the posterior end (red) and (B) the anterior end (blue) of intact specimen of *M. infundibulum*. The time difference Δt between extrema (minima) of recorded voltage traces at two points near the mid-point of the worm spaced by 2 mm is extracted; and on average a larger Δt is found for posterior stimulation than for anterior stimulation, as shown in (D). For both (A) and (B) the dotted (solid) trace shows the signal from the recording electrodes positioned closer to the posterior (anterior) end of the worm. For both stimulations positions, v_c is extracted as (2 mm)/Δt (C) Cartoon of experimental setup of extracellular and intracellular recordings for measuring v_c and $\Phi_{in}^{meas}(t)$ respectively. (D) Average value of v_c measured for posterior stimulation ($v_{c,p}$) plotted versus v_c for anterior stimulation ($v_{c,a}$) for n=15 worms with 100 AP recordings per stimulation position per worm. Error bars denote s.d. (E) Representative intracellular recordings of $\Phi_{in}^{meas}(t)$ from excised giant axon of *M. infundibulum* for posterior (red) and anterior (blue) stimulation. (F) Calculated time derivative of $\Phi_{in}^{meas}(t)$ for data shown in (E).

tracellular AP voltage $\Phi_{in}(z_0, t)$ is recorded at a point denoted z_0 at the mid-point of the model axon. Detected signals are digitized (National Instruments USB-6259) at 100 kHz, smoothed using a rectangular 7-point moving average (see Figure 3.15E), and the temporal derivative is calculated (see Figure 3.15F). We find $(\partial\Phi_p/\partial t)/(\partial\Phi_a/\partial t) = 0.97 \pm 0.11$ (mean $\pm$ s.d. of 21 pairs of measurements of $\partial\Phi/\partial t$ taken in 3 worms, each with 7 measured AP trials with posterior stimulation and 7 with anterior stimulation). Combining the results of the intracellular and extracellular measurements, the expected ratio of B_p/B_a is then $v_{c,a}/v_{c,p} \times (\partial\Phi_p/\partial t)/(\partial\Phi_a/\partial t) = 1.35 \pm 0.25$, (mean $\pm$ s.d.), which is consistent with the ratio of $B_p/B_a = 1.41 \pm 0.22$ measured with NV-diamond magnetometry.

Previous calculations based on cable theory [186] suggest that this asymmetry in v_c (and hence $B^{meas}(t)$) is expected for axons exhibiting a tapered radius over their length, as is the case for the giant axon in *M. infundibulum* [171]. Tapered axon AP simulations are performed using the NEURON software [187], a numerical modeling package based on cable theory. The *M. infundibulum* giant axon is modeled as a cylindrically symmetric cable of length $5\lambda_{AP}$, (where $\lambda_{AP} = v_c t_R$ and t_R is the AP impulse rise time) and with a linearly tapered diameter from 400 μm at the anterior to 50 μm at the posterior. The chosen geometric parameters are consistent with axons used in the present magnetic studies [171]. The intracellular conductivity is set to 1.47 $\Omega^{-1}m^{-1}$, a value typical for *M. infundibulum* [184]. Simulated AP signals are recorded at the mid-point of the model axon so that the sealed-axon boundary conditions can reasonably be neglected. An asymmetry in $\partial\Phi/\partial t$ and v_c is observed depending upon whether the AP is initiated at the posterior (smaller) or anterior (larger) end of the model axon, with $v_{c,p}/v_{c,a} = 0.63$ and $(\partial\Phi_p/\partial t)/(\partial\Phi_a/\partial t) = 0.87$. The expected ratio of B_p/B_a from the simulations is then $v_{c,a}/v_{c,p} \times (\partial\Phi_p/\partial t)/(\partial\Phi_a/\partial t) = 1.4$, which is consistent with the asymmetry observed in NV-diamond magnetic measurements and electrophysiology measurements of APs in *M. infundibulum*. These results demonstrate

the capability of our technique to measure small differences in magnetic signal waveforms correlated with differences in conduction velocity, which in the present study have contributions from differences in axon morphology.

Transverse sections shown in Figure 3.14(A) are prepared from a typical *M. infundibulum* specimen, which has been anesthetized and fixed in a solution of 4% paraformaldehyde (PFA) overnight. The fixed worm is mounted to a paraffin block and sectioned, yielding slices of width 4 μm. The slices are treated with a hematoxylin and eosin stain (H&E stain) to illustrate the tissue structure. By comparison with the literature [171], the observed structure in the sections is verified and the location of the giant axon is confirmed. The sections show a distance from the giant axon center to the skin surface of 900 ± 200 μm, and a taper in the axon with decreasing diameter from anterior to posterior.

3.3.5 Systematic Checks

Technical Systematics

Systematic Check	**Result**	**Systematic Ruled Out**
No axon stimulation	$B^{\text{meas}}(t) \to 0$	Non-axonal signals, stimulation artifacts
Move extracellular electrodes	$B^{\text{meas}}(t) \to B^{\text{meas}}(t)$	Cross talk between magnetometer and extracellular electrodes
Monitor resonance at opposite slope	$B^{\text{meas}}(t) \to -B^{\text{meas}}(t)$	Non-magnetic artifacts
Add 180° to lock-in phase	$B^{\text{meas}}(t) \to -B^{\text{meas}}(t)$	Cross talk between magnetometer and extracellular electrodes
Change sign of bias field	$B^{\text{meas}}(t) \to -B^{\text{meas}}(t)$	Magnetic artifact from movement of axon

Table 3.2: Systematic Checks

As summarized in Table 3.2, we present the results of multiple tests performed to verify that the observed $B^{meas}(t)$ arises solely from an axon AP (i.e., intracellular axial current): (i) observation of a non-zero $B^{meas}(t)$ signal requires successful AP stimulation and propagation as determined by electrophysiology measurements of the extracellular action potential $\Phi_{ex}(z,\rho,t)$, and the observed $B^{meas}(t)$ is synchronized with $\Phi_{ex}(z,\rho,t)$ to within experimental error; (ii) crosstalk ('pickup artifacts') during data acquistion between the recorded $\Phi_{ex}(z,\rho,t)$ and $V_{LIA}(t)$ is ruled out through varying the recording electrode placement and observing no change in $B^{meas}(t)$; (iii) the origin of the NV-observed $B^{meas}(t)$ signal is demonstrated to be magnetic by switching to an LIA voltage zero-crossing with slope dV_{LIA}/df of opposite sign and observing inversion of $B^{meas}(t)$; (iv) similarly, inverting the phase of the LIA reference signal ϕ_{LIA} by 180° produces the same result, also confirming the magnetic origin of the signal sensed by the NV ensemble; and (v) time-varying magnetic fields from motional artifacts, e.g., specimen-induced instrument motion in the presence of a gradient in the bias field B_0, are ruled out by reversing the orientation of the permanent magnet and observing inversion of $B^{meas}(t)$.

Biological Systematics

An investigation of whether muscle presence affects the observed $B^{meas}(t)$ in intact worm studies is described herein. As shown in Figure 3.16(A), specimens sometimes display an extended duration (5 to 10 ms typical), temporally delayed (2 to 20 ms typical) extracellular voltage signal, which is eliminated upon perfusion of 10% ethanol, suggesting a muscular signal origin. The delayed signal is easily resolved from the neuron extracellular AP signal, which exhibits shorter delay after stimulation and 1 ms duration. Figure 3.16(B) shows extracellular voltage measurements from an intact worm after 15, 30, 45 and 60 repeated stimulations at 0.5 Hz. The delayed extracellular signal is observed to decrease with the

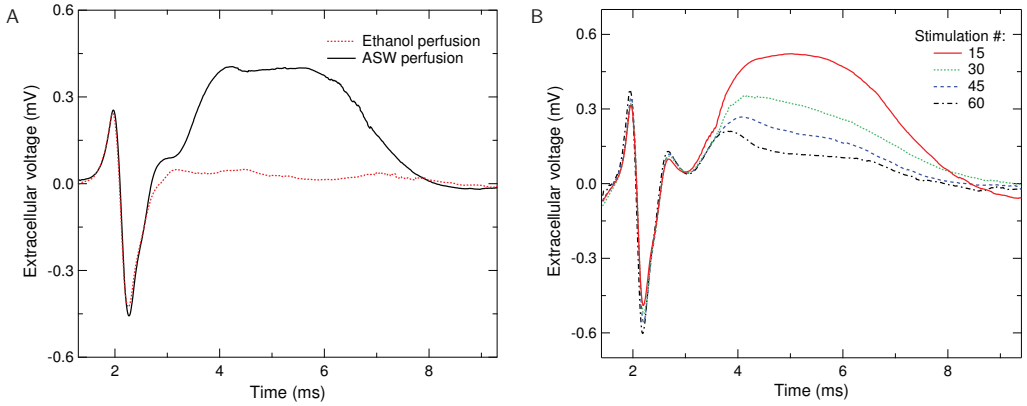

Figure 3.16: Impact of muscle signal. (A) Measured time traces of extracellular voltage Φ_{ex}^{meas} following AP stimulation of intact *M. infundibulum* at the organism posterior with 0.5 Hz repetition rate. Red (dotted) trace shows a single trial Φ_{ex}^{meas} from a worm perfused in a solution containing 10% ethanol and 90% ASW, which temporarily anesthetizes the muscles without affecting the giant axon AP. Black (solid) trace shows a single trial Φ_{ex}^{meas} from the same worm stimulated roughly 20 minutes after perfusion is returned to 100% ASW. The delayed signal from 3 ms to 7 ms is not present in the anesthetized worm but returns after the worm's muscles become responsive again, strongly suggesting that the delayed signal is associated with muscle activity. (B) Measured time traces of single trial extracellular voltage Φ_{ex}^{meas} following AP stimulation of intact *M. infundibulum* with conditions the same as in (A), with ASW perfusion. Data shown are for the 15th (red, solid), 30th (green, dotted), 45th (blue, dashed), and 60th (black, dot-dashed) AP stimulation. The signal from 3 ms to 7 ms is diminished by repeated stimulation, consistent with observed fatigue of the worm's muscles.

number of consecutive stimulations, an effect attributed to muscle fatigue and consistent with independent observations in the literature [175]. Additionally, the shape of $B^{meas}(t)$ is observed to be consistent between excised axons and intact worms, with both found to be in qualitative agreement with predicted $B^{meas}(t)$ derived from intracellular voltage measurements on excised axons. As discussed previously, the amplitude decrease of $B^{meas}(t)$ in intact worms versus excised axons is attributed to greater standoff distance between sensor and axon location in intact worms. Thus, due to the ease of fatigue, the temporal delay, and the qualitative and temporal agreement of expected and observed shapes of $B^{meas}(t)$, the

presence of the muscle is determined to be unlikely to affect the observed traces of $B^{meas}(t)$ for intact worms.

3.4 Current Inversion Discussion

Because axonal currents drive changes in membrane potential in passive electrical structures [188], understanding and characterizing axonal currents into and out of the soma can elucidate questions of computation and summation in passive membranes. Thus, measurements of axonal currents can provide insight into electrical dynamics within both active and passive neuronal structures.

From the simple magnetic model of a cylindrical axon, the axial current density J_a is given by $J_a(r,t) = 2B(r,t)/(\mu_0 r)$. From a measurement of B(r,t), the only remaining parameter required to determine the current density is the radial distance to the neuron center r, as the magnetic permeability of biological tissue is well known not to differ significantly from μ_0 [189]. The simplicity of the magnetic inversion process for 1D wire-like systems was briefly discussed in Chapter 2, but will be repeated here in a biological context.

In contrast, to extract $J_a(r,t)$ from a voltage measurement requires the knowledge of multiple additional parameters. Using Ohm's law applied to neural structures [190], the axonal current can be defined as $J_a(r) = \sigma \Delta\Phi(r)$, where σ is the internal conductivity and Φ is the intracellular voltage. For axially symmetric axons the spatial gradient may be related to the temporal derivative by $\partial\Phi/\partial z = -\frac{1}{v_c}\partial\Phi/\partial t$ as long as the conduction velocity v_c is well known. Thus, both conduction velocity and electrical conductivity must be well characterized to relate voltage measurements to axonal current. However, without prior knowledge of v_c, a numerical spatial gradient of the intracellular voltage would need to be calculated, which would require multiple simultaneous, spatially separated measurements of

the active neuron. Such measurements necessitate high spatial and temporal resolution to extract J_a [191], along with high SNR, as the calculation of spatial gradients of a measured field map amplifies high spatial-frequency noise [132, 134, 192]. Furthermore, the measured extracellular signal is known [143] to provide an even poorer reconstruction of the intracellular action potential due to variations and uncertainties in bath conductivities and in the effective resistance and capacitance of the measurement probes.

3.5 Future Directions

3.5.1 Extension to Non-Cylindrical Geometries

The calculations above rely on a wire-type model to approximate neuronal activity of the giant axon of *M. infundibulum*. As discussed previously, the axial symmetry of the giant axon justifies use of this model. For activity in other neuronal processes that do not possess axial symmetry such as the soma [190], different models can be used to predict the magnetic signal waveforms.

The geometry of the soma may be approximated to first order as an isotropic spherical cell. The spread of current in this cell model has been studied extensively [188, 193–195] in the context of calculating steady state membrane potentials in response to current injections. Several relevant conclusions from these calculations are: (i), the time constant of responses to a change in current in the soma is up to three orders of magnitude faster than axonal membranes [190]; (ii), in steady state, the voltage distribution constitutes an isopotential with small local variations occurring near the sites of current injection; and (iii), for cell bodies that are ellipsoidal rather than spherical, the voltage distribution deviates more globally from an isopotential, as further discussed herein.

To apply these conclusions toward estimating the magnetic field signal from a neuron

cell body at an NV sensor layer, we relate the magnetic field to the dominant intracellular current through the Biot-Savart law, and we apply the same assumption used in the axon model, namely that the dominant currents are Ohmic. We determine the spatial distribution of intracellular currents, and thus detected magnetic fields at the nearby NV sensor layer, from the gradients of the intracellular voltage [190]. For current injected into the center of an isotropic conducting spherical soma, the spatial voltage gradient, and thus the current flow, is directed radially outward due to spherical symmetry. Radial current sources in a spherical conducting medium do not produce a net magnetic field [109].

Next we more formally treat the case wherein the current injection point is on the surface of the soma, at $r = a$, $\theta = 0$, $\phi = 0$ in spherical coordinates, where a is the radius of the spherical soma. The spread of current from this injection point is azimuthally symmetric (independent of ϕ). For a current step from I=0 to some value I_0 initiated at t=0, the voltage response inside the soma is given by [188]:

$$V_i(r,\theta,t) = \frac{I_0 R}{4\pi a^2} \sum_{n=0}^{\infty} \left[(2n+1)(r/a)^n \frac{(n+1)\sigma_e P_n(cos\theta)(1 - exp(-t/\tau(1+\alpha_n)))}{(n\sigma_i + (n+1)\sigma_e)(1+\alpha_n)} \right], \quad (3.10)$$

where $\alpha_n \equiv \frac{Rn(n+1)}{a(n/\sigma_e + (n+1)/\sigma_i)}$.

Here $P_n(\cos\theta)$ are the Legendre polynomials and τ is the time constant of the membrane, which can be expressed using an RC-circuit analogy as an effective resistance R times an effective capacitance C. The conductivities σ_i (internal) and σ_e (external) arise here due to the continuity boundary conditions at the surface of the membrane. The leading term in the summation, (n=0), represents an isopotential, having no spatial dependence:

$$V_{i,n=0}(r,\theta,t) = \frac{I_0 R}{4\pi a^2}(1 - e^{-t/\tau}). \quad (3.11)$$

Assuming typical values for soma electrical and geometric properties [188] yields $\frac{V_{i,n=1}}{V_{i,n=0}} \sim$

10^{-4}. Thus the isopotential remains a very good approximation for nearly all spherical soma models, even if the electrical and geometrical parameters differ somewhat from the typical values for cortical neurons considered in Reference [188]. The spatial dependence is present only in the much smaller, higher order terms.

We expect this picture to be valid near the center of the soma where the current profile is not significantly affected by irregular soma boundaries. On the cell body surface, however, there are expected to be detectable magnetic signals owing to deviations from spherical symmetry and uniform conductivity. For example, magnetic signals at the cell body surface are expected to originate primarily from axon hillocks, as these structures contain a higher density of ion channels [196].

The electrical behavior of the soma and other neuronal processes depends on intricacies of the neuronal shape [197]. Since the spherically-symmetric model presented here predicts no magnetic field signal, any field from the soma measured by a next-generation neuron magnetometer indicates structural or electrical non-trivialities of the cell body and could add to the present understanding of electrical dynamics in the soma. Additionally, spatially inhomogeneous transient currents in the soma are expected over very short timescales compared to the cellular membrane RC time constant [195]. The rapid spread of currents and equilibration into somas has been demonstrated through voltage imaging methods [191] where, in videos of the propagation of a voltage wavefront, the soma becomes an isopotential in less than the duration of a single post-processed frame after interpolation ($\sim$ 10 μs). We anticipate that with enhanced temporal resolution in a next-generation diamond magnetic imager for neurons, we could observe magnetic signals due to spatially varying transient currents within the soma, although in the near term this will likely require repeated stimulations and temporal averaging.

Furthermore, as the geometry of an axon hillock is similar to that of a compressed

tapered axon, we envision that the technique and analysis presented in this work could provide insight into future studies of electrical activity of axon hillocks and ultimately aid in improving understanding of action potential initiation [198].

3.5.2 Extension to Mammalian Neuron Studies

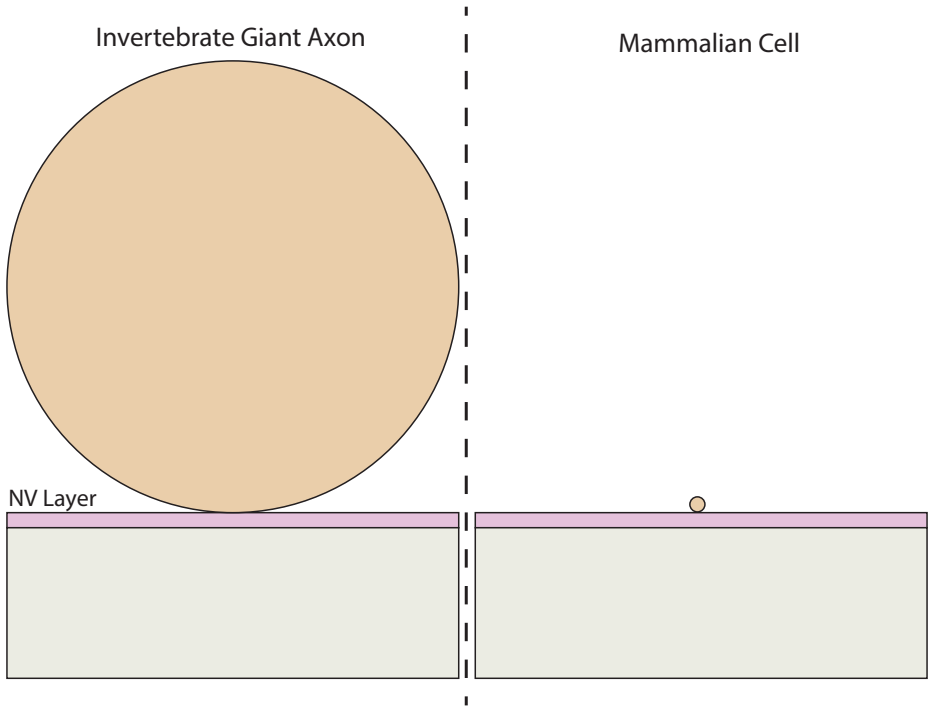

Figure 3.17: Comparison between length scale of giant axons and mammalian cells.

Realization of sufficient magnetometer sensitivity is anticipated to be the primary challenge to extending NV-diamond magnetic imaging to mammalian neurons and from single neurons to networks of neurons. Figure 3.17 highlights this challenge through the large size differences between giant axons and mammalian cells. Luckily, the magnetic field amplitude measured at the surface of the cell is expected to $\sim$ 1 nT. However, much less sensing volume is available to achieve the needed sensitivity. In contrast, implementation of magnetic

imaging with micron-scale spatial resolution and $\sim$ 100 μm field of view is expected to be relatively straightforward when not considering sensitivity, as it mainly requires applying previously developed wide-field NV-diamond magnetic imaging technology demonstrated with biological specimens [1, 15] to the present and anticipated enhanced-sensitivity magnetometer. Sensitivity rather than spatial resolution is thus the chief limit to reconstructing neuronal currents from acquired magnetic field maps using an NV-diamond magnetic imager. In the absence of noise and sampling artifacts, the biomagnetic inverse problem [132] can be uniquely solved for 2D networks close [45] to the diamond sensing layer. As discussed in Chapter 2, 3D networks are more problematic: not only are magnetic signals smaller due to greater source-sensor standoff distance, but the problem is ill-posed and the parameter space of possible current distributions is large. In all cases, prior knowledge about the network structure under study, as could be obtained with a bright field confocal microscope or other traditional optical methods, may be used to further constrain solutions, thereby increasing reconstruction accuracy and decreasing magnetometer sensitivity requirements.

Resolving activity from non-axonal processes in dense 3D networks with both high spatial and high temporal resolution is a significant challenge in neuroscience [199], which we regard as a longer-term goal that may realistically require additional structural knowledge of the network, such as a confocal scan, along with further sensitivity enhancements of the magnetic imaging technique and the extension of vector capabilities (see AppendixB). We regard the task of achieving the necessary sensitivity to map neuronal network dynamics as a practical challenge, albeit a difficult one, which is limited more by a need for engineering advances in NV-diamond magnetometry than by fundamental limitation of NV diamond sensing.

Chapter 4

Diamond Improvement and Scalability

4.1 Diamond Improvements

The development of a repeatable and scalable process to develop a large number of high quality diamonds with homogeneous properties is essential to the continued development of NV diamond sensing and imaging [56,200,201]. There are many diamond related parameters that need to be considered when optimizing for a given application [56]. Some procedures like improving ^{12}C isotopic purity and strain homogeneity are beneficial for all experiments and measurement protocols. However, other diamond parameters like [NV], T_2^*, and contrast come with necessary trade-offs where the improvement of one parameter will come at the cost of another. For example, increasing the nitrogen concentration (and thus NV concentration once irradiated and annealed) of a diamond can increase fluorescence, but will come at the cost of broader line-widths (shorter T_2^*) [21, 61]. On the other hand, decreasing the nitrogen concentration (and thus NV concentration) will have the effect of increasing T_2^*,

but at the cost of fluorescence and measurement contrast due to charge state instabilities [202]. More information on ensemble dephasing and the diamond spin bath can be found in References [21, 61, 106, 108]. This chapter will explore a few of these directions, the tools developed to improve our characterization of relevant parameters, and collaborative efforts with diamond growers to improve the diamond growth iteration process and find more optimal growth conditions.

4.2 Strain and Stress Inhomogeneity

Crystal lattice strain can be introduced into the diamond in one of several ways (Figure 4.1). Strain with large spatial length scales generally propagate from the diamond substrate crystal. A strain of particular focus in this work are dislocations at the substrate-NV layer growth interface due to imperfections at the growth interface. These dislocations will propagate as the layer is grown and will be particularly pernicious to NV imaging experiments because of the small characteristic length scales and large spatial gradients. A final class is strain that is incorporate post-growth either through mechanical methods (scratching the diamond surface or indenting the surface) or through implantation of various particles (ions, electrons, etc.) and causing sub-micron length scales strain features. This section will focus primarily on the first two sources of strain, but the third source is of particular interest for ongoing work in developing a dark matter detector based on strain in the diamond lattice [203] and improvements in strain background in general is useful for this work as well.

One significant limitation to a QDM's sensitivity is intrinsic diamond stress variation, which inhomogeneously shifts the NV ground-state resonance frequencies and spoils the NV spin dephasing time [21]. Diamond crystal stress and strain are therefore important

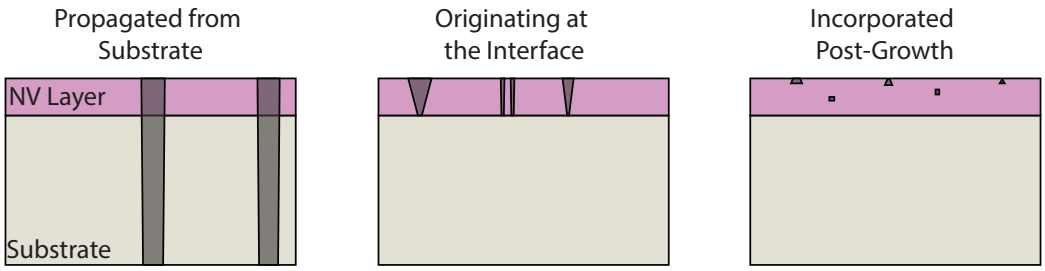

Figure 4.1: Cartoons of different ways strain features can be incorporated into the NV layer. One of the dominant ways strain is incorporated is propagation of strain from the diamond substrate.

to understand and minimize when optimizing NV magnetometry [54, 180] and magnetic microscopy. Strain can impact magnetometry in two important ways: (i) it can degrade magnetic sensitivity through degrading ensemble contrast and T_2^* (linewidth) and (ii) it can introduce systematics into magnetic images if not corrected.

4.2.1 NV Experiment and Strain Measurement Protocols

We used an ensemble NV surface layer to image diamond stress across a millimeter-scale field of view, and explore how stress inhomogeneity impedes NV magnetic microscopy. A 532 nm laser illuminates the micrometer-scale NV layer at the top surface of a diamond chip (4 mm $\times$ 4 mm wide and 0.5 mm thick) and an optical microscope images the spin-state-dependent NV fluorescence onto a camera (Figure 4.2). Probing the transition frequencies between NV ground-state sublevels by sweeping the frequency of an applied microwave field yields an optically-detected magnetic resonance (ODMR) spectrum in each pixel. From the resulting 2D map of NV resonance frequencies, we extract magnetic field components and crystal stress tensor elements (which have units of pressure). As crystal stress and strain are related through Young's modulus (1050-1210 GPa for diamond [204]), we refer to the crystal defects that induce stress within the diamond (shifting the NV ground-state sublevels and causing birefringence) as strain defects.

We first demonstrate the NV stress imaging technique with diamond Sample A from Table 4.1, which contains a nitrogen-rich layer (25 ppm, 13 μm thick) grown on an electronic-grade single-crystal substrate with ppb nitrogen density. This sample was electron-irradiated and annealed to increase the NV density. We also apply the NV stress imaging technique to several other diamonds (Samples B through J), which exhibit a variety of strain defects.

The NV center in diamond consists of a substitutional nitrogen atom in the carbon lattice adjacent to a vacancy (Figure 4.3(A)). It has an electronic spin-triplet ground state ($S = 1$) with magnetic sublevels $m_s = \{-1, 0, +1\}$. The sublevel energies shift in response to local magnetic fields, crystal stress, temperature changes, and electric fields. We measure these energy shifts using ODMR spectroscopy, where a resonant microwave field induces transitions between the $m_s = 0$ and ± 1 sublevels and causes reduced NV fluorescence under continuous illumination by 532 nm laser light (Figure 4.3(B)). Each NV is oriented along one of four crystallographic directions (labeled with the index $\kappa = \{1, 2, 3, 4\}$). An NV ensemble usually contains an equal distribution of NVs for each κ. The ODMR spectra from all NV orientations yields the information to reconstruct stress tensor elements and vector magnetic field components [1].

Previous diamond strain imaging studies used X-ray topography, Raman spectroscopy, cathodoluminescence, and birefringence to characterize diamond strain and how it affects diamond applications [206–208]. By comparison, NV stress imaging gives a more direct characterization of how diamond stress inhomogeneity affects NV magnetic imaging, as both techniques probe the NV ODMR frequencies. In addition, NV stress imaging yields quantitative maps of the diamond stress tensor components localized in the NV layer with micrometer resolution [209]. The stress tensor reconstruction can help identify how strain features formed during diamond sample preparation and thereby inform future sample fabrication.

Sample	Dimensions	[N] in layer	Layer Thickness	Substrate	Irradiated/ Annealed?	References
A	4×4×0.5 mm^3	25 ppm	13 µm	CVD	Yes / Yes	Studied here
B	4×4×0.5 mm^3	20 ppm	4 µm	CVD	Yes / Yes	Sample D4 in Ref. [1]
C	5×5×0.4 mm^3	10 ppm	40 µm	CVD	Yes / Yes	-
D	2×2×0.5 mm^3	$2\times10^{11}/cm^2$ dose	20 nm	CVD	14 keV $^{14}N^+$ / Yes	Sample D1 in Ref. [1]
E	1.7×1.5×0.5 mm^3	10 ppm	40 µm	CVD	No / No	Sample C in Ref. [21]
F	4×4×0.3 mm^3	0.75 ppm	140 µm	HPHT	No / No	Sample B in Ref. [21]
G	4.5×4.5×0.5 mm^3	20 ppm	4 µm	CVD	Yes / Yes	Used in Ref. [205]
H	4×4×0.5 mm^3	27 ppm	13 µm	CVD	Yes / Yes	-
I	4×4×0.5 mm^3	7.2 ppm	0.9 µm	CVD	Yes / Yes	Sample D2 in Ref. [93]
J	4×4×0.5 mm^3	26.8 ppm	13 µm	CVD	Yes / Yes	Sample D3 in Ref. [1]

Table 4.1: Properties of all diamond samples studied in this work. Sample F has a nitrogen-enriched chemical vapor deposition (CVD) layer grown on top of a diamond substrate made by high-pressure high-temperature (HPHT) synthesis. All other samples have electronic-grade single-crystal (ELSC) substrates grown by CVD. Sample D is a $^{14}N^+$ beam implant, and the other samples were grown with a nitrogen-rich layer. Strain maps for all samples are given in Appendix C.

4.2.2 Relevant Hamiltonian

We now describe how to extract the local magnetic field and crystal stress from the measured NV resonance frequencies. The NV ground-state Hamiltonian in the presence of stress and a static magnetic field is: [27–29]

$$\begin{aligned} H_\kappa = &(D + M_{z,\kappa})\, S_{z,\kappa}^2 + \gamma \vec{B} \cdot \vec{S}_\kappa \\ &+ M_{x,\kappa} \left(S_{y,\kappa}^2 - S_{x,\kappa}^2\right) \\ &+ M_{y,\kappa} \left(S_{x,\kappa} S_{y,\kappa} + S_{y,\kappa} S_{x,\kappa}\right) \\ &+ N_{x,\kappa} \left(S_{x,\kappa} S_{z,\kappa} + S_{z,\kappa} S_{x,\kappa}\right) \\ &+ N_{y,\kappa} \left(S_{y,\kappa} S_{z,\kappa} + S_{z,\kappa} S_{y,\kappa}\right). \end{aligned} \tag{4.1}$$

Here, $D \approx 2870$ MHz is the zero-field splitting, $S_{i,\kappa}$ are the dimensionless spin-1 projection

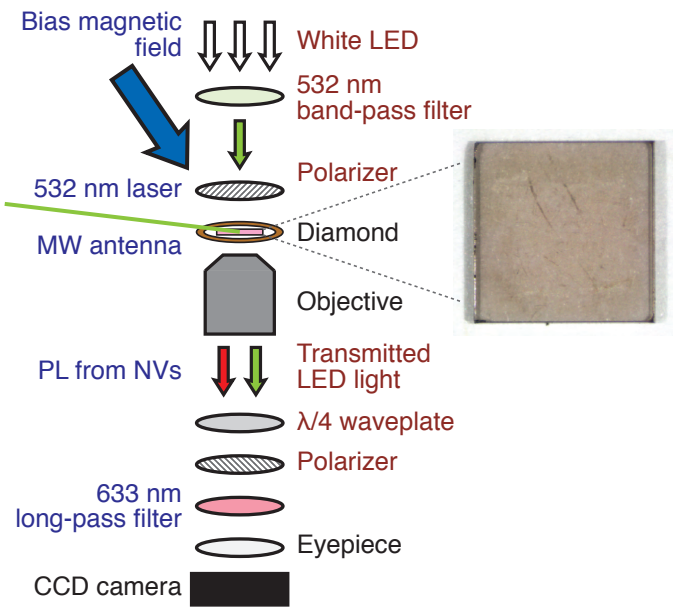

Figure 4.2: Schematic of the combined NV stress and birefringence imager. The NV stress imager (blue labels) uses a 532 nm laser to illuminate the diamond, an applied microwave field to drive transitions between NV ground-state sublevels, and a bias magnetic field. The birefringence imager (red labels) uses an LED illuminator, two linear polarizers, and a quarter-wave plate. Both imagers use the same microscope objective and CCD camera (black labels) to collect and image the transmitted light. The photograph on the right shows the diamond Sample A studied in this work.

operators, $\gamma = 2.803 \times 10^4$ MHz/T is the NV electronic gyromagnetic ratio, $\vec{B}$ is the magnetic field in the NV coordinate system, and $M_{i,\kappa}$ and $N_{i,\kappa}$ are terms related to the crystal stress and temperature. The indices $i = \{x, y, z\}$ represent the coordinate system for the particular NV orientation. We neglect the electric-field contributions to Equation 4.1, as explored in greater depth below.

Other spin-stress terms

Using second-order perturbation theory, we estimate the potential corrections of the neglected spin-stress terms $\{M_{x,\kappa}, M_{y,\kappa}, N_{x,\kappa}, N_{y,\kappa}\}$ on the NV transition frequencies. These

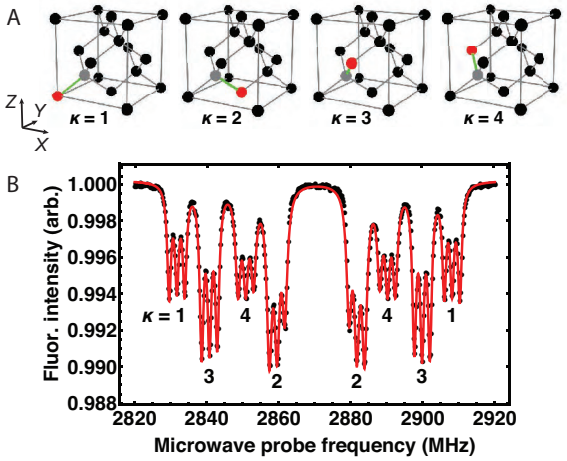

Figure 4.3: (A) NV centers in the diamond lattice, with the four NV axes shown in green [29]. Carbon atoms are black, nitrogen atoms are red, and vacancies are gray. (B) Example ODMR spectrum with $\vec{B} = \{220, 593, 1520\}$ μT in the diamond chip coordinate system (fit function plotted in red). The labels indicate the resonances from the different NV orientations. Each NV resonance is split into three lines due to hyperfine interactions with the spin-1 ^{14}N nucleus.

calculations justify disregarding these terms in our analysis, keeping only the $M_{z,\kappa}$ spin-stress term. For simplicity, we do this analysis for the projection magnetic microscopy case, where $\vec{B} = B_z\hat{z}$, with $B_z \approx 1$ mT in our experiments. Note that the contributions from the neglected spin-stress terms may become significant if the Zeeman effect is small in comparison, which can happen if $\vec{B}$ is largely perpendicular to the NV z-axis in a vector magnetic microscopy experiment.

For the $M_{x,\kappa}$ and $M_{y,\kappa}$ spin-stress terms, the $m_s = \pm 1$ electronic sublevel energies are shifted by $\pm\frac{M_{x,\kappa}^2+M_{y,\kappa}^2}{2\gamma B_z}$ while the $m_s = 0$ electronic sublevel is unaffected. For a typical 100 kHz spin-stress contribution, this perturbation shifts the NV transition frequencies by 200 Hz.

For the $N_{x,\kappa}$ and $N_{y,\kappa}$ spin-stress terms, the $m_s = \pm 1$ electronic sublevel energies are shifted by $\frac{\pm(N_{x,\kappa}^2+N_{y,\kappa}^2)}{2(D+M_{z,\kappa}\pm\gamma B_z)}$ while the $m_s = 0$ electronic sublevel is shifted by $-\frac{N_{x,\kappa}^2+N_{y,\kappa}^2}{2(D+M_{z,\kappa}+\gamma B_z)}-$

$\frac{N_{x,\kappa}^2+N_{y,\kappa}^2}{2(D+M_{z,\kappa}-\gamma B_z)}$. When $\gamma B_z \ll D$ and $M_{z,\kappa} \ll D$, the NV transition frequencies shift by approximately $\frac{3(N_{x,\kappa}^2+N_{y,\kappa}^2)}{2D}$ and $\frac{N_{x,\kappa}^2+N_{y,\kappa}^2}{2D}$. For a 100 kHz spin-stress contribution, this perturbation shifts the NV transition frequencies by at most 5 Hz. Note that this estimate is just for illustration, as experimental values for the spin-stress coupling constants for $N_{x,\kappa}$ and $N_{y,\kappa}$ are not currently reported to our knowledge [27, 29], though Reference [28] calculated estimates for them numerically. The above transition frequency correction estimates justify our rationale to neglect these spin-stress terms in our analysis.

Stress and electric-field contributions to the NV ground-state Hamiltonian

Crystal stress and electric field are often intertwined through the piezoelectric, pyroelectric, and ferroelectric effects. However, the bonds between carbon atoms in the diamond lattice are covalent bonds, meaning diamond should have no permanent or induced electric dipole moment in its unit cell. Thus, in the absence of defects, stress within diamond does not cause an electric field or vice versa, but this does not mean they are unrelated. For example, an NV center can sense an electric field from nearby charged defects, which can also cause normal stress due to lattice deformation.

From Reference [28], the electric-field contributions to the NV ground-state Hamiltonian are:

$$\begin{aligned} H_{E,\kappa} = d_{||}E_z S_{z,\kappa}^2 + d_\perp[(S_{y,\kappa}^2 - S_{x,\kappa}^2)E_x + (S_{x,\kappa}S_{y,\kappa} + S_{y,\kappa}S_{x,\kappa})E_y] \\ + d'_\perp[(S_{x,\kappa}S_{z,\kappa} + S_{z,\kappa}S_{x,\kappa})E_x + (S_{y,\kappa}S_{z,\kappa} + S_{z,\kappa}S_{y,\kappa})E_y]. \end{aligned} \tag{4.2}$$

In this expression, $\vec{E}$ is the electric field in the NV coordinate system, and $\{d_{||}, d_\perp, d'_\perp\}$ are NV ground-state electric dipole parameters [20]. The spin-stress terms in Equation 4.1 and the $\vec{E}$ terms affect the same spin terms in the NV Hamiltonian, though the former originate from a stress tensor and the latter originate from a vector electric field. When performing vector magnetic microscopy or projection magnetic microscopy with $|\vec{B}| > 1$

mT, only the $M_{z,\kappa}$ and E_z terms matter, and the off-diagonal terms can be ignored.

Because of the similarity between how $M_{z,\kappa}$ and E_z enter the NV Hamiltonian, at first glance it may be unclear whether our NV ODMR measurements are imaging inhomogeneity caused by $M_{z,\kappa}$, E_z, or both. Herein we argue that our imaging experiments are primarily sensitive to $M_{z,\kappa}$, while E_z may contribute to lineshape broadening.

κ	NV z-axes	Stress tensors	$M_{z,\kappa}$
1	[111], [$\bar{1}\bar{1}\bar{1}$]	$\begin{pmatrix} \sigma_{XX} & \sigma_{XY} & \sigma_{XZ} \\ \sigma_{XY} & \sigma_{YY} & \sigma_{YZ} \\ \sigma_{XZ} & \sigma_{YZ} & \sigma_{ZZ} \end{pmatrix}, \begin{pmatrix} \sigma_{YY} & \sigma_{XY} & \sigma_{YZ} \\ \sigma_{XY} & \sigma_{XX} & \sigma_{XZ} \\ \sigma_{YZ} & \sigma_{XZ} & \sigma_{ZZ} \end{pmatrix}$	$a_1[\sigma_{XX}+\sigma_{YY}+\sigma_{ZZ}]$ $+2a_2[\sigma_{XY}+\sigma_{XZ}+\sigma_{YZ}]$
2	[$\bar{1}\bar{1}$1], [11$\bar{1}$]	$\begin{pmatrix} \sigma_{XX} & \sigma_{XY} & -\sigma_{XZ} \\ \sigma_{XY} & \sigma_{YY} & -\sigma_{YZ} \\ -\sigma_{XZ} & -\sigma_{YZ} & \sigma_{ZZ} \end{pmatrix}, \begin{pmatrix} \sigma_{YY} & \sigma_{XY} & -\sigma_{YZ} \\ \sigma_{XY} & \sigma_{XX} & -\sigma_{XZ} \\ -\sigma_{YZ} & -\sigma_{XZ} & \sigma_{ZZ} \end{pmatrix}$	$a_1[\sigma_{XX}+\sigma_{YY}+\sigma_{ZZ}]$ $+2a_2[\sigma_{XY}-\sigma_{XZ}-\sigma_{YZ}]$
3	[$\bar{1}$1$\bar{1}$], [1$\bar{1}$1]	$\begin{pmatrix} \sigma_{XX} & -\sigma_{XY} & \sigma_{XZ} \\ -\sigma_{XY} & \sigma_{YY} & -\sigma_{YZ} \\ \sigma_{XZ} & -\sigma_{YZ} & \sigma_{ZZ} \end{pmatrix}, \begin{pmatrix} \sigma_{YY} & -\sigma_{XY} & -\sigma_{YZ} \\ -\sigma_{XY} & \sigma_{XX} & \sigma_{XZ} \\ -\sigma_{YZ} & \sigma_{XZ} & \sigma_{ZZ} \end{pmatrix}$	$a_1[\sigma_{XX}+\sigma_{YY}+\sigma_{ZZ}]$ $+2a_2[-\sigma_{XY}+\sigma_{XZ}-\sigma_{YZ}]$
4	[1$\bar{1}\bar{1}$], [$\bar{1}$11]	$\begin{pmatrix} \sigma_{XX} & -\sigma_{XY} & -\sigma_{XZ} \\ -\sigma_{XY} & \sigma_{YY} & \sigma_{YZ} \\ -\sigma_{XZ} & \sigma_{YZ} & \sigma_{ZZ} \end{pmatrix}, \begin{pmatrix} \sigma_{YY} & -\sigma_{XY} & \sigma_{YZ} \\ -\sigma_{XY} & \sigma_{XX} & -\sigma_{XZ} \\ \sigma_{YZ} & -\sigma_{XZ} & \sigma_{ZZ} \end{pmatrix}$	$a_1[\sigma_{XX}+\sigma_{YY}+\sigma_{ZZ}]$ $+2a_2[-\sigma_{XY}-\sigma_{XZ}+\sigma_{YZ}]$

Table 4.2: Stress tensors and $M_{z,\kappa}$ terms for each NV orientation, calculated using the coordinate systems used in Figure 4.3(A), and also in Table 1 of Ref [29].

Our diamond samples contain NV ensembles with equal populations oriented along opposite z directions (for example, [111] and [$\bar{1}\bar{1}\bar{1}$]). There are eight NV z directions (two for each κ). Usually the NVs pointing along opposite directions behave identically, allowing us to group them together with the same κ label. Calculating the stress tensor and the $M_{z,\kappa}$ for each NV orientation (Table 4.2) we see that the NV sub-ensembles with z-axes pointing in opposite directions have the same $M_{z,\kappa}$ and the same resonance frequencies.

Although the stress tensor contributions affect the [111] and $[\bar{1}\bar{1}\bar{1}]$ NV orientations the same way, this is not true for the E_z electric field contribution. The E_z term shifts the NV resonance frequencies by equal and opposite amounts ($\pm d_{||} E_z$) for NVs with opposite z-axes. This causes a lineshape splitting or broadening rather than a common-mode shift. We did not observe such splittings in our NV magnetic resonance spectra (Figure 4.3(B)), though a weak E_z may contribute as a linewidth broadening. Therefore, the common-mode NV resonance frequency shifts we measure are caused by $M_{z,\kappa}$ terms only. One can imagine extracting E_z from the NV resonance linewidths, but this may be difficult because the linewidth also depends on the magnetic field inhomogeneity, $M_{z,\kappa}$ inhomogeneity, microwave power, and laser power.

Simplified Hamiltonian

Based on the previous sections, if $|\vec{B}| > 1$ mT, as is the case in this work, the contributions from the $\{M_{x,\kappa}, M_{y,\kappa}, N_{x,\kappa}, N_{y,\kappa}\}$ terms are negligible, and Equation 4.1 simplifies to

$$H_\kappa = (D + M_{z,\kappa}) S_{z,\kappa}^2 + \gamma \vec{B} \cdot \vec{S}_\kappa. \tag{4.3}$$

When $\vec{B}$ is aligned along the z-axis for one NV orientation, the Hamiltonian for the selected orientation reduces to

$$H_\kappa = (D + M_{z,\kappa}) S_{z,\kappa}^2 + \gamma B_z S_{z,\kappa}, \tag{4.4}$$

and the resonance frequencies are

$$f_\pm = (D + M_{z,\kappa}) \pm \gamma B_z. \tag{4.5}$$

Measuring $f_\pm$ yields the magnetic field projection B_z and the $M_{z,\kappa}$ for that NV orientation. This measurement forms the basis of a sensing modality called Projection Magnetic Microscopy (PMM) [1], where we align the bias magnetic field along the z-axis of each NV

orientation and record the associated resonance frequencies individually. An alternative sensing modality, called Vector Magnetic Microscopy (VMM) [1], allows us to determine $\vec{B}$ and all four $M_{z,\kappa}$ terms from a single measurement (Figure 4.3(B)). In VMM, the selected bias magnetic field generates unique Zeeman splittings and non-overlapping ODMR spectra for each NV orientation. We extract the magnetic field components and $M_{z,\kappa}$ values by fitting Equation 4.3 for all four NV orientations. Both VMM and PMM yield the same $M_{z,\kappa}$ results.

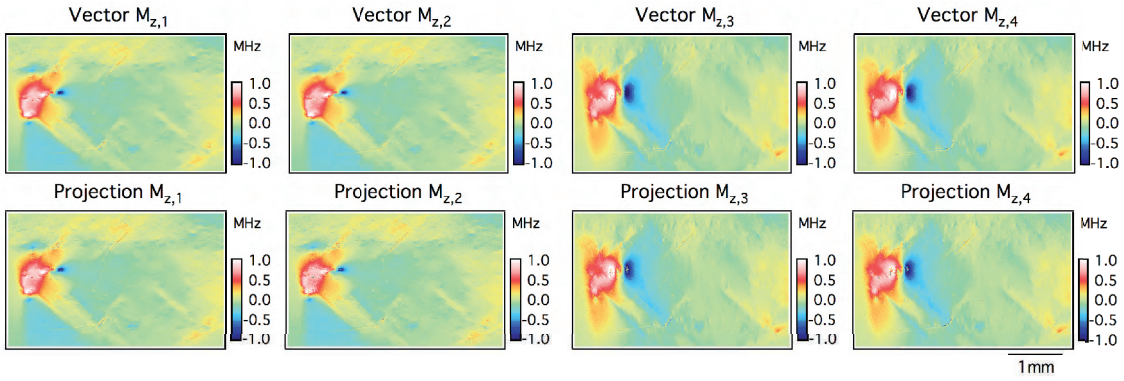

Figure 4.4: A comparison of $M_{z,\kappa}$ maps for X-shaped defects in Sample B obtained using vector magnetic microscopy (VMM) and projection magnetic microscopy (PMM). We varied the laser polarization angle and the bias magnetic field in between measurements, keeping the diamond region constant.

Figure 4.4 confirms that the VMM and PMM methods yield the same $M_{z,\kappa}$ information despite the differences between these schemes. VMM yields all $M_{z,\kappa}$ maps simultaneously without having to adjust the bias magnetic field and laser polarization angle (or rotate the diamond). PMM is optimized for measuring one $M_{z,\kappa}$ at a time, and the procedures for lineshape fitting and $M_{z,\kappa}$ extraction are simpler [1]. As a further check, we rotated the diamond chip by 90° about the Z-axis. The resulting $M_{z,\kappa}$ and stress maps were consistent with the unrotated maps, transforming as expected for a 90° rotation. Based on this analysis, we used VMM in this work to measure the four necessary $M_{z,\kappa}$ maps (which we refer to as

"NV $M_{z,\kappa}$ imaging") needed to reconstruct stress tensor elements for each pixel, as shown below.

4.2.3 Stress tensor reconstruction

In each pixel, the stress tensor components can be determined from the four $M_{z,\kappa}$ parameters, allowing us to generate a quantitative image of the local stress across the diamond. Following the derivations in References [27–29], we obtain:

$$\begin{aligned} M_{z,1} &= a_1\sigma_{\text{diag}} + 2a_2\left[\sigma_{XY} + \sigma_{XZ} + \sigma_{YZ}\right], \\ M_{z,2} &= a_1\sigma_{\text{diag}} + 2a_2\left[\sigma_{XY} - \sigma_{XZ} - \sigma_{YZ}\right], \\ M_{z,3} &= a_1\sigma_{\text{diag}} + 2a_2\left[-\sigma_{XY} + \sigma_{XZ} - \sigma_{YZ}\right], \\ M_{z,4} &= a_1\sigma_{\text{diag}} + 2a_2\left[-\sigma_{XY} - \sigma_{XZ} + \sigma_{YZ}\right] \end{aligned} \tag{4.6}$$

Here, $\{a_1, a_2\} = \{4.86, -3.7\}$ MHz/GPa are spin-stress coupling constants [27], σ_{ij} are elements of the 3×3 stress tensor in GPa, and $\sigma_{\text{diag}} \equiv \sigma_{XX} + \sigma_{YY} + \sigma_{ZZ}$. The σ_{ii} are normal stress terms, while σ_{XY}, σ_{XZ}, and σ_{YZ} are shear stress terms. The σ_{ij} are written in the diamond unit cell coordinate system $\{X, Y, Z\}$ (rather than the NV coordinate system $\{x, y, z\}$ for a given κ), and are felt by all four NV orientations. Each NV orientation exhibits the same $a_1\sigma_{\text{diag}}$ contribution to $M_{z,\kappa}$. The a_2 contributions change as we transform the stress tensor for each of the four NV orientations.

Solving the previous equations to extract σ_{diag}, σ_{XY}, σ_{XZ}, and σ_{YZ} in each pixel

yields:

$$\begin{aligned}
\sigma_{\text{diag}} &= \frac{1}{4a_1}\left[M_{z,1} + M_{z,2} + M_{z,3} + M_{z,4}\right], \\
\sigma_{XY} &= \frac{1}{8a_2}\left[M_{z,1} + M_{z,2} - M_{z,3} - M_{z,4}\right], \\
\sigma_{XZ} &= \frac{1}{8a_2}\left[M_{z,1} - M_{z,2} + M_{z,3} - M_{z,4}\right], \\
\sigma_{YZ} &= \frac{1}{8a_2}\left[M_{z,1} - M_{z,2} - M_{z,3} + M_{z,4}\right]
\end{aligned} \tag{4.7}$$

The measurements presented here are only sensitive to the total normal stress σ_{diag} rather than the individual σ_{ii} contributions [27]. A more involved algorithm could use VMM spectra measured at several magnetic fields and keep all of the terms in Equation 4.1 to obtain each σ_{ii} separately.

Since $M_{z,\kappa}$ and σ_{diag} change with temperature as the diamond lattice constant changes, $M_{z,\kappa}$ and σ_{diag} can only be evaluated up to an overall constant [24, 25]. However, the shear stress terms should be unaffected by temperature changes, and thus shear stress images are absolute. For measurements acquired with 10 mK temperature stability, an NV $M_{z,\kappa}$ imager can determine $M_{z,\kappa}$ to about 1 kHz, or ∼0.1 MPa. As a further example, a 1 $\mu\text{T}/\sqrt{\text{Hz}}$ magnetic sensitivity per pixel (28 $\text{kHz}/\sqrt{\text{Hz}}$ frequency sensitivity) corresponds to approximately 10 $\text{MPa}/\sqrt{\text{Hz}}$ stress sensitivity for a given pixel.

Figure 4.5 shows the measured $M_{z,\kappa}$ maps and the resulting $\{\sigma_{\text{diag}}, \sigma_{XY}, \sigma_{XZ}, \sigma_{YZ}\}$ maps for Sample A, illustrating a practical example of NV $M_{z,\kappa}$ and stress imaging. This diamond has a variety of strain features (their origins are described below), in addition to more homogeneous regions. For Sample A and most of the other diamond samples we investigated in this work, we found the shear stress inhomogeneity was greater in σ_{XY} than in σ_{XZ} or σ_{YZ} due to the propagation of defects and dislocations along the growth direction. The $M_{z,\kappa}$ variations were usually due to σ_{diag} and σ_{XY} inhomogeneity in roughly equal amounts.

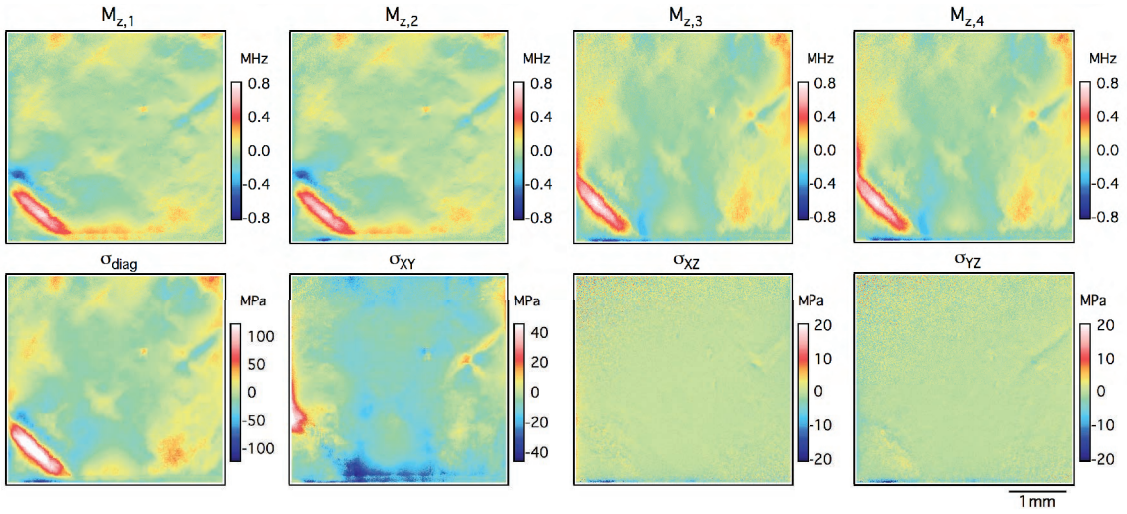

Figure 4.5: Example NV $M_{z,\kappa}$ and $\{\sigma_{\text{diag}}, \sigma_{XY}, \sigma_{XZ}, \sigma_{YZ}\}$ maps for Sample A. After measuring the $M_{z,\kappa}$ maps in the top row from the NV resonance frequencies, we calculate the stress tensor element maps in the bottom row using Equation 4.7. The diamond chip has high-stress and low-stress regions, and most of the $M_{z,\kappa}$ inhomogeneity comes from σ_{diag} and σ_{XY} stress terms.

4.2.4 Comparison with birefringence imaging

Here we compare NV stress imaging to birefringence imaging, which is a prominent characterization tool in the diamond community [206, 210]. In this work, both methods were implemented within the same optical microscope for a straightforward comparison (Figure 4.2). Both the NV $M_{z,\kappa}$ terms and the diamond refractive index depend on crystal stress, but NV stress imaging more directly captures relevant information about stress inhomogeneity in the NV layer and its effects on NV sensing. This makes NV stress imaging the more appropriate tool for optimizing NV diamond samples for magnetic microscopy.

In a birefringent material, light with orthogonal polarizations transmitted through a sample of thickness L accumulates a relative optical retardance phase $\delta = \frac{2\pi}{\lambda}\Delta n L$, where λ is the wavelength and Δn is the difference in refractive indices for orthogonal polarizations. We used a rotating-linear-polarizer method, also known as Metripol, to extract $|\sin\delta|$ by probing

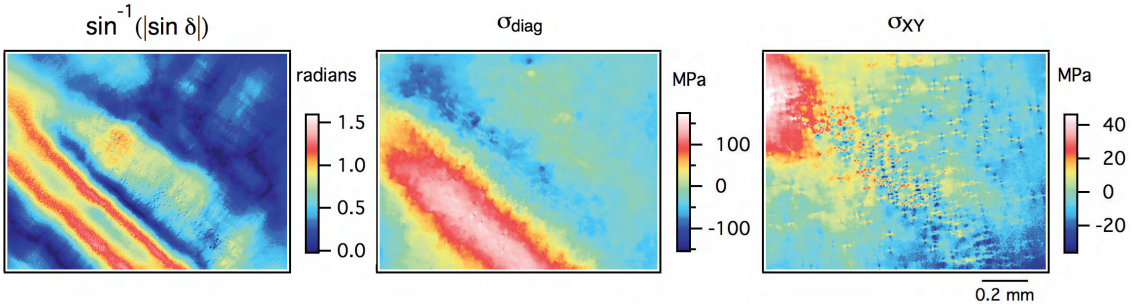

Figure 4.6: Birefringence $\sin^{-1}|\sin\delta|$ and NV stress maps for the lower-left corner region of Sample A. Both techniques show similar phenomena, though the NV stress imaging maps are immune to the $\delta > \pi/2$ phase ambiguity, can resolve the petal-shaped defects localized in the NV layer, separate out strain phenomena into different stress tensor contributions, and predict how strain features affect the NV magnetic microscopy performance.

the sample with light of varying polarization angles [211, 212]. The measured transmission intensity I_i for a given polarizer rotation angle α_i is:

$$I_i = \frac{1}{2} I_0[1 + \sin 2(\alpha_i - \phi)\sin\delta]. \tag{4.8}$$

Here I_0 is the transmittance of a given pixel and ϕ is the retardance orientation angle. Sweeping α_i across 180° of polarization rotation allows us to determine I_0, $|\sin\delta|$, and ϕ.

Birefringence imager

For birefringence measurements (see Figure 4.2), light from a white LED illuminator passes through a 532 nm bandpass filter and a linear polarizer mounted to a motorized rotation stage before illuminating the diamond sample. The light transmitted through the birefringent diamond is collected by a 4× or 10× microscope objective. The light then passes through a circular analyzer consisting of a zero-order $\lambda/4$ wave plate aligned at 45° to a linear polarizer. The transmitted light is imaged with a CMOS camera through an eyepiece lens. We save camera images while sweeping the polarizer rotation angle α_i through 180°,

usually in 10° steps. To alternate between birefringence and NV $M_{z,\kappa}$ imaging, we swap between the circular analyzer and the longpass filter before the camera.

Extracting birefringence parameters

Here we summarize the equations describing rotating-polarizer birefringence measurements, derived in References [211, 212]. The transmission intensity I_i for polarizer angle α_i is

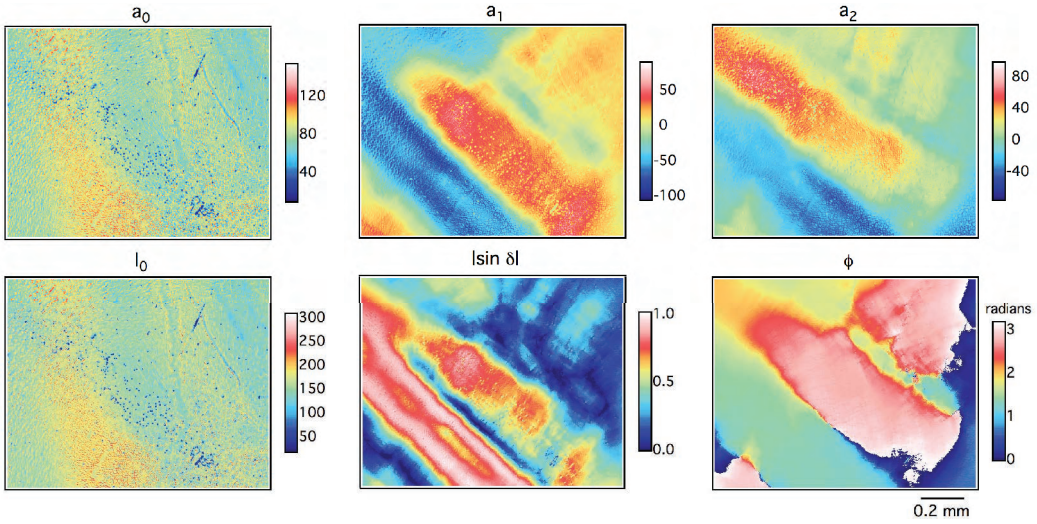

Figure 4.7: Complete birefringence parameter maps for Sample A.

$$I_i = \frac{1}{2} I_0 [1 + \sin 2(\alpha_i - \phi) \sin \delta], \tag{4.9}$$

where I_0 and I_i are the initial and transmitted intensities, ϕ is the retardance orientation angle, $\delta = \frac{2\pi}{\lambda} \Delta n L$ is the optical retardance phase, and α_i is the angle of the first polarizer. This equation can be rewritten in a more convenient form

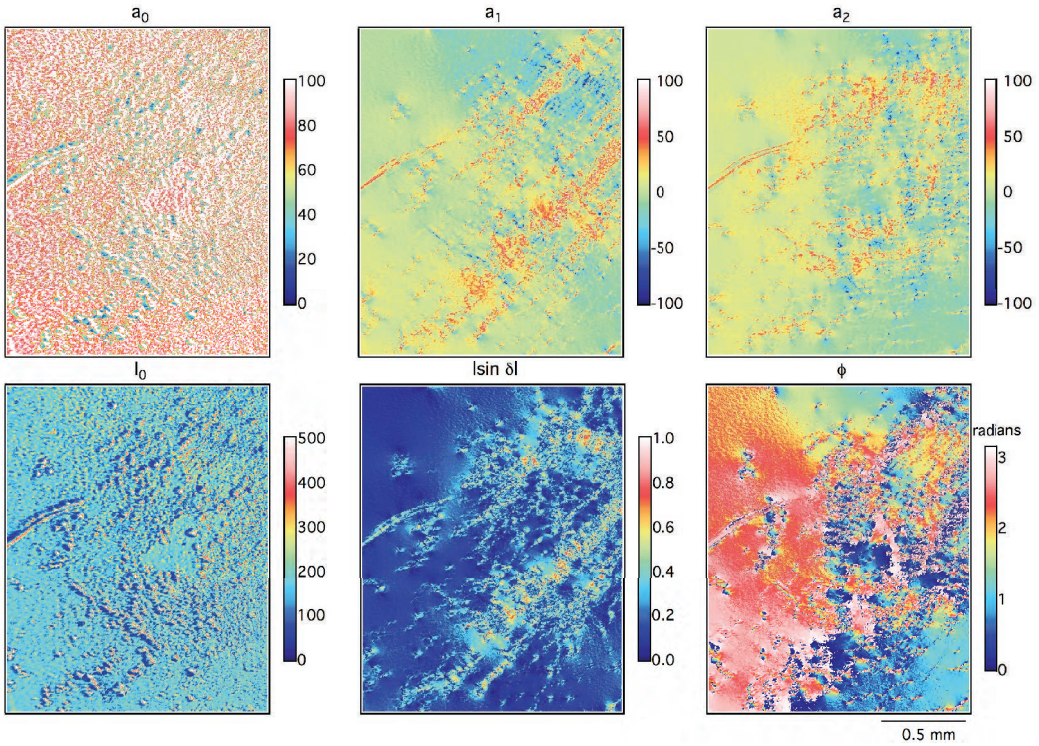

Figure 4.8: Complete birefringence parameter maps for Sample C.

$$I_i = a_0 + a_1 \sin 2\alpha_i + a_2 \cos 2\alpha_i, \tag{4.10}$$

$$a_0 = \frac{1}{2} I_0, \tag{4.11}$$

$$a_1 = \frac{1}{2} I_0 \sin\delta \cos 2\phi, \tag{4.12}$$

$$a_2 = -\frac{1}{2} I_0 \sin\delta \sin 2\phi. \tag{4.13}$$

Solving for the optical parameters of interest yields

$$I_0 = 2a_0, \tag{4.14}$$

$$\sin\delta = \frac{({a_1}^2 + {a_2}^2)^{\frac{1}{2}}}{a_0}, \tag{4.15}$$

$$\phi = \frac{\pi}{2} + \frac{1}{2}\mathrm{sgn}(a_2)\arccos\left[\frac{-a_1}{({a_1}^2 + {a_2}^2)^{\frac{1}{2}}}\right]. \tag{4.16}$$

One way to extract a_0, a_1, and a_2 from a series of images with varying α_i is to fit intensities in each pixel with Equation 4.14. However, this strategy is computationally intensive, especially when imaging over many pixels in a large field of view. Stepping α_i through N equal angles, we can exploit trigonometric properties to write the expressions below as a sum over the angles from $\alpha_1 = 180°/N$ to $\alpha_{\max} = 180°$:

$$a_0 = \frac{1}{N}\sum_{i=1}^{N} I_i, \tag{4.17}$$

$$a_1 = \frac{2}{N}\sum_{i=1}^{N} I_i \sin 2\alpha_i, \tag{4.18}$$

$$a_2 = \frac{2}{N}\sum_{i=1}^{N} I_i \cos 2\alpha_i, \tag{4.19}$$

$$\alpha_1 = 180°/N, \quad \alpha_{\max} = 180°. \tag{4.20}$$

Figures 4.7 and 4.8 include examples of this reconstruction procedure for $N = 18$ with Samples A and C.

4.2.5 Birefringence-to-stress model

In order to test the agreement between birefringence imaging and NV stress imaging, we use the photo-elastic equation to convert Δn to a stress (or strain) value. The stress and strain inhomogeneity through the diamond is linearly proportional to the Δn we measure [213–215].

Following these references, we assume an isotropic stress-optic coefficient, q_{iso}, and relate stress to Δn via

$$|\Delta n| \sim \frac{3}{4} n^3 q_{iso} \sigma \text{ and } |\Delta n| = \frac{|\delta|\lambda}{2\pi L}. \tag{4.21}$$

Here $q_{iso} \approx (q_{11} - q_{22}) \approx q_{44} = 0.301 \times 10^{-12}$ Pa^{-1} [215], $n = 2.42$ is the diamond refractive index [216], L is the diamond thickness, λ is the optical wavelength, and $|\delta|$ is magnitude of the optical retardance phase from $|\sin\delta|$.

Solving for σ yields

$$|\sigma| \sim \frac{2}{3\pi} \frac{|\delta|\lambda}{L n^3 q_{iso}}. \tag{4.22}$$

A phase accumulation of $|\delta| = \pi/2$ gives $|\sigma| \sim 85$ MPa, which is the maximum stress we can measure without order ambiguity for an optical path length of 500 μm.

Minimum detectable stress using birefringence imaging

The above method can yield a rough estimate for the minimum detectable stress using birefringence. A well-optimized system can detect down to $|\sin\delta| \approx 0.001$ [212]. This gives an approximate [213, 215] minimum stress detected using the isotropic photo-elastic constants and assuming a constant stress throughout the 500 μm thickness of diamond of ∼0.1 MPa. More generally, we can write this as 50 MPa· μm for an arbitrary optical path length through the sample thickness. This value is typically limited by optical element quality, optical alignment, and employed calibration schemes. In our birefringence imager we can detect a minimum of $|\sin\delta| \approx 0.005$, giving a minimum-detectable stress of 0.5 MPa (250 MPa· μm). This value is limited by the employed optical elements, LED illumination power, and residual misalignment of the circular analyzer.

4.2.6 Comparing birefringence and NV $M_{z,\kappa}$ measurements for Sample A

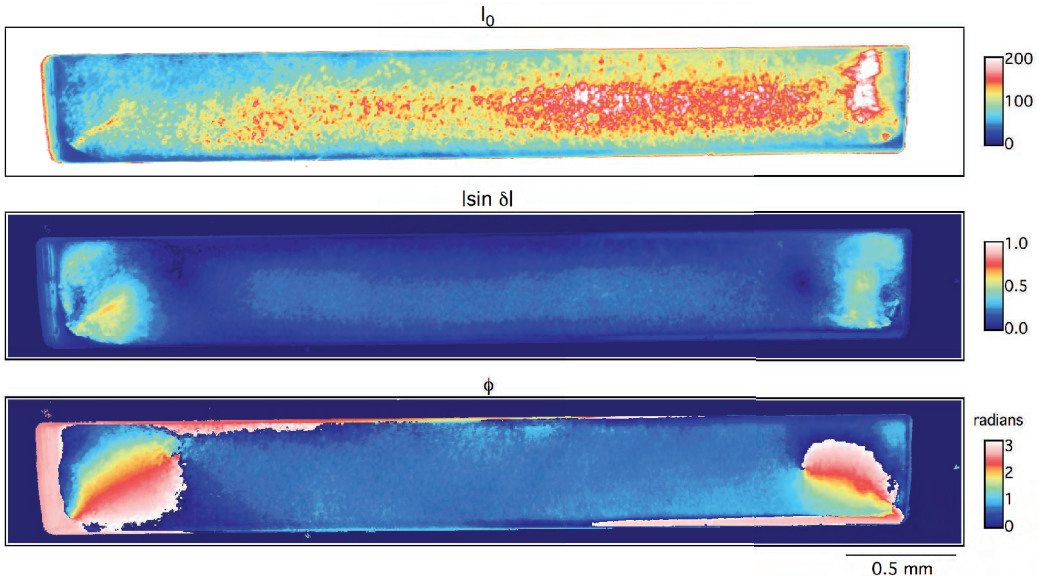

Figure 4.9: Birefringence maps measured through a side face of Sample A. The speckle in the transmission image is due to one of the edges of the diamond in the optical path not being polished. This limits what can be quantitatively said about the distribution of strain, however, sources can be roughly localized.

We used Sample A for a quantitative comparison of stress magnitudes generated using the NV $M_{z,\kappa}$ and optical birefringence methods. This sample contains regions which adequately fulfill the approximations needed for the rough isotropic model. It displays a relatively uniform spatial strain pattern in the X-Y imaging plane. Furthermore, Sample A is polished on its top and bottom faces and one of its side faces. This allows us to partially image its birefringence through the sides of the diamond. These measurements, shown in Figure 4.9, show a generally uniform depth distribution of strain in the center of the diamond, validating the use of the birefringence-to-stress approximate model above.

One of the current limitations of the birefringence method is order ambiguity in the measurement of $|\sin\delta|$. For high-strain regions, the accumulated phase difference through the sample thickness is greater than $\pi/2$, leading to ambiguity when calculating δ and stress

from $|\sin\delta|$. As described above, the maximum stress magnitude is ~85 MPa for $L = 500$ μm and $\lambda = 532$ nm (Equation 4.22). To unambiguously determine the stress magnitude from birefringence in samples with larger stress would require thinner (smaller L) samples or alternative methods [217]. An example of this type of phase ambiguity can be seen for a sample region of interest in Sample A shown in Figure 4.10 (the diagonal red stripe on the left side of the image) where $|\sin\delta|$ reaches its maximum value of 1 before decreasing in the middle of the stripe.

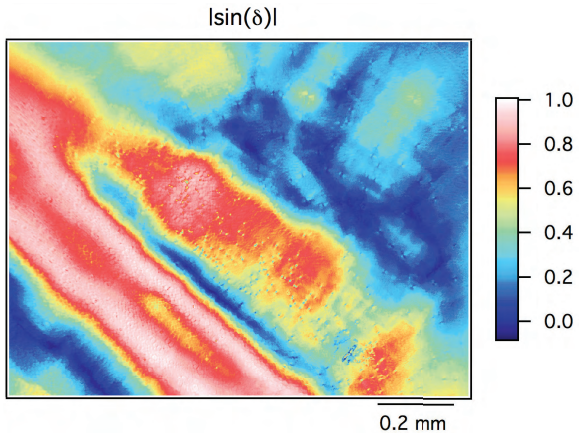

Figure 4.10: A $|\sin\delta|$ birefringence map for a diagonal stripe strain defect in Sample A. Despite the order ambiguity, the maximum stress measured using the birefringence and the $M_{z,\kappa}$ imaging techniques are consistent.

Figure 4.11 compares the birefringence map with the NV σ_{XY} map for a petal-shaped strain defect. The birefringence data is plotted as $\sin^{-1}(|\sin\delta)|$ to make all images linear in the strain amplitude. Although both images show a strain feature with four lobes, the shapes are qualitatively dissimilar, with one rotated 45° with respect to the other. The lobe orientations in the $|\sin\delta|$ map are consistent with a dislocation bundle [218]. In birefringence imaging and X-ray topography studies from Reference [206] dislocation bundles were found to diverge as they propagated through the diamond thickness. Such divergence may explain the difference in the spatial structure observed between the $|\sin\delta|$ map, which is integrated

over the full 500 μm thickness, and the σ_{XY} map, which shows stress in only the top 13 μm of the diamond (Figure 4.11). In addition to the large petal feature, we also observe smaller petal defects in the σ_{XY} maps that are not present in the birefringence maps. These features likely originate at the interface of the 13 μm thick N-doped layer with the diamond substrate; the short vertical extent of these features put them below the birefringence sensitivity limit.

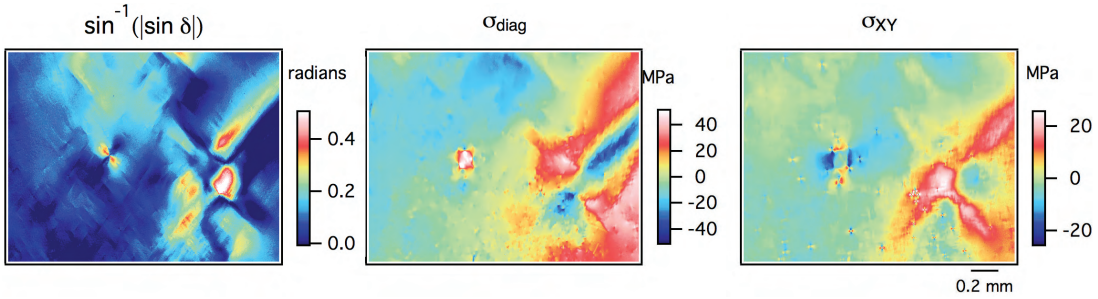

Figure 4.11: A zoomed-in region on Sample A showing a large petal-shaped defect originating from a dislocation bundle, imaged with birefringence and NV $M_{z,\kappa}$ imaging. The NV measurement is only sensitive to the stress in a 13 μm layer, and shows some smaller petal-shaped defects not observed the birefringence measurement.

Figures 4.6 and 4.11 shows a comparison between $\sin^{-1}|\sin\delta|$, σ_{diag}, and σ_{XY} maps collected using birefringence and NV stress imaging with the same diamond field of view. Despite the general similarity in results between the two methods, there are some stark differences. The σ_{XY} map shows petal-shaped strain features in the NV layer, whereas the birefringence map (which integrates phase retardance through the entire thickness) does not capture these fine details. Furthermore, the NV stress maps can distinguish that the diagonal stripe causing $M_{z,\kappa}$ inhomogeneity arises from σ_{diag} stress, while the petal-shaped strain features are caused by σ_{XY} stress. We can exploit such component-separated NV stress maps to investigate the sources and phenomenology of observed strain features.

Crystal strain and δ are linearly related through the diamond photo-elastic parameters [213, 219–221]. However, this relationship typically assumes uniform stress over the

optical path, meaning that the δ we measure is integrated over L even though the strain may be localized to one layer. By comparison, the NV $M_{z,\kappa}$ technique provides stress information localized to the NV layer, and converting from $M_{z,\kappa}$ to stress tensor elements is more straightforward.

Figure 4.6 illustrates an additional limitation for birefringence imaging. For high-strain regions, the integrated δ through the sample thickness may be greater than $\pi/2$, leading to ambiguity when calculating stress from $|\sin\delta|$ since multiple δ values can yield the same $|\sin\delta|$. This occurs in the middle of the stripe feature in Figure 4.6, where the reconstructed δ reaches its maximum value of $\pi/2$ before decreasing. NV stress imaging is not susceptible to this ambiguity. The NV σ_{diag} map instead shows that the stress amplitude increases to the middle of the stripe. Accounting for the extra $\sim \pi/4$ of phase accumulation in the birefringence map yields a maximum stress amplitude of ∼130 MPa, which is consistent with the 140 MPa maximum stress amplitude in the σ_{diag} map. Despite the $|\sin\delta|$ ambiguity, the NV and birefringence methods yield consistent stress measurements.

4.2.7 Technical comparisons between NV $M_{z,\kappa}$ imaging and birefringence imaging

Advantages of NV $M_{z,\kappa}$ imaging

Here we list technical advantages of NV $M_{z,\kappa}$ imaging over birefringence imaging.

1. An NV $M_{z,\kappa}$ imager measures the stress within the microscope depth-of-field, localizing the depth to within few micrometers in the optical diffraction limit or up to a few nanometers in a shallow nitrogen implant or delta-doped layer [75]. A birefringence imager integrates optical retardance through the entire diamond thickness (typically hundreds of micrometers), making depth information difficult to assess.

2. Since optical retardance increases with diamond thickness, birefringence imaging can be difficult for thin diamonds (30 μm thickness). Similarly, order ambiguity complicates analysis of birefringence measurements with thick diamond samples when $|\delta| > \pi/2$.

3. Extracting Δn and stress from a birefringence image requires knowledge of n and L. Other polarization effects like circular birefringence can lead to incorrect conclusions about the magnitude of the linear birefringence [222].

4. While a birefringence measurement is useful for qualitative comparisons and phenomenology, an NV $M_{z,\kappa}$ measurement is more quantitative and easier to interpret. Interpreting Δn information into an absolute stress or strain is model dependent [213].

5. With a birefringence imager, the extracted optical retardance depends on the illumination wavelength(s), polarizer orientations, and birefringence in other optical components or glass. An NV $M_{z,\kappa}$ imager avoids these complications, such that measured stress inhomogeneity maps should be independent of the fluorescence microscope employed.

6. Detecting whether a diamond is uniformly compressed or dilated with a birefringence measurement is challenging. An NV $M_{z,\kappa}$ measurement would see compression and dilation as a uniform shift of all four $M_{z,\kappa}$ parameters [223]. Similarly, while $M_{z,\kappa}$ images yield all shear stress terms, birefringence imaging is only sensitive to σ_{XY} shear terms (in the plane perpendicular to the optical axis) for a given measurement [224].

7. NV $M_{z,\kappa}$ imaging requires optical access from one polished side of the diamond. Birefringence imaging requires an uninterrupted optical path through the diamond, which may be impossible if the diamond is mounted on an opaque substrate or if the back

surface is too rough.

Advantages of birefringence imaging

In spite of the above drawbacks, birefringence imaging may be preferable under certain conditions discussed below.

1. Birefringence imaging is a faster experiment; it requires at minimum a single camera image (or a few images if using multiple waveplate orientations). An NV $M_{z,\kappa}$ measurement needs a few hundred camera images (roughly 50 microwave probe frequencies per NV frequency). In addition, obtaining a sufficient signal-to-noise ratio to fit the NV ODMR lineshape in each pixel usually requires averaging. This makes birefringence imaging useful for quickly characterizing diamond substrates.

2. A birefringence measurement has one main parameter to optimize before measuring: namely, the $\lambda/4$ waveplate and linear polarizer should be maintained at 45° with respect to one another. For an NV experiment, the laser polarization, microwave field, and bias magnetic field must all be optimized.

3. Just as strain inhomogeneity can complicate an NV magnetic microscopy experiment, magnetic field inhomogeneity can complicate an NV $M_{z,\kappa}$ experiment. A birefringence experiment is insensitive to magnetic fields.

4. NV $M_{z,\kappa}$ imaging is difficult in diamonds with low NV density, broad ODMR linewidths, or weak fluorescence contrast. One example of low-NV diamonds are the high-purity diamond samples used as substrates for growth of nitrogen-enriched layers. It is imperative that these seed diamonds contain low strain inhomogeneity, as strain defects tend to propagate into the nitrogen-enriched layer. Birefringence imaging is a more fitting choice to characterize strain in such high-purity diamonds.

5. In diamonds with a thick NV layer (compared to the microscope depth-of-field), fluorescence light from out-of-focus NVs can enter the microscope, complicating the ODMR $M_{z,\kappa}$ interpretation and potentially blurring the $M_{z,\kappa}$ map. This phenomenon is visible in Sample C, where the stress maps are blurred by the 40 μm NV layer when compared to the birefringence measurements.

4.3 Stress and NV magnetometry

NV $M_{z,\kappa}$ inhomogeneity causes each NV in an ensemble to have different resonance frequencies, which reduces the magnetic sensitivity and degrades NV magnetometer performance [21]. A useful NV-magnetometer figure of merit is the slope of the ODMR lineshape $|F'(f)|$, where f is the probe-microwave frequency and $F'(f)$ is the derivative of the NV fluorescence intensity at frequency f (Figure 4.3(B)). The maximum $|F'(f)|$ slope is proportional to the quantity C/Γ, where C is the fluorescence contrast and Γ is the resonance linewidth. $M_{z,\kappa}$ inhomogeneity reduces magnetic sensitivity by making the resonance lineshape broader, the contrast weaker, and thus the maximum slope $|F'(f)| \propto C/\Gamma$ smaller [21].

For NV-diamond magnetometers that use fewer probe microwave frequencies for improved magnetic sensitivity, $M_{z,\kappa}$ inhomogeneity is even more detrimental. High-sensitivity magnetometers [54] typically measure at two microwave frequencies (called the "two-point method" or "Lock-In ODMR") instead of probing the full width of the ODMR lineshape (the "full-sweep method") [1]. The two microwave frequencies are typically chosen to maximize the two-point responsivity (defined as the change in fluorescence per unit frequency shift of the NV resonance). If $M_{z,\kappa}$ varies substantially over the field of view, no pair of frequencies can be optimal for all NVs, resulting in decreased sensitivity for many pixels in the magnetic image. A larger variation in $M_{z,\kappa}$ across the ensemble also implies a narrower

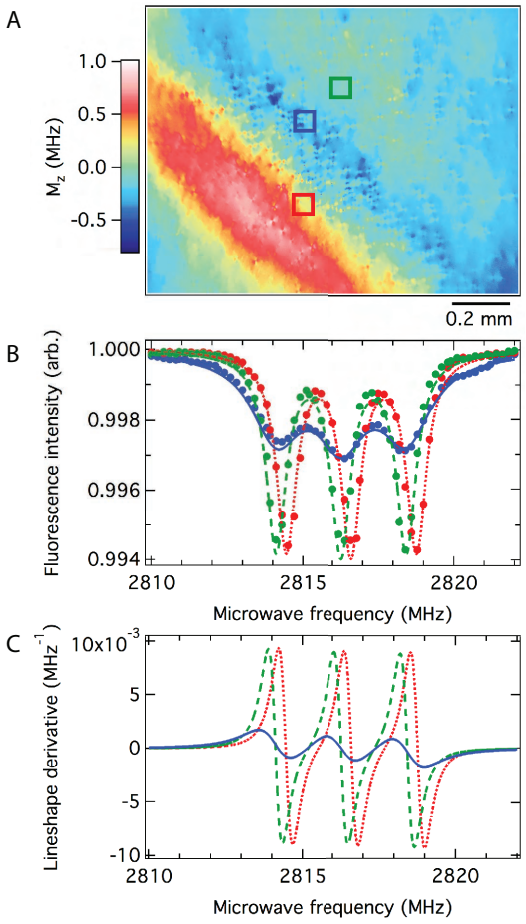

Figure 4.12: (A) Zoomed-in $M_{z,\kappa}$ map (lower-left corner of Figure 4.5), showing the locations of the example pixels. (B) Fitted ODMR spectra for example pixels (i), (ii), and (iii) (green, red, and blue, respectively). Each has varying $M_{z,\kappa}$ gradients and offsets. (C) Derivatives $F'(f)$ for the ODMR lineshapes plotted in (b). Pixel (i) has the best C/Γ slope and two-point responsivity, while pixel (ii) has poor C/Γ slope and two-point responsivity due to the high $M_{z,\kappa}$ inhomogeneity in this pixel. Pixel (iii) has a good C/Γ slope but a poor two-point responsivity, since the $M_{z,\kappa}$ offset means we probe this pixel at a sub-optimal microwave frequencies compared to the others.

magnetic-field range before the NVs in some pixels fall out of resonance. As such, $M_{z,\kappa}$ inhomogeneity limits the field of view and dynamic range of high-sensitivity NV magnetic imagers.

Figure 4.12 shows a zoomed-in $M_{z,\kappa}$ map together with single-pixel ODMR spectra

corresponding to regions of Sample A with different local strain properties. For example, one pixel shows a region with a low $M_{z,\kappa}$ gradient and offset from the mean (i); a second pixel shows a region with a low $M_{z,\kappa}$ gradient and a high $M_{z,\kappa}$ offset (ii); and a third pixel shows a region with a high $M_{z,\kappa}$ gradient and a low $M_{z,\kappa}$ offset (iii). These local strain conditions are caused by a ∼0.3 MHz $M_{z,\kappa}$ offset in the diagonal stripe and high $M_{z,\kappa}$ variation in the ∼30 μm petal defects. Pixels (i) and (ii) have a comparable C/Γ slope and therefore a comparable NV magnetic sensitivity when using the full-sweep method. However, when using the two-point method optimized for pixel (i), pixel (ii) will have a poor responsivity due to its large $M_{z,\kappa}$ offset. By comparison, pixel (iii) will exhibit poor performance with both methods. As these example pixels demonstrate, $M_{z,\kappa}$ inhomogeneity reduces the magnitude and uniformity of the magnetic sensitivity across an image.

As shown in Figure 4.13, $M_{z,\kappa}$ gradients can also distort the single-pixel ODMR spectra, making lineshape fitting more difficult. For large gradients, the Lorentzian fit functions we use to extract the ODMR center frequencies may not describe the $M_{z,\kappa}$-broadened lineshapes accurately, potentially causing strain features to appear as systematic errors in the magnetic images. The strain gradients within each pixel in Sample C lead to worse fit residuals (suggesting that a Lorentzian fit function is not the best choice), and also cause lineshape broadening. Ideally the single-pixel $M_{z,\kappa}$ inhomogeneity should be small compared to the other factors that determine the NV resonance linewidth (magnetic inhomogeneity, microwave field strength, and laser intensity), which is often ∼0.5 to 1 MHz full width at half maximum.

4.3.1 Strain feature survey and effects on NV magnetometry

We used NV $M_{z,\kappa}$ imaging to study and categorize different types of strain features in diamond samples. As shown in the regions highlighted in Figure 4.14, different types of

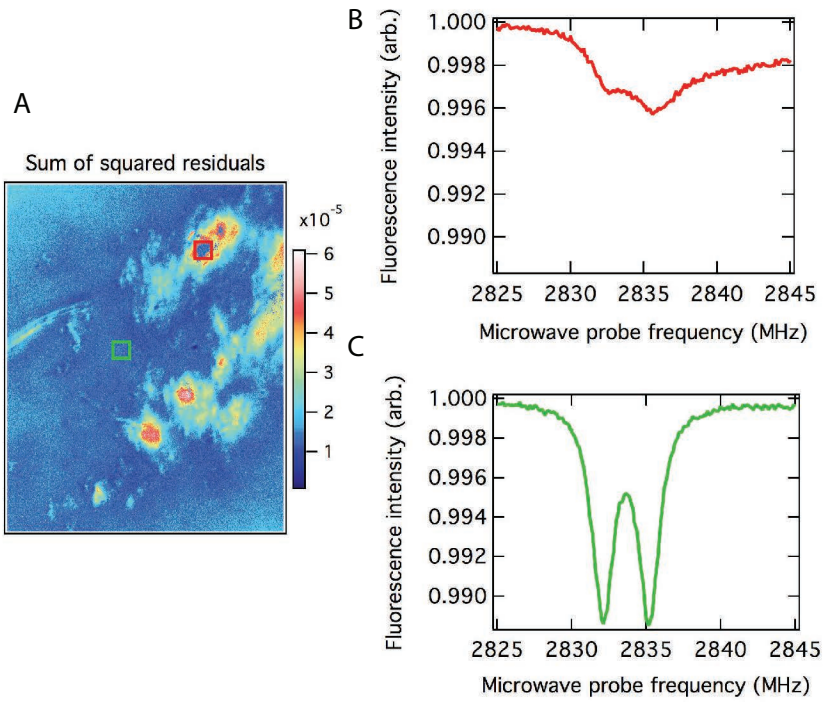

Figure 4.13: (A) Sum of squared residuals for a region of Sample C. (B)-(C) ODMR lineshapes for the $m = 0$ to -1 transition for a high-strain (red) and low-strain (green) region. The locations of these regions within the image are represented in (A) with red and green boxes. In addition to causing lineshape broadening, the strain gradient in each pixel leads to worse fit residuals. Each NV resonance is split into two lines due to hyperfine interactions with the spin-1/2 ^{15}N nucleus.

strain features have a variety of typical dimensions, $M_{z,\kappa}$ amplitudes and gradients, and stress tensor contributions. From our $M_{z,\kappa}$ maps, we categorized strain features into general types. We identified how each type impacts the C/Γ slope and two-point responsivity. Here we concentrate on strain features observed in Sample A, but more examples can be seen in the Appendix.

Figure 4.14(A) shows the same field of view as in Figure 4.12. The broad-scale plastic deformation in the diagonal stripe is perhaps associated with the lower-left corner of the diamond sample, as high stress is common at sharp corners, edges, and fractures. The stress from the diagonal stripe is largely σ_{diag} stress, causing millimeter-scale $M_{z,\kappa}$ gradients,

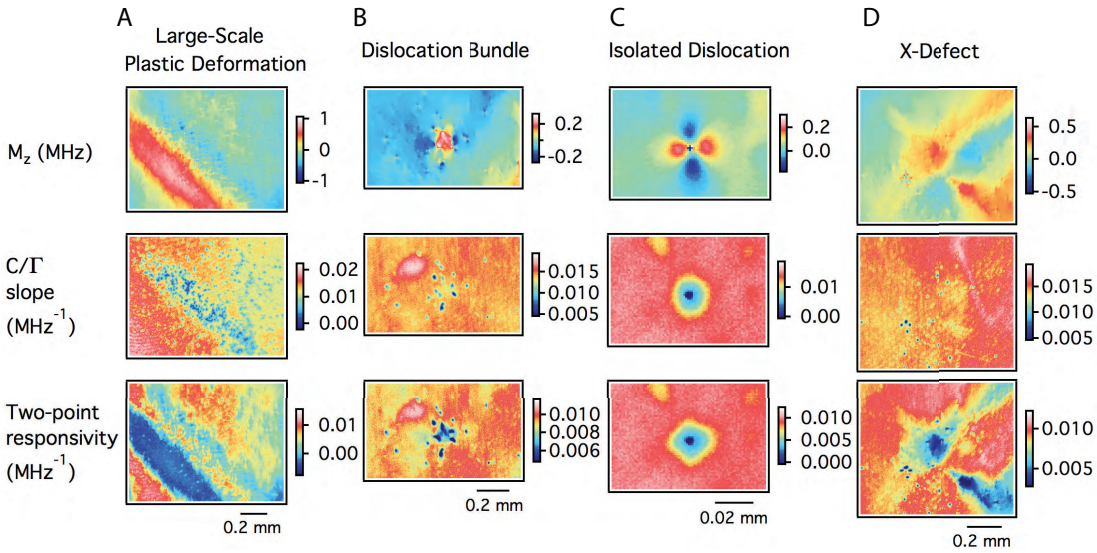

Figure 4.14: Comparisons between $M_{z,\kappa}$, C/Γ slope, and two-point responsivity for common strain feature types found in Sample A. The C/Γ and responsivity maps are related to the magnetic microscopy performance when using the full-sweep method and the two-point method, respectively. Note that the two-point responsivity is more susceptible to $M_{z,\kappa}$ inhomogeneity, while the full-sweep method can tolerate some range of $M_{z,\kappa}$ offsets.

resulting in a wide span in NV resonance frequencies (∼1 MHz). As anticipated, the diagonal stripe spoils the two-point responsivity while the full-sweep C/Γ slope is largely unaffected. In this example the $M_{z,\kappa}$ span is large enough to cause a negative responsivity in the diagonal stripe, as the resonance frequency is offset far enough that one of the probe frequencies is on the opposite side of its resonance peak.

The 20-30 μm petal-shaped strain defects in Figure 4.14(A) and Figure 4.6 are caused by lattice dislocations that can form on top of the seed crystal during homoepitaxial growth, as studied in previous work [206, 210, 225–227]. The three types of lattice dislocations (edge, screw, and mixed dislocations) contribute to different crystal stress terms [228]. The petal features appear most strongly in the σ_{diag} and σ_{XY} maps (and to a lesser degree in the σ_{XZ} and σ_{YZ} maps), which suggests that the petal-shaped strain features we observed are predominantly caused by edge and mixed dislocations.

Figure 4.14(B) shows a ∼200 µm strain feature (likely caused by a dislocation bundle), surrounded by smaller petal-shaped defects. From birefringence imaging, we know that such strain features are typically edge dislocations (with σ_{diag} and σ_{XY} stress). They often have four quadrants with lines emanating from the center along the [001] and [010] directions, and are a few hundred micrometers across [218]. The lobes appearing in the σ_{diag} and σ_{XY} NV stress maps are rotated by 45°. These characteristics lead us to conclude that this strain feature is a dislocation bundle. For this particular strain feature, the range of $M_{z,\kappa}$ values is narrow enough that it has only a minor effect on NV magnetometry performance for both the full-sweep and two-point methods.

Figure 4.14(C) shows a prominent ∼30 µm dislocation strain feature. Here the single-pixel $M_{z,\kappa}$ gradients are substantial enough to spoil the NV magnetic sensitivity of both methods. Severe $M_{z,\kappa}$ gradients also interfere when fitting the ODMR spectra to a Lorentzian lineshape model, introducing systematic errors in the extracted resonance frequencies.

Figure 4.14(D) shows a ∼0.8 mm X-shaped strain feature. Though visually most similar to the petal-shaped strain features discussed above, X-shaped strain features are larger, display sharp edges pointing along the diamond [100] and [010] directions, and have no lobe structures. The X-shaped strain features also exhibit mainly σ_{diag} and σ_{XY} stress (like an edge dislocation), whereas the σ_{XZ} and σ_{YZ} values are nearly zero. Despite the similarities to the previously-discussed strain features, the origin of the X-shaped strain features remains under investigation, but is likely due to propagation of growth boundaries from the substrate. They mainly affect the two-point responsivity for NV magnetometry, whereas the full-sweep C/Γ slope is mostly immune due to the small strain gradients.

4.3.2 Improved Strain in Bulk CVD Samples

Following the development of the techniques above, we collaborated with Element Six and Lockheed Martin on the development of improved bulk ensemble high NV density diamond samples [201] and procedures that could scale to translate to optimizations in different regimes. One metric of interest was control and homogenization of the bulk strain distribution in these diamonds. To mitigate potential strain issues, CVD substrates and pre-synthesis etches were carefully controlled to minimise the density of dislocations present in the high-[N] material grown, according to the methods previously identified in the literature [206]. Deposition conditions were also controlled for the duration of the growth runs to avoid the formation of non-epitaxial crystallites.

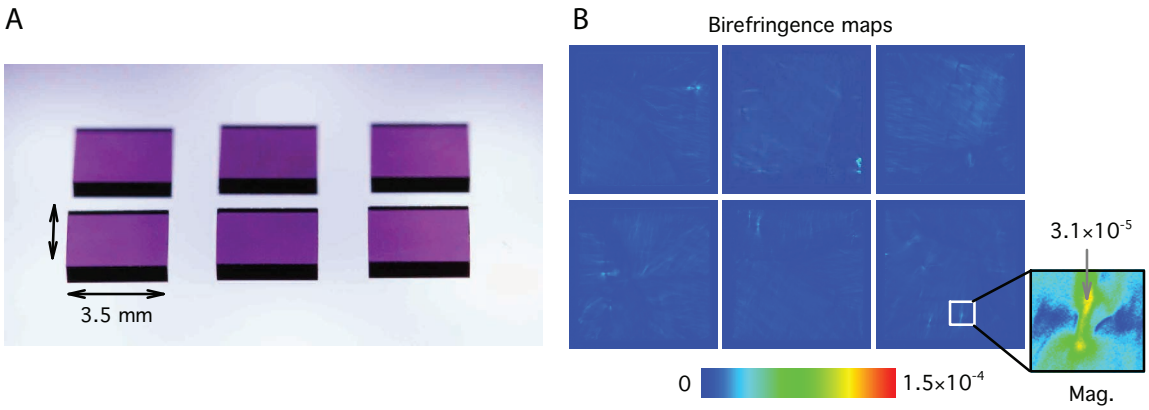

Figure 4.15: (A) Photograph of 6 samples (0.005% ^{13}C) with approximately 900 µm thickness, after irradiation and annealing to create ≈ 3.8 ppm [NV]. (B) Birefringence images of the plates in (A) as measured on a Metripol microscope.

To characterise the success of these simple strain mitigation strategies, the birefringence and NV^- spin properties were studied. These measurements employed two 100 µm-thick freestanding plates produced from a sample grown with ^{13}C depleted to 0.005 % and subsequently irradiated and annealed. This thickness was chosen to improve the planar spatial resolution of CW-OMDR-based imaging and reduce inhomogeneities in the applied

magnetic, optical, and MW control fields.

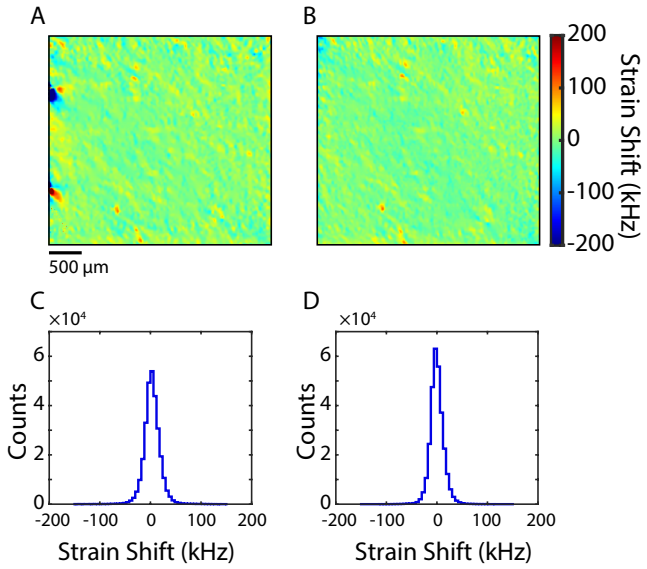

Figure 4.16: (A) Map of extracted strain-induced NV resonance shifts for a $(3.6\times3.6\times0.1)\,\mathrm{mm}^3$ freestanding plate produced from a thicker sample. (B) Map of extracted strain-induced NV resonance shifts for a second freestanding plate produced from a different portion of the sample used to produce the plate shown in (A). (C,D) Histograms of the strain shift values shown in (A) and (B), respectively.

The strain environment of each sample was first characterised using Metripol birefringence imaging and representative images are shown in figure 4.15(B). In these samples, an average birefringence $\Delta n \approx 7(1)\times10^{-6}$ was determined with peak values of $\Delta n \sim 3\times10^{-5}$ in isolated petal features (see inset of figure 4.15(B) for an example). A vast majority (>99%) of the pixel values within the birefringence image, figure 4.15(B), satisfy $\Delta n \lesssim 10^{-5}$, the standard for ultra-low birefringence diamond [206].

In order to verify the birefringence measurements and ensure the homogeneity of the strain environment, NV-based strain measurements were performed. Due to the thickness of the diamond substrate limiting spatial resolution [1, 31], NV strain shift measurements are only advantageous for probing the strain environment for length scales larger than the

thickness of the diamond, 100 µm. Maps of these shifts for the two samples are shown in figures 4.16(A,B) and histograms of the measured shifts are shown in figures 4.16(C,D), respectively. Both samples exhibit minimal strain inhomogeneity with a distribution in strain-induced shifts of approximately 25 kHz full-width half-maximum (FWHM). These measurements demonstrate lower levels strain control in these CVD process relative to previous thin-layer samples shown in the previous sections for typical examples of N-doped CVD diamond layers, with strain-induced shifts on the order of hundreds of kHz to MHz). The shared spatial variations in the strain inhomogeneity between figure 4.16(A) and 4.16(B) are a consequence of the two samples being cut from the same original diamond sample (particularly visible along the bottom edges of the diamond plates).

4.3.3 Improved Strain in N-Doped Layer CVD Samples

Following the success of controlling strain in bulk, high NV density samples, similar methods were applied to a new iteration of N-doped layer diamonds. The introduction of the N-doped layer introduces complications due to the proximity to a growth interface (see Figure 4.1), which can increase the density of dislocation defects depending on the surface preparation [206]. Furthermore, due the need to preserve a well-defined layer some methods like post-growth HPHT treatment of the diamond to homogenize [56] are not applicable.

Utilizing a similar protocol as the bulk diamonds above [201], these newer diamonds have a 1.7 μm layer of 17 ppm ^{15}N, irradiated and annealed to create 1-2 ppm of NV. Better surface control was maintained for these samples in the preparation and growth, enabling improved strain in these layers (see Figures 4.17 and 4.18) compared to the previous diamonds (see Figure 4.5). Initially, the M_z strain maps were acquired with a 4x objective in the same setup (Figure 4.2). The homogeneity of the strain of the field of view was significantly improved compared to previously measured samples (see Figure 4.5 and Appendix).

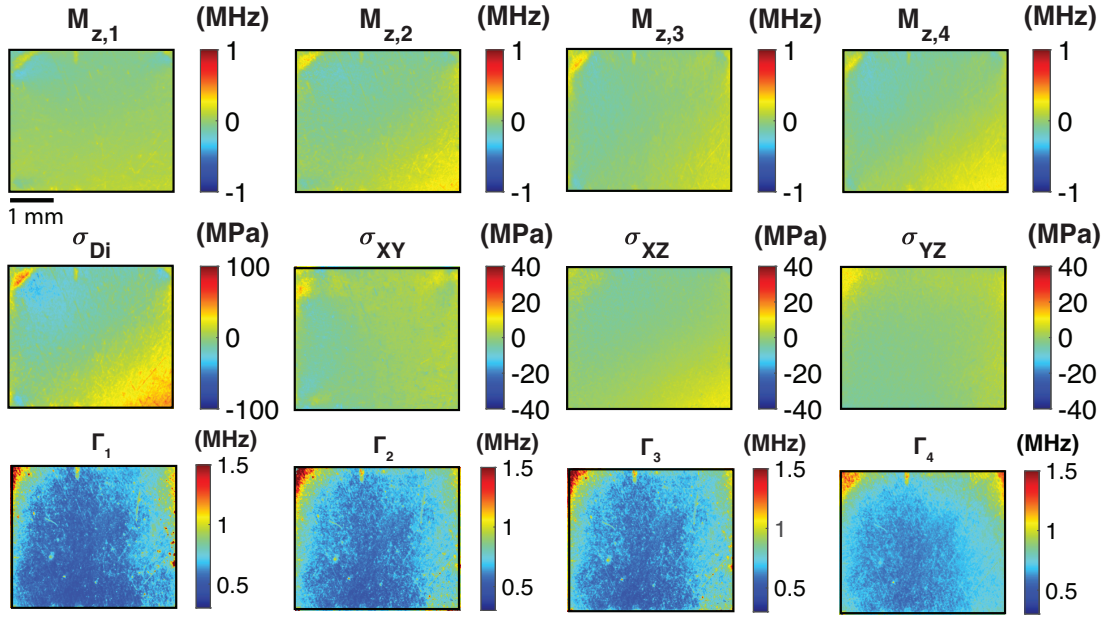

Figure 4.17: Widefield (4× objective) NV strain images of improved thin layer ($\sim$ 1.7 µm) diamond. Features are plotted on the same scale bars as Figure 4.5 to illustrate the improvement in strain control with the latest iteration of samples. The ODMR linewidth reveals the presence of subtle strain features through local broadening.

Given the thinness of the NV layer compared to past samples available, this sample was better optimized for characterizing the small length-scale strain variations in diamond. The first indication of the presence of smaller scale strain variations was inhomogeneity of the ODMR linewidth. Generally the ODMR linewidth is most strongly impacted by inhomogenous MW fields over the field of view (part of this can be seen on the edges of the diamond in Figure 4.17). However, for the experimental setup a large enough MW loop was used where in the center of the diamond, the ODMR broadening was limited by NV-N (assumed to be homogeneous) and the spatially varying features are due to strain gradients over the measurement pixel (see Figure 4.14).

These observations of smaller scale phenomena motivated switching to a higher magnification objective (20x) to more effectively resolve the small scale phenomena and minimize

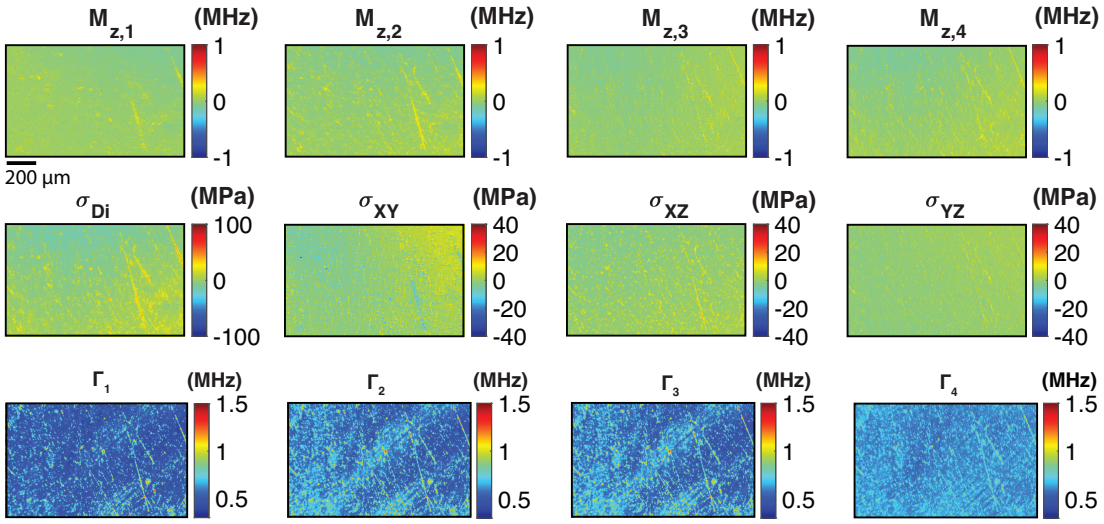

Figure 4.18: Widefield (20× objective) NV strain images of improved thin layer ($\sim$ 1 µm) diamond. Some of the remnant features on this short length scales are due to polishing damage in the diamond substrate [206] and cause local strain inhomogeneities. There are even smaller dislocations apparent as small dots in the linewidth images.

gradients over a given pixel. On even smaller length scales the strain environment was favorable compared to previous samples (Figure 4.6) and the predominant features in the M_z maps are scratches due to polishing damage. However, in the linewidth maps, on top of the broadening due to the polishing damage, there appear to be dislocations and strain on even smaller length scales. Probing strain on these smaller length scales is an ongoing area of effort and we are actively undertaking measurements to characterize the sub-micron strain environment for (i) further optimization of diamond growth and NV formation and (ii) characterizing the background environment for projects that seek to use strain in the diamond lattice as a directional detector of dark matter [203].

4.4 Ensemble Charge State Characterization and Control

As mentioned in Chapter 1, the nitrogen vacancy defect in diamond occurs predominantly in one of two charge states, NV^0 and NV^- [229]. The exact ratio and distribution of the different NV charge states in ensemble diamonds can dependent on a variety of factors including local defect environment (nitrogen donors or other defects that act as charge donors or charge traps) [77, 202, 230–233] and the properties of the illumination source [77, 84, 202, 234, 235] among many other conditions. The NV charge state is of significance due to the contribution of charge state to measurement contrast. Measurement contrast is linearly related to shot-noise limited magnetic sensitivity [56] for all measurement modalities (CW ODMR, Ramsey, Hahn Echo, CPMG, etc.) explored in this work. Thus any parameter that degrades contrast will be maximally detrimental to sensing effort and should be understood and controlled. Conventionally the NV charge state is measured through techniques like Fourier transform infrared spectroscopy (FTIR) [236], ultraviolet-visible spectroscopy (UV-Vis), or electron paramagnetic resonance (EPR) [237,238]. However, these methods are typically not performed under representative magnetic sensing conditions (laser power, microwave power, bias magnetic field, temperature, etc.) and will not necessarily be predictive of the expected charge state during a magnetometry experiment [56]. This section focuses on the development of a measurement protocol that enables *in-situ* characterization of the NV charge state under nominal sensing conditions, the insights these experiments afford, and ongoing efforts to improve the NV charge state under sensing conditions.

4.4.1 Charge State Measurement Technique

At room temperature, the photoluminescence spectrum from NV^0 and NV^- centers are overlapping, making it difficult to determine the ratio of charge states from the photoluminescence spectrum alone (Figure 4.19). A general technique is required to determine the

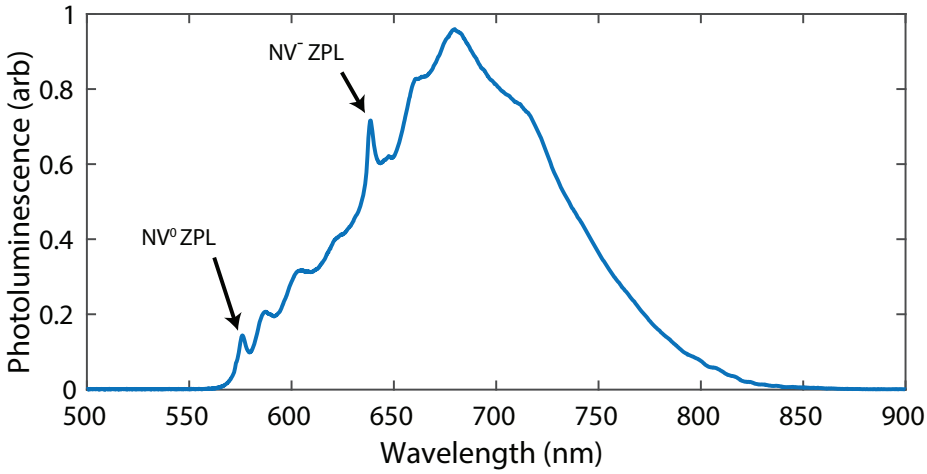

Figure 4.19: Example ensemble photoluminescence (PL) spectrum. The PL distribution from the NV^0 defects overlap with the PL distribution from the NV^- defects making it challenging to determine the total amount of photoluminescence from each charge state.

charge state from the PL spectrum that does not rely on fitting to universal or representative NV^0 and NV^- basis functions. This general method would allow for the determination of NV charge state under a wide variety of conditions and be robust to temperature [239], illumination properties [56,202], and local strain [240], which can modify the shape of the PL spectrum. Given these needs, we developed a microwave assisted spectroscopy technique to determine the steady-state charge state in an NV ensemble [80]. This technique utilizes the existing experimental infrastructure (laser source and microwave driving) within most NV experimental setups to determine the charge state basis functions. Once the representative basis functions are known, we can decompose the measured experimental photoluminescence into its constituent NV^0 and NV^- components.

4.4.2 Experimental Method

The total photoluminescence spectrum is composed of an assumed NV^- basis function (for the given experimental conditions) times some scaling factor a_{NV^-} plus an assumed basis

NV^0 basis function times another scaling factor a_{NV^0} (see Equation 4.23).

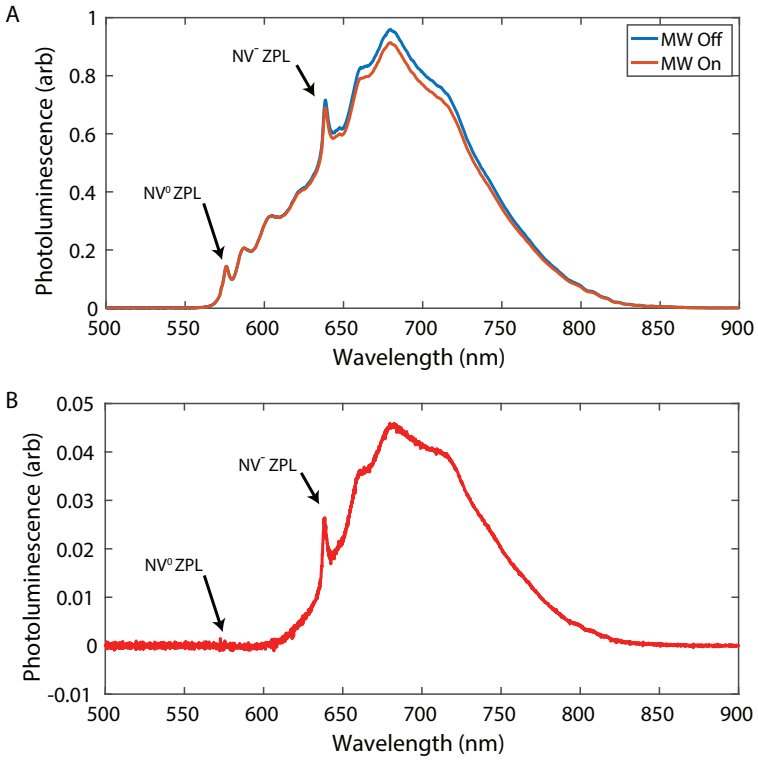

Figure 4.20: (A) Example ensemble photoluminescence (PL) spectrum with the microwaves Off (Blue) and microwaves On (Orange.) (B) The MWs selectively modulate the NV^- photoluminescence. The difference spectrum (MW Off - MW on, Red) shows that the predominant feature left is the NV^- spectrum.

$$PL_{\text{MW Off}}(\lambda) = a_{NV^-} PL_{NV^-}(\lambda) + a_{NV^0} PL_{NV^0}(\lambda) \tag{4.23}$$

The PL ratio (Ξ_{PL}) of the charge states can be determined through the ratio of the area under each curve for each charge state.

$$\Xi_{PL} = \frac{\sum_\lambda a_{NV^-} PL_{NV^-}(\lambda)}{\sum_\lambda a_{NV^0} PL_{NV^0}(\lambda)} \tag{4.24}$$

The PL fraction (Ψ_{PL}) is also defined to give a sense of the what fraction of NVs are in the negative charge state, which is the relevant metric for mapping charge state

photoluminescence ratio degradation to measurement contrast degradation.

$$\Psi_{PL} = \frac{\sum_\lambda a_{\mathrm{NV^-}} PL_{\mathrm{NV^-}}(\lambda)}{\sum_\lambda a_{\mathrm{NV^0}} PL_{\mathrm{NV^0}}(\lambda) + \sum_\lambda a_{\mathrm{NV^-}} PL_{\mathrm{NV^-}}(\lambda)} \tag{4.25}$$

In order to connect back to growth parameters, the charge state concentration ratio needs to be calculated from the photoluminescence ratios. Given that the NV^- excited state lifetime in bulk diamonds, $\tau_{\mathrm{NV^-}} = 8\ ns$ [241], is shorter than the NV^0 [241] lifetime, $\tau_{\mathrm{NV^0}} = 20\ ns$, these photoluminescence ratios are modified by the ratio of luminescence lifetimes, $\alpha \sim \frac{20\ ns}{8\ ns} = 2.5$ to get the charge state concentration ratio $\Xi_{Charge} = \frac{[\mathrm{NV^-}]}{[\mathrm{NV^0}]} = \frac{1}{\alpha}\Xi_{PL}$. The correction for the charge fraction is similar, $\Psi_{Charge} = \frac{[\mathrm{NV^-}]}{[\mathrm{NV^0}]+[\mathrm{NV^-}]} = \frac{1}{1+\alpha/\Xi_{PL}}$. This lifetime dependent correction factor needs to be modified for more accurate concentration ratios depending on the excitation wavelength [241] and type of diamond being studied [242].

Resonant CW MWs are applied to selectively modulate the NV^- photoluminescence by an amount C (see Equation 4.26 and Figure 4.20), which depends on the MW power and detuning. This process is complicated by the presence of spin-dependent ionization [80], characterized by C_{SI}, but this effect generally has marginal consequence on the final result. The dominant contribution of NV^- PL in the difference spectra is apparent in Figure 4.20(B).

$$PL_{\mathrm{MW\ On}}(\lambda) = (a_{\mathrm{NV^-}} - C)PL_{\mathrm{NV^-}}(\lambda) + (a_{\mathrm{NV^0}} - C_{SI})PL_{\mathrm{NV^0}}(\lambda) \tag{4.26}$$

The PL difference spectrum due to the application of resonant MWs is defined as:

$$PL_{\mathrm{Diff}}(\lambda) = PL_{\mathrm{MW\ Off}}(\lambda) - PL_{\mathrm{MW\ On}}(\lambda) = C\ PL_{\mathrm{NV^-}}(\lambda) + C_{SI}\ PL_{textNV^0}(\lambda) \tag{4.27}$$

where $C \gg |C_{SI}|$.

Finding the NV^0 Basis

Starting from the difference spectrum (Equation 4.27 and Figure 4.20), the NV^0 basis function is found by finding a scale factor, S_{NV^0}, such that ($PL_{NV^0} = PL_{\text{MW Off}} - S_{NV^0} PL_{\text{Diff}}$) is orthogonal to the NV^- spectrum. However, we need a good metric or guide star for when there is no longer contributions from NV^- in the spectrum. Fortunately, the NV^- zero phonon line (see Figure 4.19) is a stable, sharp feature that is a defining feature of the NV^- spectrum.

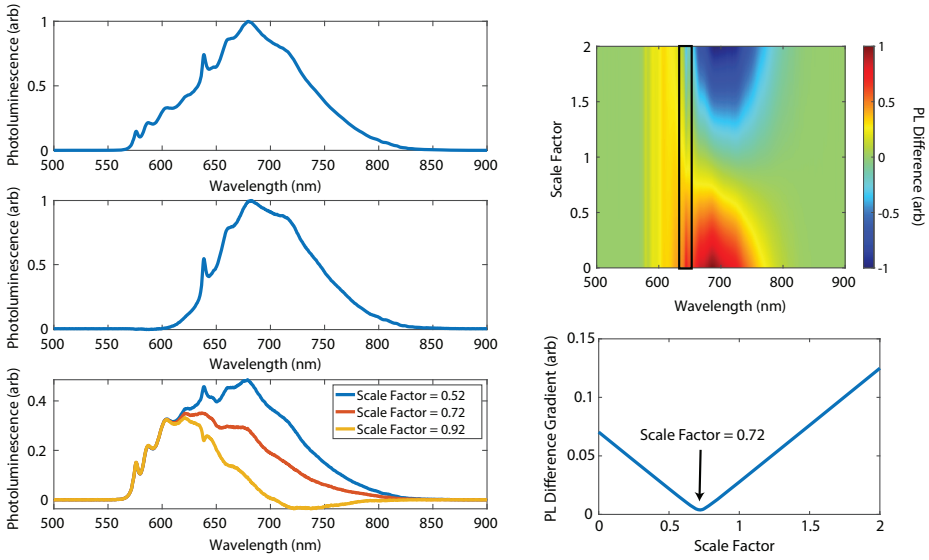

Figure 4.21: Determination of the correct NV^0 basis spectrum. Starting from the MW Off spectrum and the difference spectrum, a series of candidate NV^0 basis functions are calculated by sweeping over a wide range of scale factors, S_{NV^0}.

The optimal scale factor, S_{NV^0}, is found (Figure 4.21) through a numerical optimization process where many different values of S_{NV^0} are sampled and the proposed NV^--free spectrum is analyzed for each values. If the value of S_{NV^0} is too small, then not enough of the NV^- spectrum is removed and the NV^- ZPL is visible. If S_{NV^0} is too larger, then too much of the NV^- spectrum is removed, and a negative dip at the NV^- ZPL is created. The optimal scale factor is found by evaluating the two-dimensional gradient of these proposed

difference spectra averaged over the NV^- wavelengths ($\sim$ 630-645 nm, black box in Figure 4.21) and finding the scale factor that minimizes the local gradient. Once the optimal scale factor has been found, then a pure representation of the NV^0, is also known.

Finding the NV^- Basis

Once PL_{NV^0} has been found, a similar process (see Figure 4.22) as above is applied to find the correct scale factor for determining the correct NV^- basis. (This step is needed because of the spin dependent ionization that causes NV^0 PL information to leak into the MW difference signal.) The scale factor, S_{NV^-}, such that $PL_{NV^-} = PL_{\text{MW Off}} - S_{NV^-}PL_{NV^0}$ has no NV^0 characteristic to it needs to be found.

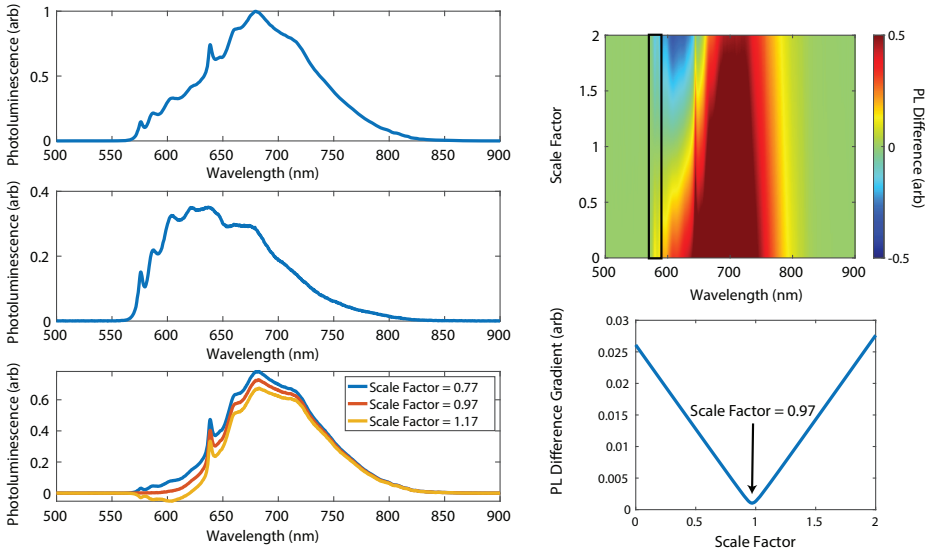

Figure 4.22: Determination of the correct NV^- basis spectrum. Starting from the MW Off spectrum and the difference spectrum, a series of candidate NV^- basis functions are calculated by sweeping over a wide range of scale factors, S_{NV^-}.

The only difference between this step and the previous process to find the NV^0 basis is that the local gradient of the proposed difference spectra is averaged over wavelengths in the vicinity of the NV^0 ZPL (570 nm to 580 nm). Once the correct scale factor S_{NV^-} has been

found, then both the pure NV^0 and NV^- PL spectrum are known, and the experimental spectrum can be decomposed.

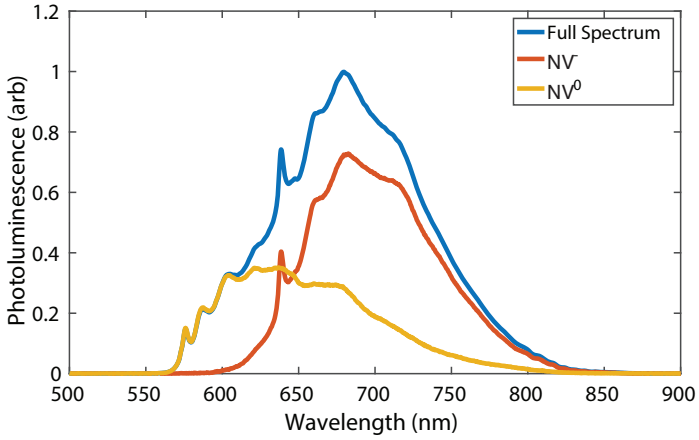

Figure 4.23: Displaying the decomposition of the full PL spectrum into the NV^- component and the NV^0 component.

PL Ratio (Ξ_{PL})	PL Fraction (Ψ_{PL})	Charge Ratio (Ξ_{Charge})	Charge Fraction (Ψ_{Charge})
1.70	0.63	0.68	0.40

Table 4.3: Summary of different parameters used for describing the charge state properties of the diamond for an assumed correction factor, $\alpha = 2.5$.

Once the PL spectra are known then the different summary parameters (PL Ratio, PL Fraction, Charge Ratio, and Charge Fraction) can be calculated using the previously defined equations for Ξ_{PL}, Ψ_{PL}, Ξ_{Charge}, and Ψ_{Charge}. From these results, the value of looking at both the PL metrics and charge metrics can be seen. More than half (~63%) of the PL coming from the diamond is NV^-, but less than half of the actual NVs in the diamond are NV^-.

4.4.3 Impact of Charge State on Sensing Parameters

Following the determination of a representative NV^0 and NV^- basis, we can use these representative spectra in numerical simulations to understand how different charge state ratios would impact future measurements and the dependence on experimental choices, such as long pass filter cut-off wavelength. Long pass filters on the collection side of the optics are utilized to (i) block green excitation beam from hitting the sensor and (ii) minimize the degradation of measurement contrast due to NV^0 PL.

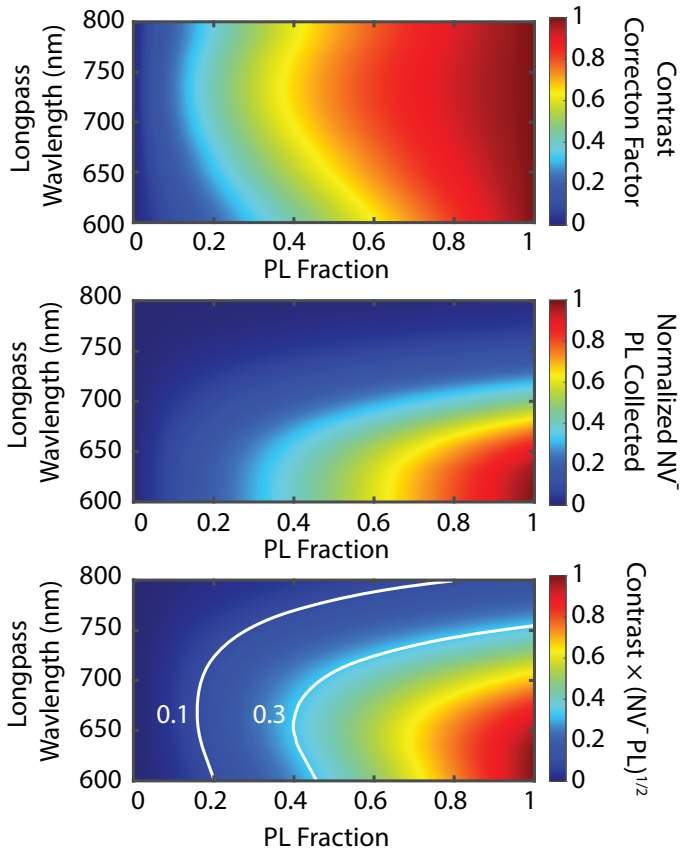

Figure 4.24: Numerical simulations to determine the influence of the PL fraction on measurement contrast and amount of NV^- PL collected as a function of the long pass filter.

The optimal cut-off wavelength for the filter depends on the charge state ratio. For

example, in an idealized scenario with the diamond containing 100% NV^-, a shorter cut-off wavelength would be wanted on the longpass filter to maximize the amount of red photons collected. However, in the opposite scenario, where the diamond is almost entirely (99.9%) NV^0, then a longer wavelength cutoff would be used to maximize collection at the tail of the NV^- spectrum. For cases in between, there is a balancing game between optimizing measurement contrast and not wasting signal carrying photons, which is explored in greater depth below.

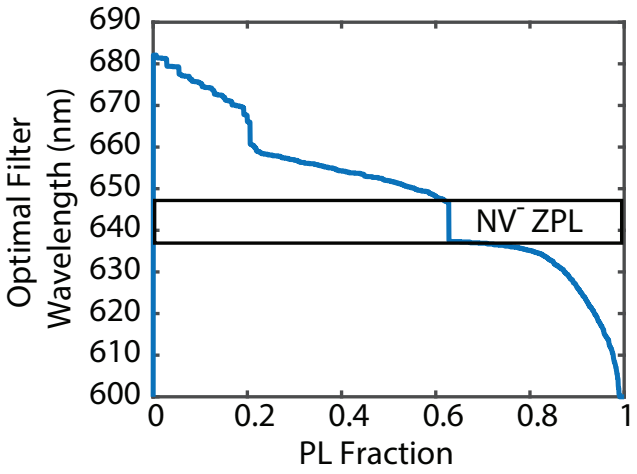

Figure 4.25: Optimal longpass optical filter cutoff wavelength for each PL fraction.

We performed numerical simulations to determine the effect of PL fraction and longpass wavelength cut-off on measurement sensitivity. The PL spectra determined above are used as the basis functions. Instead of the collected PL being defined as $\sum_\lambda (a_{NV^-} PL_{NV^-} + a_{NV^0} PL_{NV^0})$, the longpass filter modifies the function to become $\sum_{\lambda_{cut}}^{\infty} (a_{NV^-} PL_{NV^-} + a_{NV^0} PL_{textNV^0})$. Figure 4.24 illustrates the detrimental effect of charge state on achievable measurement performance where sensitivity can be degraded by a factor of $\sim$10 in the low PL fraction limit. For each PL fraction, the longpass filter wavelength, which maximizes the sensitivity metric $C \times \sqrt{\sum NV^- PL}$ is plotted. The results matches the intuition mentioned

previously. For very high PL fractions, where most of the light is NV^-, low cut-off wavelengths should be used to maximize the NV^- signal. There is a jump near a PL fraction of 0.6 where the optimal wavelength is in the vicinity of the NV^- ZPL. The non-monotonic response of the PL in this region causes the sharp jump. This sensitivity degradation, even when utilizing a near optimal filter, is a likely culprit in the limited sensitivity in the Ramsey Imaging experiments in Chapter 6.

4.4.4 Power Dependence

In an experimental setup, two parameters largely determine the ratio of the different charge states: (i) the laser power (intensity) used and (ii) diamond properties (neutral substitutional nitrogen: $[N_s^0]$ and concentration of charge traps) [202]. This section will primarily focus on the laser power dependence and the implications for the experimental setups in Chapter 6.

The charge state decomposition method was utilized to understand the role of laser excitation intensity on the stability of the NV charge state. The instability of the charge state has been previously documented [77, 202], but the diamonds utilized predominantly in these studies had much higher nitrogen concentration, which is likely to improve the NV charge state stability.

We set up a confocal microscopy system to have a well-defined beam spot [201]. Knowledge of the optical intensity and not just the input power is necessary for comparing results between setups and looking for general trends or comparing samples. Using an epi-illumination microscope configuration, 5-1000 mW of 532 nm laser light was focused through the sample with a beam-waist of 20 μm for these studies. Figure 4.26 dramatically illustrates the deleterious effects of intense laser intensity on the ensemble charge state. At the highest optically intensities, a very small fraction of the PL originates from NV.

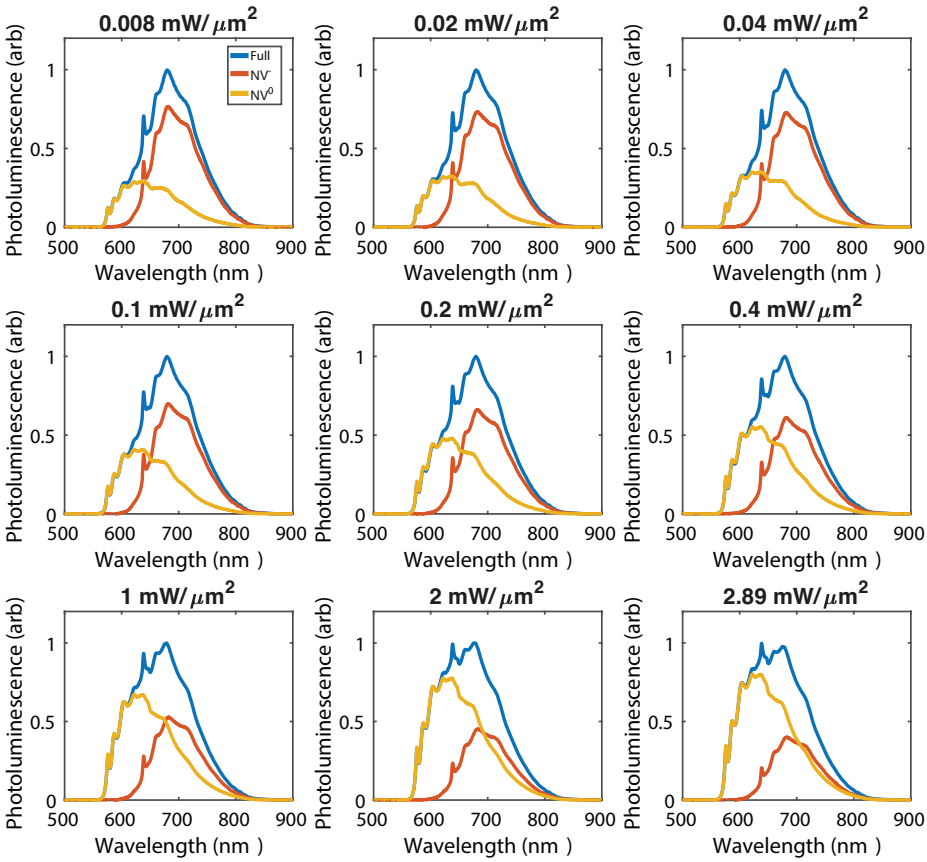

Figure 4.26: Decomposition of the PL into the different charge state components with increasing laser intensity for the layer diamond.

4.4.5 Improved Charge State Stability with Diamond Growth Optimization

We have identified two major ways that charge state stability and robustness can be controlled through diamond growth and processing. As mentioned in Reference [202], the nitrogen concentration plays an important role in determining both the steady state charge state ratio and the robustness of the charge state to differing laser powers. Furthermore, for a given nitrogen concentration, the diamond growth process can be optimized to minimize charge traps that diminish the charge state and robustness to an increase in the intensity of laser power [201]. Importantly, we found [201] that measurements of the substitutional

nitrogen charge state fraction (N_S^0/N_S) following diamond growth is predictive of the NV^- charge state following irradiation and annealing. This suggests that a predominant factor degrading charge state is the presence of unwanted defects acting as charge traps in the diamond. Furthermore, we demonstrated that the amount of these unwanted defects correlated strongly with the color of the diamond, hinting that these unwanted defects have broad optical absorption spectrum. [201] The determination of these quick and simple methods for predicting charge state performance following diamond growth enabled the development of new diamond samples with better charge state properties.

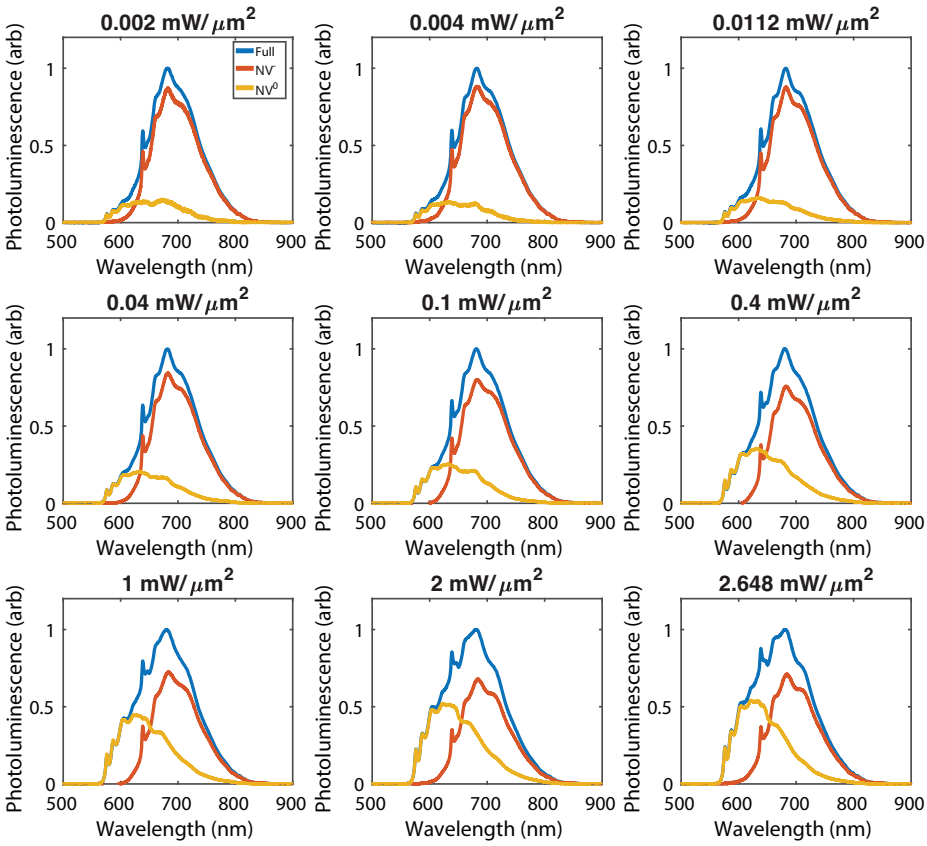

Figure 4.27: Decomposition of the PL into the different charge state components with increasing laser intensity for the improved bulk diamond material.

With the improved diamond material, the PL fraction remained much more stable

compared to the layer sample (see Figure 4.27). Figure 4.28, illustrates the improved charge state fraction of the improved diamond samples produced in Reference [201], compared to previously samples available. Furthermore, this study illustrated that large differences in low-intensity charge state fractions (comparing original bulk to improved bulk processes) do not translate to improved charge state stability for high optical intensities.

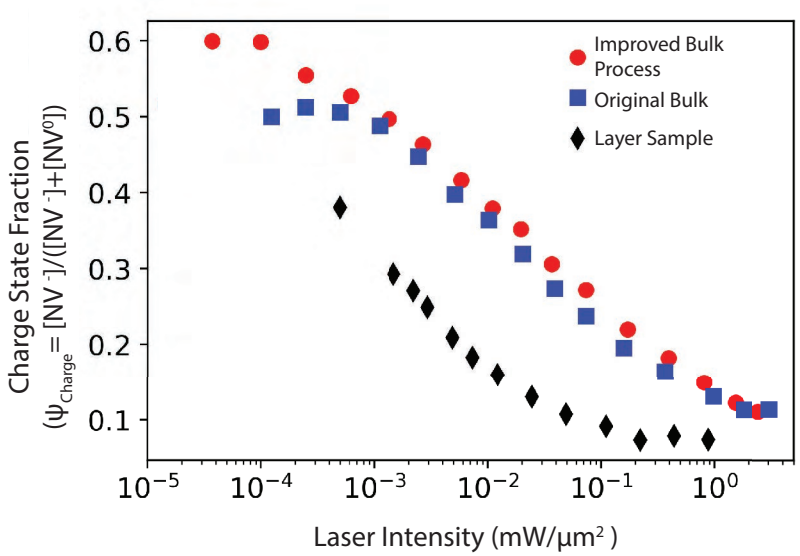

Figure 4.28: Summary of the charge state fraction as a function of laser intensity for three different samples .

Further work is needed to probe all the factors influencing charge state and efficient methods to stabilize the charge state with high laser intensity. Some areas we are further exploring include: (i) effect of laser spot size (relative to charge diffusion length scales); (ii) effect of different colors of illumination and their duty cycle; (iii) mapping out nitrogen concentration dependence; and (iv) other protocols to improve charge state under intense green illumination.

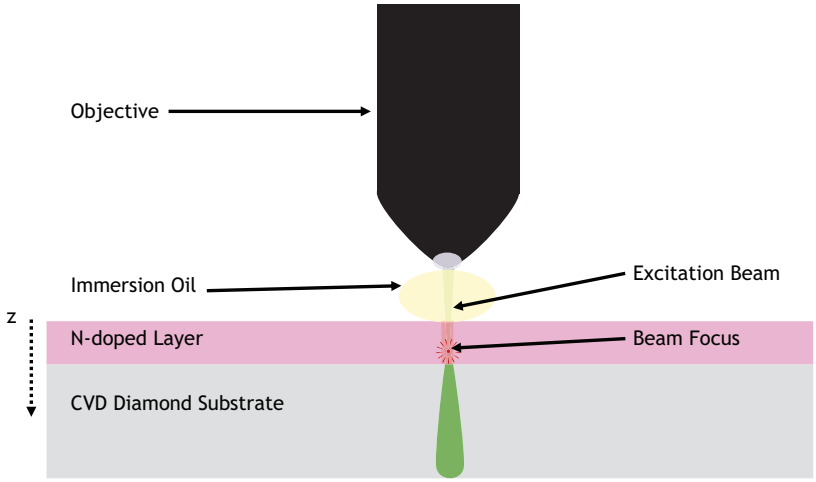

Figure 4.29: Overview of confocal depth scanning

4.5 Scalability of Thin Layer Diamond Sensors

The results above illustrate the importance of developing methods to assist in the feedback and iteration process of diamond development. In particular the thickness of the N-doped CVD layer plays an important role in the imaging resolution and performance of a NV diamond magnetometer. However, during the CVD process the introduction of varying amounts of nitrogen can change the growth rate. Historically, the resultant N-doped layer thickness has been characterized through a destructive measurement, known as Secondary Ion Mass Spectroscopy (SIMS.) In SIMS, a primary ion beam is focused onto the surface, creating a hole and causing the emission of secondary ions. These secondary ions are collected and the charge to mass ratio is measured through a mass spectrometer to create a qualitative measurement of the composition at a certain depth. However, sending out test samples to have SIMS performed caused delays in growth iteration, were generally expensive, and destructive to the samples, so we developed an alternative method to determine the N-doped layer thickness post growth.

We developed a scheme (see Figure 4.29 that utilizes modeling of the distorted confocal

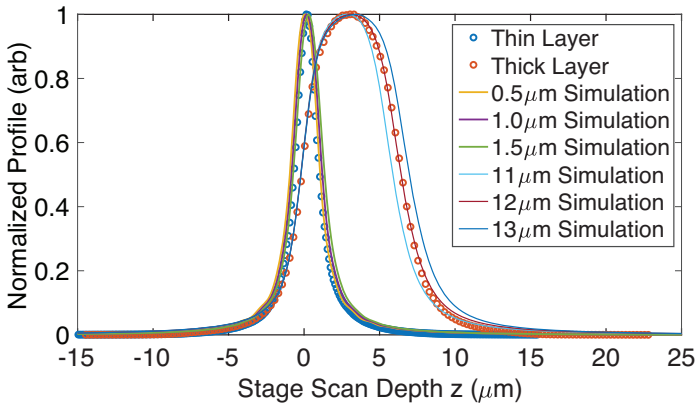

Figure 4.30: Calibration scans to demonstrate the effectiveness of the method for thin (1 μm) layer and thick layer (10 μm) diamonds. The results were compared to SIMS measurements of the same and showed agreement to within 20%, which is sufficient for needed applications.

point spread function (PSF) at the diamond interface to have an efficient way to characterize charge state. However, using a high NA objective to focus deep into a surface with a high index of refraction results in aberrations [243, 244] and large distortion of the PSF. Through modelling the expected PSF and comparing the simulations with the measurements we were able to utilize this method to show agreement with conventional methods (Figure 4.30) and for quality control of a large batch of samples (Figure 4.31).

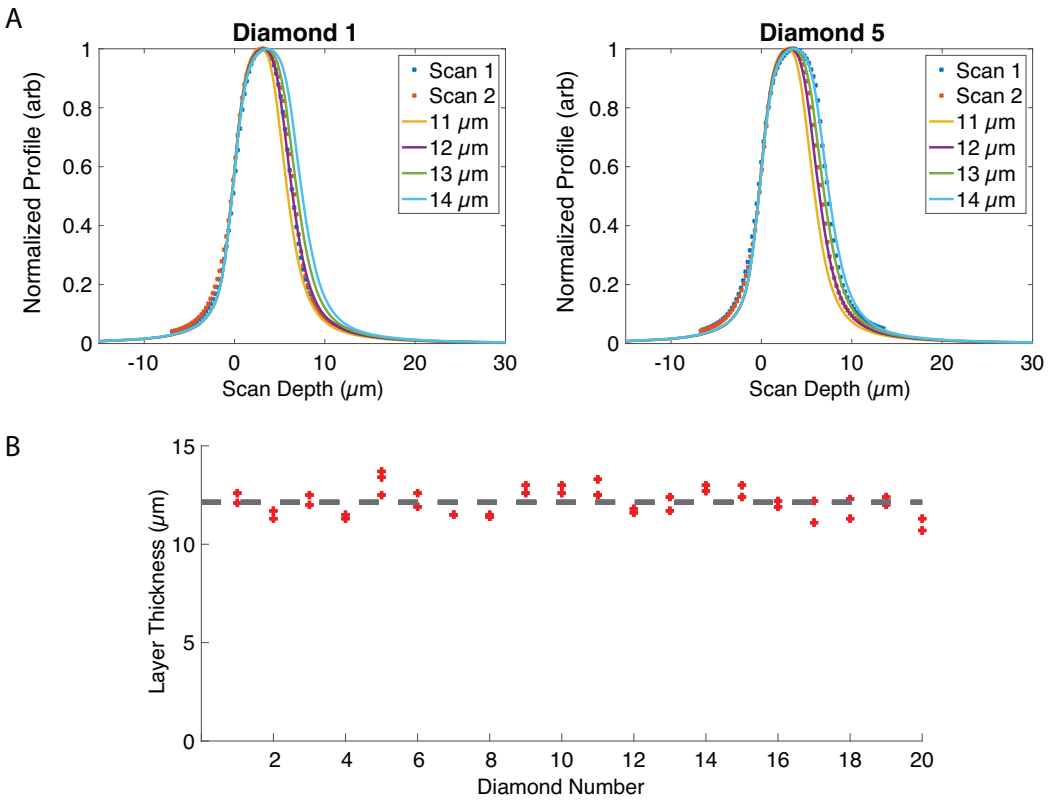

Figure 4.31: Following the initial demonstration, the method was used to analyze a batch of samples to characterize sample to sample variability, which is a function of the diamond substrates and the plasma conditions in the growth chamber.

Chapter 5

Widefield Imaging of Static Fields

5.1 Applications of a Quantum Diamond Microscope (QDM)

QDM magnetic field imaging has been applied to a diverse range of applications across numerous fields of research. For every given application, the appropriate experimental protocol must be chosen for optimal performance, including the desired temporal resolution and magnetic frequency range. This subsequently dictates the QDM component implementation. Table 5.1 lists the application target areas for the various QDM techniques and respective frequencies. This section will give a brief overview of the range of widefield imaging applications possible.

The next two chapters focus on work done in the Broadband (0-1 MHz) category of applications. The experiments described in these chapters were being conducted simultaneously in different experimental set ups and it makes sense to introduce the measurement of static fields first due to large number of use cases of this technique and it sets up the basics for a lot of protocols that will be utilized. This chapter focuses on measurements where the duration of a single experiment can be anywhere from 30 seconds to 30 minutes. The following chapter will focus on techniques that can image quasi-static fields with repetition

	Broadband DC - 1MHz	Narrowband 1kHz-20MHz	Narrowband 10MHz- 100GHz
Techniques	**Continuous Wave (CW) ODMR** **Lock-In CW ODMR** Pulsed ODMR **Ramsey**	Hahn Echo Dynamical Decoupling DEER Spectroscopy	CW ODMR (Contrast and Linewidth) Rabi Spectroscopy T_1 Relaxation
Applications	Paleomagnetism and Rock magnetism **Biomagnetism** Solid State Magnetism **Low Frequency Electronics**	RF Electronics Solid State Magnetism NMR Spectroscopy	MW Electronics Solid State Magnetism EPR Spectroscopy NMR Spectroscopy

Table 5.1: QDM Techniques and Applications. Overview of techniques and potential applications for widefield magnetic imaging.

rates up to $\sim 5\ kHz$.

5.2 QDM Imaging of Integrated Circuit Activity

Securing integrated circuits against manufacturing flaws, hardware attacks, and software attacks is of vital importance to the semiconductor industry [245]. Hardware attacks often modify the physical layout of an integrated circuit, thereby changing its function. This type of attack can occur at any stage of the globalized semiconductor supply chain, and can range from insertion of malicious Trojan circuitry during the design and fabrication stages [246], to modification or counterfeiting during packaging and distribution stages [247]. Horizontal integration of the industry has led to contracting of integrated circuit fabrication, packaging, and testing to offshore facilities, resulting in a reduction of secure oversight and quality control [248]. Additional growth of the secondhand electronics market has led to a drastic increase in counterfeit integrated circuits [249]. Detection of integrated circuit tampering or counterfeiting has consequently become essential to ensure hardware can be trusted. Similar issues affect quality control of unintended manufacturing flaws.

Magnetic field emanations from integrated circuits afford a powerful means for non-

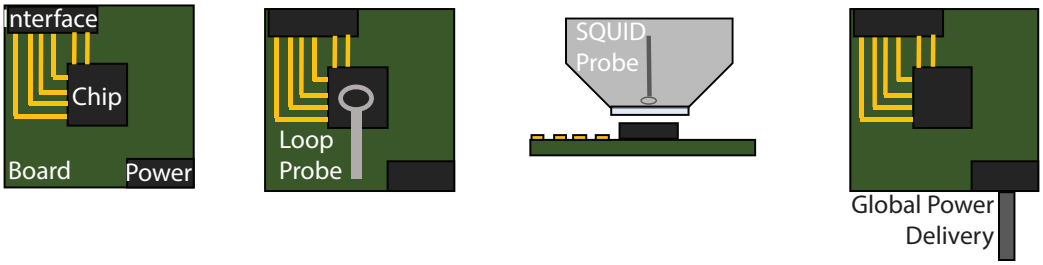

Figure 5.1: Rough schematic of an integrated circuit on a circuit board. Examples of three other (non-QDM) techniques that can be used to measure the activity of the chip. Loop probes can be used to inductively measured the fast oscillating fields due to the clocks and switching of the boards and can be scanned over the chip. SQUID probes can be used in a similar manner to measure lower frequency magnetic fields, but possess constraints due to the need to be operated in a cryogenic environments. In some modalities the power being delivered to the board can be monitored and signatures in the power delivery can be utilized to get information about the operational state of the chip.

destructive physical testing. Magnetic fields are generated by current densities in integrated circuits resulting from power and clock distribution networks, input/output lines, word and bit lines, and switching transistors. These currents are present in all operating logic and memory chips and can be leveraged for studying the operational behavior of an integrated circuit during task execution. In general, the resulting integrated circuit magnetic fields pass through many standard integrated circuit materials, and will vary spatially and temporally in ways that correlate with both integrated circuit architecture and operational state. Thus, combined high-resolution and wide-field-of-view mapping of magnetic fields may yield simultaneous structural and functional information, and may be suitable for identification of malicious circuitry or Trojans [250,251], counterfeit detection [252], fault detection [253,254], and manufacturing flaws [255]. However, leveraging magnetic field emanations is challenging due to the tremendous complexity of circuits integrating billions of transistors of minimum feature sizes down to tens of nanometers, with interconnects distributed across multiple levels of metallization [256]. Multi-layered metal interconnects and three-dimensional stacking

give rise to complex magnetic field patterns that are difficult to invert; and large stand-off distances of magnetometers reduce amplitudes of magnetic fields and spatial resolution [45].

We demonstrate how these challenges can be approached using a Quantum Diamond Microscope (QDM) [1, 200, 257] augmented with machine-learning classification techniques. With the QDM, we perform simultaneous wide field-of-view, high spatial resolution, vector magnetic field imaging of an operational field-programmable gate array (FPGA). FPGAs are configurable integrated circuits that are commonly used for diverse electronics applications. Systematic and controlled variation of the circuit activity in the FPGA generates complex magnetic field patterns, which we image with the QDM. The QDM employs a dense surface layer of fluorescent nitrogen-vacancy (NV) quantum defects in a macroscopic diamond substrate placed on the integrated circuit under ambient conditions. The electronic spins associated with NV defects have well-established sensitivity to magnetic fields [258–260].

To date, the QDM's unique combination of magnetic field sensitivity, spatial resolution, field-of-view, and ease of use has allowed it to be used to measure microscopic current and magnetization distributions from a wide variety of sources in both the physical and life sciences [15, 54, 145, 261–264]. Complementary to scanning techniques (see Figure 5.1) for characterizing integrated circuit magnetic field emanations, which include wire loops [265], probe antennas [266], magnetic force microscopy [254], SQUID magnetometers [251], and vapor cell magnetometers [267], the QDM employs a non-scanning imaging modality [200] that provides simultaneous high-resolution (micron-scale) and wide-field (millimeter-scale) vector magnetic imaging, while operating under ambient conditions. This capability allows for monitoring of transient behavior over sequential measurements of a magnetic field, providing a means to study correlations in signal patterns that can evolve more quickly than a single-sensor scan time. In addition, the QDM's simultaneous magnetic imaging modality is not subject to the reconstruction errors and drift that can arise from a scanned probe. With

these distinctive advantages, the QDM technique is a promising approach for non-destructive physical testing of integrated circuits.

5.2.1 Setup Details

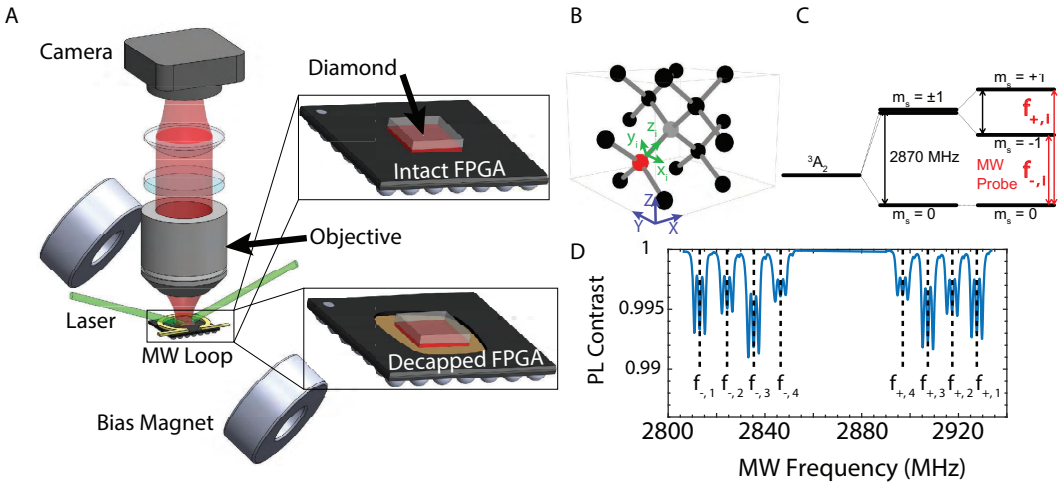

Figure 5.2: (A) Schematic of the Quantum Diamond Microscope (QDM) experimental setup with insets showing the diamond in contact with intact and decapsulated FPGAs. The diamond is positioned such that the NV layer is in direct contact with the FPGA, as indicated by the red layer in the insets. (B) Diamond crystal lattice with the nitrogen (red) vacancy (grey) defect. Lab frame coordinates (X,Y,Z) and NV frame coordinates for a single defect (x,y,z) are shown. (C) The ground state energy level diagram for an NV with fine structure and Zeeman splitting. (D) Example ODMR spectral data for an applied bias field of $(B_X,B_Y,B_Z) = (2.0\ 1.6\ 0.7)$ mT, showing resonance frequencies of $f_{\pm,i}$ with $i = 1, 2, 3, 4$ indicating each of the four NV axes. Hyperfine interactions between the NV^- electrons and the spin-1 ^{14}N nucleus result in splitting of each NV resonance into three lines.

A schematic of the QDM is shown in Figure 5.2(A). The magnetic field sensor consists of a 4 mm × 4 mm × 0.5 mm diamond substrate with a 13 μm surface layer of NV centers. The diamond is placed directly on the integrated circuit with the NV layer in contact with the integrated circuit surface. The diamond is grown by Element Six Ltd. to have an isotopically pure NV layer consisting of [^{12}C] ∼ 99.999%, [^{14}N] ∼ 27 ppm, and [NV^-] ∼ 2 ppm. Light

from a 532 nm, CW laser (Lighthouse Photonics Sprout-H-10W) optically addresses the NV layer with beam power of about 500 mW uniformly distributed over the 4 mm × 4 mm NV layer. A flat-top beam shaping element (Eksma Optics GTH-5-250-4-VIS) and a cylindrical lens (Thorlabs LJ1558RM-A) create a rectangular beam profile (6 mm × 6 mm) incident on the top face of the diamond at a sufficiently shallow angle of incidence (4°) relative to the top diamond surface to illuminate the entire NV layer. NV fluorescence is collected with a low magnification objective (Olympus UPlanFL N 4x 0.13 NA) to interrogate a large field-of-view of about 3.7 mm × 3.7 mm. The fluorescence is filtered with a 633 nm longpass filter (Semrock LP02-633RU-25) and imaged onto a CMOS camera (Basler acA1920-155um). Resulting CW ODMR data is transferred to a computer where it is processed and analyzed with custom software utilizing LabVIEW and MATLAB [144].

A pair of 5 cm diameter SmCo permanent magnets (Super Magnet Man) is placed on opposing sides of the diamond to apply a uniform bias magnetic field (bias field) of $\mathbf{B}_0 = (B_X,\ B_Y,\ B_Z) = (2.0,\ 1.6,\ 0.7)$ mT to separate the resonances of the different NV axes (see Figure 5.2(D)). X, Y, Z are the laboratory frame Cartesian coordinates with the X-Y plane defined as the surface of the diamond in Figure 5.2(B). $\mathbf{B}_0$ induces a $\pm g_e \mu_B \mathbf{B}_0 \cdot \mathbf{n}$ Zeeman splitting of the spin triplet NV $m = 1$ and $m = -1$ ground states along each of four tetrahedrally defined NV symmetry axes, $\mathbf{n}$, with Landé g-factor g_e, and Bohr magneton μ_B. The hyperfine interaction between the NV and the ^{14}N isotope nuclear spin (I=1) results in an additional triplet level splitting. The four symmetry axes of the NV, shown in Figure 5.2(B), are leveraged for vector magnetic field imaging using $\mathbf{B}_0$ projection onto all four NV axes [55]. The ground state energy level diagram of a single NV axis is depicted in Figure 5.2(C), neglecting hyperfine structure.

A 6 mm diameter copper wire loop made from 320 μm diameter magnet wire delivers 1 W of GHz-frequency microwave fields (TPI-1001-B and amplified with a Mini-Circuits

ZHL-16W-43S+ amplifier) to drive the NV electronic spin transitions, $m_s = 0 \leftrightarrow -1$ or $m_s = 0 \leftrightarrow +1$, denoted by $f_{-,i}$ and $f_{+,i}$, respectively, see Figure 5.2(C). The microwave power chosen is sufficiently low to not effect the observed normal function of the integrated circuit. The microwave field is modulated on and off through the use of a solid-state switch (ZASWA-2-50DRA+) controlled by a DAQ (NI-USB 6259) and synchronized with the frame acquisition of the camera to correct for laser intensity fluctuations and drift.

5.2.2 Board Details

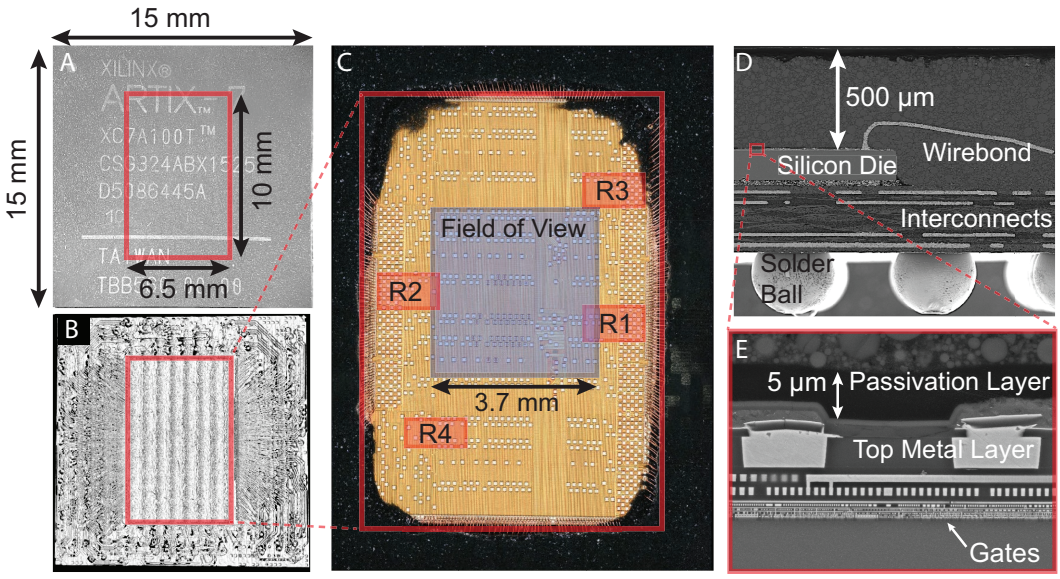

Figure 5.3: (A) Intact Xilinx 7-series Artix FPGA with die location and dimensions indicated in red (B) X-ray image of the FPGA package determining the position and size of die outlined in red (C) A high resolution image of the decapsulated FPGA with the fixed diamond measurement field-of-view indicated with a blue box, and the location of ring oscillator clusters indicated by red boxes labeled R1 - R4. (D) Scanning electron microscope (SEM) image of the FPGA cross-section showing the 500 μm stand-off distance between the chip die and the top layer. (E) Close-up of the SEM focusing on the metal layers of die. The thickness of the passivation layer is 5 μm and sets the minimum stand-off distance for the decapsulated measurements.

The Xilinx 7-series Artix FPGA (XC7A100T-1CSG324C) shown in Figure 5.3(A) and

5.3(B) is selected for this study due to its versatility, general availability, and affordability. This FPGA is a 15 mm × 15 mm wirebonded chip, fabricated in the TSMC 28 nm technology node, that has a ∼ 6.5 mm × 10 mm silicon die with eight clock regions. Digilent Nexys A7 development boards are used to operate and configure the Artix-7 FPGA. Two chips were used: one intact Artix 7 and decapsulated (decapped) Artix 7 that was prepared using a Nisene JetEtch Pro CuProtect decapsulator.

The die of the Artix-7 FPGA is covered by roughly 500 μm of epoxy resin packaging material, separating the diamond from the die for the intact configuration. This stand-off distance leads to smaller field amplitude at the NV sensor layer and acts as a low-pass filter decreasing the effective QDM spatial resolution of FPGA current sources [45]. To bring the diamond closer to the die, one of the Artix-7 FPGAs is decapsulated (decapped) using a Nisene JetEtch Pro CuProtect decapsulator. This process uses fuming sulfuric and nitric acid to remove the packaging material, exposing the die while leaving the FPGA electrically functional, including preservation of the copper wirebonds.

The large current draw and controllable location and size of ring oscillators make them ideal functional units for this study [268, 269]. Patterns of ring oscillators are implemented using the Xilinx Vivado Design Suite® to create distinguishable current distributions on the FPGAs for measurement by the QDM. Clusters of three-inverter ring oscillators are synthesized, placed, and routed to four different predefined clock regions on the FPGA, with clear spatial separation and spanning a majority of the die surface as shown in Figure 5.3(C). A cross section of the die is shown in Figures 5.3(D) and 5.3(E). The clusters consist of variable numbers of ring oscillators allowing for incremental increase or decrease of the current draw at the different locations on the FPGA. The active states of the FPGA are defined by ring oscillator clusters implemented in one of the predefined regions, and the idle state is defined as the FPGA powered on with no implemented ring oscillators. These

active and idle states of the FPGA are used to create a lock-in type measurement of the chip activity. The ordering of states during a series of measurements are randomized to reduce susceptibility to systematic noise sources.

The structure of the wire-bonded Artix 7 die, shown in Figure 5.3(D), is optimal for studies of patterns of power delivery within the top metal layers of the FPGA. The thickest layers of the metal stack are usually closest to the top side of the package in wirebonded chips. These thick layers are used for power distribution due to their relatively low resistance characteristics compared to the other layers of the integrated circuit. Clock distribution networks and inputs/outputs (I/Os) occupy the next thickest layers, and data signals are in the lowest and thinnest metal layers. Prominent magnetic fields from the current densities in the power distribution network are therefore most easily detected with topside access of a wirebonded device. Magnetic field patterns from the lower-level data signals are likely not distinguishable with the present measurements. Note that Figure 5.3(D) reveals large wire interconnects in the package substrate connecting the wirebonds and solder balls. These wires are deeper in the chip and are likely observable as low spatial frequency components in the magnetic field. As will be seen below, static fields from solder balls and other magnetic materials are also observable with the QDM; but can be distinguished from functional current flow by differential ring oscillator measurements.

State Dependent Current Delivery to Development Board

The global DC current delivered to the Nexys A7 development board is measured as a function of the number of active ROs to obtain an approximation of the current required by the FPGA for each state. The current was determined by measuring the voltage across a fixed resistance at the input of the development board. The time variation of the voltage was recorded on a fast (1 GHz) oscilloscope.

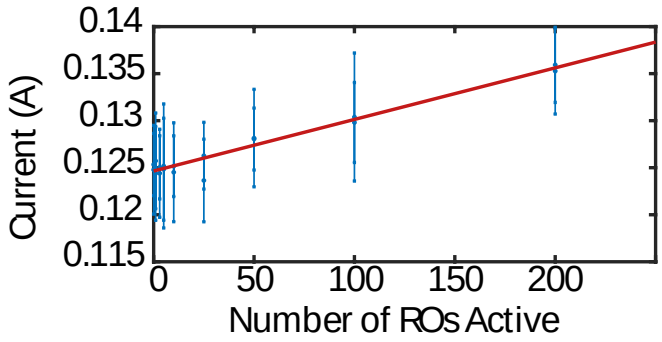

Figure 5.4: Plot of the measured DC current delivered to the development board as a function of the number of ROs active in Region 1 of the FPGA. The large error bars result from the activity of other components on the development board, independent from the FPGA, that draw varying amounts of current over the duration of a given measurement.

The Nexys A7 contains many components in addition to the Artix 7 FPGA and has many processes running in parallel to the FPGA. The measured voltage is consequently dependent on other processes executing on the board that are independent of the FPGA activity. This results in a voltage signal full of extraneous spikes and other information, degrading confidence in the measurement of DC currents (see Figure 5.4). The voltage was measured on the scope for 1 ms at a sampling rate of 1 GHz. The current was calculated through precise measurement of the resistance used.

This process was repeated twice for each FPGA activity state, with ROs activated in Region 1. The resulting data is plotted in Figure 5.4. The error bars represent the standard deviation of the voltage over the 1 ms of signal acquisition. The current scales linearly with the number of ROs (0.055(6) mA per active RO) see Fig 5.4 The resultant linear fit is shown below.

$$I_{tot} = 0.055(6)(mA/RO)N_{RO} + 125(4)mA \tag{5.1}$$

Assuming a simple model of the current being confined to a single wire-like structure and a stand-off distance of $\sim 15\mu m$ yields approximate scaling of 500 nT/RO. This is likely an over-

estimate because the currents are distributed over many wires and there can additionally be cancellation from neighboring sources. The activity state dependent current measured at the input are not necessarily fully representative of the state dependent current on the die due to the complexity of components on the development board interfacing between the FPGA and the external power supply. However, these measurements are useful for informing general trends and magnitudes of current consumption of the FPGA.

5.2.3 Hamiltonian and Analysis Method

The intensity of optically induced NV fluorescence decreases for microwave fields on resonance with one of the spin transition energies. This decrease results from the $m = \pm 1$ spin-selectivity of the non-optical, intersystem crossing (ISC) mediated decay pathway for optically excited NVs [16]. The resonance frequencies between NV ground-state sublevels are determined from the ground-state Hamiltonian

$$\begin{aligned} H/h = &\left(D(T) + M_z\right) S_z^2 + \gamma \left(B_x S_x + B_y S_y + B_z S_z\right) \\ &+ M_x \left(S_y^2 - S_x^2\right) + M_y \left(S_x S_y + S_y S_x\right) \end{aligned} \tag{5.2}$$

for the projection of $\mathbf{B}_0$ along a single NV axis, where h is Planck's constant, $D(T) \approx 2870$ MHz is the temperature dependent zero field splitting, T is the temperature, S_k are the dimensionless spin-1 Pauli operators, $\gamma = 2.803 \times 10^4$ MHz/T is the NV gyromagnetic ratio, B_k are the components of $\mathbf{B}_0$ in the NV frame, and M_k are crystal stress terms [31]. Electric field terms contribute minimally [56, 270] and are neglected in the NV Hamiltonian presented due to their minimal contribution to the present study. The interaction between an external electric field and the NV^- electronic spin state is described by the ground state Hamiltonian [270]

$$H_{E-field} \approx d_{\parallel} E_z S_z + d_{\perp} E_x (S_y^2 - S_x^2) + d_{\perp} E_y (S_x S_y + S_y S_x) \tag{5.3}$$

Electric fields couple weakly to the NV ground state Hamiltonian due to the relatively small dipole moments $d_{\parallel} \approx 3.5 \times 10^{-3}$ Hz/(V/m) and $d_{\perp} \approx 0.17$ Hz/(V/m) [56, 270]. Similarly to the stress contribution to the Hamiltonian, the perpendicular components of the electric field are suppressed by the application of an on-axis bias magnetic field B_z [56].

Consider an extreme situation where a changing chip function causes a change in potential of 1 V between traces separated by 10 μm. The resulting electric field in the gap between the traces is of the order 10^5 V/m. For on-axis electric field components this would lead to shifts in the NV zero-field splitting of 350 Hz. In addition, using the known temperature dependence of the NV zero-field splitting, $\partial D/\partial T \approx -74$ kHz/C [25], this electric field induced shift of 350 Hz appears equivalent to a temperature change of 5×10^{-4} °C. The electric field contribution is consequently insignificant, and is thus neglected from the analysis.

Cartesian coordinates $k = x, y, z$ are defined in the NV frame with z along the selected NV axis, see Figure 5.2(B). The contribution of the hyperfine interaction between the NV and ^{14}N nuclear spin is treated as a constant, 2.158 MHz energy level splitting and is not shown explicitly in Equation 5.2. Sweeping the frequency of the applied microwave fields across the range of resonant frequencies and collecting the NV fluorescence results in an optically detected magnetic resonance (ODMR) spectrum. Figure 5.2(D) depicts the resulting ODMR measurements for a bias field alignment where each NV axis experiences a different projection of the bias magnetic field.

Continuous-wave (CW) ODMR is used to image static FPGA magnetic fields. CW ODMR leverages continuous application of the laser and microwave field. This approach yields wide field-of-view images with high spatial resolution and good magnetic field sensitivity, while minimally perturbing the sample under study [1, 200]. A diamond with sufficiently low M_z inhomogeneity across the field-of-view is used to minimize degradation of perfor-

mance [31]. Further suppression of strain contributions is achieved with application of the static bias field, $\mathbf{B}_0$. Thus, the M_x and M_y terms in Equation 5.2 are negligible [21, 31]. The ground state Hamiltonian along a single NV axis reduces to

$$H/h \approx (D(T) + M_z)S_z^2 + \gamma B_z S_z + \gamma B_x S_x + \gamma B_y S_y, \tag{5.4}$$

and is used to determine the CW ODMR resonance frequencies for each pixel in a QDM image, and thereby to determine the magnetic field image from the sample FPGA.

CW ODMR measurements are taken with the FPGA in both active and idle states. The duration of each measurement is ~ 5 min per NV axis for each state. Such extended measurements are insensitive to transient effects on time scales shorter than the measurement; and sensitive to environmental drifts on the time-scale of the measurement. Magnetic field contributions from the ring oscillators are determined by subtracting the measured idle-state ODMR frequencies from the measured active-state ODMR frequencies, yielding the overall magnetic field due to the ring oscillators alone. For such measurements, the NV ground-state Hamiltonian is given by:

$$\begin{aligned} H/h \approx \left(D + \frac{\partial D}{\partial T}\Delta T + M_z\right) S_z^2 + \gamma(B_z + \Delta B_z)S_z \\ +\gamma(B_x + \Delta B_x)S_x + \gamma(B_y + \Delta B_y)S_y \end{aligned} \tag{5.5}$$

Here, terms with Δ originate from the FPGA active states and $\partial D/\partial T \approx -74$ kHz/°C [25]. Following these definitions and treating the off-axis magnetic fields as perturbative, the idle and active-state resonant frequencies for the upper (f_+) and lower (f_-) transitions of a single NV axis (i) are given by [21]

$$f_{\pm,i,Idle} \approx (D + M_z) + \frac{3\gamma^2}{2D}\left(B_x^2 + B_y^2\right) \pm \gamma B_z \tag{5.6}$$

and

$$\begin{aligned} f_{\pm,i,Active} \approx & \left(D + \frac{\partial D}{\partial T}\Delta T + M_z\right) \\ & + \frac{3\gamma^2\left[(B_x + \Delta B_x)^2 + (B_y + \Delta B_y)^2\right]}{2\left(D + \frac{\partial D}{\partial T}\Delta T + M_z\right)} \\ & \pm\gamma(B_z + \Delta B_z). \end{aligned} \tag{5.7}$$

Treating the off-axis magnetic fields as perturbative, the difference between the active and idle state ODMR resonance frequencies is given by [21]:

$$\begin{aligned} f_{\pm,i,Active} - f_{\pm,i,Idle} \approx & \left(D + M_z + \frac{\partial D}{\partial T}\Delta T\right) + \frac{3\gamma^2\left[(B_x + \Delta B_x)^2 + (B_y + \Delta B_y)^2\right]}{2\left(D + M_z + \frac{\partial D}{\partial T}\Delta T\right)} \\ & \pm\gamma(B_z + \Delta B_z) - (D + M_z) - \frac{3\gamma^2\left(B_x^2 + B_y^2\right)}{2(D + M_z)} \mp \gamma B_z \end{aligned} \tag{5.8}$$

In the limit of $D \gg \frac{\partial D}{\partial T}\Delta T$, M_z the denominators in the off-axis magnetic field terms simplify to $2D$, giving:

$$\begin{aligned} & f_{\pm,i,Active} - f_{\pm,i,Idle} \approx \left(D + M_z + \frac{\partial D}{\partial T}\Delta T\right) + \frac{3\gamma^2\left[(B_x + \Delta B_x)^2 + (B_y + \Delta B_y)^2\right]}{2D} \pm \gamma(B_z + \Delta B_z) \\ & -(D + M_z) - \frac{3\gamma^2\left(B_x^2 + B_y^2\right)}{2D} \mp \gamma B_z = \frac{\partial D}{\partial T}\Delta T + \frac{3\gamma^2\left[2B_x\Delta B_x + \Delta B_x^2 + 2B_y\Delta B_y + \Delta B_y^2\right]}{2D} \pm \gamma\Delta B_z \end{aligned} \tag{5.9}$$

Terms on the order ΔB_X^2 and ΔB_Y^2 are negligible and can be ignored, as are terms dependent on off-axis magnetic fields given that $\frac{\gamma B_X}{D} < 10^{-2}$. These terms only impact the common mode splitting (i.e., temperature measurements) and do not couple into measurements of B_Z to first order.

The desired FPGA state-dependent magnetic field projection on each NV axis, $\Delta B_{z,i}$, and the change in local temperature, ΔT, are given by:

$$\begin{aligned}\Delta B_{z,i} &= \frac{1}{2\gamma}\left(\Delta f_{+,i} - \Delta f_{-,i}\right), \\ \Delta T &= \frac{1}{2\frac{\partial D}{\partial T}}\left(\Delta f_{+,i} + \Delta f_{-,i}\right),\end{aligned} \tag{5.10}$$

where $\Delta f_{\pm,i} = f_{\pm,i,Active} - f_{\pm,i,Idle}$. The off-axis magnetic fields of the sample are suppressed by the zero-field splitting; thus terms dependent on ΔB_x and ΔB_y are sufficiently small to be neglected in Equation 5.10. Terms dependent on B_x, B_y, B_z, D, and M_z are canceled by subtracting the idle resonance frequencies from the active state resonance frequencies. Determining the resonance frequencies from all four NV orientations for vector measurements, labeled by $i = 1, 2, 3, 4$ in Figure 5.2(D), enables solving for the vector magnetic field in the lab frame

$$\begin{aligned}\Delta B_X &= \frac{\sqrt{3}}{2\sqrt{2}}\left(\Delta B_{z,2} + \Delta B_{z,4}\right), \\ \Delta B_Y &= \frac{\sqrt{3}}{2\sqrt{2}}\left(\Delta B_{z,1} + \Delta B_{z,3}\right), \\ \Delta B_Z &= \frac{\sqrt{3}}{4}\left[\left(\Delta B_{z,1} - \Delta B_{z,3}\right) - \left(\Delta B_{z,4} - \Delta B_{z,2}\right)\right],\end{aligned} \tag{5.11}$$

where X, Y, Z are recalled to be the laboratory frame shown in Figure 5.2(B).

The ODMR lineshape for NV ensembles is well described by a Lorentzian lineshape [21, 104].

The center frequencies of the measured ODMR resonance features are determined by fitting the spectra with Lorentzian curves. The relevant measurement parameter for magnetometry is the Lorentzian line center, denoted x_0, which is extracted by fitting the data with a Lorentzian function given by [1]:

$$F = 1 + F_0 + \frac{C_1\gamma^2}{(x - x_0 + A)^2 + \gamma^2} + \frac{C_2\gamma^2}{(x - x_0)^2 + \gamma^2} + \frac{C_3\gamma^2}{(x - x_0 - A)^2 + \gamma^2} \tag{5.12}$$

where F_0 is an offset, C_1, C_2, and C_3 are the contrast values for the different hyperfine features of a given resonance, γ is the resonance linewidth, x_0 is the line center, and A is the hyperfine splitting treated as a constant 2.158 MHz (which is a reasonable approximation for this application). This fit is performed for each of the 8 (4 crystal axes and 2 electronic transitions) different resonance groupings. The contrast is treated as three different parameters for the three hyperfine features to account for differences due to extra small peaks from the forbidden hyperfine transitions [55]. The resonances are sufficiently broadened by the MW power and high [N] of the diamond to allow for the linewidth to be treated as one parameter [1].

ODMR spectra for vector measurements of a ^{14}N diamond sample contain 24 resonance features, Figure 5.2(D) (3 hyperfine features $\times$ 2 electronic spin transitions $\times$ 4 NV axes). The resonance frequencies of Equation 5.10 are extracted from the data by fitting all the Lorentzian parameters from above for every pixel in the field-of-view [1]. Furthermore, the contrast and linewidth of the resonances are determined, giving additional state dependent information that can additionally be used for probing high frequency magnetic fields [66]. GPU-based fitting algorithms [271] speed up this computationally intensive fitting and enable rapid analysis of a large number of measurements.

Multimodal Imaging: Multimodal Imaging: Magnetic Field, Contrast, Linewidth, and Temperature

Determining the value of the resonance line centers requires fitting Lorentzian functions to the measured ODMR resonance features as described in the previous section. An example of the B_z field image determined from fitting to the measured ODMR spectra in each camera pixel is shown in Figure 5.5(A). Fitting also extracts the Lorentzian linewidth and contrast [43], which contain useful information about the properties of magnetic fields emanating

from the circuit, and in future work can be used as additional inputs to machine learning models to fingerprint IC activity.

The activity state-dependent linewidth is dependent on several physical phenomena including magnetic field and strain gradients within a pixel, variations in the magnetic field over the measurement time, and spatial variations in the laser, microwaves, and bias field. Figure 5.5(B) shows an example of the calculated linewidth images for the idle and 200 RO active states. As indicated by a white arrow in Figure 5.5(B), one can see the effect of a strong broadening mechanism, which is likely due to strong zero-mean time varying magnetic fields (since this feature does not appear in the magnetic field map in 5.5(a)). Similar types of features can be seen in the Lorentzian contrast images of the idle and 200 RO state in Figure 5.5(C). However, due to the strong dependence of the contrast on optical power [43] these maps are more sensitive to interference fringes. These fringes are likely due to reflections of the green laser from the passivation layer of the decapsulated chip.

Temperature changes in the diamond are determined from common mode shifts of NV resonance line centers. The common mode shift for each pixel is calculated and then all the pixels are averaged together to give a single value for the bulk crystal temperature. The thermal conductivity of single crystal diamond is large enough that the diamond equilibrates to a uniform temperature on time scales much shorter than the measurement time. As such, wide field-of-view ensemble NV measurements in diamond are not well-matched for imaging temperature variations and are not suitable for determining regional activity on the IC based on thermal signatures. The changes in bulk crystal temperature can be used to improve state classification through understanding of power consumption in the chip, but do not allow for spatial selectivity.

In future work, the multimodal information from the magnetic field maps, linewidth, contrast, and temperature will be used to create a more detailed fingerprint of IC activity.

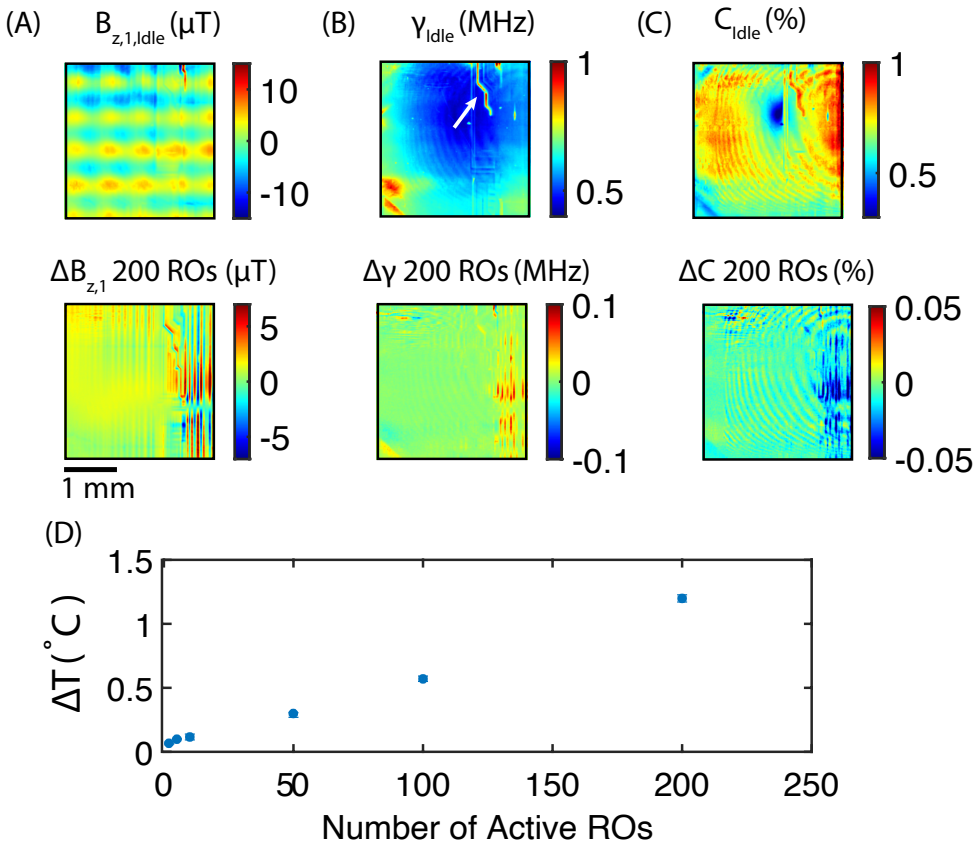

Figure 5.5: QDM images of activity (idle and 200 ROs in Region 1) from the decapsulated FPGA, based on various parameters emerging from the Lorentzian fit to NV ODMR spectra. (A) Images of the projection of magnetic field onto NV axis one. (B) Resonance linewidth images show a strong dependence on other features like MW power, laser power, strain gradients, time varying magnetic fields, and temporal variations that are fast relative to the measurement time. (C) Resonance contrast images contain similar information to the linewidth, but are strongly influenced by variations in the laser over the field-of-view. (D) Change in the average state dependent temperature is shown as a function of the number of active ring oscillators in Region 1.

These physical parameters provide a rich dataset of features that afford further dimensionality for characterization and classification.

Measured Noise Floor, Measurement Duration, and Sensitivity

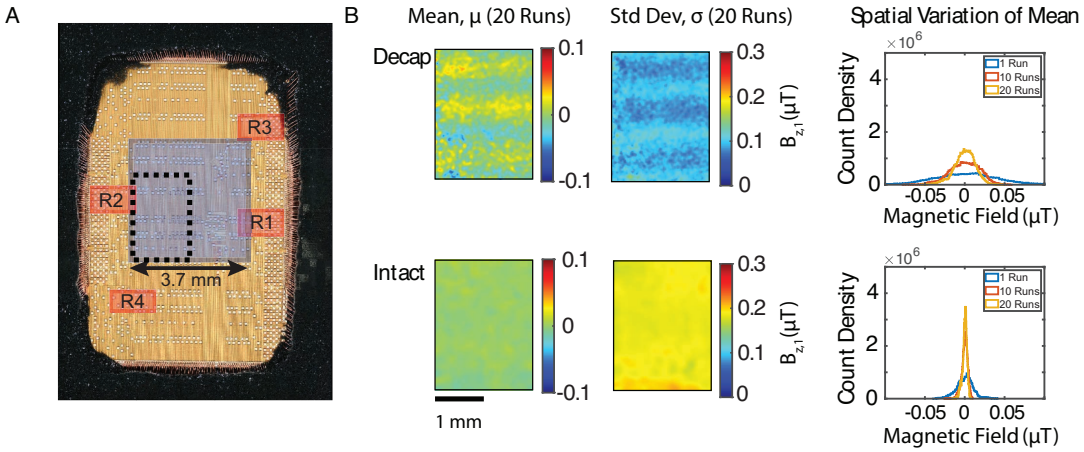

Figure 5.6: (A)Dashed line indicates subset of pixels used for calculation of mean and standard deviation of QDM performance when measuring spatially varying, quasi-static magnetic fields. This region of the FPGA is relatively quiet while in the 0 RO/Idle State. (B) Mean and standard deviation of QDM imaged magnetic fields averaged over 20 runs, and the noise floor achieved in the mean data as a function of number of runs averaged together. Width of the histogram gives the noise floor: $\sim$ 20 nT for the Decap dataset measurements and $\sim$ 2 nT for the Intact dataset.

Properly calibrated and corrected measurements of a quiet subregion of the FPGA should result in a uniform magnetic field in all the pixels of the subregion. Any variation in the measured magnetic field across these pixels is a result of noise such as technical noise or more fundamental noise sources like shot noise. The dashed line in Figure 5.6(A) indicates one such low-activity subregion that is selected to exclude spatial current source variations of the idle state. The spatial noise floor is defined as the full-width-at-half-maximum of the histogram of magnetic field values of all the pixels in the subregion. Measurements over multiple experimental runs are averaged together to determine the magnetic field in each

pixel. The histogram is plotted multiple times for a variable number of averaged runs. As the number of averaged runs increases, the width of the histogram narrows, demonstrating the suppression of noise with averaging over many runs.

The spatial noise floor is thus an important figure-of-merit for characterizing QDM performance when measuring spatially varying, quasi-static magnetic fields. Twenty different data collection runs were utilized for this analysis. The mean and standard deviation for each pixel over these 20 measurements were calculated and plotted over the subsection field-of-view in Figure 5.6(B). The scaling of the noise floor as a function of number of runs for this dataset is indicated by a plotted histogram of the mean pixels after 1, 10, and 20 data collection runs. The high frequency spatial variation in the decapsulated (decap) data leads to a broader distribution of mean values. In contrast, the larger stand-off distance of the intact data allowed for more aggressive binning and Gaussian filtering to be utilized. This binning and filtering resulted in a lower noise floor for the intact data (2 nT) compared to the decap data (20 nT). This noise floor is likely due to a combination of photon shot noise, laser intensity noise, and/or electronic noise from the camera.

The duration of a given measurement is important for practical applications of the QDM and can limit feasibility of collecting large datasets needed for training more advanced machine learning models. A more detailed discussion on factors impacting measurement duration and bandwidth is given in Ref. [200].

Total measurement time is the net result of multiple factors including the camera exposure time, the number of camera frames averaged together per microwave (MW) frequency, the number of MW frequencies monitored, and the associated data transfer and processing time. The measurements presented in the paper have an exposure time of $\sim$4 ms, which is sufficient to nearly saturate the pixel wells of the camera. Full-sensor readout, defined as using all camera pixels, is used to measure the wide field-of-view while maintaining high

spatial resolution. The full-sensor readout from the specific camera used in this study is about 6 ms and limits the fastest effective frame rate. Furthermore, this fixed readout time prevents the ability to increase the speed of measurements through decreasing the exposure time. Laser intensity variation over the duration of a measurement is generally a significant source of noise and each frame with MWs on is followed by a frame with MWs off to correct for this, doubling the time required for collecting data.

Measuring the ODMR spectrum over many MW frequencies improves the fidelity of fitting to determine the magnetic field, and ameliorates large perturbations in the magnetic bias field, diamond strain, and temperature. Measuring many frequencies per ODMR resonance also minimizes linewidth and contrast variations from influencing the magnetic field reconstruction. Typically, 60-80 MW frequencies are swept to sample a span of approximately 10 MHz for each ODMR resonance. The sweep covers 2 resonances for the single-axis measurements and 8 resonances for the 4-axis vector measurements. The ODMR spectrum is measured multiple times until the averaged spectrum of a single pixel has a signal to noise ratio of >10. For the single axis measurements this usually requires a measurement time of 5 minutes and for the 4-axis vector measurements this requires 20-30 minutes. Every measurement results in an ODMR spectrum for each of the ∼1200 × 1200 camera pixels. Given the measured noise floor of ∼ 20 nT for 20 measurements, a 5 minute duration per measurement gives an approximate volume normalized sensitivity of 5 $\mu T \mu m^{3/2}$ $\text{Hz}^{-1/2}$ for all the pixels in the field-of-view. This experiment is optimized for a high dynamic range with high fit fidelity over a large field-of-view for thousands of measurements, motivating slower, more robust techniques to determine the FPGA state dependent magnetic fields. To compare with scanning techniques, the resulting effective measurement scan speed is 200 μs per pixel.

The required measurement duration can be decreased by using a low magnification,

high NA objective [272] to allow for the acquisition of a large field-of-view with much higher photon collection efficiency [273]. To take advantage of this larger photon flux, a camera is needed that can handle the increased photon rate [200, 274]. Furthermore, fewer MW frequencies can be monitored to optimally sample the ODMR spectra [54, 90], thereby minimizing the time spent sweeping MW frequencies. Measurements can be further sped up by decreasing the field-of-view; allowing for the excitation laser to be focused onto a smaller area, enabling the use of a higher magnification objective, and requiring readout from a fewer number of pixels. Further optimization is needed to achieve ∼kHz scale QDM magnetic imaging over mm fields of view.

5.2.4 Vector Magnetic Imaging

Figure 5.7(A) shows QDM vector magnetic field images measured on the decapsulated FPGA for clusters of $N = 200$ ring oscillators in two of the predefined regions indicated in the Vivado floor planner, labeled R1 and R2 in Figure 5.3(C). The vector magnetic field images are derived from CW ODMR measurements using Equations 5.10 and 5.11. Observed maximum magnetic field variations are on the order of ~ 15 μT with a noise floor of ~ 20 nT. Spatial variation of the magnetic field is located on the right of the field-of-view for R1 and on the left for R2. This localization corresponds to the positions of R1 and R2 on the Vivado floor planner, indicating that high current densities for power distribution are concentrated to the region of activity on the die. The vector magnetic field measured in the idle state with 0 ring oscillators, shown in the bottom row of Figure 5.7(A), reveals the structure of the ball grid array that connects the FPGA to the Digilent board. The state dependent magnetic fields due to the ring oscillator current densities (see Equation 5.11) are thus measured in superposition with the spatially inhomogeneous field resulting from the ball grid array.

The presence of a non-zero B_Y component in R1 and R2, as seen in Figure 5.7(A)

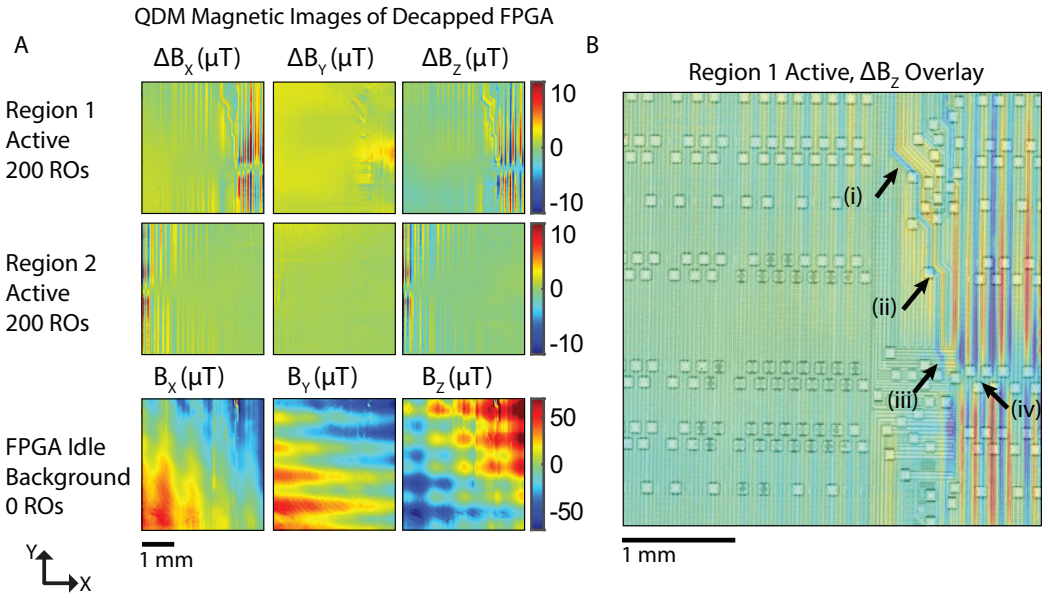

Figure 5.7: (A) QDM vector magnetic field maps of the decapped FPGA for different ring oscillator clusters activated in regions, R1 and R2. The location of the 3.7 mm × 3.7 mm diamond field-of-view is fixed on the FPGA for all magnetic field images (see Figure 5.3(C)). State dependent magnetic field changes $(\Delta B_X, \Delta B_Y, \Delta B_Z)$ are calculated by subtracting background idle magnetic field images from active magnetic field images. Wires on the top metal layer are generally oriented in the Y direction yielding prominent ΔB_X and ΔB_Z fields. ΔB_Y magnetic field maps show contributions from deeper sources. Background magnetic field maps of the idle FPGA with 0 ring oscillators show variations of the field from the mean. Several different background fields are evident: a gradient from the bias magnet, distortion of the bias field from the ball grid array, and background current delivery. (B) ΔB_Z for 200 ring oscillators in R1 plotted in transparency over a high resolution optical image of circuit die. Regions of interest discussed in the text are indicated by (i),(ii),(iii), and (iv).

indicates contributions to the magnetic field from current density sources that run underneath and perpendicular to the visible traces of the top metal layer. These sources are likely a combination of currents in the lower layers of the metal stack and in the interconnects between the wirebonds and ball grid array seen in the SEM image in Figure 5.3(D). Discontinuities present in the B_X and B_Z fields indicate a change of the current direction guided by through-silicon vias in the Z direction that connect the different, stacked metal layers. R3 and R4, seen in Figure 5.3(C), are both outside the measurement field-of-view. However, in both cases, state-dependent current is measured in locations corresponding to the direction of current flow in the appropriate location on the die as discussed in Figure 5.9. This demonstrates the possibility to determine circuit activity outside of the diamond periphery by observing correlated magnetic fields within the nominal field-of-view.

An optical image of the die through the diamond is used to spatially align the magnetic field measurement with the high resolution optical images taken of the decapsulated chip. Spatial variation of the B_X and B_Z magnetic field components corresponds well with the physical features of the top metal layer. Figure 5.7(B) shows a zoomed-in overlay of the B_Z field for 200 ring oscillators in R1 with the optical image of the die, demonstrating feature alignment. Distinct features are visible in the fields that correspond to physical structures, including bends in the wires labeled (i) and (ii) in the figure. Some features in the magnetic field map do not correspond to any visible features on the top metal layer, such as the magnetic trace indicated by (iii) or the discontinuity in field direction indicated by (iv).

Line plots of the magnetic field are shown in Figure 5.8 to elucidate features associated with a subset of the magnetic field images in Figure 5.7. Specifically, data for the magnetic field magnitude of each vector component is plotted along line cuts taken above, below, and at the location of the ring oscillators. The sign change of the magnetic field is easily observable above and below the ring oscillators for the ΔB_X and ΔB_Z image slices. These

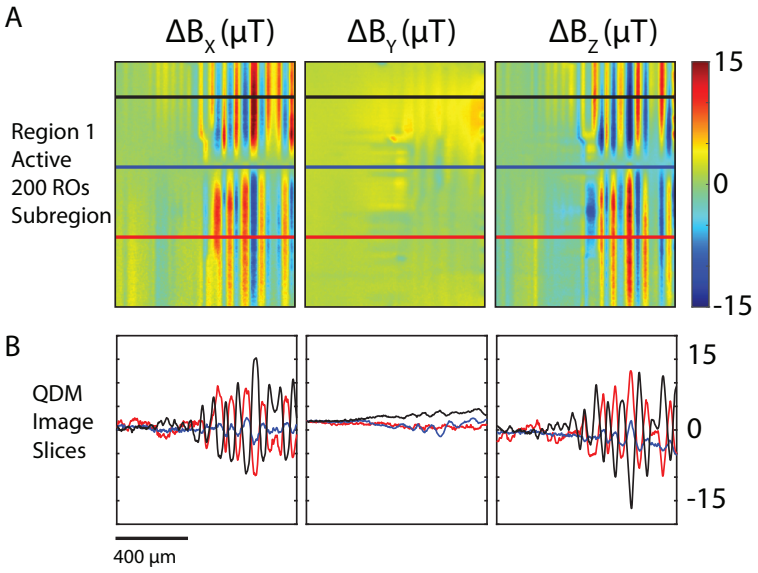

Figure 5.8: QDM vector magnetic field images of the decapsulated FPGA. (A) State dependent vector field images for 200 ROs active in Region 1. (B) Slices (line cuts) of the vector magnetic field images from (A). Black, red, and blue lines in (B) correspond to slices in (A) and are located above, below, and at the location of ring oscillator region R1, respectively.

fields suggest the presence of additional current routing by vias and other structures below the plane of the top metal layer.

Ring Oscillator Activation in Different Regions

The decapsulated FPGA was programmed to have clusters of ROs activated in four distinct location-locked regions as shown in Figure 5.9(A). ROs were active in only one region at any time. The previous discussions focused mostly on two regions, R1 and R2, that were within the QDM field-of-view. The other two regions, R3 and R4, were outside of the QDM field-of-view, and were activated to search for extended indicators of regional activity. Figure 5.9(B) shows that activity state-dependent magnetic fields are evident for 200 ROs in R3 and R4, even though both regions are outside the measurement field-of-view. These measurements take advantage of the extended current routing networks on the chip. One

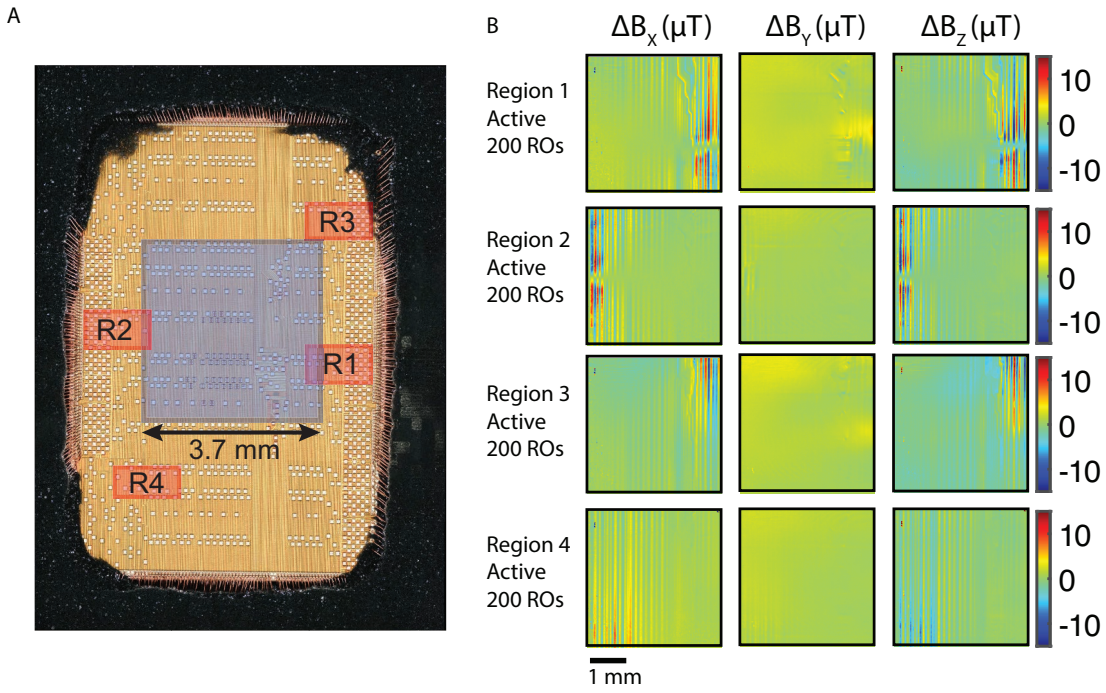

Figure 5.9: QDM vector magnetic field images of decapsulated FPGA (A) Location of the active RO regions (red boxes) relative to the QDM field-of-view (grey box). (B) Spatial fingerprint of vector magnetic field maps for ROs active in each of the four different regions.

can start to infer some general trends about shared resources on the FPGA. For example, activation of 200 ROs in R1 and R3, both on the right side of the die, gives rise to strong ΔB_Y fields in similar locations in the field-of-view.

Larger Measurement Stand-off Distance Using a 40 micron NV Layer

An additional 5 mm × 5 mm × 0.5 mm diamond was used in the QDM to probe an intermediate stand-off measurement distance for both the decapsulated and intact FPGAs. This diamond had a 40 μm surface layer of NV centers consisting of [^{12}C] ∼ 99.95%, [^{15}N] ∼ 10 ppm, and [NV] ∼ 1 ppm. The diamond was placed directly on the FPGA with the NV layer in contact with the FPGA surface. The thicker NV layer gives rise to a larger effective stand-off distance because the average NV within the ensemble is farther away from the magnetic field source. The resulting magnetic field maps, shown in Figure 5.10, have coarser spatial resolution for the decapsulated measurements due to the larger stand-off distance. Consequently, the subtle features seen in data presented in Figure 5.7 are no longer visible.

Despite the lower resolution, such a diamond could be advantageous for the optimization of measuring intact ICs where the higher spatial frequencies are already suppressed by the large stand-off distance caused by the package. Also, a thicker NV layer will improve magnetic field sensitivity due to the larger number of total NVs contributing to the signal. Another feature of this diamond that can prove advantageous for future measurements is the larger, 5 mm × 5 mm area of the diamond. These larger dimensions allow for a wider field-of-view showing, more of the activity from R1 and R2 simultaneously, as shown in Figure 5.10.

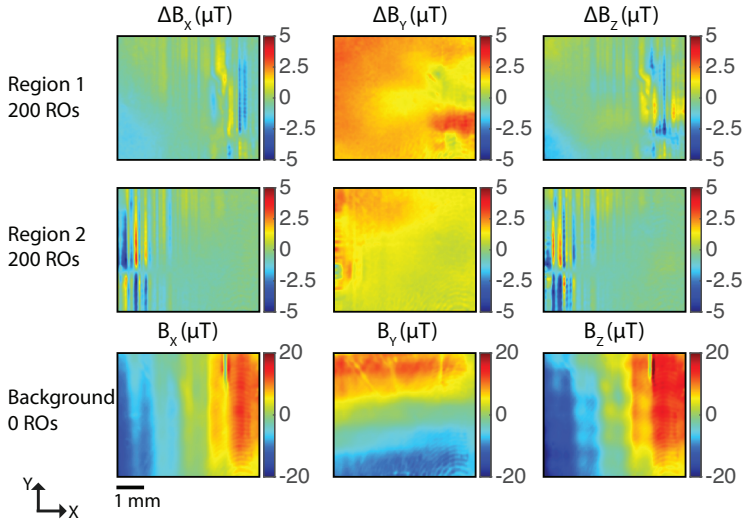

Figure 5.10: A diamond with a thicker NV layer was used to take the same vector magnetic field measurements presented in Figure 5.7 for the decapsulated FPGA. The thicker NV layer results in a larger effective measurement stand-off distance, resulting in lower resolution images of the spatial variation of the magnetic field.

5.2.5 Single Axis Magnetic Imaging

Single NV-Axis QDM measurements [1] are used to collect a large data set of magnetic field images from ring oscillator clusters for classification. These data are taken by monitoring the outermost ODMR spectral features ($f_{-,1}$ and $f_{+,1}$) with the same bias field in the lab frame, and the laser polarization and microwaves optimized for the NV axis being monitored to improve measurement contrast [1]. Projection imaging is useful for large data acquisition due to the speedup in measurement time; however, the vector nature of the field is not captured. The laser polarization and microwaves are optimized for the single NV axis being monitored. Measuring only a single pair of resonance features results in a $\sim 4\times$ speed up by reducing the number of swept microwave frequencies by a factor of four.

Figure 5.11(A) shows example projection magnetic field images, averaged over ten measurements, for 5, 50 and 200 ring oscillators in regions 1 and 2 for the decapsulated FPGA

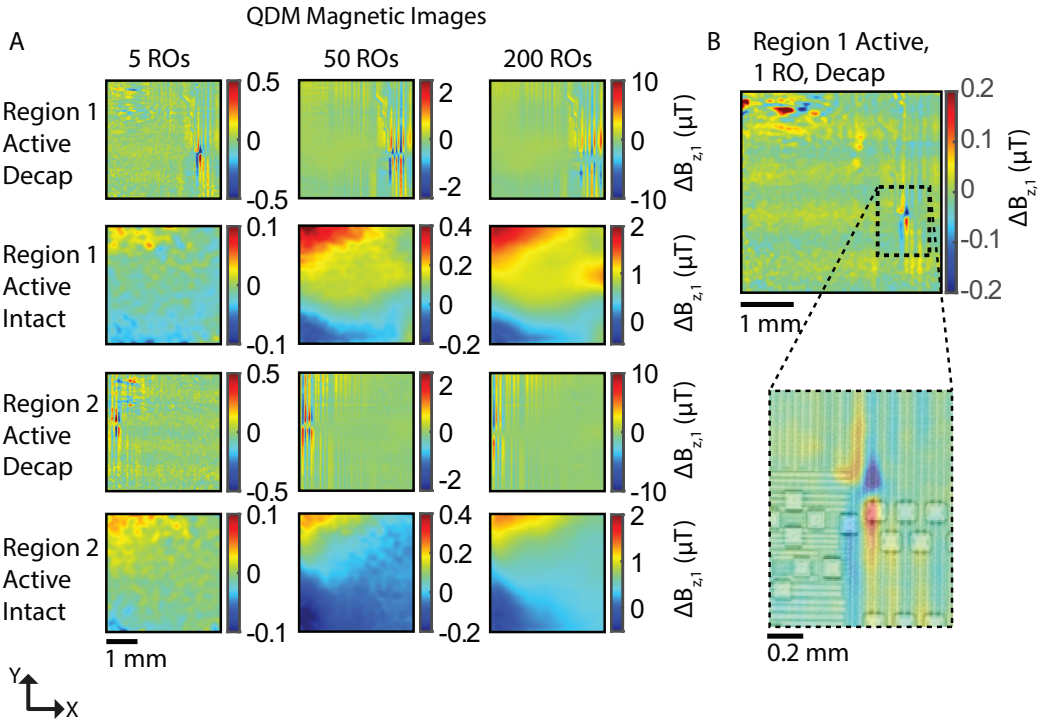

Figure 5.11: (A) QDM magnetic images indicate sensitivity to changing the number of ring oscillators in different regions for the decapsulated and intact chip when performing overlapped measurements. Different scale bars are used for feature clarity. (B) Decapsulated QDM data of $\Delta B_{z,1}$ for a single active ring oscillator in Region 1, demonstrating measurement sensitivity to the magnetic field from current supplying 1 ring oscillator. Inset: Overlay of the magnified single ring oscillator magnetic field image with a high resolution optical image of the circuit die. Each image is the average of 10 QDM (nominally identical) measurements.

and the intact FPGA. Magnetic fields are generally reduced with diminishing numbers of ring oscillators, due to the smaller current densities required for power distribution to smaller clusters. The maximum field amplitude is found not to scale linearly with number of ring oscillators due to the currents being distributed over a differing number of wires on the top metal layer. The $\sim$ 200 nT magnetic field arising from a single ring oscillator is detectable for the decapsulated chip, Figure 5.11(B), given the experimental noise floor of 20 nT. The overlay of the measured magnetic field and the top metal layer illustrates potential location of vias where current is routed to deeper metal layers.

Magnetic fields measured for the intact chip are decreased in magnitude and have lower intrinsic spatial resolution due to the large stand-off distance, compared to the decapsulated chip. The suppression of higher spatial frequency signals at large stand-off distances allows for more aggressive binning and spatial filtering of the intact data, without sacrificing spatial resolution and field information. This approach enables a lower noise floor of 2 nT for the intact chip data, which partially overcomes the reduction of field amplitude with distance. For some regions of the field-of-view the noise floor is limited by state-independent variation in the magnetic field likely due to long-time power instability of the board. In order to enhance sensitivity and push the speed at which measurements can be taken, diamonds with thicker NV layers can be utilized to increase total fluorescence at the cost of spatial resolution. Such methodology may be especially beneficial when performing intact measurements, where the spatial resolution is already limited by the package stand-off distance.

The dependence of current on the ring oscillator cluster size leads to state dependent temperature changes of the FPGA, which are determined from NV ODMR measurements using Equation 5.10. Due to the high thermal conductivity of the diamond chip, there is no spatial structure in the resultant temperature maps. However, from temperature measurements over the entire field-of-view, we are able to determine a scaling of $\sim .0075°C$

per active ring oscillator; with a temperature increase of $\sim 1.5°C$ for the 200 ring oscillator state.

Representative Images for Low Number of Active ROs

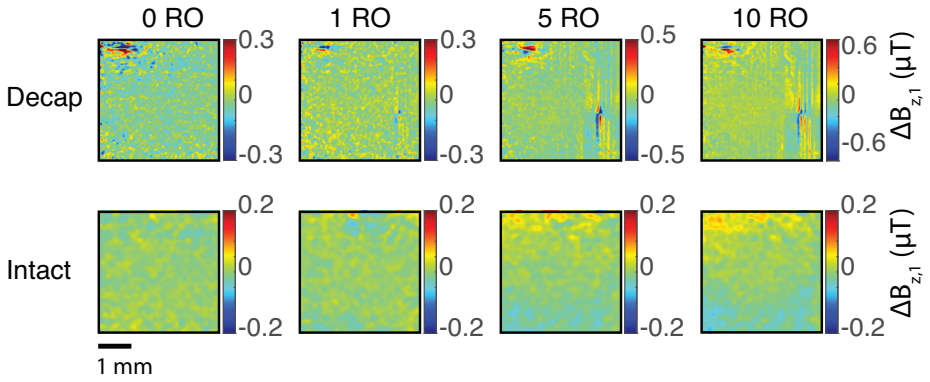

Figure 5.12: Representative QDM images of single runs of activity states with small numbers of RO that are used as inputs for the machine learning classification. The differences in the decapsulated chip states are observable through inspection, but the intact chip state differences are more subtle.

Representative QDM images taken from a series of measurements for single acquisitions of low numbers of ROs are given in Figure 5.12 for decapsulated and intact chips. Long term drift and large background fields are corrected for by subtracting off the nearest idle (0 RO) state in the measurement series. The measured states of the decapsulated chip are relatively easy to classify by visual inspection, consistent with the perfect accuracy in classification presented in Table 5.2. The differences between states are more subtle in the intact data for low number of active ROs. The high classification accuracy (80%) achieved in Table 5.2 for these states illustrates the value of the machine learning classifier.

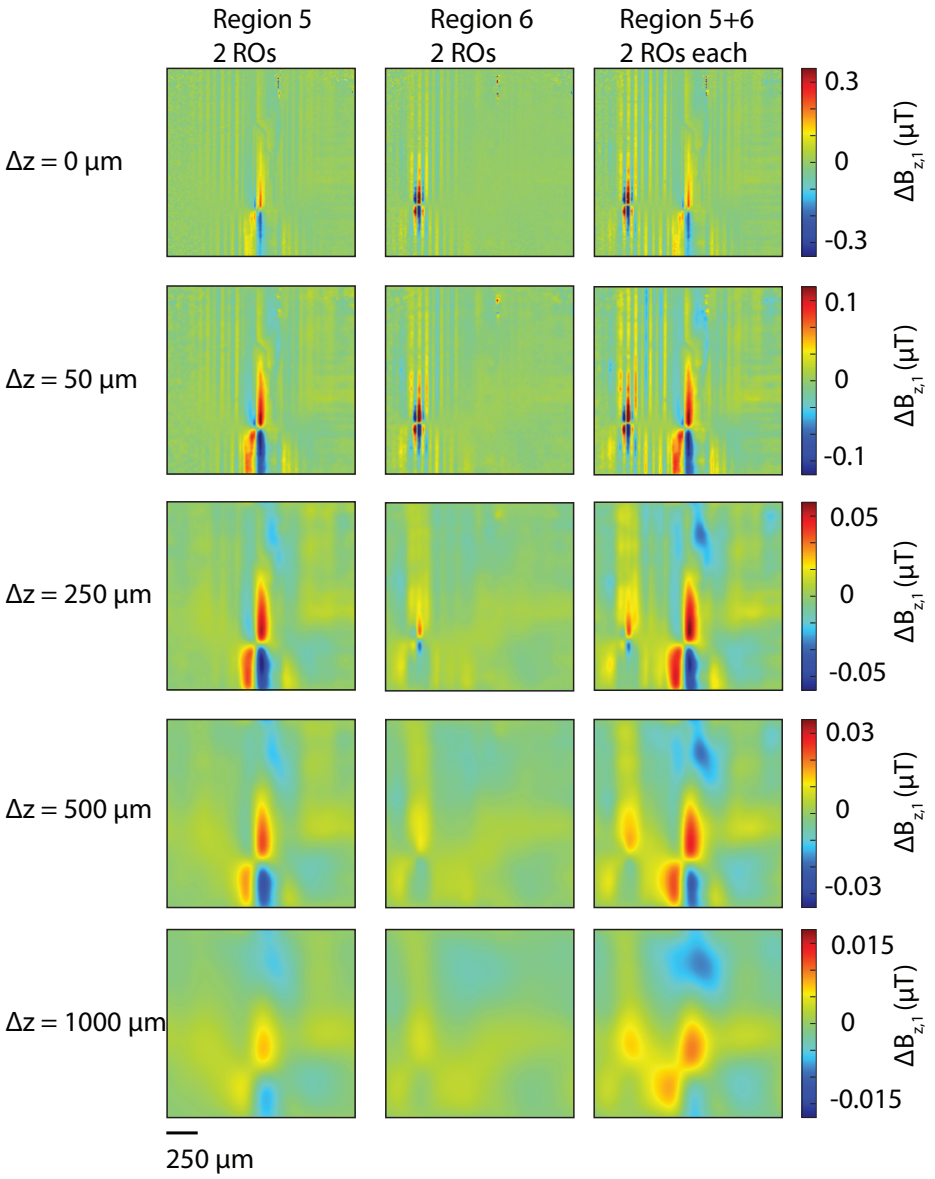

Figure 5.13: Subset of the extended QDM magnetic field dataset with 2 ring oscillators (ROs) active in region 5, region 6, or region 5 and region 6 simultaneously. The top row is high SNR data of 100 measurements taken from the decapsulated chip. Subsequent rows show the calculated magnetic image at different stand-off distances of $\Delta z = 50\ \mu m$, 250 μm, 500 μm, and 1000 μm. The $\Delta z = 500\ \mu m$ row is the closest approximation of measurements taken of an intact chip.

Spatially Distributed RO Dataset

An extended dataset of magnetic field images was collected to further elucidate the impact of the number of measurements per state on the prediction accuracy, as well as the impact of measurement stand-off distance on the ability to discriminate between spatially separated activity on the integrated circuit. Two proximal regions, defined as Region 5 and Region 6, were used to further test spatial discrimination capabilities of PCA and SVM. The data consist of 100 measurements taken per state on the decapsulated chip for 12 different states. The states were composed of clusters of 0, 2, 4, or 6 ring oscillators that are activated in Region 5, or Region 6, or simultaneously in both Region 5 and Region 6.

The effect of measuring at different stand-off distances is simulated using upward continuation [45] to calculate the expected magnetic field at a large stand-off distance, Δz. Figure 5.13 shows the average of the 100 measurements for 3 of the 12 different states and projections at $\Delta z = 0$ μm (decapsulated dataset), 50 μm, 250 μm, 500 μm (analog to an intact chip), and 1000 μm.

Distinct spatial patterns are evident for the activation of 2 ring oscillators in region 5 and region 6. Specifically, a greater number of oscillations in the magnetic field polarity are present in region 6 compared to region 5. This difference is the result of different routing of power distribution in the top metal layer. Upward continuation of the data results in a decrease the magnetic field amplitude that occurs more rapidly in region 6 as a function of stand-off distance than in region 5. This difference is expected due to the cancellation of the large number of oscillating fields from neighboring wires in region 6. Even at $\Delta z = 1000$ μm, there is clear spatial desirability between all of the states, which is further quantified with PCA and SVM analysis.

5.2.6 Interpretation of the Sources

The QDM magnetic field images shown in Figures 5.7 and 5.11 result from current density sources located at various depths in the decapped and intact FPGA. Current is distributed in the interconnect layers of the silicon die and the package substrate. Each layer acts as a quasi two-dimensional current source contributing to the overall magnetic field detected by the NVs. The stand-off distance between the NV sensing plane and the current sources determines which metal layer dominates the field measurement. Generally, small wire features close to the sensing plane will dominate for small stand-off distance and large wire features far from the sensing plane will dominate for large stand-off distances.

For example, the 21 μm wide wires of the top metal layer contribute to the measured ΔB_X and ΔB_Z fields in the QDM images of the decapped FPGA, as seen by the spatial features of the fields in Figure 5.7. Topside decapsulation removes the 500 μm of epoxy packaging above the die shown in the SEM in Figure 5.3(E). This results in a $5-10$ μm stand-off distance between the top metal layer and the NV sensing plane, which is sufficiently small to resolve the spatial variation of fields resulting from currents in the top metal layer. Fields from smaller wires in the metal stacks below the top metal layer are too distant to contribute significantly to the measured field.

The measured magnetic field distributions for both the decapsulated and intact chips include contributions from large current sources far from the NV sensing plane. These sources consist primarily of the metal layers of the 400 μm thick package substrate. The 300 μm silicon die separates the NV layer from the top of the package substrate for the decapsulated chip. An additional separation of $\sim$500 μm due to the epoxy gives a total stand-off distance of about 800 μm for the intact chip. These large current sources result in the broad features of the measured ΔB_Y data for the decapsulated chip in Figure 5.7(A), and of the measured $\Delta B_{z,1}$ for the intact chip in Figure 5.11(A). The dominant contribution

of the substrate layers explains differences in the measured fields of the intact chip compared to those of the decapsulated chip, even when the latter are low pass filtered to account for the difference in measurement stand-off.

Comparison of the measured data with finite element analysis simulations support the interpretation of the data as resulting from contributions of current sources in different layers at different depths from the NV plane. The finite element analysis model, constructed in COMSOL Multiphysics, consists of 21.6 μm wires in the top metal layer with inter-wire spacing of 12.7 μm, and 100 μm thick metal wires in the package substrate layer with inter-wire spacing of 100 μm. An inter-layer separation of 300 μm represents the thickness of the silicon die. A current of $\sim$10 mA is applied to the wires in each layer with alternating bias to approximate the current of 200 active ring oscillators. Plots of B_Z for planes at 25 μm and a 500 μm above the top metal layer are given in Figure 5.14 for comparison with the NV measurements at the nominal stand-off distances for decapsulated and intact chips respectively. The spatial features of the small wires are only evident in the B_Z field of the plane with small stand-off, whereas the contribution of the large wires dominates at large stand-off distances.

The measurements presented in Figures 5.7 and 5.11 are the net static magnetic fields resulting from steady-state ring oscillator operation in the FPGA. The static fields are interpreted to result from a time-averaged superposition of dynamic current draws from the top metal layer to the transistor level. The ring oscillators used for this experiment each consist of three CMOS inverters that sequentially switch state during ring oscillator operation. A small, short-circuit current spike occurs in every inverter that switches state (due to simultaneous conduction through the two transistors of the inverter inducing a transient current path from supply voltage to ground). However, the individual switching of the inverters in the ring oscillators is not temporally synchronized, resulting in a time-

averaged, steady-state current draw from the top metal layer, and a consequently measurable static magnetic field as seen in Figure 5.4.

5.2.7 COMSOL Simulations

The stand-off distance between the NV measurement plane and the magnetic field sources impacts the measurement sensitivity and spatial resolution. The FPGA contains multiple layers of interconnects: eleven metal layers in the silicon die and additional metal layers in the package of the FPGA that connect the bond wires to the ball grid array. These structures are visible in the SEM images of the FPGA cross section shown in Figure 5.3. The metal layers in the silicon die have micron to sub-micron length scales, whereas the package interconnects have 10-100 μm length scales.

The current densities in these metal layers act as sources of the measured magnetic fields. The stand-off distance of the NV layer and the sources determines which metal layer contributions dominate. The NV layer was within ∼5-10 μm of the top metal layer of the die and within 300 μm of the package interconnects for the decapsulated chip. The resulting field measurements were dominated by the close, top metal layer. The resin-epoxy layer of the intact chip increased the stand-off distance of the NV plane to 500 μm from the top metal layer and 800 μm from the package interconnects. The resulting field measurements for the intact chip were dominated by the large and distant package interconnects.

This near- and far-field behavior of static magnetic fields is demonstrated using finite element analysis modeling with the commercial finite element software COMSOL 5.4 (Comsol, Inc.). The model geometry, depicted in Figure 5.14, includes the 21.6 µm wide wires of the top metal layer with 12.6 µm inter-wire spacing and the 100 µm wide wires of the package interconnects with 100 µm inter-wire spacing. The two layers are defined in the X–Y plane and are separated in Z by the 300 µm of the silicon die. The governing

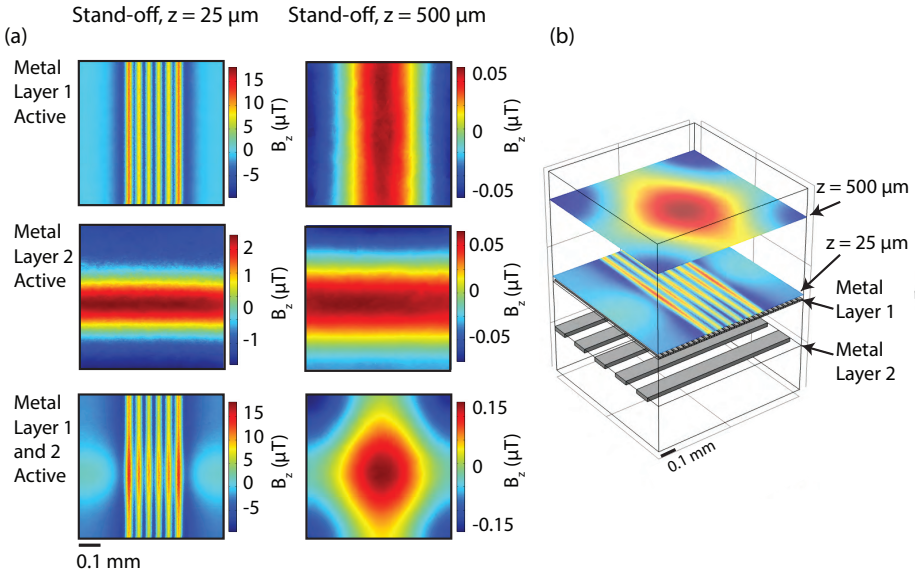

Figure 5.14: (A) COMSOL Simulations of magnetic fields from a configuration of two layers of metal wires representing the small top metal layer (denoted metal layer 1) of the FPGA die and the large interconnect wires (denoted metal layer 2) of the package. The simulations reveal that different features have an importance that is weighted by the stand-off distance. Small, nearby sources dominate with small stand-off distance, and large, far away sources dominate with large stand-off distance. (B) 3D visualization of the measurement planes relative to the position of the current sources.

magnetostatic equation $\nabla \times \mathbf{H} = \mathbf{J}$ is solved for the model geometry with $\mu\mathbf{H} = \mathbf{B}$, with a magnetic insulation boundary condition, $\mathbf{n} \times \mathbf{A} = 0$ for $\mathbf{B} = \nabla \times \mathbf{A}$, and a current of ∼10 mA applied with reverse bias on a subset of adjacent wires in each layer. The current magnitude was chosen to be similar to the measured current drawn by the board with 200 ROs active on the FPGA. A tetrahederal mesh was used consisting of elements half the size of the 12.6 µm wire spacing in the vicinity of the top metal layer, and scaled up for regions of the computational domain far away from the wires.

The magnetic inductance $\mathbf{B}$ is solved for everywhere in the domain using COMSOL's Magnetic Fields (mf) module. The calculation is completed in two stages: the current density in the wire domains is initially solved for using the applied current condition and the electrical conductivity of the wires, $\sigma = 6{\times}10^7$ S/m; the current density is then used as the source term to determine the magnetostatic fields.

Figure 5.14 plots the resulting magnetic fields for three cases: (i) a current bias applied to the wires in both metal layers, (ii) a current bias applied to wires in only the top metal layer, (iii) a current bias applied only to wires in the package (bottom) layer. The resulting X–Y magnetic fields for each case are plotted at two Z stand-off distances, 25 μm and 500 μm, corresponding to the decapsulated and intact chip measurement configurations respectively. For the case of current applied to both metal layers, the magnetic fields from the small wires of the top metal layer are seen to dominate for the measurement plane with small stand-off distance, whereas the magnetic fields from the wires of the bottom interconnect layer are seen to dominate for the large stand-off distance.

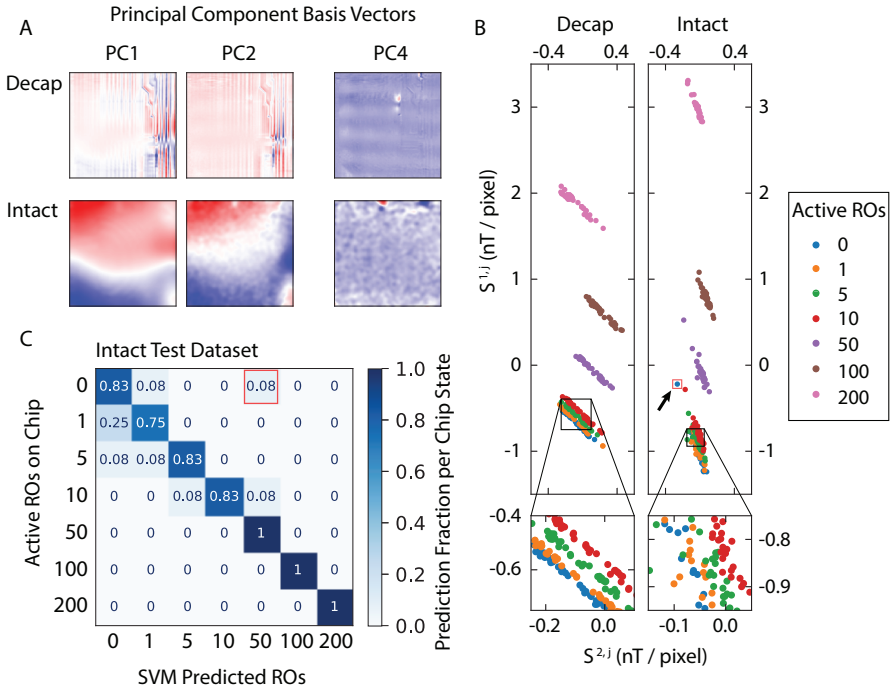

Figure 5.15: Principal component analysis (PCA) and support vector machine (SVM) classification of QDM images. Region 1 is active with 0, 1, 5, 10, 50, 100, or 200 ring oscillators. (A) Example principal component basis vectors plotted as images for both decapsulated (decap) and intact data sets. PC1 and PC2 are shown to exemplify principal components that resemble magnetic field images and thus will be useful in chip state classification. PC4 is shown as an example principal component that captures activity state independent variations and thus will not be useful in chip state classification. (B) The PCA score for PC1, $S^{1,j}$, is plotted against the score for PC2, $S^{2,j}$, for each magnetic field image, $\mathbf{B}^j$, as a demonstration of state distinguishability . This distinguishability is evidenced by the separation of colors representing differing numbers of active ring oscillators. Insets magnify the scores for small numbers of ring oscillators, and show greater fidelity of state separation in the decapsulated data set compared to the intact data set. (C) Table of SVM predictions on the test set for the intact images. For each unique value of active ring oscillators, there are 12 images in the test set. Rows indicate the fraction of images predicted for each of the possible chip states. All but one prediction (indicated by the red boxes in (B) and (C)) lie on or near the main diagonal demonstrating the high predictive power of the SVM classifier. The corresponding table for the decapsulated data set is not shown, as the main diagonal would contain 1's and the off diagonals would contain 0's due to the perfect separability of each state (see Table 5.2).

5.3 Machine Learning Analysis

Forward modeling of the current distributions and resulting magnetic fields for the different ring oscillator states programmed on the FPGA is an intractable problem without complete knowledge of the wire layout and current paths. Interpretation of the QDM measurements by comparison with forward-model simulations is therefore limited to the arguments such as those presented in the previous section. However, automated machine learning algorithms can be applied to the QDM data to discriminate between and ultimately classify the different operating states. Ideally, a magnetic field image is used as input to an machine learning algorithm, and the functional state, defined as the number of active ring oscillators in this initial demonstration, is determined as the output. In practice, this problem is approached with a limited data set of magnetic field images for each FPGA state; and a dimensionality reduction algorithm is employed before applying a classification technique using the Python [275] package `scikit-learn` [276].

5.3.1 Data Preprocessing

QDM data undergoes a series of preprocessing steps in preparation for dimensionality reduction and classification. Only images with Region 1 active are used so that the number of ring oscillators is predicted by the classification scheme. The number of ring oscillators activated for any given image is one of 0, 1, 5, 10, 50, 100, or 200. The data set consists of 40 QDM images per ring oscillator state for the decapsulated chip and 32 images per ring oscillator state for the intact chip. These $M \times N$ images are subsequently binned such that the decapsulated images contain 600×606 pixels and the intact images contain 300×303 pixels, while covering the same field-of-view. Measurements of the idle state (0 ring oscillators) are randomly taken during data collection to account for long term drifts. These idle state measurements are subtracted from active state images nearest in time. The intact and

decapsulated data sets are split into training and test sets so that the prediction accuracy of the trained model can be estimated on data that the training procedure has not encountered. The splits are 75%/25% for the decapsulated images and 64%/36% for the intact images.

5.3.2 QDM Image Dimensionality Reduction

Each magnetic field image is composed of $\sim 10^5$ pixels and thus occupy a high dimensional space for classification. Principal component analysis [277, 278] (PCA) is therefore used to reduce the dimensionality of the classification problem. PCA is a well-established technique that determines the highest variability axes of a high-dimensional data set. PCA amounts to an eigenanalysis where the eigenvectors, called principal components, correspond to the axes of interest; and the eigenvalues relate to the amount of data variance along the respective principal components.

PCA is applied separately to the data sets of the decapsulated chip and the intact chip with the `scikit-learn` class `decomposition.PCA()` and yields principal components such as those plotted in Figure 5.15(A). Spatial patterns evident in the principal components are also present in the magnetic field images of Figure 5.11(A), confirming that these features are physically significant and important for distinguishing between different samples. There exist as many principal components as dimensions in the data set; however, only the first several principal components capture non-noise based information. We determine that >99% of the variance in the intact and decapsulated data sets is captured by the first 9 principal components, which are therefore the only principal components used in this analysis.

The scores of these first 9 principal components are used to effectively reduce the dimensionality of the magnetic field images from $\sim 10^5$ pixels to 9 scores. The principal component scores, $S^{i,j}$, are determined by taking the dot product of the i^{th} principal component, defined as $\mathbf{W}^i$, with the j^{th} image, $\mathbf{B}^j$, and normalized by the total number of pixels.

This gives

$$S^{i,j} = \frac{1}{MN} \sum_{m=1}^{M} \sum_{n=1}^{N} W^{i}_{m,n} B^{j}_{m,n} \tag{5.13}$$

for the first 9 principal components. Figure 5.15(B) shows examples of the PCA scores: the score for PC1 is plotted against the score for PC2 for each magnetic field image of both the decapsulated and intact data.

The plot is color coded by number of active ring oscillators showing that these two scores are useful in distinguishing the number of active ring oscillators on the FPGA for both decapsulated and intact measurements. Classification of the active number of ring oscillators is accomplished by using the first 9 PCA scores as input to a support vector machine (SVM) classifier algorithm. The spread of data points along a fixed slope for each state in Figure 5.15(B) is consistent with small offsets between different image acquisitions.

In addition to the PC 1 score versus PC 2 score plot shown in Figure 5.15(B), Figure 5.16 shows all 10 pairs of scores for PCs 1 through 5 in both the decapsulated and intact datasets. The scores are normalized by the number of pixels in each image (different for the decapsulated and intact datasets) so as to give an idea of the contribution of each PC to the magnetic field images.

PCs that are useful in chip activity state classification are distinguishable from those that are not. For example, in the decapsulated dataset, PC 4 does not well separate differing numbers of ring oscillators (ROs), which is expected as it had the lowest importance factor of the first 5 PCs. Furthermore, PC 5 is useful in separating 1, 5, and 10 ROs, while PCs 1 and 2 are useful in separating 50, 100, and 200 ROs. In the intact dataset, PCs 1 and 2 are the most useful and PCs 4 and 5 are the least useful as expected from their high and low importance factors, respectively.

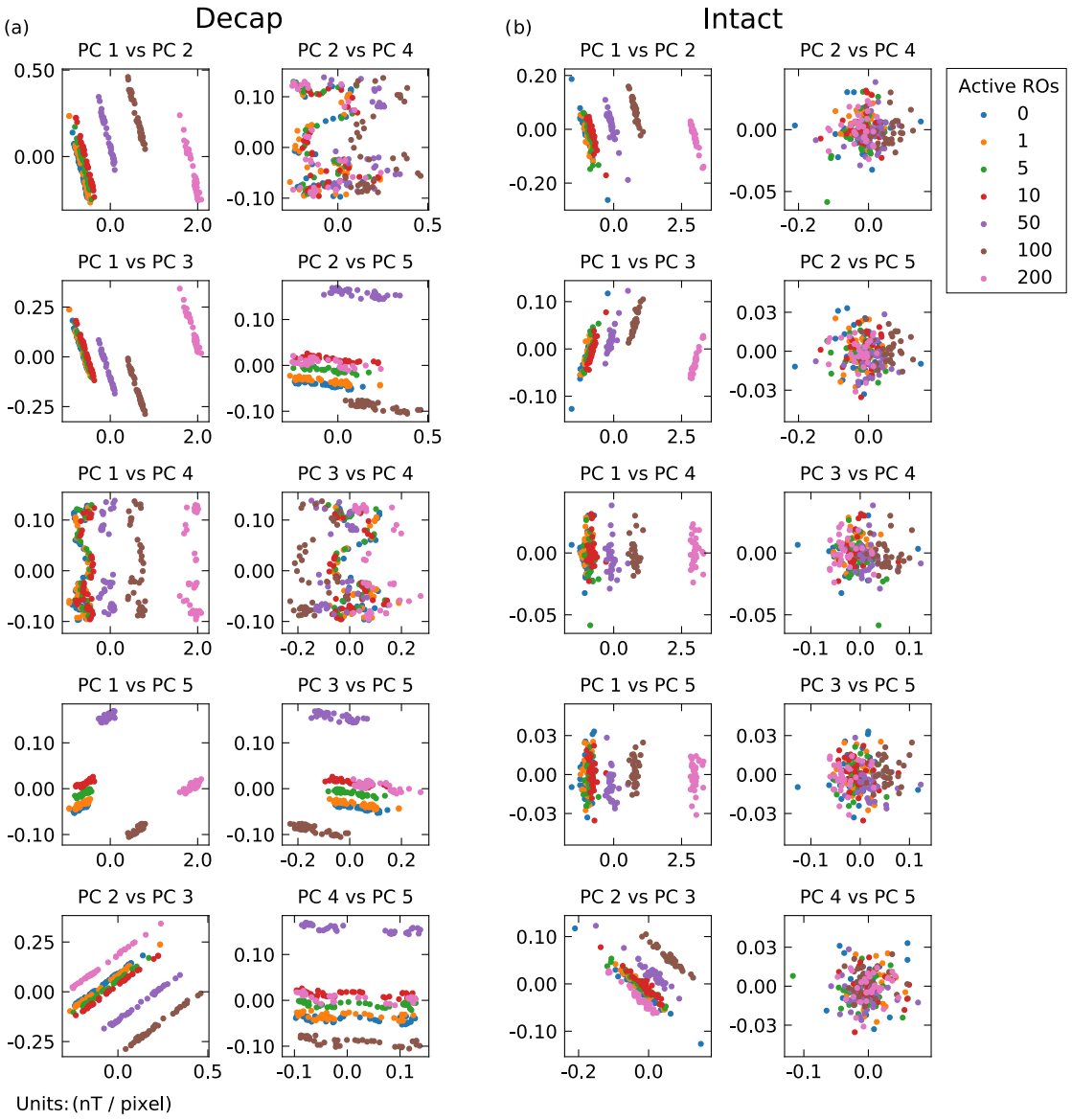

Figure 5.16: (A) Pairs of PC scores plotted against each other for PCs 1 through 5 in the decapsulated (decap) dataset. Units are nT / pixel and active number of ring oscillators (ROs) is color coded according to the legend. (B) The analogous plot for the intact dataset.

Noise Propagation in PCA

A better intuition for the spread of datapoints in the PC score plots is obtained from looking at the impact of two simple sources of extraneous variation on the value of the PC score.

These sources are spatially uniform offsets (for example, this well approximates drifts in the bias field or temperature variations) and Gaussian noise from shot noise on the pixels. As defined previously, the PC score is:

$$S^{i,j} = \frac{1}{MN} \sum_{m=1}^{M} \sum_{n=1}^{N} W^{i}_{m,n} B^{j}_{m,n} \tag{5.14}$$

where each image is composed of $M \times N$ pixels, $\mathbf{B}^j$ is the magnetic field image, and $\mathbf{W}^i$ is the i'th principal component.

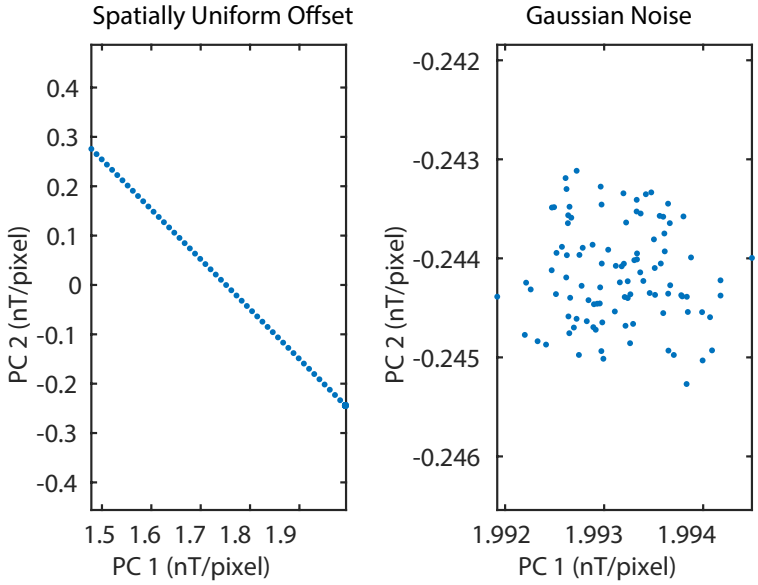

Figure 5.17: The impact of different noise sources on PCA, shown for an example of the QDM magnetic image for 200 ROs on the decapsulated chip. (A) A spatially uniform offset of 10 nT is added between each point along the line. (B) Gaussian noise with standard deviation of 100 nT is added. Note the dramatically different scales between the two plots.

A spatially uniform offset, Δ, is a constant value added to every pixel of an image, and can propagate through to the principal component analysis. The first two principal

components of the decapsulated and intact chip analysis are used to explicitly determine the nature of Δ propagation through the PC analysis. The addition of Δ to a magnetic field image will result in an additional contribution, $\delta_\Delta S^{i,j}$, to the PC score giving

$$\begin{aligned} S^{i,j} + \delta_\Delta S^{i,j} &= \frac{1}{MN}\sum_{m=1}^{M}\sum_{n=1}^{N} W^i_{m,n}(B^j_{m,n} + \Delta) \\ &= \frac{1}{MN}\sum_{m=1}^{M}\sum_{n=1}^{N} W^i_{m,n}B^j_{m,n} + \frac{1}{MN}\sum_{m=1}^{M}\sum_{n=1}^{N} W^i_{m,n}\Delta \end{aligned} \tag{5.15}$$

The first term is just the original score, Eq. 5.13, for the magnetic field $B^j_{m,n}$, so $\delta_\Delta S^{i,j}$ can be solved for directly. Since Δ is a spatially uniform offset, it can be pulled out of the summation

$$\delta_\Delta S^{i,j} = \frac{\Delta}{MN}\sum_{m=1}^{M}\sum_{n=1}^{N} W^i_{m,n} \tag{5.16}$$

Each PC score will have a different value $\delta_\Delta S^{i,j}$ from the offset Δ due to the summation. The expected slope of the line for the PC2 versus PC1 plotted in Figure 5.15 is determined by $\delta_\Delta S_1/\delta_\Delta S_2$; this ratio gives a slope of -0.99, consistent with the slope in Figure 5.15. Any spatially uniform variations for a given FPGA activity state between different images will fall on a line with this slope. For the intact dataset, the principal components are different and the expected slope of variation is $\delta_\Delta S_1/\delta_\Delta S_2 \sim -3.03$, which is consistent with the Figure 5.15.

The addition of spatial Gaussian noise ($X_{m,n}$) with zero mean and standard deviation α to a magnetic field image will result in an additional contribution to the PC score giving

$$\begin{aligned} S^{i,j} + \delta_{\alpha X} S^{i,j} &= \frac{1}{MN}\sum_{m=1}^{M}\sum_{n=1}^{N} W^i_{m,n}(B^j_{m,n} + \alpha X_{m,n}) \\ &= \frac{1}{MN}\sum_{m=1}^{M}\sum_{n=1}^{N} W^i_{m,n}B^j_{m,n} + \frac{1}{MN}\sum_{m=1}^{M}\sum_{n=1}^{N} W^i_{m,n}\alpha X_{m,n} \end{aligned} \tag{5.17}$$

Similar to Eq. 5.16, the contribution due to Gaussian noise can be separated, yielding

$$\delta_{\alpha X} S^{i,j} = \frac{\alpha}{MN}\sum_{m=1}^{M}\sum_{n=1}^{N} W^i_{m,n}X_{m,n} \tag{5.18}$$

The value and properties of this term depend on the precise spatial distribution of $W^i_{m,n}X_{m,n}$, so no general statement can be made on the impact of Gaussian noise. Figure 5.17 shows numerical simulations for these two different possible sources of variation, spatially uniform offsets and Gaussian noise. The plots confirm the general intuition from the results of the above derivations. In the specific case of PC1 and PC2 for the decapsulated and intact chips with $\alpha \approx \Delta$, one then has $\delta_\Delta S^{i,j} \gg \delta_{\alpha X} S^{i,j}$.

Further numerical simulations would be needed for other sources of variation including multiplicative noise, spatially varying offsets, etc., due to a strong dependence on the exact spatial features of the magnetic field images and principal component basis vectors.

5.3.3 Integrated Circuit Activity State Classification

A support vector machine [279] (SVM) is the supervised classification technique used to classify the magnetic field images, leveraging their key features characterized by the PCA scores. SVMs are a set of algorithms that seek to classify samples by creating a boundary between categories of a training data set that maximizes the gap separating those categories. Samples from a test set are then classified in relation to this boundary. The `scikit-learn` class `svm.SVC()` is used as a multi-dimension, multi-category classifier. The categories for classification are the chip states given by the number of ring oscillators. The dimensionality is given by the 9 PCA scores recorded for each image.

5.3.4 Classification Results

The full machine learning model, including preprocessing, PCA, and SVM, is fit using the training set and subsequently evaluated on the test set, for both decapped and intact FPGA data. The machine learning model efficacy, summarized in Table 5.2, is determined by the accuracy of the test set evaluations. FPGA activity states are well separated in PCA-space

	Number of ROs (Region 1)							Total
	0	1	5	10	50	100	200	
Decapsulated	1.00	1.00	1.00	1.00	1.00	1.00	1.00	1.00
Intact	0.83	0.75	0.83	0.83	1.00	1.00	1.00	0.89

Table 5.2: Chip state prediction accuracy on the test dataset (ROs = ring oscillators).

for the decapsulated data set. Predictions on the test set consequently yield perfect accuracy, even for small numbers of ring oscillators, consistent with expectations.

Results for intact data set are similarly well separated for large numbers of ring oscillators, resulting in perfect prediction accuracy for $\geq$50 ring oscillators. However, FPGA activity states are not fully separated for <50 ring oscillators, resulting in imperfect predictions. Nonetheless, the trained machine learning model achieves $\sim$ 80% accuracy for each of 0, 1, 5, and 10 ring oscillator active states. Figure 5.15(C) additionally shows that incorrect predictions are nearly always close to the correct state. For example, the model predicts 5 ring oscillators correctly in 83% of test cases, with misclassifications of 0 or 1 ring oscillator otherwise. The red box in Figure 5.15(C) indicates a single case for which the classifier incorrectly predicts 50 ring oscillators for a 0 ring oscillator state. An arrow and analogous red box in Figure 5.15(B) shows that the PCA score for this state is an outlier in the data.

The positive classification results presented in Figure 5.15 give an initial demonstration of the capability of combined QDM and machine learning techniques to identify integrated circuit activity via non-invasive magnetic field imaging. The present results using ring oscillators are also potentially translatable to approaches that use the power side channel for chip activity analysis [280–282].

Spatially Distributed RO Dataset Analysis

The extended dataset presented previously was taken to further elucidate the benefit of a large number of measurements per state on the prediction accuracy. Furthermore, the definition of state for the purpose of classification was expanded to include both number of ring oscillators and region activated. This dataset was also used to determine the impact of measurement stand-off distance on the ability to discriminate between spatially separated activity on the integrated circuit. This dataset was analyzed with the state classification criteria defined to include the spatial location of the active region in addition to the number of ring oscillators per region.

The PCA + SVM analysis presented was also performed on the extended dataset. However, in the case of the extended dataset, state classification is determined by the spatial location of the active region in addition to number of ROs per region. Thus a correct classification for the purposes of model accuracy consists of correctly identifying both the active region(s) as well as the number of active ring oscillators per active state; i.e. a state is defined as [active region, number of active ROs]. Accuracy is defined as the fraction of states correctly classified. The robustness of the dataset is tested by estimating the model accuracy as a function of the dataset size, shown in Figure 5.18(A). The upward continued dataset with $\Delta z = 500\,\mu$m is used and the size of the dataset is varied from 10 samples per state to 100 samples per state. A train-test split of 64%/36% is used to mimic the analysis of the intact dataset. The training set has 100% accuracy when the number of samples per state is less than 60, but dips slightly below 100% for larger datasets. This is expected since the algorithm complexity is fixed but the absolute deviations in the data increase with sample size. Despite the increased error rate in the training set for larger samples per state, the larger datasets allow the model to learn the underlying structures of the dataset and consequently generalize better to unseen data. Thus the accuracy increases from 75% at 10

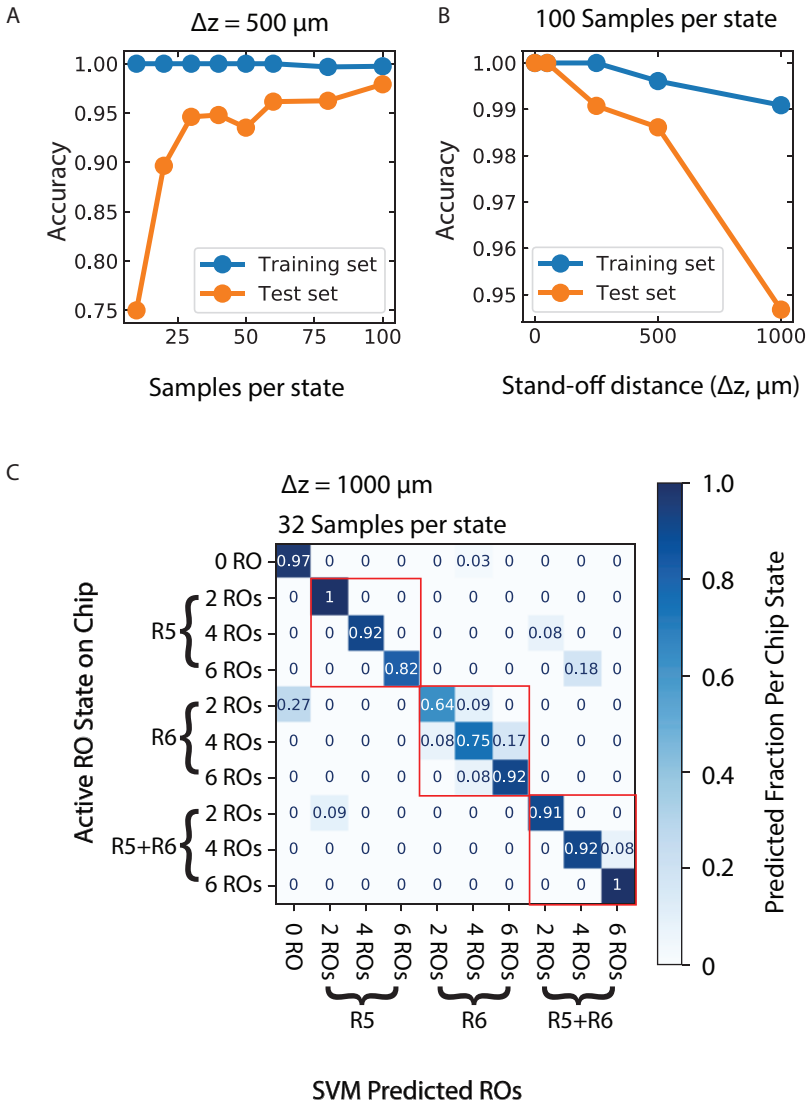

Figure 5.18: PCA + SVM model performance metrics of the extended dataset. (A) Model accuracy is plotted as a function of the size of the dataset for both the training and test sets. A stand-off distance of 500 μm is chosen to most closely replicate the intact dataset. (B) Model accuracy is plotted as a function of the stand-off distance. The full dataset is used (100 samples per state). (C) Matrix of state predictions versus active state on chip at a stand-off distance of 1000 μm. The matrix is row normalized to 1 so that each element represents the fraction of measurements of a given state that were predicted to be any state. The red boxes enclose predictions for which the predicted region and active region are the same.

samples per state to 97% with 100 samples per state. Beyond 30 to 40 samples per state, the accuracy begins to level off, suggesting that 100 samples per state is enough data to get the maximum benefit from the PCA + SVM model.

The analysis is performed at various stand-off distances to test the predictive power of the model at varying levels of signal degradation. The difference between the intact chip and the decapsulated chip is about 500μm of package material and thus $\Delta z = 500\,\mu$m is the best estimate for an analogous dataset taken from an intact chip. Figure 5.18(B) shows the model accuracy as a function of stand-off distance when the entire dataset is used (100 samples per state). As expected, perfect classification is achieved for small stand-off distances and monotonically decreases in accuracy with increasing stand-off distance. Importantly, for $\Delta z = 500\,\mu$m, $> 98\%$ accuracy is achieved on the test set, implying that an analogous intact dataset would have a high degree of spatial state classification in addition to local power classification.

Finally, to further elucidate the ability to perform spatial classification, the state by state predication rates are shown in Figure 5.18(C). Results with 32 samples per state are shown to mimic the dataset analysed previously. A stand-off distance of $\Delta z = 1000\,\mu$m is chosen to show that prediction errors occur in accordance with expectations. Figure 5.18(C) presents the fraction of images with a given state that were predicted to be each possible state. Most predictions lie on the main diagonal as the overall accuracy is about 89%. The red boxes show states from one region that were predicted to be in the same region. The majority of misclassifications are expected to lie in these red boxes. This is clearly the case, especially for region 6. In this region, 2 ring oscillators are misclassified as either 0 ring oscillators or 4 ring oscillators from the same region. 4 ring oscillators are misclassified as either 2 or 6 ring oscillators, and 6 ring oscillators are misclassified as 4 ring oscillators. The fact that this region has the highest error rate is consistent with expectation because the

features in this region become less distinguishable as stand-off distance increases. Most of the remaining misclassifications are between region 5 and regions 5+6, which is expected since these regions look visually similar as seen in Figure 5.13.

This result indicates that a high degree of spatial state classification is possible in addition to local power classification using a large number of samples per state. Large data sets such as these combined with more powerful machine learning methods have promise to enable classification of a wide array of chip activity in the context of hardware security and fault detection. Future directions for this project are discussed in greater depth in Chapter 7.

Chapter 6

Real Time Imaging of Magnetic Fields

6.1 Introduction

The ability to image small magnetic fields at >1 kHz rates in real time would allow progression in large number of applications ranging from monitoring of biological circuits to localizing transient activity in integrated circuits to monitoring magnetically labeled cells in microfluidic devices.

This chapter details the development of two different techniques being developed to enable high sampling rate magnetic imaging of DC to kHz scale phenomena. Lock-In CW ODMR Imaging is analogous to the magnetometry method detailed in Chapter 3, except the modulation of a microwave field is synchronized with camera frame acquisition rather than being collected onto a photodiode and demodulated through a lock-in amplifier. The next method, necessary for the detection of small signals, utilizes Ramsey-based magnetometry sequences to improve volume normalize magnetic sensitivity and reduces susceptibility to

Technique	**Sensitivity** ($nT\ Hz^{-1/2}\ \mu m^{3/2}$)	**Field of View**	**Temporal Resolution**	**Robustness**	**Simplicity**
Lock-In ODMR	200 to 1000	500 μm *to* 4 mm	3 kHz (Camera) ~10 to 50 kHz (NV response)	Sensitive to temperature and strain. Correct for inhomogeneities with reference frames	Relatively few technical requirements
Ramsey	10 to 100 ~ 1 (Projected)	50 μm *to* 200 μm	3 kHz (Camera) ~100 kHz (T_2^*, t_I, t_R)	Double Quantum: Robust to strain and temperature	Many components and steps needed

Table 6.1: A brief comparison of the two different fast imaging modalities utilized in this chapter is provided. Lock-In ODMR based imaging methods allows for imaging with modest sensitivity of a large field of view with minor technical requirements. Ramsey based methods allow for improved sensitivity over a smaller field of view, but in general has more stringent technical requirements.

measurement sensitivity and drift due to diamond inhomogeneities and temperature fluctuations.

6.1.1 Biological Motivation

One of the central motivations in this chapter for real time magnetic imaging is mapping biological current propagation in cellular networks, specifically cardiomyocytes [283, 284]. Unlike in neuronal networks where conduction and propagation are influenced through both electronic and chemical signalling, cardiac tissues utilize electronic signalling through the use of gap junctions to maximally synchronize neighboring cells and minimize propagation delay [285–288]. Much work has been historically done utilizing techniques like voltage imaging the map propagation of voltage signals in cardiac tissue [289]. However, imaging of the magnetic field can provide extra information about the conductivity of the tissue and the nature of the anisotropic conductivities in bidomain structures [290, 291, 291–294]. Furthermore, if voltage imaging techniques can be combined with high resolution magnetic field imaging techniques, then the spatial conductivity anisotropy [294,295] and other passive electrical properties could be mapped, which could inform studies involving accumulation of damaged tissue in cardiac muscle and the origin of cardiac disease and arrhythmia [295–298].

Furthermore, the gap junction coupling creates a large effective biological circuit where the passive properties can be probed and imaged through the injection of controlled currents [299]. This could allow for the imaging of the degradation or altering of conduction pathways.

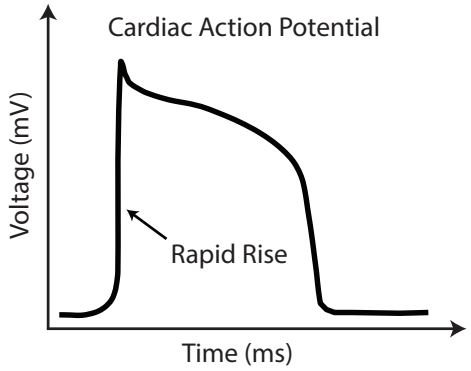

Figure 6.1: Cartoon of the cardiac action potential. This cartoon demonstrates the general features of a cardiac action potential. As presented in Chapter 3, the biomagnetic fields associated with action potentials is proportional to the time derivative. This leads to the expectation that the magnetic field will be maximal near the beginning of the pulse and modest during the fall. This is favorable because the magnetic signal occurs much earlier than the mechanical movement of the cardiomyocyte due to it beating.

A simple model and previous studies can be used to estimate the expected magnetic field strength at the surface of a cardiomyocyte and the volume normalized sensitivity needed to detect the biomagnetic field. Similar to what was found in giant axons [54], the magnetic field at the surface of a cardiomyocyte is on the order of $\sim 1\ nT$ [292]. In order to resolve the contribution of a single cell, a given sensor voxel should be no larger than $\sim (10\ \mu m)^3$. Finally, to resolve the fast temporal dynamics of the rise time of the cardiac action potential (see Figure 6.1), images should be taken with 1 ms temporal resolution. Combing all these constraints, a volume normalized sensitivity of $\eta = 1\ nT\ Hz^{-1/2}\ \mu m^{3/2}$ is required for real time magnetic imaging of cardiac activity with an SNR$\sim$1. If the requirement for single cell resolution is loosened and a sensing voxel of $(40\ \mu m)^3$ is allowed instead, then only $\eta = 8\ nT\ Hz^{-1/2}\ \mu m^{3/2}$ is required. Below, we will explore the current state of the art for

wide-field imaging sensitivity for Lock-In ODMR and Ramsey schemes and what needs to be done to approach these target sensitivities for biological applications.

6.2 Lock-In ODMR Imaging

Lock-In ODMR Imaging combines the lock-in modulation protocol of Chapter 3 and the simultaneous widefield imaging capabilities of Chapter 5 to allow for real time imaging of magnetic field on kHz time scales. Figure 6.2 shows an overview of the general protocol for a sensing sequence.

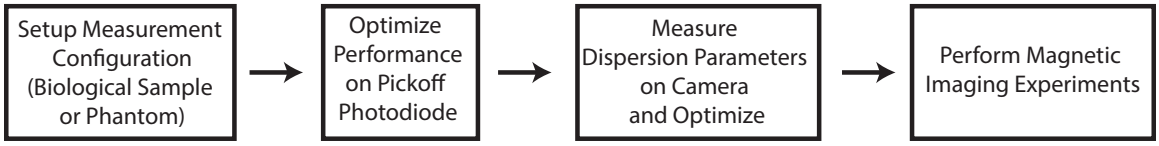

Figure 6.2: Flowchart of the experimental progression for Lock-In ODMR imaging.

6.2.1 Experimental Setup

The experimental setup shown in Figure 6.3 was designed to balance sensitive magnetic imaging, diagnostics for performance optimization, and flexibility for switching between different samples and measurement modalities.

Diamond Details

The diamond substrate used in these experiments is a 3.5 mm by 5 mm electronic grade single crystal (ELSC) chip fabricated via chemical vapor deposition by Element Six. To maximize the amount of light collected and improve performance a thick, 40 μm, layer of 10 ppm ^{15}N with isotopically purified 99.997% ^{12}C grown on top of the substrate. Electron irradiation with a dose of 3×10^{18} e/cm^2, 1 MeV electrons is used to create vacancies in

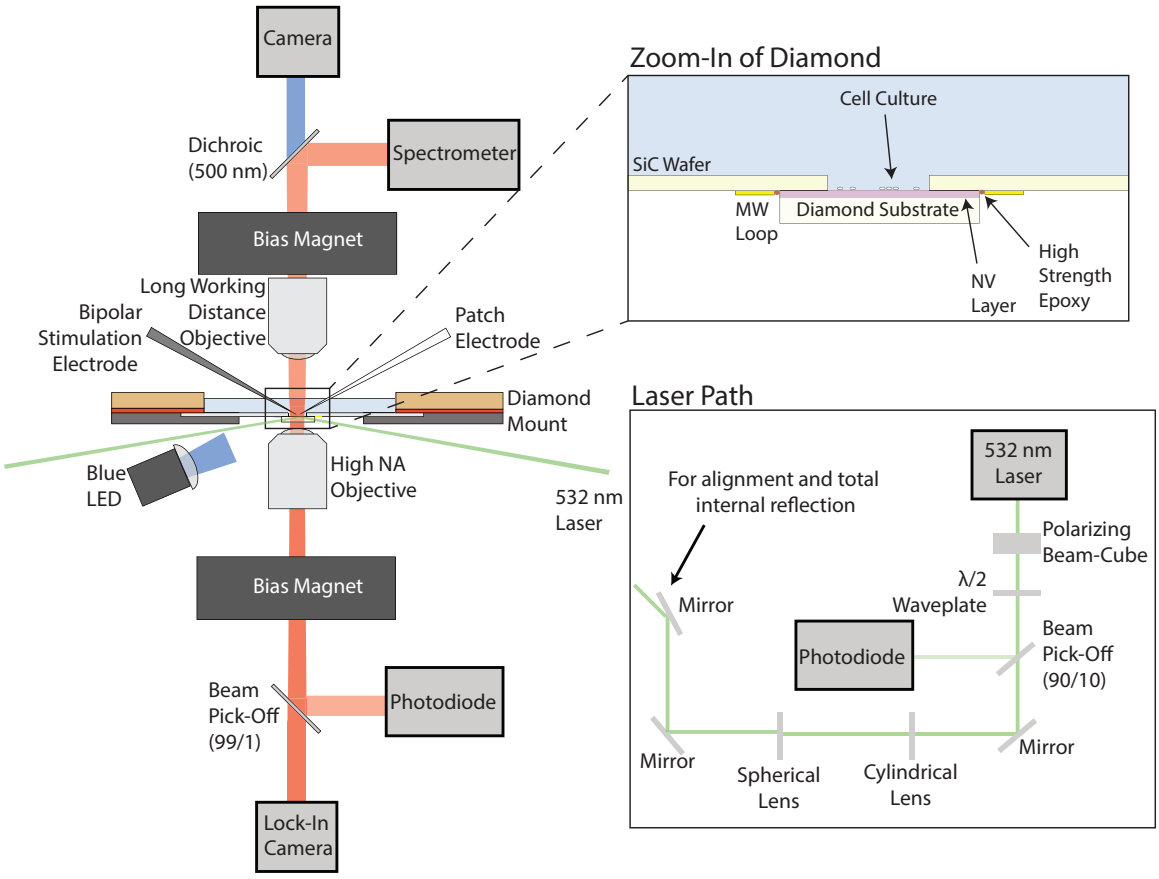

Figure 6.3: Overview of setup used for real time lock-in ODMR magnetic imaging.

the diamond lattice. Annealing at 800°C for 12 hours and 1000°C for 12 hours allows for the diffusion of vacancies to increase the concentration of NV to $\sim$ 2 ppm. The edges of the diamonds are polished optically flat by Delaware Diamond Knives to allow light to be coupled in through the sides for the total internal reflection geometry used below. The diamond is mounted to a 50.8 mm diameter, 330 μm thick semi-insulated silicon carbide (SiC) wafer for mechanical stability and thermal management. As shown in Figure 6.3, a 2 mm by 3 mm hole is laser cut in the center of the wafer to allow for the placement of samples directly on the diamond surface. Due to the need to have greater flexibility in switching samples in and out, a compact experimental mount was developed to allow for robust and repeatable performance. For the higher resolution magnetic imaging experiments performed, the 13 μm layer diamond with [^{14}N] = 27 ppm used in Chapter 3 was utilized.

Laser Excitation

A 5W laser (Coherent Verdi V-5) is used as the excitation source for the magnetic imaging measurements to minimize the contribution of laser intensity noise and allow for collection of a large amount of red fluorescence. Anywhere from 1-4 W of green laser power is employed for a given measurement depending on the experiment being performed (See Figure 6.3 for details). The effect of laser polarization noise is minimized through the use of a polarizing beam cube at the output of the laser. A zero order $\lambda/2$ waveplate modifies the polarization of the laser excitation, in order to optimize the NV response and contrast of the different NV axes for given measurement conditions. A cylindrical lens is used to asymmetrically focus the light to compensate for the elliptic beam shape resulting from the shallow incident angle used for total internal reflection. A subsequent spherical lens focuses the beam so the resulting beamspot projected on the diamond surface has a diameter of 700 μm. Finally, the excitation beam reflects off the mirror and enters the diamond at a shallow angle of $\sim 5°$.

The beam is aligned in order to illuminate the NVs at the center of the diamond on the top surface. Due to the total internal reflection, only the evanescent wave (and scattered light due to any roughness in the diamond surface) of the green excitation impinges upon the measurement sample. As discussed below, one of the optical collection paths includes a spectrometer that allows for the characterization of the amount of green light leaking into the sample above.

Optical Collection

In contrast to the oil condenser based optical collection in Reference [54], an air objective is used to create an optical image onto a camera, rather than maximizing collected light onto a single point detector. Furthermore, we designed the setup to integrated several different collection paths. In the primary collection path, NV fluorescence is collected from below with a 20× magnification, 0.75 NA air objective. This objective allows for a balance of moderate magnification with high collection efficiency and a long enough working distance to image through the 500 μm diamond substrate. A 4f arrangement of lenses is employed to project an image plane at the camera sensor. A 633 nm long pass (Semrock LP02-633RE-25) blocks a fraction of NV^0 fluorescence (as described previously in Chapter 4) and the minimal scattered green fluorescence to improve measurement contrast. For ensemble sensing and initial optimization a second path splits off a small fraction ($\sim 1\%$) of the light from the main collection path. The light is also filtered with a 633 nm long pass optical filtered and collected onto a photodiode. This optimization process will be further discussed below.

Due to the emission pattern of NVs, fluorescence exits the diamonds in all directions. The amount of light exiting through the top path versus the bottom path depends on the index interface of the optical interface (i.e., the diamond-water interface versus diamond air interface). In previous measurements [54], a reflective coating was placed on the diamond

surface to reflect the fluorescence back down and also to protect the biological sample. However, due to the need to image through the diamond for cell viability and localization of phantom wire structures, along with perturbation to the local microwave field, a reflective layer was not utilized here. This allows for a second objective (see Figure 6.3) to be used above the diamond and a second set of optical paths, denoted as the "top path". Various long-working distance objectives (Objective 1: 4x, 0.13 NA 17 mm WD, Objective 2: 10x, 0.3 NA, 10 mm working distance, or Objective 3: 20x, 0.4 NA, 10 mm working distance, depending on the situation) can be used to collect the light from the top, while being far enough away to avoid interfering with needed probe access.

In the first top path, the red NV fluorescence is reflected off of a 500 nm dichroic lens and onto a compact spectrometer (Thorlabs CCS175). NV charge state measurements (see Chapter 4) and measurements of the amount of green fluorescence scattered through the sample are performed through this optical path. The final optical path is used to characterize the sample on top of the diamond. A blue ($\sim$ 475 nm) LED is illuminated at a shallow angle for oblique illumination reflection microscopy measurements [300]. Unlabeled cells are naturally transparent and difficult to see in conventional brightfield microscopy, so oblique illumination microscopy is a simple and label free method of localizing cellular structures. The illumination wavelength is chosen to minimize overlap with the green excitation (532 nm) and NV fluorescence (550 nm to 800 nm) and to utilize the intrinsic responsivity curve of the top-path camera (Basler acA 1920-155um). Low intensity blue illumination is used to minimize detrimental effects blue illumination can have on the NV charge state [202], due to the ionization of neighboring substitutional nitrogen defects.

6.2.2 Magnet Alignment and Microwave Drive

In order to improve measurement contrast and the dispersion slope, a bias field is applied such that the ODMR resonances for the different NV classes overlap. There are three orthogonal directions of the applied bias field where this overlap is possible, one of which is where local magnetic field is aligned perpendicular to the top surface (B_Z, in the lab frame) of the diamond. Aligning the field along the B_Z direction has several benefits for this experiment, (i) as discussed in Chapter 2, measurements of B_Z magnetic fields are sensitive to both J_x and J_y current distributions, which is convenient for the planar current distributions expected for cultures and the fabricated phantoms and (ii) the configuration allows for optical access from above and below (when using ring magnets to apply the magnetic field). For the experiments discussed below a magnetic field of $(B_X, B_Y, B_Z) = (0, 0, 3.6)$ mT is applied with Samarium Cobalt (SmCo) magnets for increased temperature stability due to their low temperature coefficient compared to neodymium magnets.

The microwave field (2.7 GHz to 3 GHz) used to drive the electronic spin transitions is originally synthesized in an RF signal generator (SRS SG384). In experiments where the hyperfine resonances are driven, an additional microwave source (SRS DS345) is used to generate the sideband frequencies (100 kHz to 3 MHz). For these hyperfine driving experiments, both the original microwave field (f_{center}) and the lower frequency signal (f_{side}) are fed into a double balanced mixer (M1K) in order to generate two sets of frequencies at $f_{center} - f_{side}$ and $f_{center} + f_{side}$. The microwave signal is then sent to an amplifier (Minicircuits ZHL-16W-43-S+) to provide sufficiently high power. The amplified microwave field is applied via a ∼4 mm diameter omega-loop fabricated onto the silicon carbide wafer (see Appendix E for more details). Fortunately, Lock-In ODMR techniques do not require large microwave Rabi drive (typically $\Omega < 1$ MHz) compared to pulsed experiments like Ramsey, enabling a larger MW loop not fabricated on the diamond. One important aspect

of the microwave design was making a device that was compact and durable in biological environments like incubators or autoclaves, which precluded the use of wire bonding or metallic contacts that are not biocompatible. Two SMA to ultra-miniature coaxial connector (UMCC) adapter cables bring MWs to and from the gold structure. The UMCC connectors are attached to the gold with a stable silver epoxy (EPO-TEK H20E). To increase mechanical stability of the connectors, an additional biocompatible and autoclavable epoxy (EPO-TEK 353ND-T) is applied on the edges of the connector. After passing through the gold structure, the MWs are terminated into a 50 Ω load.

For the experimental demonstrations above only the upper transitions ($m_s = 0 \leftrightarrow m_s = +1$) were probed to optimize the sampling rate achievable with experiments. Only monitoring one transition makes imaging results especially sensitive to strain and other diamond inhomogeneities along with drifts due to temperature variations. Through taking reference measurements and monitoring changes from these references the systematics due to static lineshape and pixel inhomogeneities can be almost entirely corrected for (see Figure 6.15 below). Furthermore, through routine feedback on the microwave frequency center frequency, slow drifts due to effects like temperature stability can be corrected for due to the thermal drifts occurring on much slower timescales (minutes) than the typical experiment (milliseconds to seconds.)

6.2.3 Electronics Control

One benefit of CW ODMR Lock-In Imaging over the pulsed Ramsey imaging, to be discussed later, is the relative simplicity of the control electronics. For the lock-in ODMR experiments the timing and synchronization of the measurements is set by a waveform generator (Keysight 33622A.) The generator has two output channels and one synchronization channel. Several different waveforms relevant for different sensing modalities are stored in

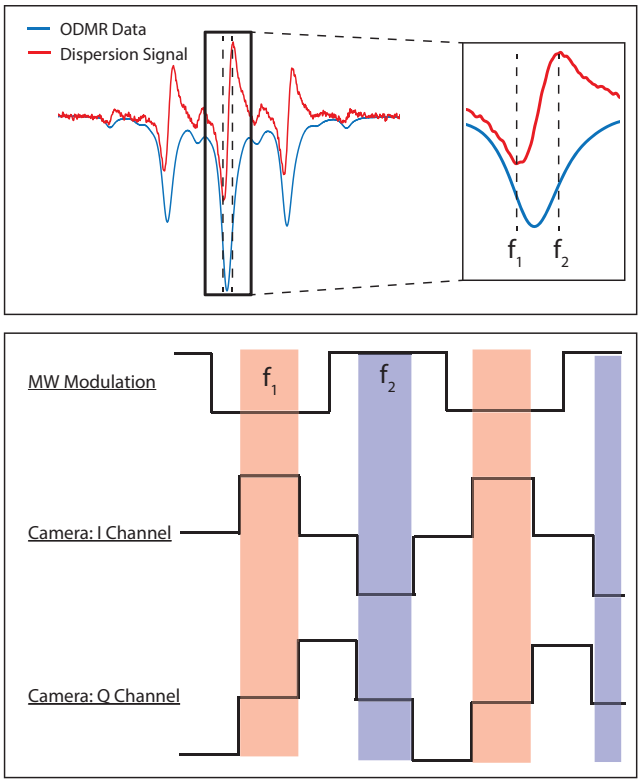

Figure 6.4: Schematic of lock in sequence utilized for real time magnetic sensing. The relative phase and duration of the different channels can be modified in order to maximize the response of one camera channel versus the other. The camera synchronization pulse happens on much slower time scales, ∼Hz, compared to the modulation time scale of 10 kHz.

memory of generator. One waveform, a rapidly varying square-wave superimposed on top of a ramping function is used for the determination of the relevant dispersion parameters. This combined ramp and square wave function is fed to the input for external control of the SRS Microwave center frequency. When the optimal sensing parameters have been determined, the output waveform switches to the second waveform, simple square wave where the high and low of the square wave corresponds to driving the microwave frequency at the positions of maximum slope magnitude on the ODMR feature (See Figure 6.4)

The synchronization output and the second channel of the Keysight waveform generator are distributed to the inputs of the lockin camera (Heliotis heliCam C3). The synchronization channel is used to signal the start of a series of measurements (synchronized with the beginning of a MW sweep) and the second channel is a square wave that sets the demodulation cycle clock for the camera's internal lock-in pixels (see Figure 6.4. The relative phase of the different output channels of the waveform generator can be modified to influence the amount of signal on one of the quadratures (I channel) compared to the other (Q channel).

After on-board subtraction of subsequent frames and summation of the signal over several cycles, the final signal is sent to the computer via a USB 2.0 interface. Currently, the size of maximum internal buffer size (∼500 frames) and slow interface between the camera and computer are limitations to achievable performance of the camera. The camera settings (camera mode, trigger source, duration of exposure, number of integrated demodulation cycles, number of frames in a given set, among others) are set through a custom LABVIEW-based interface and sent to the camera via the same USB 2.0 interface.

6.2.4 Experimental Modalities

For the experiments presented below there were three main modalities under nominal operation: (i) sensing the bare diamond (ii) sensing of wire phantoms and (iii) cells on top of the diamond. Figure 6.5 shows schematics for the latter two. For the cell experiments, neonatal rat ventricular myocytes (NRVMs) [301] were cultured on the diamond surface and experiments were perform to validate cell viability with the NV sensing protocols. For the wire phantom experiments, a wire phantom was fabricated via 3D silver ink printing [302], due to the scalability of the method for fabricating complex 3D wire geometries needed for extension of these measurements. The silver was printed onto a 1 mm^3 quartz piece that was mounted onto a large quartz slide. Thin copper magnet wire (32 AWG) leads were silver epoxied to the ends of the 3D printed silver wires to make an electrical connection. The quartz slide was cantilevered (see Figure 6.5) off a 3D printed plastic device that was mounted to a motorized micro-manipulator (Scientifica PatchStar) for precise placement of phantom relative to the diamond surface. The phantom was fabricated on a separate device from the diamond to enable fast switching between measurements and to enable measurements as a function of standoff distance to the diamond surface.

6.3 Real Time Performance Optimization

The shot noise limited sensitivity for CW ODMR based sequences depends only on the slope of the ODMR resonance, $\frac{C}{\Delta\nu}$, and the photon collection rate R (see Equation 6.1). In the following section, the dependence of the resonance slope and photon collection rate on various experimental parameters is explored in order to develop a protocol to rapidly optimize measurement performance for a wide variety of samples and experimental conditions.

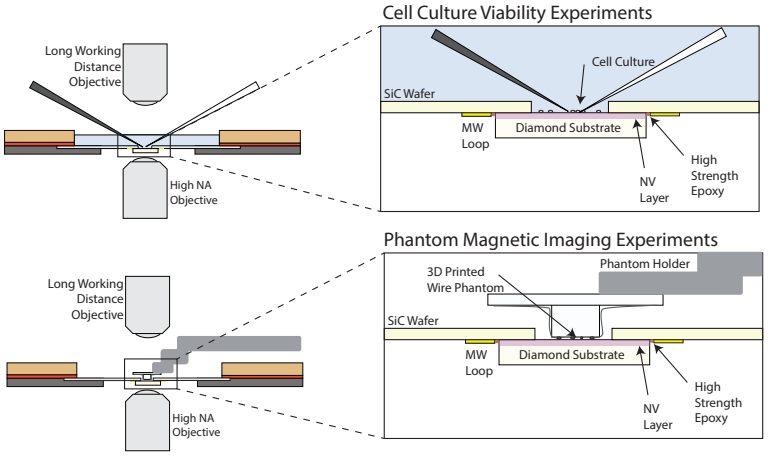

Figure 6.5: Experimental configurations used to probe cell cultures (top) or magnetic phantoms (bottom). For cell cultures probing electrodes are used to trigger biological potentials. These are replaced by a cantilever holding the magnetic phantom in magnetic imaging experiments. The experimental setup is optimized to allow for efficient switching between these two modalities.

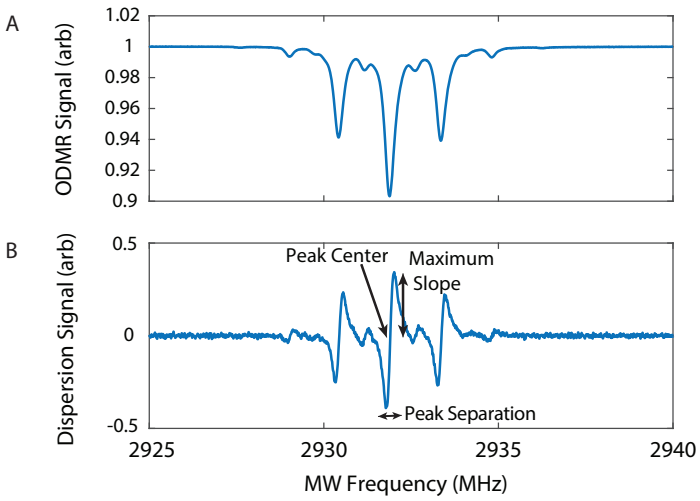

Figure 6.6: Example (A) real-time normalized ODMR and (B) dispersion signal collected on the pick-off photodiode. The dispersion signal is used to determine the maximum slope of the central ODMR feature, the position of the peak center, and separation between the points of maximum and minimum slope (peak separation).

$$\eta_{\text{CW ODMR}} \approx \frac{8\pi}{3\sqrt{3}} \frac{\hbar}{g_e \mu_B} \frac{\Delta\nu}{C\sqrt{R}} \tag{6.1}$$

The use of both the Lock-In camera and a photodiode in the main path of the optical collection allows for the real time validation and optimization of the ensemble performance of the sensor. As described above, a small fraction of the collected red fluorescence from the high NA objective below the diamond is split off and collected onto a photodiode (See Figure 6.3). The signal from the photodiode allows for high signal to noise, real time measurements of ODMR parameters, which enables immediate feedback and optimization. Figure 6.6 illustrates typical ODMR and dispersion curves measured on the pick-off path. Real time peak fitting is used to determine the positions and magnitudes of the relevant peaks and create the time traces shown in subsequent figures below.

6.3.1 Laser Power

The excitation laser power is a key component to ODMR sensitivity as it will influence both the maximum ODMR slope and the photon rates, while further influencing experimental performance through effects like laser heating via absorption.

Figure 6.7 demonstrates a measurement sequence performed over 60 seconds where the laser power was varied between 1 and 3 W and the effect on the performance parameters was monitored. The mean voltage (away from the resonances) on the pick-off photodiode was used as a proxy of the amount of red light collected and is proportional to total photon collection rate. A linear correspondence between the amount of light collected and the excitation power is observed due to the excitation intensity being much lower than the saturation intensity of the NV [52].

Although the center of the ODMR peak does not directly couple factor into Equation 6.1 knowledge of the laser power dependent variations is important as changes in the

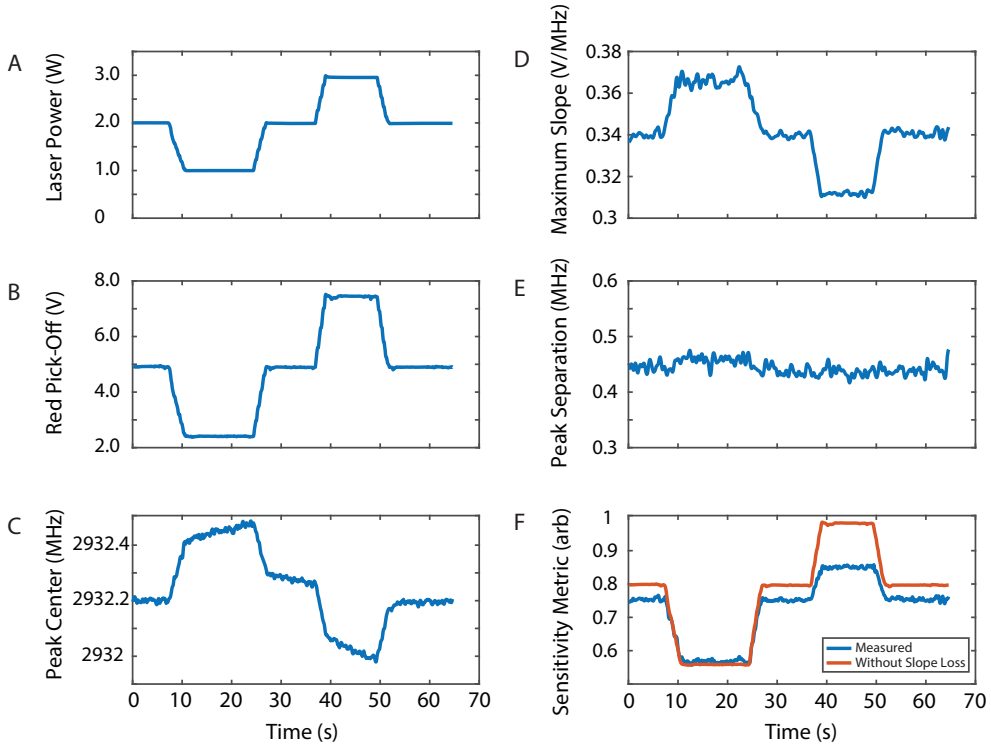

Figure 6.7: Optimization of the laser power and exploration of relevant effects. (A) The laser excitation power is varied in time and measured with a green pick-off photodiode at the laser output. (B) The red fluorescence is measured in the bottom optical path through another pick-off. The linear relationship between green excitation and red fluorescence is expected due to operating at an excitation intensity much lower than optical saturation. (C) The ODMR center frequency is monitored to probe the heating and cooling of the diamond due to changes in the optical power absorbed by the diamond. (D and E) The maximum slope is monitored and found to be inversely related to excitation power. Measurements of the peak separation (related to the ODMR linewidth) lead to the conclusion that the loss in slope is due to ODMR contrast. The loss in contrast is due to the NV charge state instabilities (even at these relatively low optical intensities, see Chapter 4). (F) The sensitivity factor, $\eta_{Improvement} = (\text{Max Slope})\sqrt{(\text{Red Pick-Off})}$, shows the relative sensitivity improvement (larger number is better here) when considering the measurement slope and the amount of light collected. The blue trace represents the actual measurement conditions, and the orange trace shows sensitivity improvement if the slope at 1W excitation was maintained.

peak position due to laser-induced heating will alter the optimal microwave frequency for sensing sequences. Operating at non-optimal MW frequencies will result in not sensing at the points of maximum slope. The amount of heating for a given change in the excitation power depends on the mounting configuration of the diamond and whether or not the fluid reservoir above the diamond (see Figure 6.3) is filled with fluid. For the configuration shown in Figure 6.7, the approximate scaling was $3°C/W$. This heating was used in later studies where the steady state temperature of the diamond plus fluid reservoir at 3 W approached the biologically relevant temperature of $\sim 35°C$ for cardiomyocytes [303].

Changes in the laser intensity led to clear variations in the dispersion slope (see Figure 6.7), where the maximum slope decreased with increasing laser power. In order to further elucidate the mechanism for this slope change, the peak separation (correlated with the ODMR linewidth) was monitored and only marginal deviations were observed. Therefore, it was inferred that degradation in the ODMR contrast was the cause of the decrease in the maximum slope. As demonstrated in Chapter 4, the ensemble charge state is both dependent on the excitation laser intensity and influences the measurement contrast. In fact, the measurements presented in Figure 6.7 were experimental basis for a lot of the charge state measurements in Chapter 4 and elucidated the need for in-situ ensemble charge state characterization. As seen in the plot of the sensitivity improvement metric (Figure 6.7) defined based on the scaling in Equation 6.1, as $\eta_{Improvement} = (\text{Max Slope})\sqrt{(\text{Red Pick-Off})}$, there is trade-off between maximum slope and amount of light collected. The orange curve depicts what the sensitivity metric would be based off the slope achieved for 1 W excitation. For 3 W excitation, the large gap between the orange and the blue curve illustrates the degradation of performance due to ensemble charge state degradation with increasing laser power. In spite of the degradation of the improvement, it is still advantages to operate at high laser intensities in this situation because the square root of the increase in photon

collection rate is greater than the loss of contrast. This tradeoff will be further explored in the later sections with Ramsey imaging where the excitation intensity is increased due to the small laser spots. Further work is needed in diamond growth and NV control (see Chapter 4) to improve the robustness of the NV charge state at high excitation intensity to minimize this mechanism for sensitivity degradation.

6.3.2 Microwave (MW) Power and Hyperfine Driving

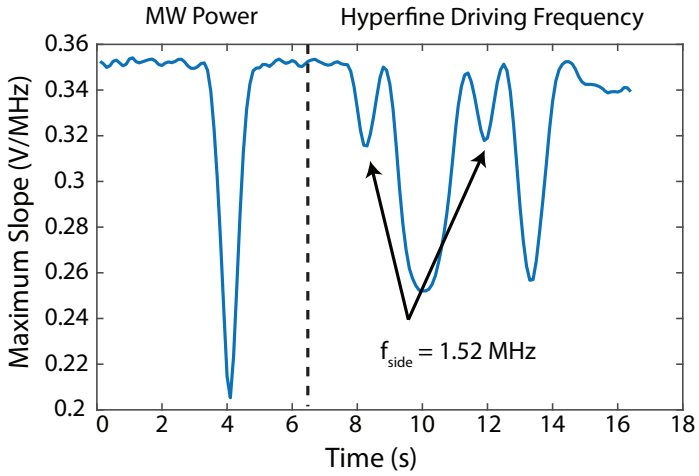

Figure 6.8: Real time performance characterization of impact on sensitivity of microwave power and hyperfine driving frequency.

As shown in Figure 6.8 and discussed in Reference [43],CW-ODMR based performance depends strongly on the microwave power used to drive transitions between the electronic spin states. Due to the competing dynamics between the microwave drive and laser excitation, there is an optimal MW power where above it the resonance broadening becomes more detrimental than the increase in the ODMR contrast (see Chapter 1) to the ODMR slope. In the first ~ 5 seconds of the data in Figure 6.8, the MW power is increased (from -5 dBm at the output of the MW source to 0 dBm) and the ODMR slope decreases. This process enables real time optimization of the MW power to address the NVs (for a given

laser power.)

In order to improve the measurement contrast and reduce the number of MW resonances that need to be addressed, the hyperfine driving technique employed in Reference [54] was modified for the ^{15}N isotope diamond used in this work. Instead of requiring three drives separated by $\sim$ 2.16 MHz, this work only required two drives separated by $\sim$ 3.05 MHz due to the nuclear spin of ^{15}N (I=1/2) and hyperfine couplings (see Chapter 1).

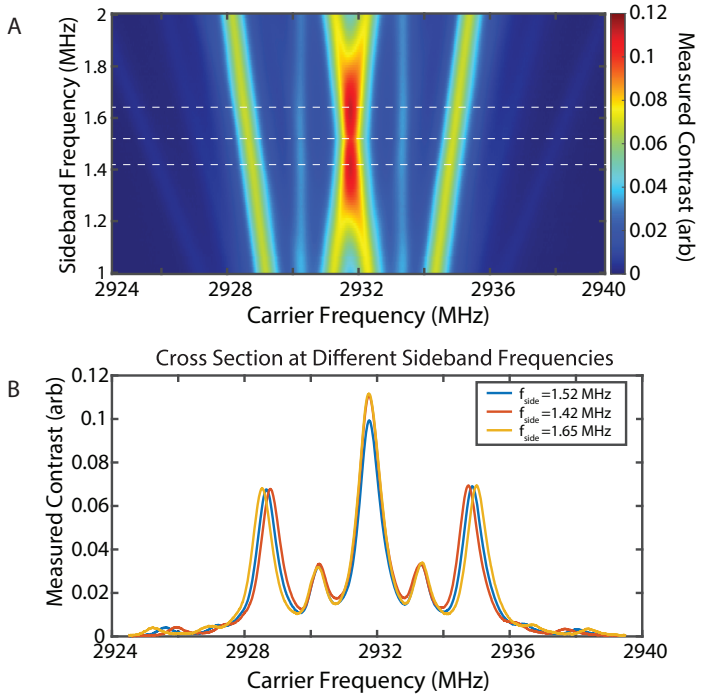

Figure 6.9: (A) Experimental 2D parameters sweep monitoring the ODMR contrast as a function of MW carrier frequency and sideband frequency. For these measurements, 100 different sideband frequencies are swept from 1 MHz to 2 MHz (B) Slices of the 2D plot in (A) are shown to further demonstrate the significant drop in contrast at the f_{side} = 1.52 MHz. For sensing experiments, f_{side} = 1.65 MHz was used to maximize measurement contrast and maximally separate the lower contrast singly driven resonance features.

As described in the equipment section, the hyperfine driving is accomplished by sending a low frequency RF signal (f_{side}) through a double-balanced mixer along with the main microwave frequency ($f_{carrier}$). In order to optimally excite the two hyperfine resonances

associated with ^{15}N, a sideband frequency of 3.05/2 MHz $\approx$ 1.525 MHz appears to be required. In the second half of the experiment in Figure 6.8, the sideband frequency was varied to confirm this intuition.

Surprisingly, driving at the $f_{side} = 1.52$ MHz resulted in a local minima of the ODMR slope, and instead driving at $f_{side} \approx 1.42$ MHz or $f_{side} \approx 1.65$ MHz maximized the ODMR slope. This effect is mapped out in greater detail below and in the Appendix. The origin of this effect relates to the lack of a quadrupolar moment in ^{15}N compared to ^{14}N and the presence of strong off-axis fields (see Chapter 1).

6.3.3 Sensing of an External Magnetic Field

As stated previously, the bias field is aligned to maximize contrast through overlapping all 4 NV classes. While improving the measurement contrast, this can complicate quantitative interpretation of the measured fluorescence in terms of magnetic fields. In the optimal configuration, the external magnetic field of interest will primarily be aligned with the local bias field, in this case the lab frame B_Z. Under these conditions, all the NV classes will shift together equally. The lack of differential shifts for each axis leads to no broadening for the ODMR resonance. However, if an external magnetic field (Figure 6.10) is applied not in the B_Z direction, different NV classes will experience different projections of the local magnetic field. Therefore, depending on the strength of the additional field, the resonances corresponding to the different axes will shift in different directions, leading to both shifts (Figure 6.11) and broadening (Figure 6.12) of the ensemble ODMR resonance.

A small external permanent magnet was used to validate the expected results from above and the results (see Figure 6.10). The permanent magnet was held above the experiment and manually moved around and rotated in accordance with the labels in the figure.

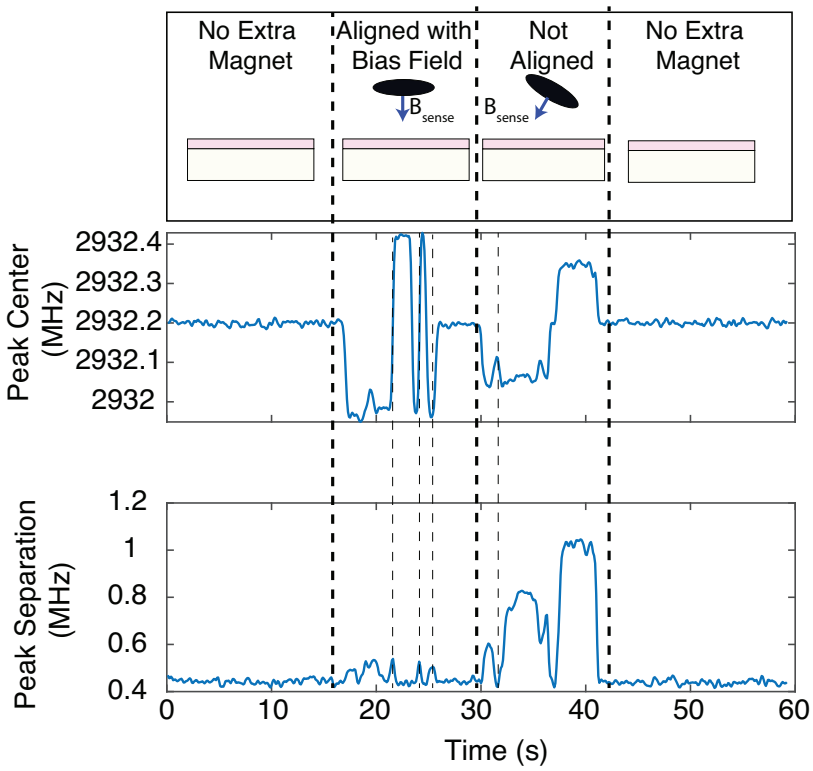

Figure 6.10: Real time magnetometry of an external permanent magnet. During the first period, no additional magnets are present. At t=15 seconds, an external magnet is brought close to the experiment aligned along with the bias field. The magnet is flipped around during this period to be aligned parallel or anti-parallel with the bias field. Slight broadening can be observed as the magnet is rotated around to the opposite polarity. At t=30 seconds, the external magnet is tilted relative the bias field and both shifts and broadening can be observed. Finally, the magnet is removed and the center and separation return to their original values.

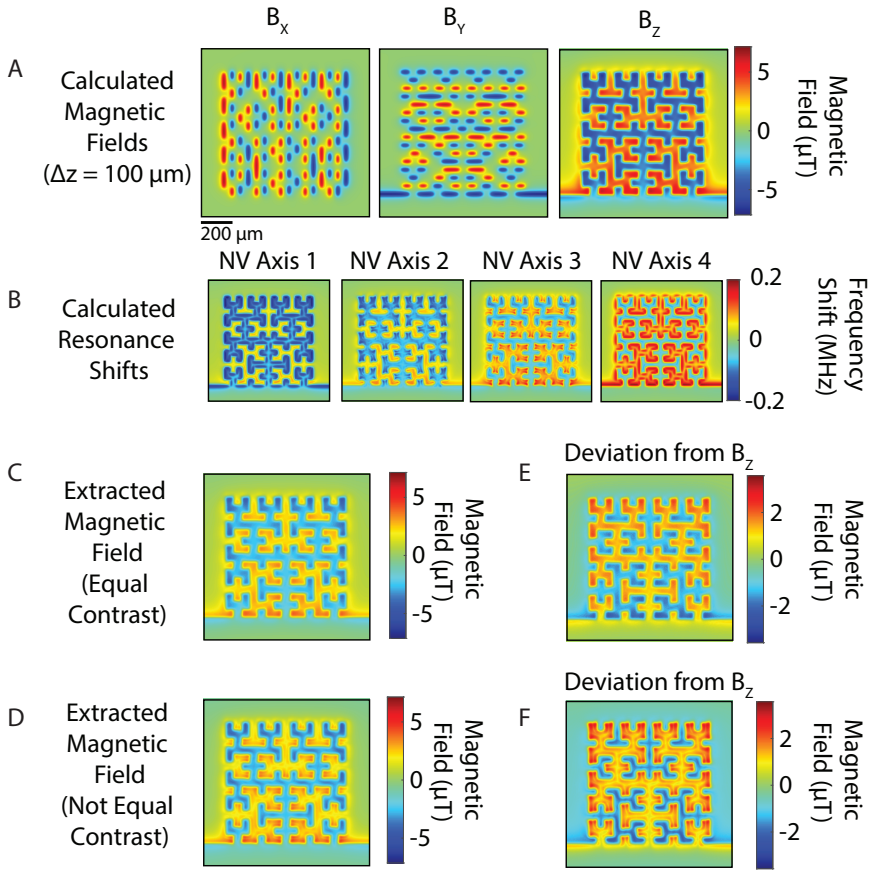

Figure 6.11: (A) Initially the vector magnetic field in the lab frame (B_X, B_Y, B_Z), is calculated for a given test current structure. (B) The lab frame magnetic field is converted to a magnetic field in the NV frame for each axis $(B_{x,i}, B_{y,i}, B_{z,i})$ and the resultant frequency shift is calculated for each axis. ODMR spectra are simulated for every pixel in the field of view and summed as done in Equation 6.2. The effective ODMR resonance for each pixel is fit and the resonance position is extracted and plotted for the case where (C) $C_1 = C_2 = C_3 = C_4$ and (D) $C_1 = C_2 = C_4, C_3 = 0$. (E) For the case with equal contrast, B_Z-like deviations from the original B_Z profile are expected due to the projection of the magnetic field on the NV axes [54, 55]. (F) A distortion in the image containing components of the B_X and B_Y magnetic field can be seen when the ODMR contrast is not balanced between all the axes.

In the example above with an external permanent magnet, the perturbation field was roughly uniform in amplitude and direction over the field of view. However, as seen in Chapter 2, there are large variations in the magnetic field amplitude and direction over the field of view when close to current sources. Simulations were performed to better elucidate the impact of both aligned and not aligned field on the fidelity of magnetic imaging experiments.

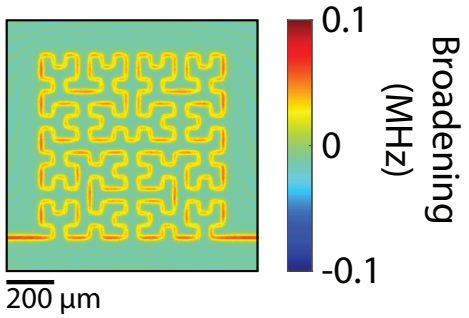

Figure 6.12: Spatial distribution of the effective ensemble line broadening due to sensing a spatially varying external field not aligned with the applied bias magnetic field, similar to Figure 6.10.

Using the methodology presented in Chapter 2, the vector magnetic field is calculated for each pixel in the field of view. For every pixel in this simulated field of view, the NV resonance frequency shift is calculated from the Zeeman Hamiltonian (see Chapter 1 and Figure 6.11). Lorentzian lineshapes for each pixel are assumed [21], and the contribution from each axis are summed together as shown in Equation 6.2.

$$S = 1 - \frac{C_1\gamma^2}{((f-f_1)^2+\gamma^2)} - \frac{C_2\gamma^2}{((f-f_2)^2+\gamma^2)} - \frac{C_3\gamma^2}{((f-f_3)^2+\gamma^2)} - \frac{C_4\gamma^2}{((f-f_4)^2+\gamma^2)} \quad (6.2)$$

The Lorentzian fit parameters are determined for the summed resonance and the new effective line-center and linewidth are plot. The line-center shift is used to calculate the magnetic field and the linewidth shows the resultant broadening of resonances due to the summation of the fluorescence from different NV axes. Two experimental configuration

regimes relevant to the imaging experiments are considered (i) the ODMR contrast for axes are equal (ii) the ODMR contrast for all axes are not equal. In both cases, it is assumed that the magnetic field shifts are small ($<$0.1 MHz) compared to the ODMR linewidth ($\sim$ 1 MHz.)

For diamonds grown without preferential orientation, there is an equal fraction of each NV class contributing to the overall fluorescence [304]. Therefore, the dominant factors influencing differential contributions from each resonance are the ODMR contrast, linewidth, and linecenter. For this analysis, we assume the intrinsic linewidths (limited by power broadening and N-NV dipolar interactions) for each pixel are the same, the line centers are dictated by the combination of the bias field and the target field, and the contrast is varied for the two cases. As discussed in Chapter 1, the ODMR contrast for different axes can be controlled via the laser polarization and microwave field.

For the condition where all the axes have equal contrast, the B_X and B_Y components of the magnetic field lead to equal shifts in both directions. The opposite shifts of the line leads to broadening, but not a shift of the resonance feature center (See Figure 6.12). If the contrast is not equal for all the axes, then there will be differential contributions and the systematic distortions will be introduced to the final magnetic image.

6.3.4 Impact of Sample Perfusion

For maintaining biological viability of the samples being studied, perfusion is often needed to replenish the nutrients and resources in the bath surrounding the cells. However, depending on the details of the perfusion, experimental systematics can be introduced which need to be considered; several of those considerations are explored in greater depth below.

One of the most prominent effects of perfusing the sample is that, depending on the temperature of the incoming liquid compared to the steady state temperature of the

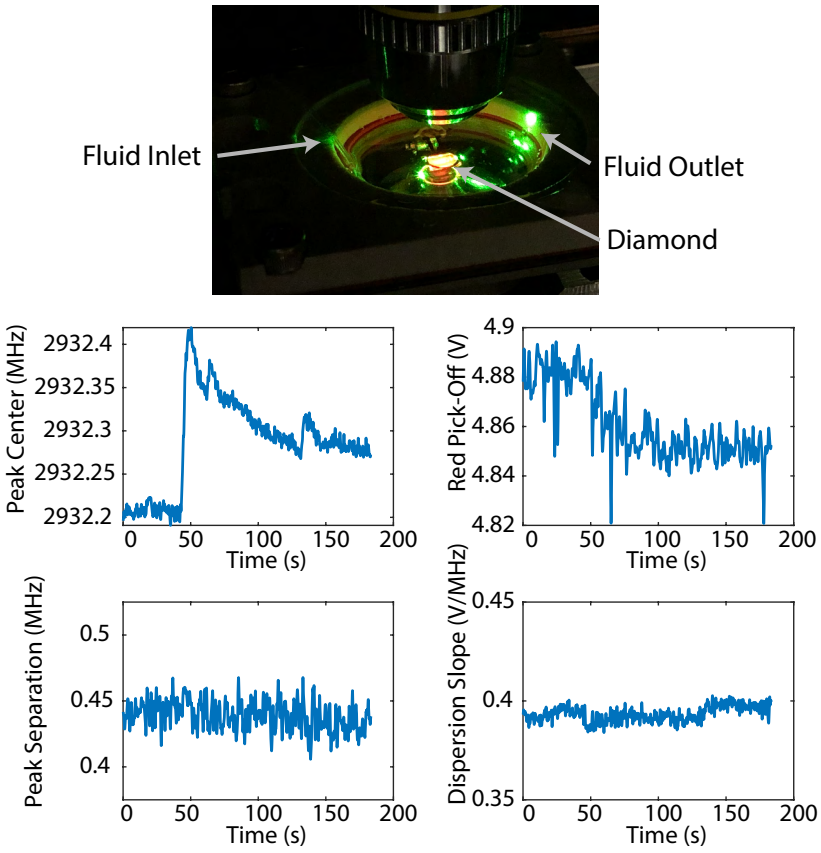

Figure 6.13: An image of the experiment showing the geometry of the fluid inlet, outlet, and reservoir relative to the diamond location. Sample perfusion begins at 50 seconds. The largest impact perfusion has on the experiment is line center shifts due to modification of the diamond temperature. Changes in the amount of red fluorescence collected due to modifications of the reflection and transmission coefficients at the diamond interface can be seen as well.

liquid around the diamond, temperature fluctuations can be introduced. In Figure 6.13, an experiment is performed where the reservoir around the diamond is initially empty. The fluid inlet in Figure 6.13 is opened and the reservoir is filled with phosphate-buffered-saline (PBS), to mimic biological media. The PBS is colder than the steady state temperature of the diamond and this leads to the positive line-center increase. Each spike in Figure 6.13 corresponds to the addition of more fluid to the bath. Due to the increased thermal mass of the PBS and its heat sinking abilities, the steady state temperature of the diamond with the PBS filled is lower than the steady state temperature of the diamond without it for constant laser power.

Another important effect is how the presence of fluid above the diamond changes the local index of refraction. The index of refraction of water and PBS is $n \approx 1.33$ [305], which is different from the normal index of refraction of air $n \approx 1$. This change from a diamond-air interface to a diamond-water interface will change the fraction of light reflecting off versus transmittance through the top surface and change the steady state optical accumulation through the objective on the bottom path. This decrease in the amount of red fluorescence as more light escapes through the top path can be seen in Figure 6.13.

The microwave loop was designed to be a waveguide that minimizes microwave reflections over a broad range of frequencies, since resonant circuits [94] are extremely sensitive to the local dielectric environment and small perturbations in the amount of fluid above the diamond. Local non-uniformities could lead to large deviations in the microwave power delivered over time. The non-resonant circuit is sufficient for Lock-In ODMR measurements where microwave power requirements are small, however, will likely become a more challenging obstacle for future pulsed measurements like Ramsey that require both robust performance and strong Rabi drives frequencies. The relative flat response of the MW loop with regard to changing levels of PBS can be seen through the relatively flat response of the

peak separation and dispersion slope. The conductivity of most biological media is likely to be a general concern needed most NV biological applications, especially those that require well calibrated, strong MW pulses.

6.4 Experimental Verification with Wire Phantoms

Following NV ensemble parameter optimization, the QDM needs to be configured to minimize susceptibility to parameter inhomogeneity. As discussed in Chapter 4, one significant source of sensing inhomogeneity is intrinsic strain in the diamond lattice. These inhomogeneities can impact imaging in two ways: (i) introduce systematic shifts that degrade imaging accuracy and (ii) degrade sensing parameters and lead to inhomogeneous sensitivity across the field of view [108]. Below, a method is described that is able to mitigate the effects on imaging accuracy when sensing small magnetic fields through the utilization of reference images. Unfortunately, CW ODMR-based measurement sequences will likely always have sensitivity degraded by strain inhomogeneities.

In order to overcome these effects, the spin-1 nature of the NV can be utilized by operating in the double quantum (DQ) basis [21, 108, 306, 307], which minimizes sensitivity to strain while maintaining sensitivity to magnetic fields. Such a sequence and preliminary results are described at the end of this chapter.

Impact of Static Lineshape Variations

Here we consider static lineshape variations due to inhomogeneities in the diamond strain, laser illumination, microwave driving, and static bias field and their impact on ability to image magnetic fields. Specifically, we want to consider the measurement modality (Lock-In ODMR) where we are only sampling two points on opposite sides of the ODMR resonance at the points of maximum slope and recording the difference. Through monitoring only

two points, we are able to speed up the measurements and have high bandwidth magnetic field imaging, but at the cost of being more sensitive to these inhomogeneities and other systematics.

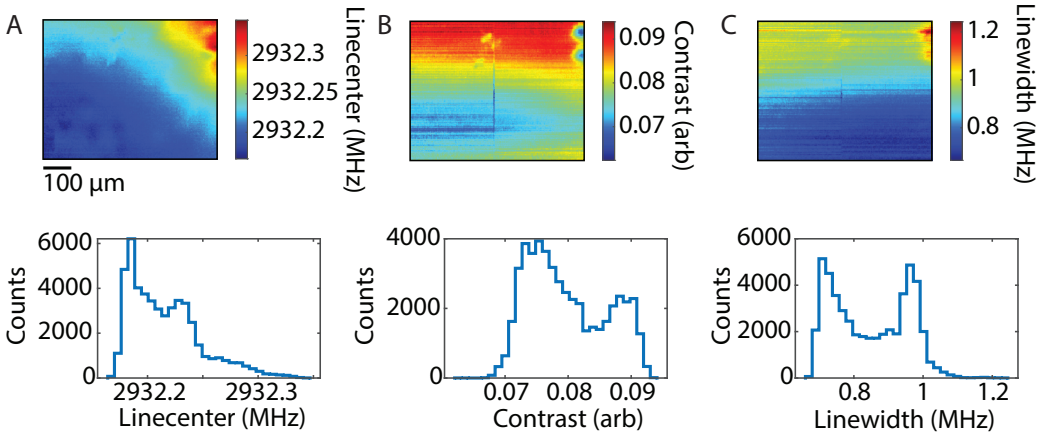

Figure 6.14: Representative experimental ODMR parameter variations across a QDM measurement field of view. (A) The linecenter is impacted by gradients in the bias magnetic field and strain defects. (B) The contrast is impacted by strain inhomogeneities, the laser profile, and the MW gradient. (C) The linewidth is often impacted by strain gradients causing ensemble broadening and microwave power gradients [43].

For this analysis, we measured the ODMR linecenter (f_0), linewidth (γ), and contrast (C) over the field of view and propagate spatial variations through a numerical simulation of the Lorentzian parameters and sensing scheme. The resultant fluorescent signals are analyzed for different correction schemes to verify feasibility. Equation 6.3 illustrates the challenge of trying to disentangle the contribution of a magnetic field in the presence of a large background of spatially varying parameters, especially in the case of δ terms $\gg \Delta B$, which is typical for biological systems and current diamond inhomogeneities.

Where f_{dev} is chosen such that if ΔB and all δ terms go to 0, then $S_{\text{Lock-In}} = 0$.

$$S_{\text{Lock-In}} = \frac{(C+\delta C)(\gamma+\delta\gamma)^2}{(f-(f_0+\delta f_0)+\Delta B+f_{dev})^2+(\gamma+\delta\gamma)^2} - \frac{(C+\delta C)(\gamma+\delta\gamma)^2}{(f-(f_0+\delta f_0)+\Delta B-f_{dev})^2+(\gamma+\delta\gamma)^2} \tag{6.3}$$

Based on the distribution of ODMR parameters in Figure 6.14, ODMR spectra for each pixel are simulated. The points of maximum slope are determined and the value of the fluorescence contrast (S) is plotted for each pixel (see Figure 6.15). The dominant variations in the $f_0 - f_{dev}$ images (S_-) and $f_0 + f_{dev}$ images (S_+) are due to primarily linewidth and contrast variations. To emulate what is done by the camera, the difference between frames is defined as $\Delta S = S_- - S_+$. If there are no inhomogeneities in the ODMR parameters and no applied spatially varying magnetic field, then $\Delta_S = 0$ should hold for all the pixels in the field of view. Residual deviations in the line-center due to magnetic and strain gradients dominate the ΔS_0 image. If a small magnetic field is applied and the process is repeated, then the residual line-center deviations still dominate the image of ΔS_B. Only when the difference $\Delta S_B - \Delta S_0$ is taken can the applied magnetic field be observed (see Figure 6.15D). The normalized change in fluorescence due to the magnetic field is three orders of magnitude smaller than residual inhomogeneity contribution, necessitating this reference subtraction. The method of subtracting off reference images to elucidate the contribution of small extra fields is analogous to the method utilized in Chapter 5.

6.4.1 Real Time QDM Magnetic Images

Following the optimizations and considerations in the previous sections, real time magnetic imaging can be performed. Figure 6.16 reveals the structure of the 3D printed [302] silver wire phantom used in this study, along with associated QDM images with no current applied to show static systematics in the ODMR line center, peak separation, and maximum slope. The complex shape was chosen to be evocative of the complicated patterns of dendritic

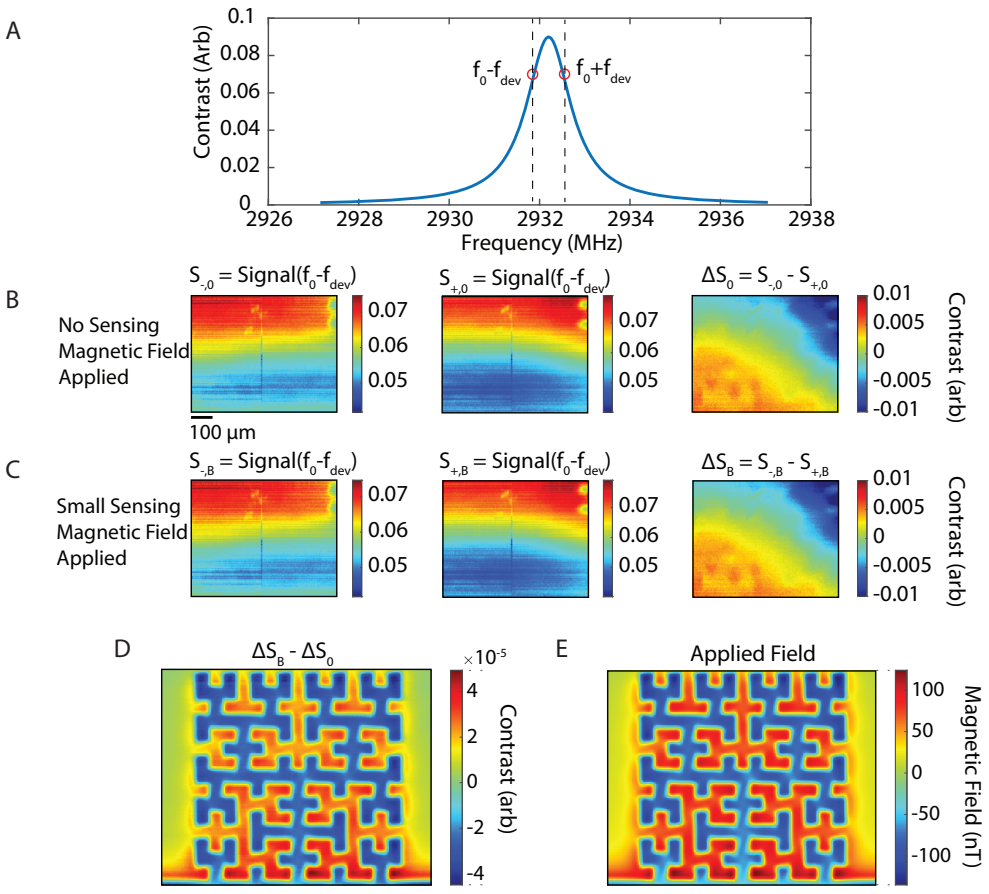

Figure 6.15: Numerical simulation of protocol to sense magnetic small magnetic fields in the presence of spatial variations. (A) Representative ODMR simulation of a single resonance feature. The points of maximum slope magnitude (red circles) are sampled. (B) A reference frame is simulated without an applied magnetic field to be sensed. For the parameter variation in Figure 6.14, the expected fluorescence contrast at the points of maximum slope and their difference is shown. The inhomogeneities over the field of view dominate the signal, ΔS_0. (C) A sensing frame ΔS_B is simulated with a small applied magnetic field ($\sim 100\ nT$). However, the variations of the field of view still dominate the signal and the magnetic field can not be observed due to its small shifts relative the the background variations. (D) However, if reference subtraction, $\Delta S_B - \Delta S_0$, is performed, the magnetic field becomes visible with minimal perturbations compared to the applied field (E) due to the applied field and inhomogeneities being small compared to the ODMR linewidth.

structures in dense cellular networks. The outer ring around the wires allowed for all wires to have return paths to ground. The top objective is used to position the wire phantom above the diamond with the transmitted light from the blue LED below. The excitation laser is turned and the phantom can be aligned relative to the laser spot. Since the phantom is mounted to a 3D micro-manipulator, the stage with the phantom can be placed precisely in z to minimize the distance between the phantom and the NV surface of the QDM. The reflection of the red fluorescence off of the phantom collected through the bottom objective is used to determine when the phantom is in contact with the diamond (see Figure 6.16).

Similarly to what was seen previously, the ODMR parameters are not uniform over the field of view (Figure 6.16D-F). The line-center image is dominated by magnetic gradients and strain. However, the introduction of the phantom distorts the peak-separation and maximum slope image. This distortion is due to the interaction between the conductive silver phantom and the MWs needed to drive the NVs. The complicated pattern of wires in the phantom leads to many different wire loops, perfect for inducing MW currents and creating inhomogeneous MW fields. Additional perturbations in the maximum slope signal can be seen correlating with reflections of light off of the metallic phantom. The perturbations introduced by the phantom structure and due to the natural variations in the diamond and laser spot are small enough for the reference correction of Figure 6.15 to be effectively utilized.

The leads coming from the wire phantom are next connected to another signal source and a 200 Hz square wave is applied. In a given measurement sequence, 50 frames are recorded at 1 kHz and the data is saved. Figure 6.17 illustrates representative real time QDM images of the magnetic field profile associated with the current propagation. A maximum magnetic field amplitude of $\sim 10\ \mu T$ is measured. Lock-In CW ODMR magnetic imaging protocols work best for magnetic field shifts smaller than linewidth of the ODMR feature

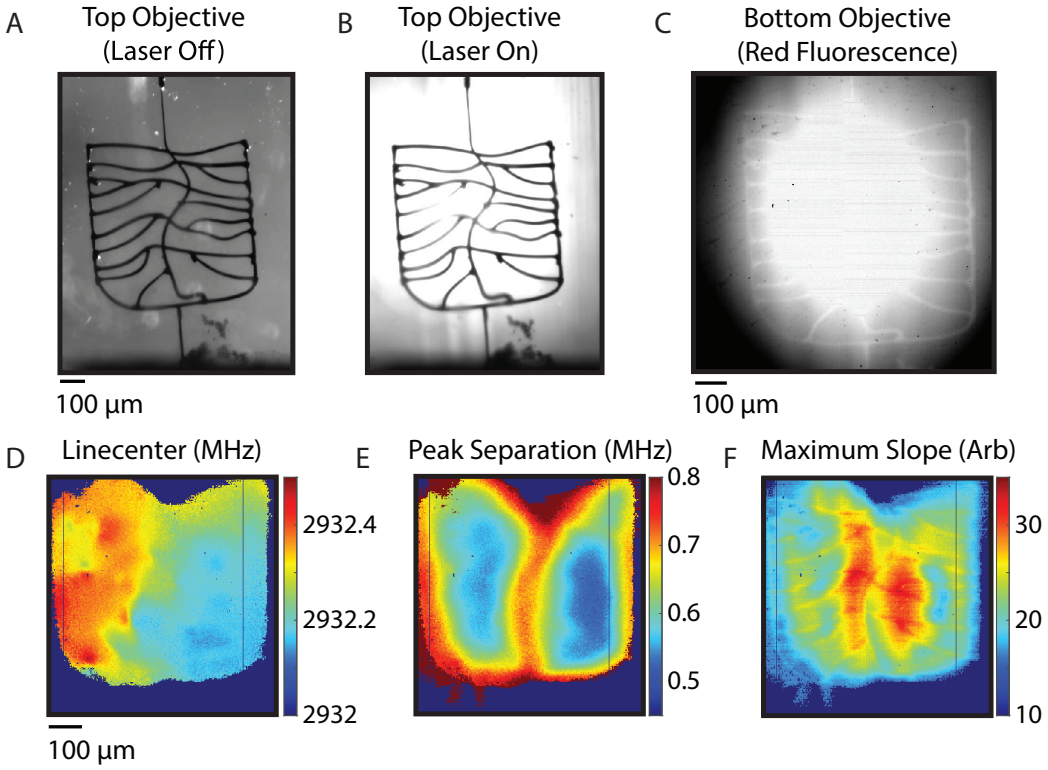

Figure 6.16: Placement of wire phantom and characterization of QDM static systematics and variations with no external current applied. (A) Transmitted light from the blue LED is collected through the top optical path onto the camera. (B) Through modification of the optical filters on the top path, the transmitted red fluorescence is imaged. This procedure allows for placement of the phantom relative to the position of the excitation laser spot. (C) The bottom optical path is utilized to ensure the phantom is making contact with the diamond surface. The phantom holder is lowered until sharp reflections of the silver phantom wires can be seen in the bottom objective. (D) The ODMR static linecenter variation is dominated by diamond strain inhomogeneities and bias magnetic field gradients. (E) The ODMR peak separation spatial variation is dominated by microwave power inhomogeneity due to induced microwave fields in the phantom structure. (F) The ODMR maximum slope variation is predominantly controlled by laser power inhomogeneities over the field of view.

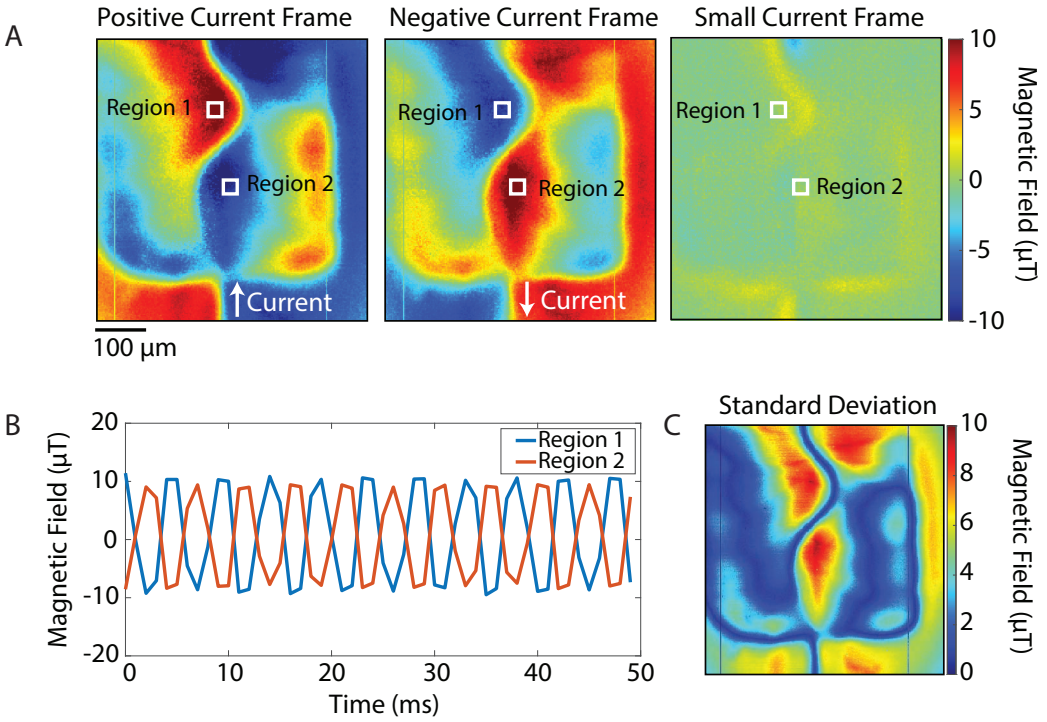

Figure 6.17: Following the optimization of sensing parameters, a square wave current waveform at 200 Hz is applied to the phantom and Lock-in CW ODMR imaging performed. The image is sampled at 1 kHz. (A) Three real time snapshots of the magnetic field are shown for when there is positive current applied, negative current applied, and near a zero crossing where almost no current is applied. (B) Two regions (where the field is of maximal amplitude, but opposite polarity at a given time) are monitored to show the oscillating waveform of the magnetic field. (C) A standard deviation of the magnet field over a given measurement cycle is plotted to illuminate subtle features associated with current propagation along the smaller paths of the structure.

in order to stay in the linear regime of the ODMR response. For the ODMR linewidth in this work, this requirement translates to the imaged magnetic field being < 25 μT, so we are safely within the linear sensing regime.

The observed magnetic field profile in Figure 6.17 is dominated by the outer loop and the middle wire. This is likely due to the 3D printing process for the phantom, where the outer structures were deposited first and are the thickest wires. The smaller interconnects (see Figure 6.16A) between the larger wires were printed later. The difference in timing of the connection likely influenced the conduction due to the possible formation of an oxide layer on the silver surface between prints. However, the standard deviation of the real time magnetic video, Figure 6.17C, reveals that even though the effect is small the contribution due to these smaller wires is detectable. Another source of the spatial features is the thickness of the NV layer in the diamond used for this study. The 40 μm layer is relatively thick and blurs out fine spatial features due to averaging the magnetic field over the layer (see Chapter 1). For future studies, there will be a trade-off between the amount of light collected due to layer thickness (real time performance/sensitivity) and the achievable spatial resolution.

6.4.2 Static Magnetic Field Imaging with a 13 μm NV Layer

To validate the results above for magnitude of field and spatial patterns, along with further pushing QDM imaging resolution, the magnetic field from the wire phantom was measured with a 13 μm thick NV layer (same diamond as Chapter 3), using a static current.

The only experimental modification needed relates to hyperfine driving due to the 13 μm NV layer diamond employing the ^{14}N isotope. The hyperfine driving setup was modified [54] to properly drive the ^{14}N hyperfine resonances. Instead of using calibrated fluorescence changes to monitor the magnetic field as done in Figure 6.17, this protocol measures the full dispersion curve (see Figure 6.6) and extracts the peak positions with

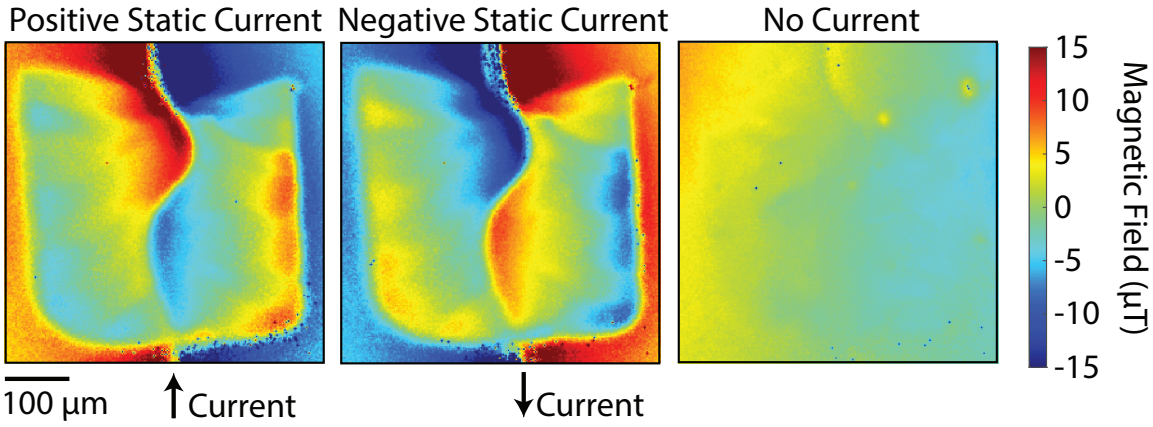

Figure 6.18: Higher resolution QDM magnetic imaging of static current flowing through the phantom with a 13 μm NV layer diamond. The positive and negative current images are corrected by subtracting off the image taken with no current applied.

one second of measurement time per average to determine the local magnetic field. To improve the signal to noise ratio and image quality, 100 dispersion traces are averaged together before the peaks are fit to. There is generally good agreement in the magnetic field profile between the two measurements in spite of the different diamonds, phantom position, and likely different stand-off distances. Furthermore, the contributions due to the smaller wires coming off the main branch are more visible in these images, which is likely due to a combination of better SNR and higher resolution due to the thicker layer.

This measurement validates the potential of Lock-In CW ODMR to be used not just for imaging time varying magnetic fields, but improved sensitivity imaging of static fields as well, such as those in Chapter 5. Typically, static QDM measurements are limited by saturation of the camera and ability to correct for laser intensity variations. Modification of existing experiments to implement lock-in-based imaging schemes is likely to improve measurement performance in the near term. Furthermore, sweeping out the full ODMR or dispersion spectra allows for imaging magnetic fields with much larger dynamic range compared to the two point lock-in method described above, at the cost of measurement

time.

6.4.3 Sensitivity Characterization

In order to gauge how far away the achieved QDM performance is from that needed for applications of interest, it is important to calculate the volume normalized sensitivity. For imaging applications, an important sensitivity metric is the spatial standard deviation. This determines the ability to differentiate a spatially varying magnetic field from noise. A quiet region of the single frame with small current was used to calculate the standard deviation. A 100 $\mu m \times 100$ μm box of pixels is chosen and the standard deviation over this box is calculated (see Figure 6.19).

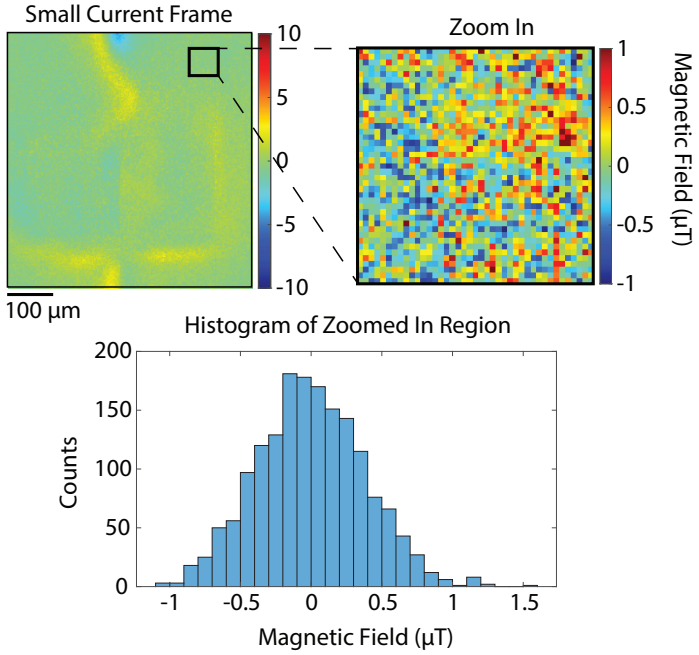

Figure 6.19: A frame from Figure 6.17, where the applied current was minimal was utilized to extract the spatial noise floor. A 100 $\mu m \times 100$ μm region was selected and the standard deviation over this region was calculated. From this standard deviation, the volume normalized sensitivity was calculated through the sampling rate (1 kHz) and the NV voxel size, (2 $\mu m \times 2$ $\mu m \times 40$ μm).

From the spatial magnetic field standard deviation (0.5 μT), the volume normalized sensitivity is approximated by correcting for the voxel size (2 $\mu m \times 2$ $\mu m \times 40$ μm) and sampling rate (1 kHz), leading to a volume normalized magnetic sensitivity of $\eta \sim 200\ nTHz^{-1/2}\mu m^{3/2}$. The large aspect ratio of the sensing voxel implies that further binning could be used to improve the spatial noise floor without degrading imaging resolution.

Recalling the previous estimate that sensitivity $\eta \approx 1 - 8\ nTHz^{-1/2}\mu m^{3/2}$ will be required for real time imaging of cardiac magnetic fields, one can see that there is still a significant need to improve performance for such biological current imaging with Lock-In CW ODMR methods. For example, with the current level of performance $(200/8)^2 = 625$ events would need to be averaged to achieve a signal to noise ratio of 1 for the measurements with $(40\ \mu m)^3$ voxels. To enable meaningful analysis of the signals, an SNR of much higher than 1 (typically ~ 10) is necessary; this raises the number of events averaged to 62,500. This level of repeatable averaging is not easily achievable in most biological experiments, therefore greatly enhanced volume-normalized QDM sensitivity will be needed. Nonetheless, the sensitivity achieved in this work is sufficient for wide-field imaging of transient activity in integrated circuits [146]; and application of the protocol demonstrated here to the experiments in Chapter 5 would enable vastly improved performance.

6.5 Biocompatibility Measurements

Despite not being sensitive enough to image the magnetic fields associated with cardiomyocyte activity, the QDM using the Lock-in CW ODMR technique serves as an important test-bed for validating the biological compatibility of new tools and protocols. In this section we describe efforts to culture the cells on the surface of a QDM diamond and experimental validation of cell viability through monitoring of the beating of the cardiac cells in the

presence of typical 532 nm laser powers used for NV excitation.

6.5.1 Initial Cardiac Studies

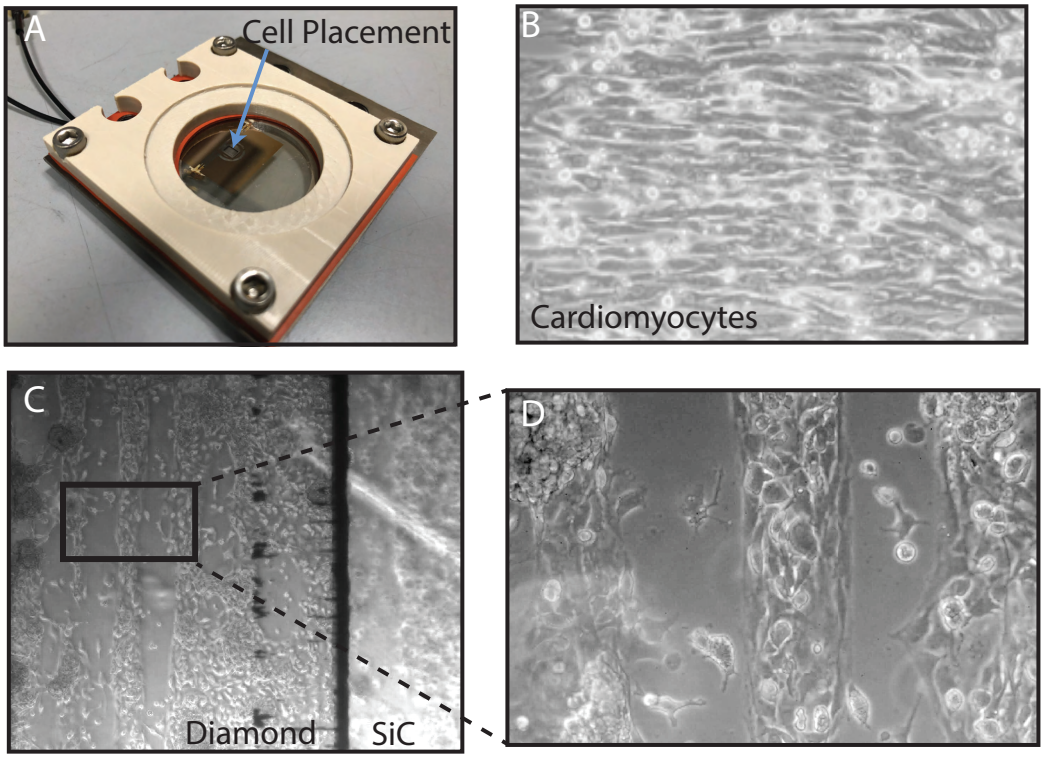

Figure 6.20: (A) Diamond mount designed to optimize biocompatibility and NV measurements. (B) Cardiac cells cultured on the diamond surface without patterning. The cells form an aligned structure and possess a characteristic synchronized beating motion. (C) Cells patterned in stripes to create clearly defined spatial structures needed for future magnetic imaging experiments. (D) Zoom in showing cells with characteristic length scales of ~ 10 μm across.

The diamond holder (Figure 6.20(A)) was optimized to balance mechanical stability, biocompatibilty, minimize magnetic perturbations, improve thermal stability, and ability to quickly switch out components through careful material choice, fabrication design, and several iterations. Initially, neonatal rat ventricular myocytes (NRVMs) [301] were plated on the diamond surface and allowed to develop over a period of 2-3 days in a bio-incubator. Cell

viability was checked through direct observation of the cells in an inverted microscope and observing characteristic beating of the cells and synchronization over time. Cells were seeded uniformly on the diamond surface and allowed to develop into uniform cardiac tissue (see Figure 6.20(B)). To develop the infrastructure and capabilities for studying propagation in nontrivial spatial structures (as done in Chapter 3), as well as probing geometry and dimensionality dependent propagation [308], micro-contact printing [309] was used to pattern 100 $\mu m\times$ 3 mm stripes of cells on the diamond surface. The relatively small surface area (2 mm by 3 mm) available for the patterning process and the differing surface chemistry of diamond compared to other conventional biological substrates led to initial challenges with the patterning of cells, but through several iterations we were able to produce repeatable and functional cell patterns (see Figure 6.20(A,B)).

Cellular Activity Monitoring in a QDM Setup

In order the validate the compatibility of short-term NV diamond magnetic field measurements with cardiac cells, the cells were monitored and recorded through the top objective. Figure 6.21 illustrates the value of shallow angle illumination, where there is enough optical contrast to monitor the displacement of the cell as a function of time. We used the average cell displacement as a real time metric of cardiac cell activity. Figure 6.21 illustrates an experiment where the cells were initially beating at a steady rate under low power optical illumination and where the bath temperature was 25°C, much lower than the physiologically preferred temperature of 37°C. When the 532 nm laser excitation power was increase to 3W, the extra 2W of power lead to a heating of 8°C, bringing the diamond temperature to 33°C and increasing the beat frequency.

Further study is needed to characterize the cellular response to the high MW powers needed in Ramsey-like sequences, which will be necessary for further QDM sensitivity

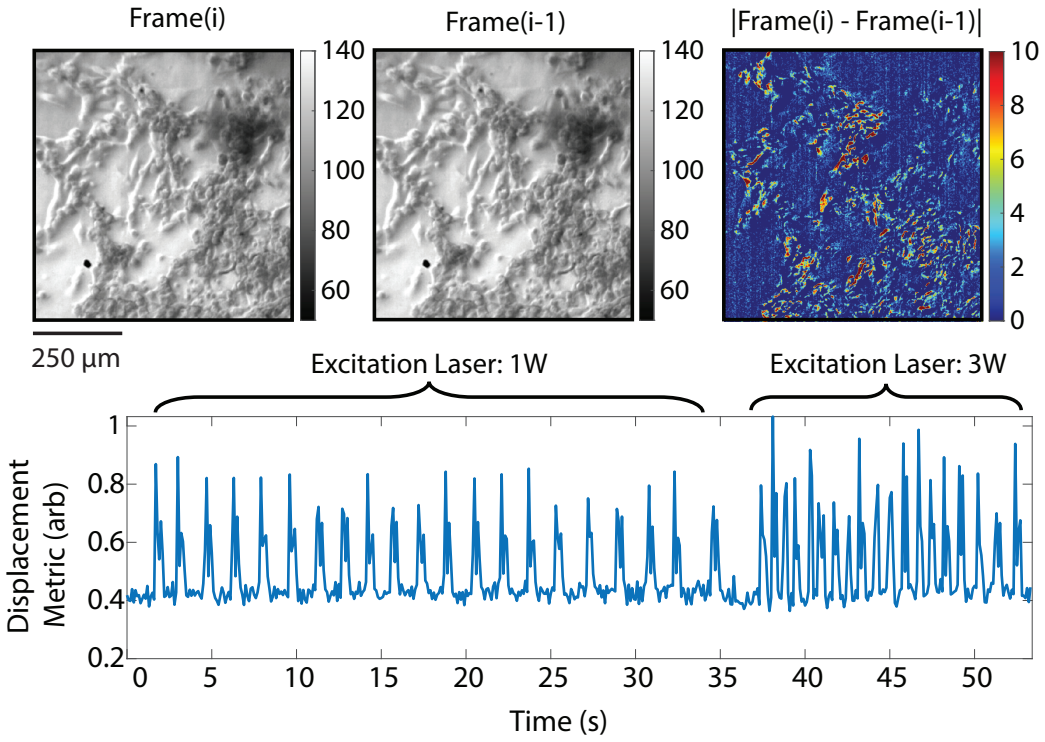

Figure 6.21: Utilization of the top objective to monitor cardiomyocyte activity. The displacement of the cell from frame to frame is used as a label free method for monitoring cell activity. The average displacement is used as a metric to track the activity and response of cardiomyocytes to external stimuli. In this experiment, the green NV excitation power was increase from 1 W to 3W. This increase in power increased the temperature of the diamond, which caused the cells to beat faster.

improvement.

6.6 Ongoing Development of Ramsey Imaging

In order to both improve volume normalized magnetic sensitivity and decrease the influence of diamond inhomogeneities for imaging small signals, more advanced protocols than Lock-In CW ODMR are needed [56, 107, 108]. Ramsey-based sensing sequences are pulsed protocols that enable higher sensitivity measurements for a given measurement volume while maintaining sensitivity to static and quasi-static external magnetic fields. This section gives a brief update on current progress on the development and application of Ramsey-based imaging experiments in two different setups.

6.6.1 Ramsey Imaging of Phantom Structures

In the first experiment (see Refs. [107] for more details), a modified experimental setup based on Figure 6.3, was designed to combine the engineering advancements demonstrated in the Lock-In CW ODMR setup with compatibility for Ramsey sensing sequences. The main differences between the Lock-In CW ODMR setup and the Ramsey imaging setup are the optics for focusing the excitation beam into a smaller laser spot and the smaller MW loop needed to achieve large Rabi frequencies (5-10 MHz) for pulsed control. Through focusing the laser and utilized the smaller MW loops, short initialization times and fast Rabi frequencies are achieved, enabling sensitive Ramsey experiments.

In an initial demonstration of Ramsey imaging sensitivity (Figure 6.22), current was passed through a small imaging phantom (shaped like a snail) of palladium fabricated on an SiC wafer. Palladium was used to lower the conductivity of the structure. We found that using gold or other metallic phantoms resulted in significant microwave inhomogeneities due to MWs being induced within the phantom partially cancelling the local MW field. During

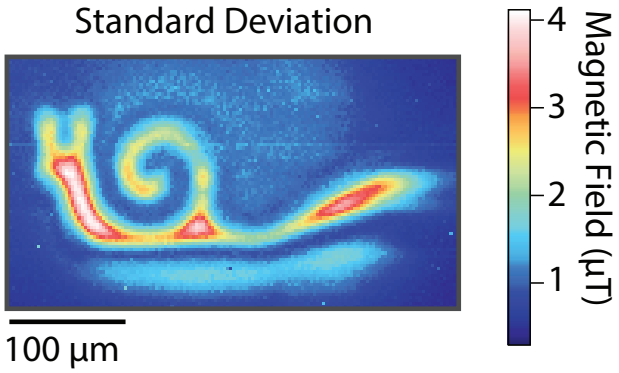

Figure 6.22: Example magnetic field imaging from Ramsey phantom experiments.

a Ramsey magnetometry sequence, a volume normalized sensitivity of 100 $nTHz^{-1/2}\mu m^{3/2}$ was achieved [107].

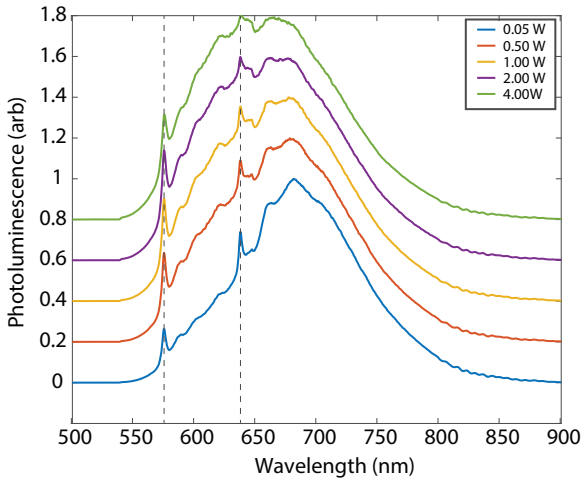

Figure 6.23: Example PL spectra for the diamond used in the Ramsey phantom imaging experiments. One of the major factors limiting performance was the poor charge state stability at high green excitation powers.

However, this sensitivity was significantly worse than originally anticipated for Ramsey-based measurements. After putting a spectrometer into the collection path of the setup (see Figure 6.23) we were able to determine that the poor charge state of the NV layer diamond

at high laser powers (3-4 W) was likely the leading cause of sensitivity degradation. For the highest powers in Figure 6.23, there is not even a visible contribution to the PL at the NV^- ZPL. This process motivated a lot of the work in Chapter 4, and this sample used in the Ramsey experiments was the layer sample studied in the charge state measurements.

6.6.2 Double Quantum Ramsey Imaging to Mitigate Sensor Inhomogeneities

In a separate experimental setup, [21, 108], Ramsey-based measurements were being developed for diamond characterization studies and to demonstrate the capabilities of Double Quantum (DQ) coherence for canceling inhomogeneities in diamond performance. As stated in Chapter 1, operating in the DQ coherence basis mitigates the contribution of of longitudinal strain and temperature variations on the NV. For spatially varying strain as in seen in Chapter 4, this strain variation can be a major limitation to sensor performance and limits what diamonds can be used for imaging experiments.

Through combining previous efforts of demonstrating DQ Ramsey measurements [21], with collection of light onto a camera, the homogenizing effect of DQ was directly observed (Figure 6.24) in Reference [108]. Through increased sensor homogeneity, using an improved layer sample, optimizing fluorescence collection and performance of the camera, and through the correction of residual single quantum signals, we were able to reach a volume normalized sensitivity of 38 $nTHz^{-1/2}\mu m^{3/2}$, when accounting for the size of the sensing voxels in Figure 6.24. These results are promising due to the several straightforward steps for further enhancing sensitivity: (i) improved collection efficiency; (ii) camera modifications to minimize pixel heterogeneity and improving filling factor; (iii) increased optical excitation intensity; (iv) improved NV charge state stability; and (v) implementation of spin bath driving [21] to increase T_2^*. Further information on these experiments and the relevant protocols

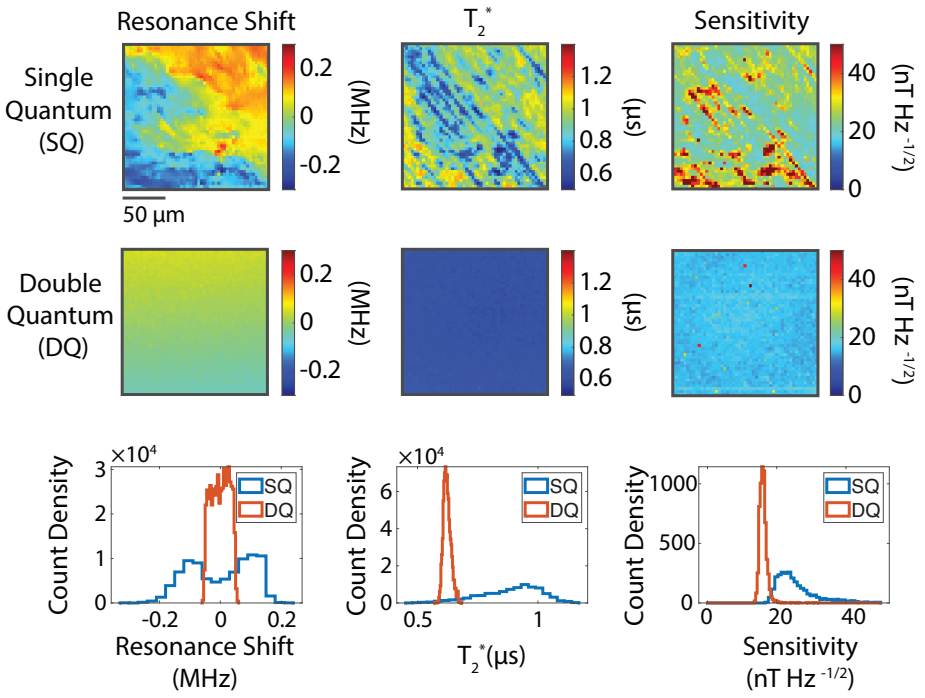

Figure 6.24: Demonstration of improved homogeneity and sensing performance with Double Quantum Ramsey (DQ) Imaging, relative to the conventional Single Quantum (SQ) coherence experiments.

can be found in Reference [108].

6.6.3 Realistic Sensitivity Projections

Based on expected diamond and experiment performance enhancements, realistic near-term and optimistic next-generation volume normalized sensitivities can be calculated to assist with feasibility estimates of future experiments. These projections are for conventional Ramsey based magnetometry experiments and do not consider other advanced protocols [56], which could lead to further improved performance.

The shot noise limited sensitivity, $\eta_{DQ,4-axis}$, for DQ Ramsey measurements with 4-axes NV axes overlapped is given by: [56, 107, 108]

	T_2^* (ns)	C'	t_I (ns)	t_R (ns)	[N] (ppm)	$[NV^-]$ (ppm)	N_{NV^-} (1 μm^3)	R (photons/s)	η (nT $Hz^{-1/2}\mu m^{3/2}$)
Near Term	500	0.05	2000	300	27	1.7	3.0×10^5	1.5×10^{10}	24
Optimistic	4000	0.08*	2000	300	2.0	1.0	1.8×10^5	9×10^9	3

Table 6.2: Sensitivity projection for near term and next generation Ramsey imaging experiments. For the next generation contrast, the number stated (0.08*) assumes that issues involving charge state for low [N] diamonds can be mitigated. Otherwise, different trade-offs will need to be made.

$$\eta_{DQ,4-axis} = \frac{1}{2}\frac{1}{2\sqrt{4/3}}\frac{\hbar}{g_e\mu_B}\frac{\sqrt{t_I+\tau+t_R}}{\tau}\frac{1}{Ce^{-\tau/T^*_{2,DQ}}\sqrt{\beta}} \tag{6.4}$$

Where $\tau_{optimal} \sim T^*_{2,DQ}/2$ and $\beta = R\tau_R$ is the number of photons collected for a given measurement.

Table 6.2 gives reasonable parameters for what is achievable in the near term and next generation with Ramsey magnetic imaging. Even further improvements can be made based on improved light collection from what is assumed in the table and other advancements in diamond growth and spin bath control. For envisioned imaging applications of neuronal currents, where real time near optical diffraction limited (1 μm) resolution imaging with ms time resolution of 1 nT fields is desired, a volume normalized sensitivity of 30 $pTHz^{-1/2}\mu m^{3/2}$ will be required.

For current optimal DC sensing methodologies, the expected optimal DC sensitivity of a single NV is on the order of 100 nT $Hz^{-1/2}$ [43, 257]. Assuming convention square-root scaling of sensitivity with the number of NVs and the number of NVs in a 1 μm^3 volume of 3.0×10^5 (see Table 6.2), the optimal performance with current Ramsey-based DC magnetometry protocols is $\sim 200\, pTHz^{-1/2}\mu m^{3/2}$. Further developments and advancements in DC magnetic imaging, sensing, and methods in general are needed to achieve the necessary levels of sensitivity for ambitious envisioned future applications.

Chapter 7

Outlook and Future Experiments

This chapter briefly goes into some future directions based off work presented in this thesis and other ongoing research efforts. The first section focuses on considerations for further improvement of diamond sensors and promising methods for going beyond the current experimental capabilities and protocols. The later sections focus on ongoing and potential applications in integrated circuits, mammalian cell measurements, cell-scale NV NMR, and dark matter detection utilizing nano-scale strain in the diamond lattice.

7.1 Improved Diamond Properties

Further exploration and optimization of the diamond parameters space for specific applications is needed. Recently, we conducted such an effort through collaboration with Element Six on diamond growth efforts and feedback on diamond quality [201]. In this effort, we worked to optimize diamond properties for a relatively high starting nitrogen concentration (20 ppm). We also worked toward minimizing unwanted defects in the diamond lattice and improving homogeneity of crystal strain to improve NV contrast, brightness, dephasing times, and repeatably for a large number of diamond samples. Further effort is needed to

expand this work to other regimes of diamond parameter space.

One particularly important parameter for framing these future efforts is the nitrogen (and resultant NV) concentration. There are two regimes of interest: low nitrogen concentration ($\sim$ 1 ppm and below) and high nitrogen concentration ($\sim$ 10 ppm and above). Due to competing optimizations, there realistically will not be one diamond type or class ideal for all applications. Careful consideration is needed regarding what needs to be sensed (signal type and sample properties), what protocols are going to be used, and what future protocols could be used in the future.

7.1.1 Low Nitrogen (and NV) Concentration Limit

One of the most important sensitivity parameters identified in Reference [56], is the ensemble NV dephasing time, T_2^*, due to the near inverse-linear scaling of sensitivity with T_2^* in the large measurement overhead limit (due primarily to long initialization pulses.) When other sources of ensemble dephasing have been controlled, the nitrogen and NV spin bath will dominate T_2^*. Lowering their concentration will allow for increases in T_2^*. However, this longer T_2^* comes at a cost in other parameters. For fixed laser intensity and collection efficiency, a lower concentration of NVs means less light will be collected, which degrades sensitivity. Furthermore, pushing to longer dephasing times puts more stringent requirements on the experimental engineering and control to ensure the experiment is not limited by other technical sources of dephasing. As discussed in Chapter 4 and in Reference [202], diamonds with lower concentrations of nitrogen are likely to have less stable NV charge states at large optical excitation intensities due to the lower density of electron donors.

A lower excitation intensity can be used to avoid the charge state instability effects, but this will decrease the amount of light collected and increase the needed initialization times, or a higher excitation intensity can be used and the measurement contrast will be

degraded due to the poor NV charge state. Discovering methods to stabilize the NV charge state at high optical intensities would increase the favorability of low nitrogen concentration diamonds.

7.1.2 High Nitrogen (and NV) Concentration Limit

In the opposite limit, diamonds with higher nitrogen (and resultant NV) densities could be pursued to utilize their increase in fluorescence, charge state stability, and compatibility with proposed NV-NV interaction sensing or decoupling schemes [310–312]. The increased charge state stability of higher nitrogen concentration samples could provide utility in allowing for higher intensity optical initialization, which would eliminate one of the biggest sources of dead time for pulsed magnetometry experiments. Furthermore, higher [N] leads to strong interactions, which under normal sensing schemes limits the dephasing times. For some applications like CW ODMR, which has been one of the most successful routes of NV sensing applications, the increased broadening due to NV-N interactions is not detrimental relative to the effects of continuous microwave and optical driving (under normal sensing conditions.) However, these stronger interactions could be canceled in some schemes [312] to improve dephasing times or these interactions could be utilized to enhance sensitivity [310, 311].

Further exploration, such as the work done [201], is needed regarding the exact trade-offs associated with using different [N]for ensemble NV sensors.

7.2 Integrated Circuit Measurement Developments

The work in Chapter 5, utilizes a static Quantum Diamond Microscope (QDM) for the imaging of natural integrated circuit activity. This new imaging modality shows significant potential due to the large amount of information gathered about current propagation in the die and the ability to use magnetic field images for state classification.

Going forward there are several areas of interest to improve and expand such QDM integrated circuit

- Decrease measurement time through optimized frequency sweeps to minimize the number of frequency points needed for given inhomogeneities over the field of view.
- Improve measurement sensitivity through utilizing Lock-In CW ODMR techniques for real time imaging of transient fields.
- Improve fitting and analysis protocols to be able to extract Lorentzian parameters and Hamiltonian fit parameters from measurements at fewer points and with lower SNR datasets.
- Expand the scope of the measurement to include different board architectures and chip types. For example, the work in Chapter 5 focused on measurements of an FPGA with a wire-bond interface. Future measurement protocols will need to be optimized for application-specific integrated circuits (ASICs) and other interface geometries such as flip-chip.
- In flip-chip geometries the measurement plane is closer to c4 bumps and other interfaces that contain magnetic components. These will likely distort the magnetic field measurements and introduce systematic effects that need to be addressed.
- For example, thicker layer samples and larger stand-off distances are likely needed to avoid measurement degradation due to the magnetic gradients introduced by the c4 bumps.
- Experimental measurements need to be expanded to include a wider set of functional activity beyond the activation of Ring Oscillators (ROs). ROs are a useful test-bed for characterizing the ability to localize functions, however, functional states more

representative of what would be seen in security applications are needed (look-up tables, registers, clocks, chip memory, etc.)

- Finally, expansion of the use of machine learning methods and neural networks can improve all aspects of this effort. From improved fitting methods that better handle sparsely sampled noisy data to classification of states-dependent magnetic images to localize defects and non-idealities, machine learning and neural network based methods have the capability to drastically improve QDM measurement performance for the integrated circuit (and likely many other) applications

7.3 Cardiac and Neuronal Measurements

A long-standing goal for QDM magnetic imaging is real-time monitoring of natural electromagnetic activity and dynamics in living cells. As discussed in Chapter 6, the volume-normalized sensitivity needed for envisioned biological applications is 10 $nTHz^{-1/2}\mu m^{3/2}$ (for coarse spatial resolution measurements) and $\sim 0.03\ nTHz^{-1/2}\mu m^{3/2}$ (for optical diffraction limited real-time measurements with good SNR). In this section we will further explore applications that can be done in the near term before these sensitivities are regularly achieved; as well as what can be done in the long term with improved measurements.

7.3.1 Signal Enhancement and Passive Cellular Properties

In the near term, it would be beneficial for biomagnetic fields to be amplified to enable effective QDM studies. Such signals can be amplified through (i) methods to increase the local density of magnetic flux lines through flux concentrators [313], which can be further improved through micro and nano-fabrication methods; and (ii) applying external signals that lead to large magnetic fields containing biologically relevant information. The section

below will focus on the second category and methods in generally where a large ,biologically relevant magnetic field can be evoked that contains nontrivial information.

Injected Currents

The injection of external currents into biological cells is conventionally known as a current-clamp [314–317] and is used to monitor evoked activity responses in cellular membranes as a function of the input current levels. In complicated neuronal networks with branching structures, the uniformity of current injection can be degraded by loss of current as a function of propagation distance [299]. Direct imaging of the magnetic fields associated with these injected currents could help inform models about current-clamping in cellular systems and compensate for varying passive properties of the cells.

However, due to chemical synapses connecting a large number of cell types (especially in neuronal systems) injected currents would not propagate from cell to cell and limit the mapping of passive properties to a single cell. A large class of cells (including cardiac cells) are coupled via gap junctions [318,319], which allow for direct electrical connections between cells and mediate a variate of functions from cellular synchronization to injury response to the immune response [318, 320–324]. This direct cellular connection allows for an electric path to flow from cell to cell enabling a variety of injected current measurements in networks of coupled cells. In the examples below we consider, structured networks of cardiac cells. One class of measurements is probing the expanse and degree of connectedness in these cellular networks [325–327]. Traditionally dyes will be injected in one cell and the extent to which the dye spreads allows for measures of which cells are connected in the network and the strength of the connections. However, these results require waiting for the dye to diffuse through the network and small-molecule dyes are needed to pass through the gap junctions. The injection of electrical currents could allow for improved measurements

through (i) not being limited by the size of the effect dye; (ii) enabling rapid spread of the currents throughout the network; and (iii) currents of different frequencies could be used to probe the complex impedances of the cellular connections. Following up on the last point, the imaging of passive properties (real and complex impedances of the cellular connections and couplings to the bath) could provide utility in monitoring cellular properties such as heterogeneous gap junction formation, arrhythmia susceptibility, and understanding of cardiac remodeling [328–330].

7.3.2 Cellular Activity Imaging

For measuring the natural biomagnetic field associated with cellular activity, improving magnetic sensitivity is the most important factor. With increased sensitivity the natural magnetic activity of a wide variety of cellular systems could be studied. Further sensitivity improvement also would enable better interpretation of the biomagnetic fields from complex 3D sources. One important application of study for 2D cultures and tissues is informing models and biophysical constraints for interpretation of 3D in-vivo measurements. An intriguing method for the obtaining 3D magnetic activity information deep into biological sources (the brain) is direct current imaging with MRI [331]. Higher resolution QDM measurements of similar systems could provide value for validating preliminary measurements.

7.4 Cellular NV NMR

One area not discussed in depth in this thesis, is the use of AC magnetometry to measure high frequency magnetic signals (see Chapter 1). A recent area of interest in the NV field has been expanding the capabilities of NV AC magnetometry toward high spectral resolution cellular scale-NMR [48,332–334]. Recently, NV-NMR chemical specificity has been achieved on the single-cell ($\sim 10\mu m$) length scale, with sufficient sensitivity to be approaching bio-

logical levels. Hyperpolarization was utilized in the latest result [334] to show sensitivity to nicotinamide, which is a component of nicotinamide adenine dinucleotide (NAD, essential to cell metabolism and other processes). In this work, we demonstrated sensitivity to 100 mM of nicotinamide and down to 1 mM sensitivity to pyridine. In-vivo studies with proton NMR spectroscopy in macroscopic samples have shown natural occurring levels of NAD on the order of 1 mM [335, 336]. Further work is needed to expand microfluidic capabilities to improve the efficiency of molecular delivery to the diamond surface and chemical specificity to improve the applicability of NV-NMR to complex cellular environments, which could have applications toward the study of cellular metabolomics [337].

7.5 Dark Matter Strain

Finally, another promising direction for NV diamond quantum sensors is to serve as a directional dark matter detector [203, 338]. Next generation WIMP dark matter detectors are likely to be limited by the neutrino background from the sun. Through the combination of conventional scintillation techniques and high resolution NV strain mapping (building off techniques from Chapter 4 and other methods), we are working on proof of principle measurements showing the feasibility of using NV-diamond substrates. One conceptual way for thinking about the project is a "solid-state bubble chamber", where interactions between proposed dark matter candidates and the diamond lattice will result in strain to the diamond lattice that can be localized through measuring the effects of strain on the NV resonance shifts (or through other methods like x-ray techniques or the creation of vacancies in the diamond lattice). These efforts have a large overlap with efforts to improve diamond sensors because of the need to create homogeneous diamonds and minimize small scale strain features to try to eliminate background signals, which could mimic expected strain tracks.

Appendix A

Extra Information for Giant Axon Detection

These sections go into extra detail on the experimental protocol and calibration from Chapter 3.

A.1 Vector Magnetometry

In contrast to scalar magnetometers, (such as vapor cell magnetometers, proton precession magnetometers, and Overhauser effect magnetometers), which measure magnitude but not direction of a magnetic field, vector magnetometers measure the magnetic field projection onto a fixed axis of the sensing device [9]. Scalar magnetometers have the property that the sensing element tends to align along the magnetic field, and thus the sensor can sense only the magnitude and not the direction. In contrast, SQUIDS, Hall probes, fluxgate magnetometers, and NV-diamond magnetometers are vector magnetometers, since the sensing element is fixed in space and does not align along the direction of the magnetic field. An NV spin is quantized along one of four crystallographic NV symmetry axes in the diamond

crystal; and therefore a single NV center senses not the magnitude of the magnetic field but rather the field projection along its own symmetry axis, defined by the line connecting the nitrogen and the vacancy.

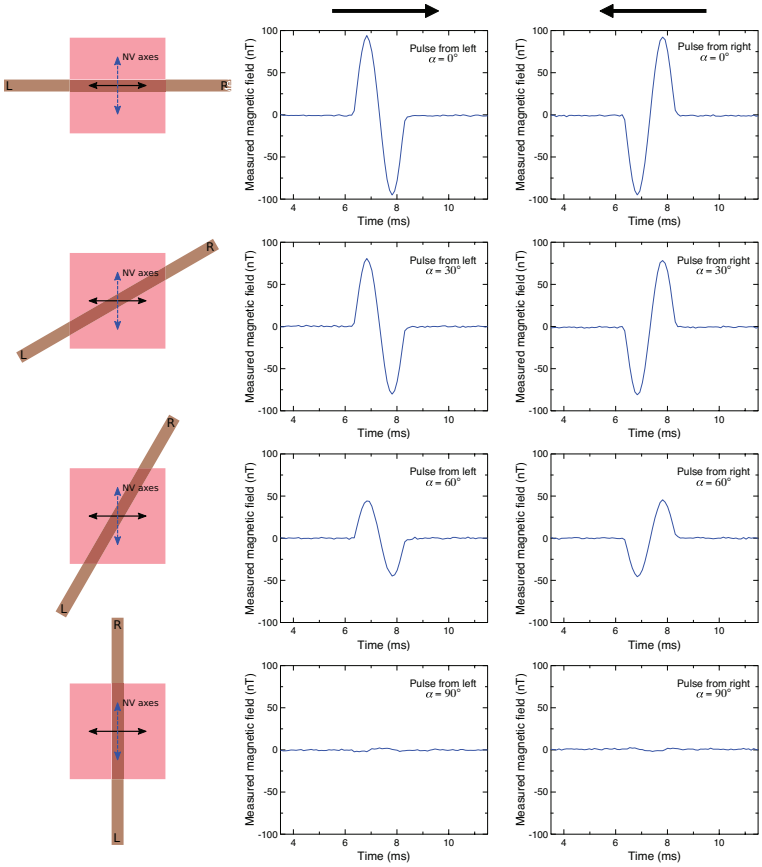

Figure A.1: Vector magnetic sensing using NV-diamond.

In a typical NV ensemble with no preferential orientation [304], the four crystallographic NV symmetry axes are equally populated [257]. An ensemble NV-diamond magnetometer can be set up to be sensitive to the magnetic field projection along a single NV axis or along a vector that equally projects onto two or more of the NV axes. The experiments detailed in this work measure the magnetic field projection along the vector that equally projects onto two NV axes; and thus the device operates as a vector magnetometer. Because

the four NV axes form a basis set that spans three-dimensional space, a local magnetic field's magnitude and direction can be reconstructed from its measured projections onto the NV axes [15, 261]

Action Potential (AP) magnetic fields are expected to encircle the axon and be directed perpendicular to the axon axis and hence the direction of AP propagation. In the magnetometer configuration detailed in this work, the sensor records the component B_x of the AP magnetic field parallel to the NV layer surface, and is most sensitive to APs from axons oriented on the diamond surface perpendicular to the x-axis. The axons are oriented roughly linearly on the diamond and perpendicular to two NV axes, maximizing the projection of the AP magnetic field $B(t)$ onto those axes, as shown in Figure 3.4, with the projection along the other two NV axes expected to be near-zero.

For an axon oriented at angle α with respect to the direction of maximum sensitivity, the sensed magnetic field is reduced by a factor $\cos(\alpha)$, $B_x(t) = B(t)\cos(\alpha)$. This relationship is demonstrated experimentally in Figure A.1 for different orientations of a current-carrying copper wire with respect to the direction of maximum sensitivity. A single period pulse of a sine wave with frequency 512 Hz is sent through the wire, resulting in a 94 nT peak amplitude magnetic field at the NV sensing layer. For any orientation in the plane except for $\alpha = 90°$, the magnetic field projection along the x-axis is nonzero, with the sign of the measured bipolar magnetic field waveform indicating the projection of the current pulse propagation direction along $\alpha = 0°$. Similarly, when measuring AP magnetic fields, the projection of the AP propagation direction along the x-axis can be determined from the magnetic time trace $B_x(t)$. Moreover, if the expected signal size for $\alpha = 0°$ is known, the angle α can be determined from a measurement of $B_x(t)$.

In a next-generation NV-diamond instrument (QDM) for magnetic imaging of networks of neurons oriented arbitrarily on the diamond surface, the component of $B(t)$ per-

pendicular to the NV layer at each point on the diamond surface can be sensed. The azimuthal AP magnetic field projections would then have opposite sign for measurement points on different sides of the axon, and $B(t)$ would in general have nonzero projection on each of the four NV axes, allowing mapping of AP propagation in the network.

A.2 Magnetic Sensitivity Determination Methods

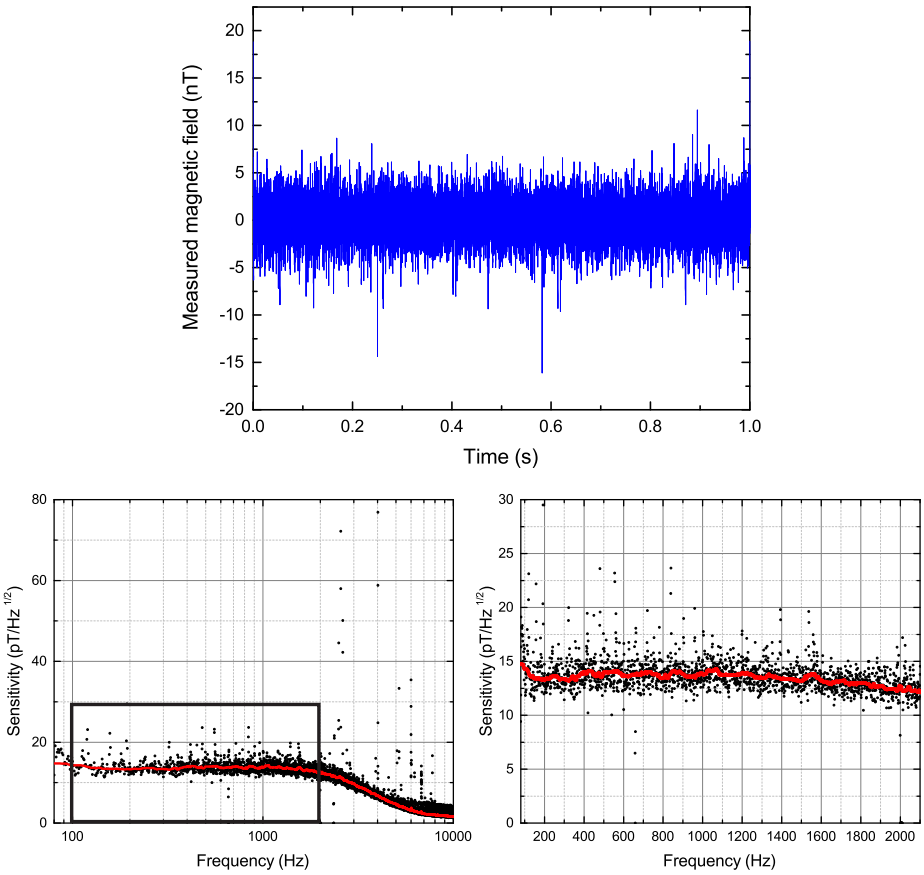

Figure A.2: Characterization of magnetic sensitivity in the time (top) and frequency (bottom) domains

As previously mentioned in Chapter 1, a magnetometer's sensitivity is defined as $\eta = \delta B\sqrt{T}$ where δB is the magnetic field signal that is as large as the noise, i.e., at

SNR=1, after measurement time T [179]. The sensitivity of our NV-diamond magnetometer is evaluated using three methods. Figure A.2 demonstrates the time domain and frequency domain signals used for sensitivity determination.

In method 1, a test magnetic field $B_{test}(t) = B_{test}\sin[2\pi f_{test}t]$ is applied for $N_{trials} = 150$, each of time $T_{trial} = 1s$, and the measured magnetic field $B^{meas}(t)$ is recorded. For each trial i the quantity:

$$x_i = \frac{1}{T_{trial}}\int_0^{T_{trial}} B^{meas}(t)B_{test}(t)dt \tag{A.1}$$

is computed. The method 1 sensitivity η_1 is:

$$\eta_1 = \frac{B_{test}^{rms}\sqrt{2}}{\mu}\sqrt{\frac{1}{N_{trials}}\sum_{i=0}^{N_{trials}}(x_i-\mu)^2 \times T_{trial}} \tag{A.2}$$

where $\mu \equiv \frac{1}{N_{trials}}\sum_{i=0}^{N_{trials}} x_i$, the factor of $\sqrt{2}$ accounts for quadrature noise, $B_{test}^{rms} = B_{test}/\sqrt{2}$, and typically $f_{test} = 250Hz$.

In method 2, $B_{test}(t)$ is applied for $N_{trials} = 150$, each of time $T_{trial} = 1s$, and $B^{meas}(t)$ is recorded. The single-sided root-mean-squared (RMS) spectral frequency profile of $B^{meas}(t)$ is defined to be $\widetilde{B}^{meas}(f)$. The method 2 sensitivity η_2 is

$$\eta_2 = B_{test}^{rms}\left\langle \frac{\frac{1}{f_{stop}-f_{start}}\int_{f_{start}}^{f_{stop}}\widetilde{B}^{meas}(f)df}{\frac{1}{\Delta f}\int_{f_{test}-\Delta/2}^{f_{test}+\Delta/2}\widetilde{B}^{meas}(f)df}\right\rangle_{N_{trials}} \times \sqrt{T_{trial}} \tag{A.3}$$

where $\Delta f = \frac{1}{T_{trial}}$, the expected value is taken over N_{trials}, and typically $f_{start} = 300Hz$, $f_{stop} = 600Hz$, and $f_{test} = 250Hz$.

In method 3, no test magnetic field is applied and $B^{meas}(t)$ is recorded for $N_{trials} = 150$, each of time $T_{trial} = 1s$; an example trace is shown in Figure 3.9. The sensitivity is then calculated as

$$\eta_3 = \sqrt{\frac{1}{T_{trial}} \int_0^{T_{trial}} [B^{meas}(t)]^2 dt \times \frac{1}{2 f_{ENBW}}}, \tag{A.4}$$

with $f_{ENBW} = 4.0kHz$ is the equivalent noise bandwidth [339].

In all evaluations of the instrument's magnetic field sensitivity, $\eta_1 \sim \eta_2 \sim \eta_3$ is found, although η_1 converges most slowly and is therefore of limited use. Over 150 trials, η_3 ranges from 15.0 to 15.8 $pT/\sqrt{Hz}$, while η_2 is 15 ± 1 $pT/\sqrt{Hz}$. We thus conclude the NV-diamond magnetometer sensitivity is 15 ± 1 $pT/\sqrt{Hz}$, also consistent with a noise floor measurement of $|\widetilde{B}^{meas}(2\pi f)|$ for $T_{trial} = 1$s averaged over $N_{trials} = 150$.

A.3 Magnetometer Calibration

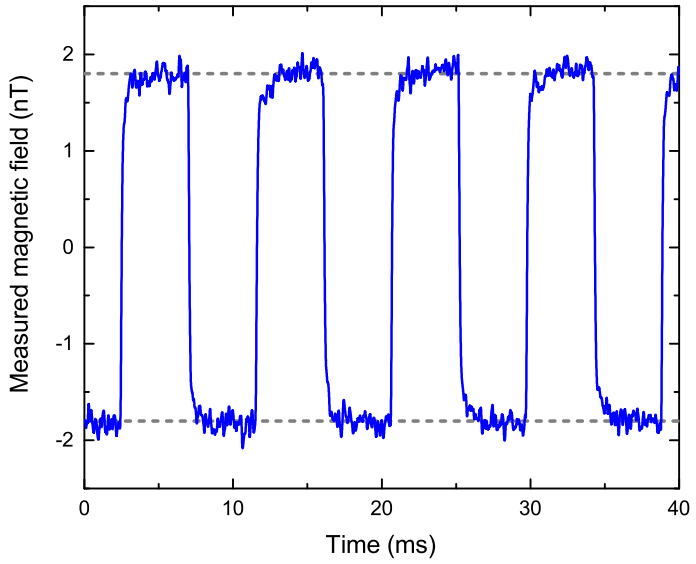

Figure A.3: Time trace for calibration of the magnetometer. Data showing measurement of a calibrated external magnetic field.

Calibration of the NV-diamond magnetometer is independently verified by applying a known test magnetic field $B_{test}(t) = B_{test}\text{square}(2\pi f_{test} t)$ with square wave amplitude B_{test} and frequency f_{test}, and confirming the magnetometer records the correct value for

$B^{meas}(t)$. The test magnetic field is produced by a multi-turn circular current loop (coil) with $N_{turns} = 7$ and radius $r_{coil} = 0.0235\ m$, located at a distance $z_{coil} = 0.103\ m$ from the diamond chip center. The coil is connected in series with an $R_{series} = 50\ \Omega$ resistor. The value of B_{test} is calculated using the formula

$$B_{test} = \frac{\mu_0 N_{turns} I_{coil} r_{coil}^2}{2\left(z_{coil}^2 + r_{coil}^2\right)^{3/2}}, \tag{A.5}$$

where I_{coil} is the current in the coil generated by driving a voltage V_{coil} (t) through the circuit. A 44 mV amplitude square wave yields $B_{test} = 1.8\ nT$, with RMS magnetic field $B_{test}^{rms} = B_{test}$. When this value of B_{test} is applied at frequency $f_{test} = 110\ Hz$, the measured value of $B(t)$ is consistent with the value of B_{test} to better than 5% as shown in Figure A.3. A calibration without harmonics is also performed by applying a 62 mV amplitude sine wave yielding a consistent value of $B_{test}^{rms} = B_{test}/\sqrt{2} = 1.8\ nT$.

A.4 Extra Biological Considerations

A.4.1 Effects of microwave fields on organisms

The observed temperature increase at the diamond sensor with MWs on versus off is 1 °C or less, with no observable damage to the biological specimens [340]. In particular, no adverse effect of the MWs is observed on the long-term health of intact worm E during the >24-hour study. However, this needs to be reanalyzed for each organism and measurement condition going forward.

A.4.2 Effects of static magnetic fields on organisms

Theoretical calculations predict a static bias field of 24 T is needed to noticeably alter neural conduction [341]. FDA guidelines allow magnetic fields up to 8 T for humans subjected

to clinical magnetic resonance imaging. Thus neither the physical magnet itself nor the modest magnetic field of 7 G (0.7 mT) at the location of the diamond is expected to result in deleterious effects to the specimens studied in this or future work.

Appendix B

Real Time Vector Magnetometry and Systematics

B.1 Extension of Lock-In CW ODMR to Simultaneous Vector Magnetometry

For arbitrary networks of cultured cells or tissues, the directionality of current flow will not be fixed to a single Cartesian axis. When currents can flow in any direction, the ability to sense all vector Cartesian components allows for the monitoring of these different directions.

The lock-in ODMR modulation technique discussed previously can be extended to allow for the simultaneous sensing of the full vector magnetic field [55], via applying a bias field that has a different projection on each of the NV axes. The focus of this section will be methods developed along with the simultaneous modulation technique to linearize the Hamiltonian response to allow for real time interpretation of the fluorescence signal.

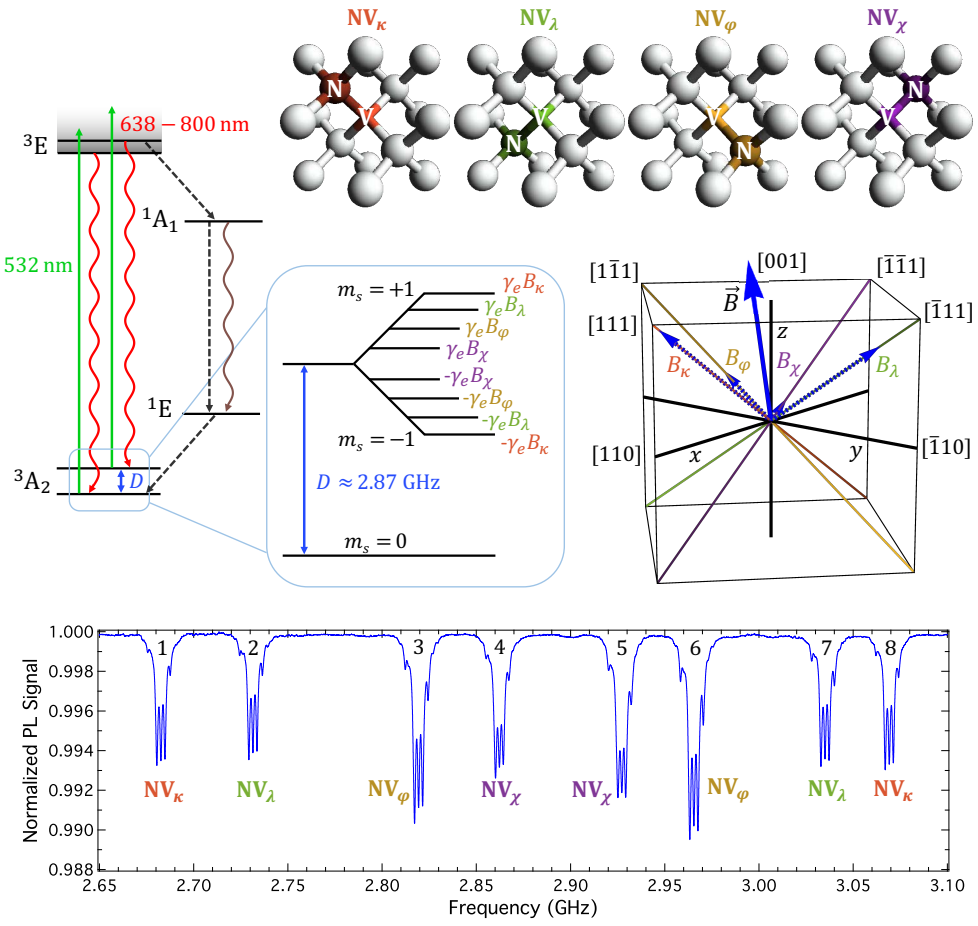

Figure B.1: Schematic showing the NV energy levels, cartoons of the NV crystal axes, direction of bias field, and the CW ODMR spectrum.

B.1.1 Bias Field Determination

The ODMR line center frequencies in the bias field $\vec{B}_0$ are measured by sweeping a single MW tone from 2.65 to 3.10 GHz and recording the PL signal; this yields an ODMR spectrum as shown in Figure B.1. Using a least-squares fit, we determine the line center of the middle hyperfine sub-feature of each of the eight m_s spin transitions. Averaging 10^3 sweeps yields the following set of line centers, which are used to fit for the static field parameters $\vec{B} = \vec{B}_0$, D, and $\vec{M}_z \equiv [M_z^\lambda, M_z^\chi, M_z^\varphi, M_z^\varphi]$:

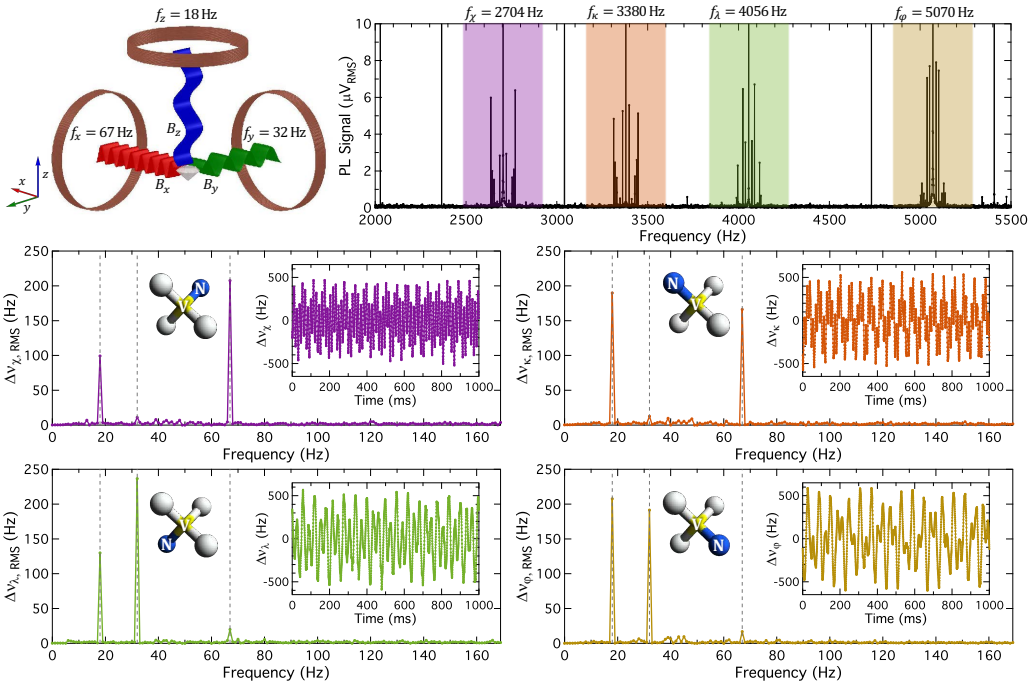

Figure B.2: The information in each NV axis is encoded in the modulation rate for the microwaves. In the lab-frame magnetic fields are applied along the B_X, B_Y, and B_Z directions with different frequencies. These different magnetic field projections can be seen in the Fourier transforms of the fluorescence time traces.

$$\vec{\nu}_{\text{ODMR}} = \begin{bmatrix} \nu_{\kappa^-} \\ \nu_{\lambda^-} \\ \nu_{\varphi^-} \\ \nu_{\chi^-} \\ \nu_{\chi^+} \\ \nu_{\varphi^+} \\ \nu_{\lambda^+} \\ \nu_{\kappa^+} \end{bmatrix} = \begin{bmatrix} 2.6825 \\ 2.7314 \\ 2.8193 \\ 2.8622 \\ 2.9272 \\ 2.9655 \\ 3.0351 \\ 3.0692 \end{bmatrix} \text{ GHz.} \tag{B.1}$$

A nonlinear least-squares (Levenberg-Marquardt) numerical minimization method is used to fit the differences between eigenvalues of the NV ground state spin Hamiltonian

$$\hat{H}^{\,i} = h(D + M_z^i)(S_z^i)^2 + g_e \mu_B \vec{B} \cdot \vec{S}^{\,i} \tag{B.2}$$

to the measured line centers for the four NV orientations $i = \lambda, \chi, \varphi, \kappa$, as described in the Supporting Information of Reference [1].

B.1.2 Linearization of Magnetic Field Shifts

Next, the Hamiltonian is linearized around the measured $\vec{B}_0$, D, and $\vec{M}_z$, to calibrate the expected frequency shifts of the four addressed NV resonance line centers in the presence of an additional small field $\vec{B}_{\text{sens}}$ to be sensed. The result of the numerical linearization is a 4×3 matrix $\mathbf{A}$, where

$$\begin{bmatrix} \Delta\nu_\lambda \\ \Delta\nu_\chi \\ \Delta\nu_\varphi \\ \Delta\nu_\kappa \end{bmatrix}_{\text{sens}} = \mathbf{A} \begin{bmatrix} B_x \\ B_y \\ B_z \end{bmatrix}_{\text{sens}} . \tag{B.3}$$

In the limit of small magnetic field and low strain, the rows of the matrix $\mathbf{A}$ are given, up to a sign, by the NV symmetry axis unit vectors $\hat{n}_i$. The left Moore-Penrose pseudoinverse $\mathbf{A}^+$ is then numerically calculated at the measured $\vec{B}_0$, D, and $\vec{M}_z$ and used to transform detected frequency shifts $\Delta\nu_i(t)$, $i = \lambda, \chi, \varphi, \kappa$ (displayed in Figure B.2 into a measured vector field $\vec{B}_{\text{sens}}(t)$, shown in Figure B.3. This linearized matrix method provides a $\sim$25,000$\times$ speedup compared to unoptimized numerical least-squares fitting of the resonance frequencies ν_i in the presence of $\vec{B}_0 + \vec{B}_{\text{sens}}$. A comparison of the two methods yields good agreement, with fractional error $\lesssim 10^{-5}$ for sensed fields $\lesssim 100\,\text{nT}$.

In the present demonstration, a subset of the detected ODMR line centers from Equation B.1 are selected for MW addressing $\vec{\nu}_{\text{MW}} = \vec{\nu}_{\text{ODMR}}\{2, 4, 6, 8\} = [\nu_{\lambda^-}, \nu_{\chi^-}, \nu_{\varphi^+}, \nu_{\kappa^+}]$. The

+ and − subscripts are dropped herein. The matrix **A** from Equation B.3, reproduced here,

$$\begin{bmatrix} \Delta\nu_\lambda \\ \Delta\nu_\chi \\ \Delta\nu_\varphi \\ \Delta\nu_\kappa \end{bmatrix}_{\text{sens}} = \mathbf{A} \begin{bmatrix} B_x \\ B_y \\ B_z \end{bmatrix}_{\text{sens}}, \tag{B.4}$$

is found by linearizing the Hamiltonian in Equation B.2 about the measured $\vec{B}_0$, D, and $\vec{M}_z \equiv [M_z^\lambda, M_z^\chi, M_z^\varphi, M_z^\varphi]$:

$$\mathbf{A} = \begin{bmatrix} \frac{\partial\nu_\lambda}{\partial B_x} & \frac{\partial\nu_\lambda}{\partial B_y} & \frac{\partial\nu_\lambda}{\partial B_z} \\ \frac{\partial\nu_\chi}{\partial B_x} & \frac{\partial\nu_\chi}{\partial B_y} & \frac{\partial\nu_\chi}{\partial B_z} \\ \frac{\partial\nu_\varphi}{\partial B_x} & \frac{\partial\nu_\varphi}{\partial B_y} & \frac{\partial\nu_\varphi}{\partial B_z} \\ \frac{\partial\nu_\kappa}{\partial B_x} & \frac{\partial\nu_\kappa}{\partial B_y} & \frac{\partial\nu_\kappa}{\partial B_z} \end{bmatrix}_{\vec{B}_0, D, \vec{M}_z}, \tag{B.5}$$

where B_x, B_y, and B_z are the lab-frame magnetic field components. The values of D and $\vec{M}_z$ are taken here to be constant during measurements, such that changes in the ODMR line centers are entirely attributed to magnetic field variations.

The assumption of constant $\vec{M}_z$ is valid in the present device because strain in the diamond is fixed and electric fields couple only very weakly to the NV energy levels at typical values of the bias magnetic field $\vec{B}_0$ [51]. Although temperature drifts couple to D with $dD/dT = 74\,\text{kHz/K}$ [25], these drifts occur on timescales of seconds to hours, and the associated changes in D are therefore outside the 5 Hz to 210 Hz measurement bandwidth of the present device. Furthermore, use of a SiC heat spreader attached to the diamond mitigates laser-induced temperature fluctuations [54]. In a vector magnetometer optimized for sensing lower-frequency magnetic fields ($\lesssim$ Hz), a changing zero-field splitting D_{sens} could also be determined along with $\vec{B}_{\text{sens}}$ from the four measured ODMR line shifts. To additionally sense any dynamic changes in $\vec{M}_z$ would require MW addressing of more than four ODMR features.

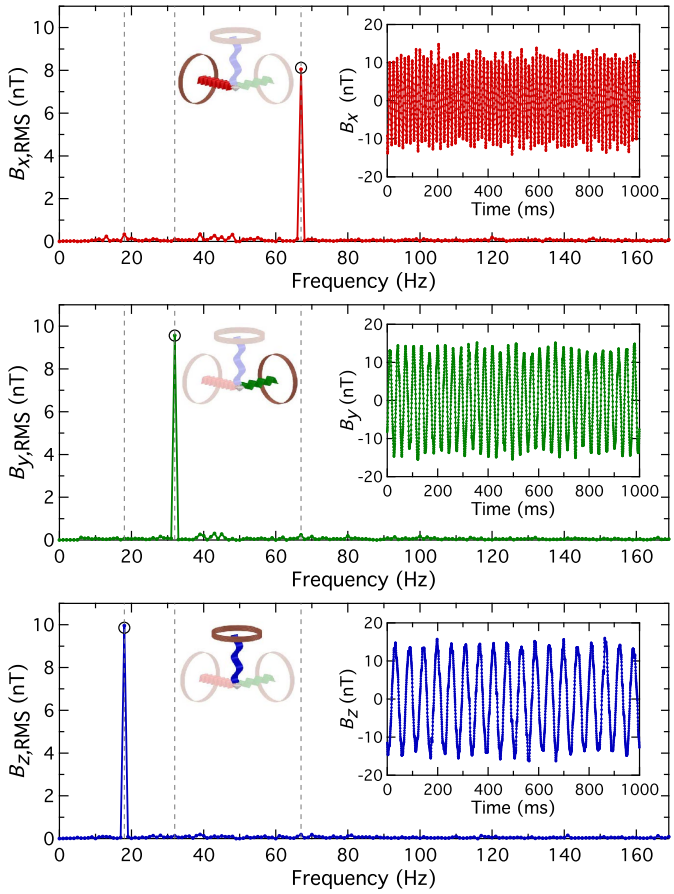

Figure B.3: Demonstration of analysis method to rapidly determine the lab-frame cartesian magnetic field components from the projections on the NV-axes.

In the simple limiting case where, for each NV orientation $i = \lambda, \chi, \varphi, \kappa$, the transverse components of the bias magnetic field are much smaller than the zero-field splitting, ($B_x^i, B_y^i \ll \frac{h}{g\mu_B} D$), and strain coupling is negligible, ($M_x^i, M_y^i, M_z^i \ll \frac{g\mu_B}{h} B_z^i$), the marginal shifts $\Delta\nu_i$, are linearly proportional to the magnetic field projections B_z^i along the respective NV symmetry axes. In this linear Zeeman regime, the rows of the matrix $\mathbf{A}$ are given, up

to a sign, by the NV symmetry axis unit vectors $\hat{n}_i$:

$$\mathbf{A}_{\text{lin}} = \frac{g_e \mu_B}{h} \begin{bmatrix} \hat{n}_\lambda \\ -\hat{n}_\chi \\ -\hat{n}_\varphi \\ \hat{n}_\kappa \end{bmatrix} = \frac{g_e \mu_B}{h} \begin{bmatrix} 0 & -\sqrt{\frac{2}{3}} & -\sqrt{\frac{1}{3}} \\ \sqrt{\frac{2}{3}} & 0 & -\sqrt{\frac{1}{3}} \\ 0 & -\sqrt{\frac{2}{3}} & \sqrt{\frac{1}{3}} \\ \sqrt{\frac{2}{3}} & 0 & \sqrt{\frac{1}{3}} \end{bmatrix}. \tag{B.6}$$

Whether the unit vector is multiplied by $+1$ or -1 depends on the sign of $B_z^i \equiv \vec{B}_0 \cdot \hat{n}_i$ and on whether the addressed transition couples the $|m_s = 0\rangle$ state to the $|m_s = +1\rangle$ or $|m_s = -1\rangle$ state.

Because the bias field $\vec{B}_0$ has non-negligible components transverse to each NV symmetry axis, the present experiment does not satisfy the requirement that only magnetic field projections on the NV symmetry axes contribute to the measured ODMR frequency shifts, and consequently $\mathbf{A}$ differs from $\mathbf{A}_{\text{lin}}$. We determine $\mathbf{A}$ numerically by evaluating the partial derivatives using a step size of $\delta B_x = \delta B_y = \delta B_z = \frac{h}{g_e \mu_B} \cdot 10\,\text{Hz}$. The matrix $\mathbf{A}$ is calculated to be

$$\mathbf{A} = \frac{g_e \mu_B}{h} \begin{bmatrix} 0.10388 & -0.89383 & -0.46341 \\ 0.90435 & 0.04596 & -0.38836 \\ 0.10524 & -0.69511 & 0.73528 \\ 0.75551 & 0.04984 & 0.66268 \end{bmatrix}. \tag{B.7}$$

The Moore-Penrose left pseudoinverse $\mathbf{A}^+$ used in the experiment to determine $\vec{B}_{\text{sens}}(t)$ is numerically computed from $\mathbf{A}$ with the MATLAB function `pinv` and is found to be

$$\mathbf{A}^+ = \frac{h}{g_e \mu_B} \begin{bmatrix} 0.08016 & 0.69252 & -0.02239 & 0.48676 \\ -0.71456 & 0.05848 & -0.50880 & 0.09912 \\ -0.39850 & -0.37710 & 0.51861 & 0.43394 \end{bmatrix}. \tag{B.8}$$

The entries of the matrix $\mathbf{A}^+$ are robust to small variation in the bias magnetic field and other Hamiltonian parameters. A $10\,\mu\text{T}$ change in B_x, B_y, or B_z changes no entry of

$\mathbf{A}^+$ by more than 1% and some by less than 0.01%. Doubling the strain parameters $\vec{M}_z$ also affects the entries of $\mathbf{A}^+$ by less (and for most entries much less) than 1%. A 150 kHz change in D (corresponding to a temperature change of 2 K [25]) affects the entries of $\mathbf{A}^+$ by 0.01% or less. Thus, drifts in temperature or in the bias electric, strain, or magnetic fields have a negligible effect on the reconstruction accuracy of $\vec{B}_{\text{sens}}$ and can be ignored.

This linearized matrix method was compared against a numerical least-squares Hamiltonian fit. The methods were compared for a range of simulated fields $\vec{B}_{\text{sens}}$ ranging from 1 nT to 100 μT. The linear transformation using $\mathbf{A}^+$ from Equation B.8 agreed with the Hamiltonian fit to better than 0.001% for $|\vec{B}_{\text{sens}}| \lesssim 100$ nT and to better than 0.3% for $|\vec{B}_{\text{sens}}| \lesssim 100$ μT. When run on the same desktop computer, the linearized matrix method determines $\vec{B}_{\text{sens}}$ from $\vec{\nu}_{\text{MW}}$ with $\sim$20 μs per measurement, whereas the least-squares Hamiltonian fit requires $\sim$500 ms per field measurement. This $\sim$25,000$\times$ speedup enables real-time vector magnetic field reconstruction from sensed frequency shifts in the present device.

Appendix C

Other Diamond Strain Maps

C.1 Survey of Other Samples from Table 4.1

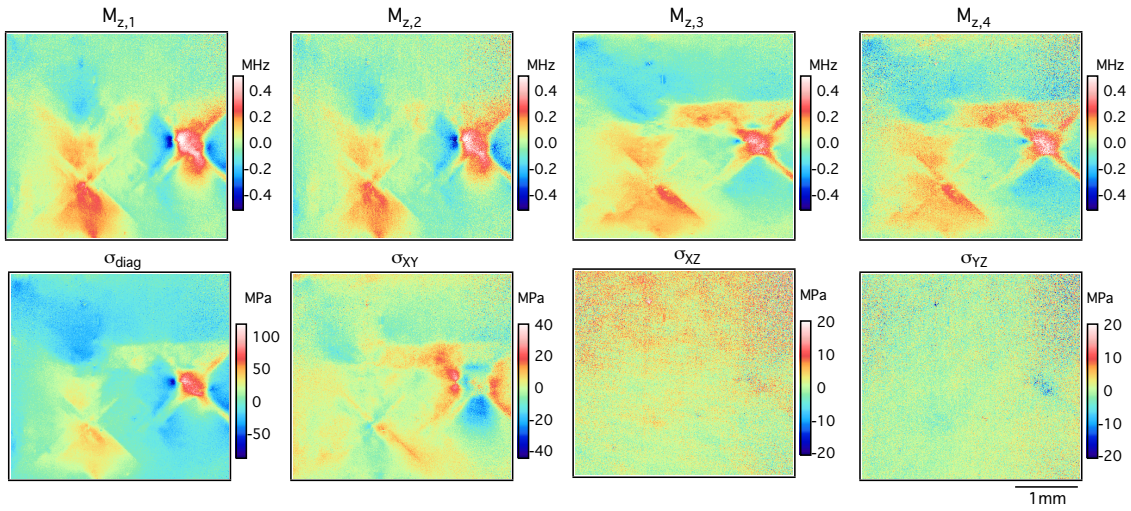

Figure C.1: NV $M_{z,\kappa}$ and $\{\sigma_{diag}, \sigma_{XY}, \sigma_{XZ}, \sigma_{YZ}\}$ maps for diamond Sample B.

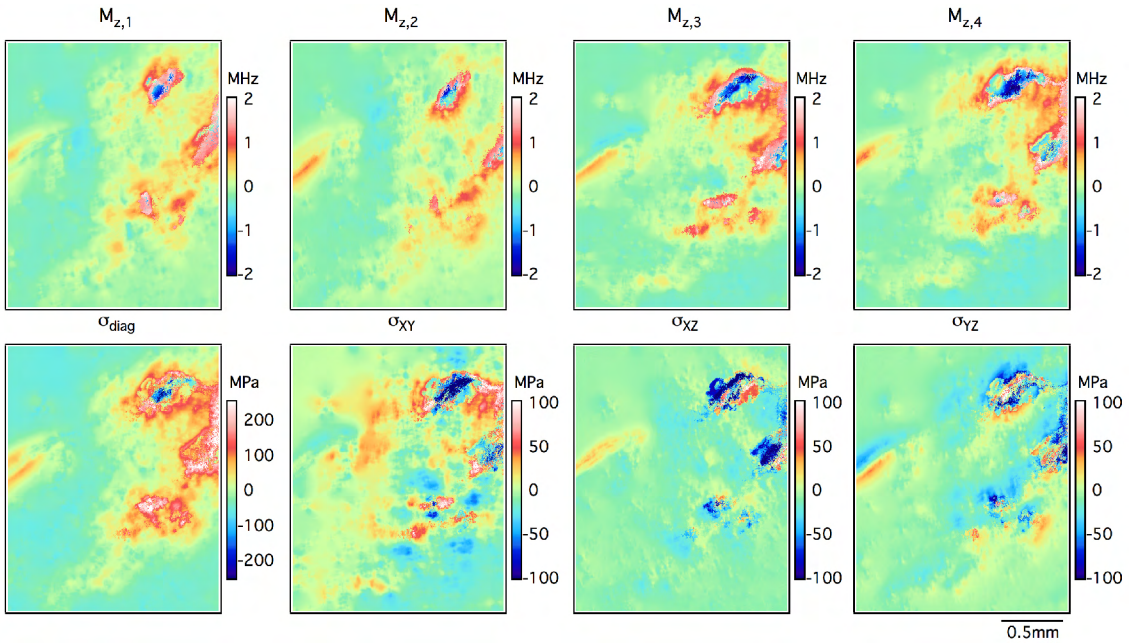

Figure C.2: NV $M_{z,\kappa}$ and $\{\sigma_{diag}, \sigma_{XY}, \sigma_{XZ}, \sigma_{YZ}\}$ maps for diamond Sample C.

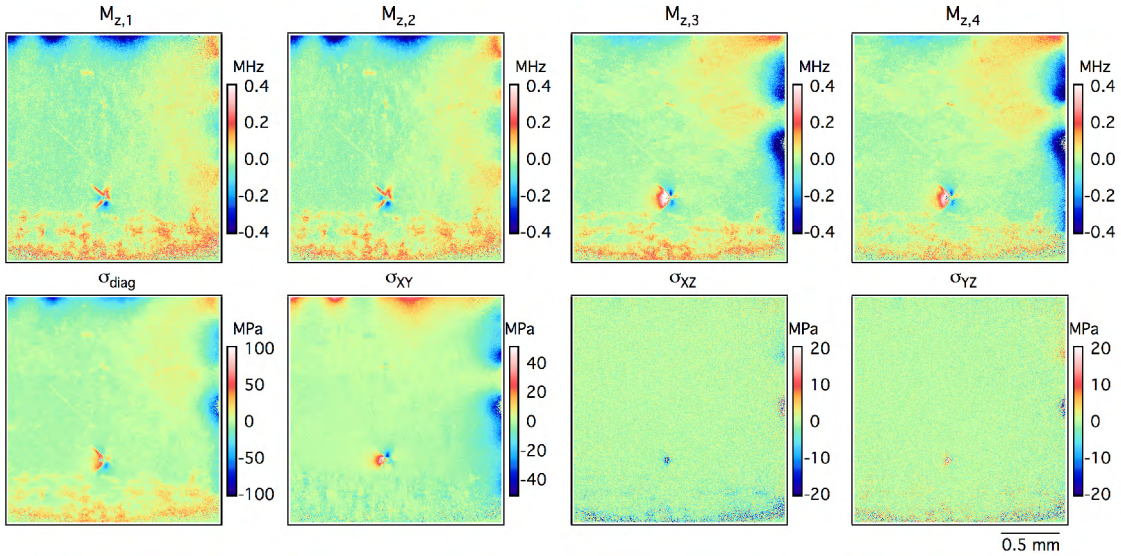

Figure C.3: NV $M_{z,\kappa}$ and $\{\sigma_{diag}, \sigma_{XY}, \sigma_{XZ}, \sigma_{YZ}\}$ maps for diamond Sample D.

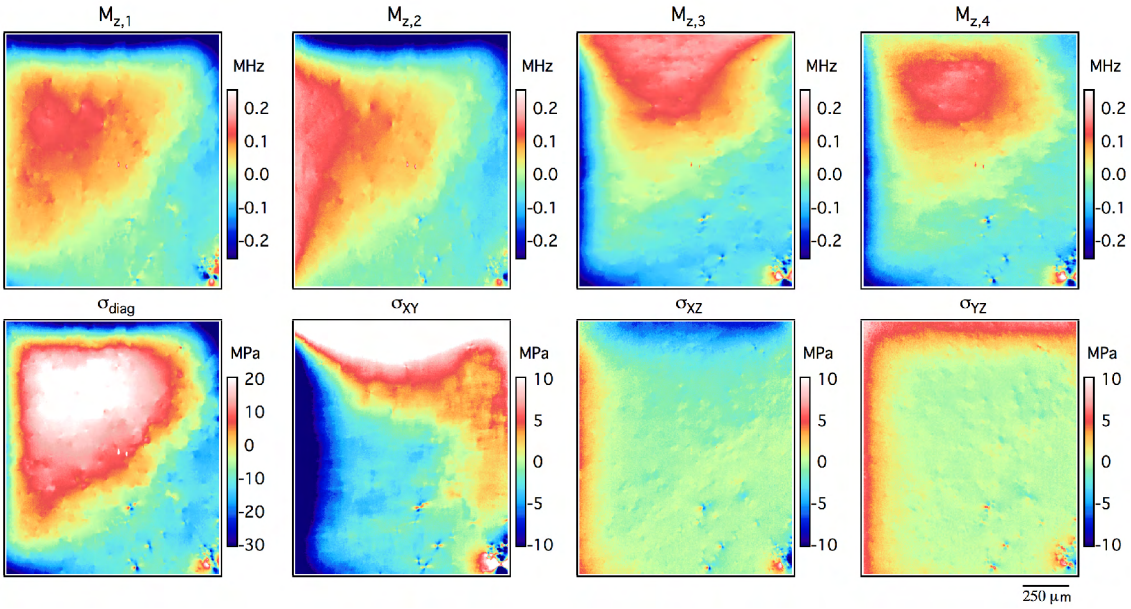

Figure C.4: NV $M_{z,\kappa}$ and $\{\sigma_{diag}, \sigma_{XY}, \sigma_{XZ}, \sigma_{YZ}\}$ maps for diamond Sample E.

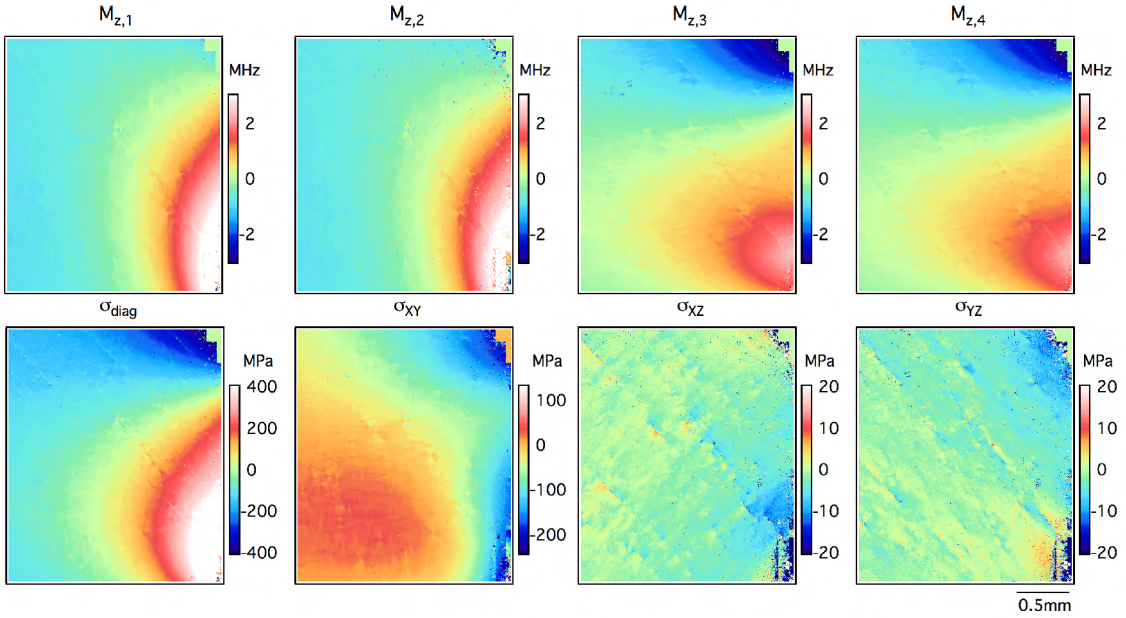

Figure C.5: NV $M_{z,\kappa}$ and $\{\sigma_{diag}, \sigma_{XY}, \sigma_{XZ}, \sigma_{YZ}\}$ maps for diamond Sample F.

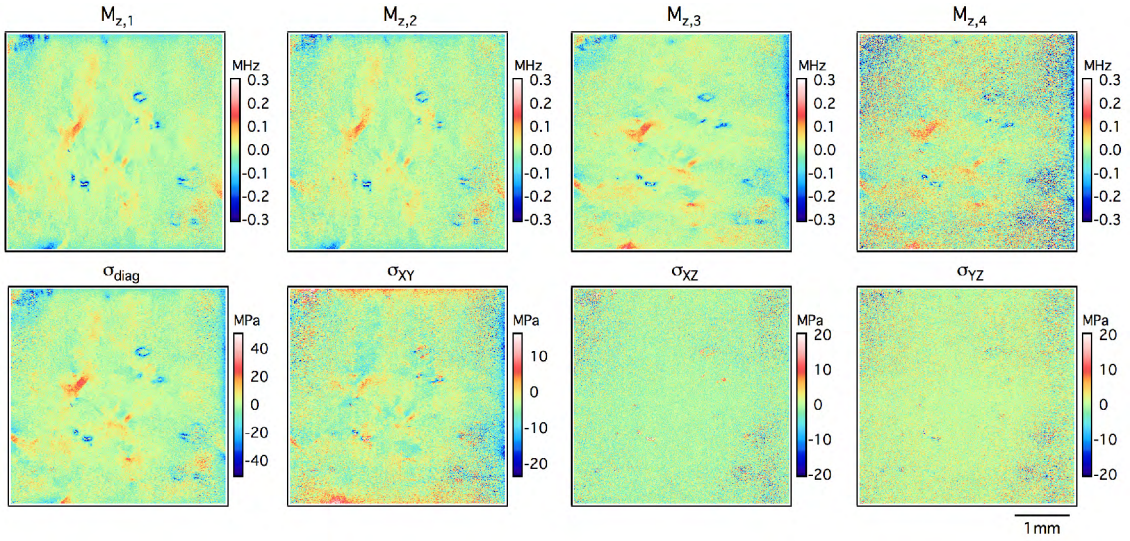

Figure C.6: NV $M_{z,\kappa}$ and $\{\sigma_{diag}, \sigma_{XY}, \sigma_{XZ}, \sigma_{YZ}\}$ maps for diamond Sample G.

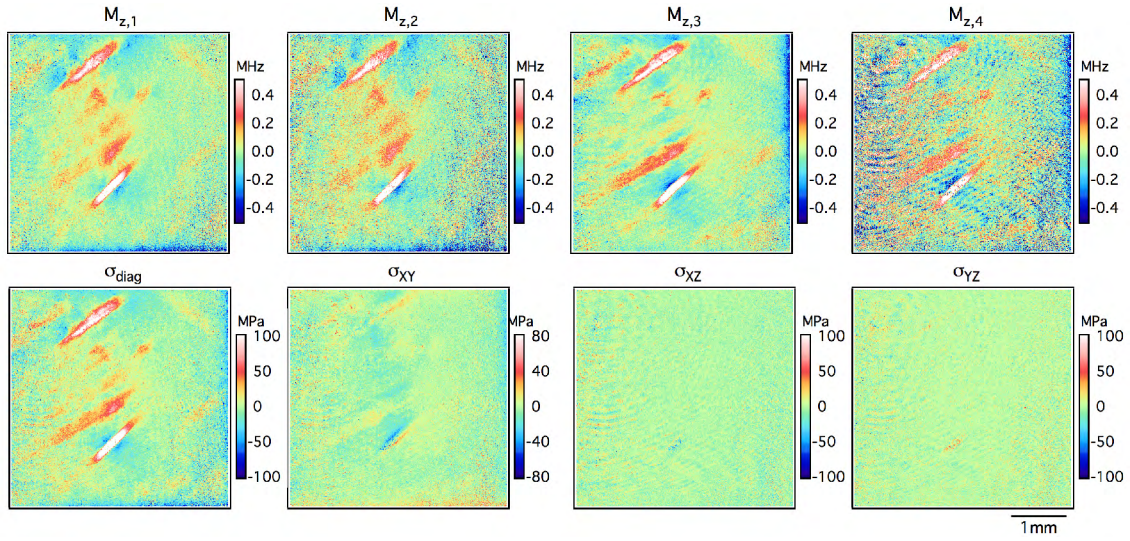

Figure C.7: NV $M_{z,\kappa}$ and $\{\sigma_{diag}, \sigma_{XY}, \sigma_{XZ}, \sigma_{YZ}\}$ maps for diamond Sample H. This data illustrates how inhomogeneity of the excitation (laser fringes) can couple into M_z measurements for low SNR measurements.

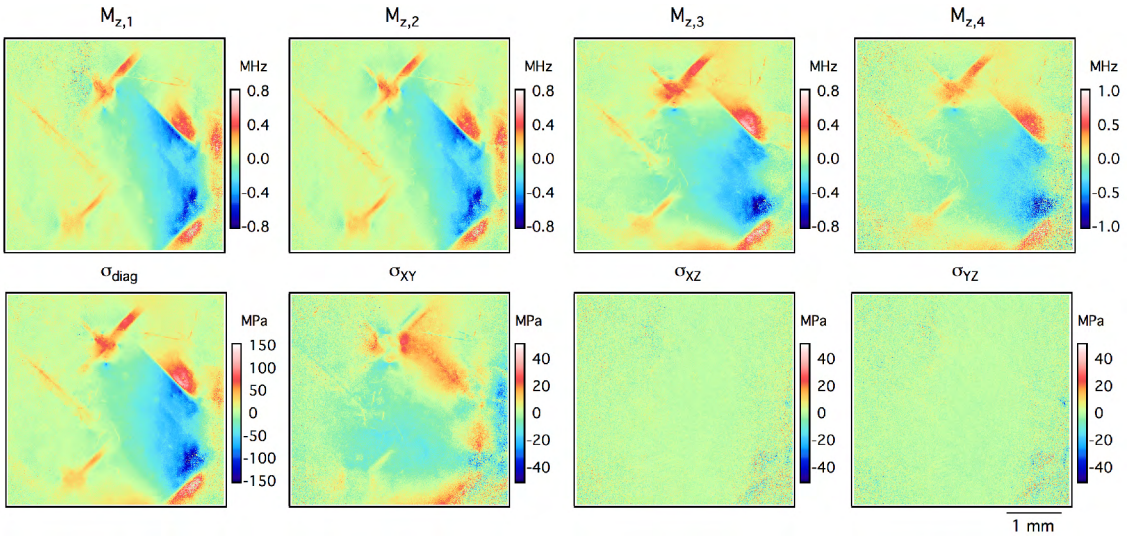

Figure C.8: NV $M_{z,\kappa}$ and $\{\sigma_{diag}, \sigma_{XY}, \sigma_{XZ}, \sigma_{YZ}\}$ maps for diamond Sample I.

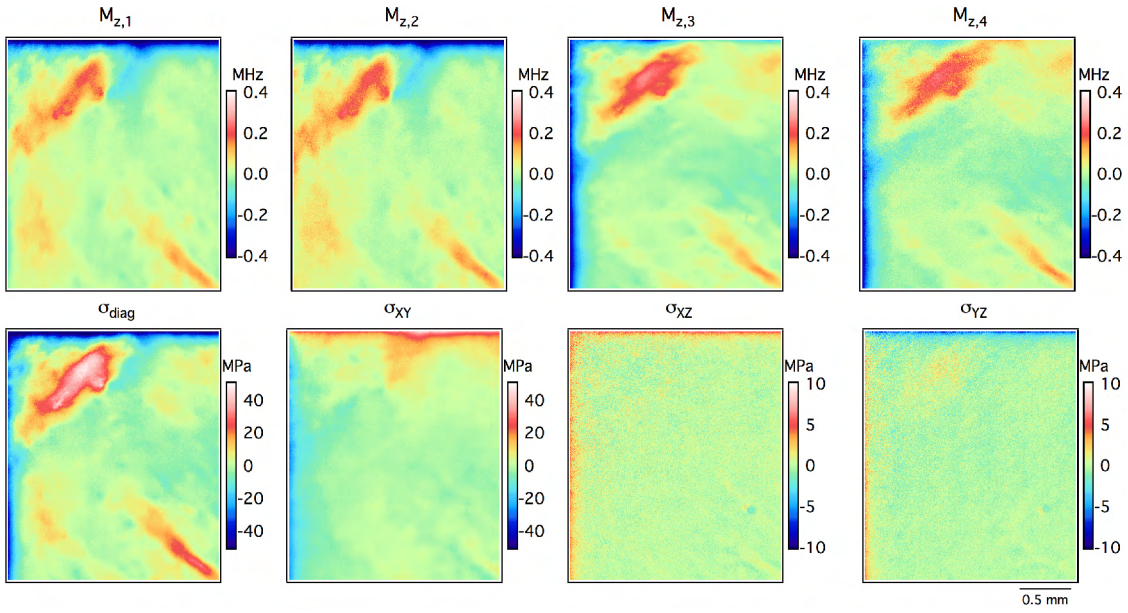

Figure C.9: NV $M_{z,\kappa}$ and $\{\sigma_{diag}, \sigma_{XY}, \sigma_{XZ}, \sigma_{YZ}\}$ maps for diamond Sample J.

Appendix D

Diamond Handling and Processing

This section gives brief insights into methods for handling and processing diamonds.

D.1 Diamond Handling

Even though diamond is mechanically robust, proper care should be taken to not chip or scratch the diamond surface. Use of metal tweezers on the diamond surface can cause chipping or cracking that degrades the diamond. Ceramic tweezers should be used whenever possible to avoid this issue.

D.1.1 How to Determine the NV Layer Side of the Diamond

One class of diamonds used extensively in this thesis (e.g., for QDM magnetic imaging) thin, high density (1 ppm to 20 ppm N), NV-layer (1-40 μm) diamonds on top of 500 μm substrates. Historically, imperfections (scratches, chips, etc) on the diamond surface or edges were used to keep track of which side was the layer containing NVs. However, this method requires the use of an optical microscope and became less efficient as diamonds were more uniform and homogeneous. It is important to know which side is the NV-layer to minimize

stand-off distance for many applications, as well as to optimize optical and MW excitation of the NVs and imaging of NV fluorescence

To assist with the process of determining the NV layer side, a quick and robust method was developed utilizing a laser pointer, laser goggles, and a reflective surface, without needing to use a microscope. This method can be characterized as "count the number of reflections." Without doing this on a reflective surface, the method can be difficult due to the high index of refraction of diamond trapping light and causing it to scatter internally.

1. Place the diamond on a reflective surface (either side down first.) Generally, I use an SiC or quartz wafer for the reflective surface because they are nearby.

2. With laser goggles on, shine the laser pointer at the diamond. Look at the interface between the diamond and reflective surface. If there are two distinct stripes, then the layer is on the top surface. If there is one distinct stripe, then the NV-layer is on the bottom surface.

3. The angle of the laser pointer and the viewing angle need to be optimized to improve contrast, but generally the method is straightforward.

4. Following the measurement of the first side, the diamond is flipped and the measurement is repeated. If the results are consistent with the previous step (first test layer side down and second test after being flipped layer side up), then there can be confidence that the layer side is known.

5. This flipping process can be repeated to ensure the results are consistent.

D.1.2 How to Find Dropped Diamonds

One of the rules of doing NV diamond research is do not lose the diamonds. Diamond chips typically range from 1 by 1 mm^2 to 5 by 5 mm^2, with thickness of about 0.5 mm, and when

held in tweezers can go flying across the room with a slight mishandling. One of my roles in the group has been finding diamonds that were dropped or misplaced and I have had a relatively high success rate and have never lost or dropped a diamond myself. (I have handled >600 diamonds throughout my graduate career.)

Below I outline the general protocol used for finding diamonds when they have been lost and precautions to take to minimize the chance of losing a diamond.

General Precautions

- When working on an optics table, make sure to apply tape over all threaded holes on the table not being used. This should be done before any diamond experiments and minimizes the chance of a diamond falling down one of the holes.

- Always have secondary containment for the diamonds when handling them. (Do not carry the diamond with just tweezers from a setup to another part of the lab.) Whenever possible place the diamond in a secondary container (dish, plate, etc.) as soon as possible when moving diamonds around.

- Keep the lab clean. Vacuuming, sweeping, and dusting the lab regularly can help minimize background shards on the ground, which can look like diamond chips. (It is surprising how little shards of glass, salt, or silicon wafers can look like diamonds when searching.)

- Keep a large number of strong flashlights on hand. The reflection off the diamond surface can be very valuable in providing contrast when looking for diamonds.

- When handling several diamonds (for example: cleaning or annealing a batch of diamonds), always make sure to count the number of diamonds every step along the

way. Never dispose of secondary waste (solvents, etc) until all diamonds have been accounted for.

- Designate specific diamond handling areas in the lab; a place where diamonds need to be extensively handled or attached to other components. There should be secondary and tertiary containment in this area and all possible cracks where diamonds could fall through should be sealed.

Finding a Dropped Diamond

1. If a dropped diamond is not immediately found, alert the rest of the lab that the diamond has been lost. This minimizes foot traffic in the area (a diamond could be kicked around of people are walking around) and allows for designated lab members to assist with searching for the diamond.

2. Make note of what you were doing when the diamond was lost (was it knocked off a platform, did it jump out of the tweezers, was it lost when transferring between fluid containers, etc.). This information can help inform where the diamond is most likely to be and what search-perimeter needs to be set up around the area.

3. Check your clothes and shoes thoroughly to ensure the diamond is not stuck to you. (If it is stuck to you and you walk out of the lab, the diamond could fall off anywhere in the lab or outside the lab and it would be near impossible to find.)

4. Using the high-power flashlight and shining it at the floor at a shallow angle to improve contrast, do a fine search of the floor around the experiment. Once the floor has been cleared and if the diamond has not been found, invite one or two other lab-mates into the vicinity of the experiment to assist with search the optics table and other locations.

5. Hold a discussion with the lab-mates to give details on what was happening when the diamond was lost; and in what general direction the diamond went (if you know the details). Depending on the size of the search area, divide it up among the different individuals and have each person search different regions at a time. By the end of the search all the people should have searched all the possible regions (for redundancy in case a person missed the diamond when searching).

6. Unless the details of how the diamond was lost adds contrary information, the most attention should be spent in close proximity to where the diamond was lost. All experimental components should be checked with high power flashlights and the optics table should be thoroughly searched.

7. If the search process continues and all the people involved feel they have thoroughly searched and have not found the diamond, then other approaches are needed. For example, if the threaded holes on an optics table were not covered then an endoscope might be needed, or an experiment might need to be disassembled to look through the individual components.

8. Once the area around the experiment has been cleared, a vacuum with a fresh filter bag and relatively modest suction could be utilized to try to pull the diamond for hidden corners. (This method is risky and should be used as one of the last-resorts.) The vacuum filter can then be searched through (with mask and gloves) in order to try to locate the diamond.

9. The most important step in the process: Do not stop searching and be systematic.

D.2 Cleaning

One important process for applications is ensuring the diamond surface is clean. This section reviews what to do when the diamond needs to be cleaned. For most of the NV-layer and bulk ensemble NV studies in this dissertation, the contribution from near surface NVs is minimal, so less work is needed regarding proper termination and treatment of the diamond surface.

The major times diamonds need to be cleaned:

- Before and after annealing
- When removing adhesives (superglue or various epoxies)
- When removing accumulated junk or dust from a diamond sample

For acid cleaning and other related processes needed for near-surface studies the protocols in Reference [332] can be followed. For the vast majority of the work done in this thesis, the diamonds are cleaned via a process of heated sonication in acetone followed by isopropyl alcohol and finally in DI water. This is finished with drying off the diamond using compressed air (nitrogen gas bottle). When not being used the diamonds are stored in sample boxes with Thorlabs lens tissue.

D.3 Annealing

One non-significant component of my experimental work over the years has been annealing diamonds to relieve strain and to create NVs following electron irradiation. More details about the annealing process and the specific furnace used can be found in Reference [332]. In total, I have annealed more than 400 diamond plates, films, and anvil cells throughout my graduate career from a wide variety of research groups. Different protocols need to be

developed depending on the diamond type, NV properties, and goal of the anneal. Further work is needed to improve the effectiveness and efficiency of annealing [56] especially when trying to minimize the influence of other parasitic defects [342].

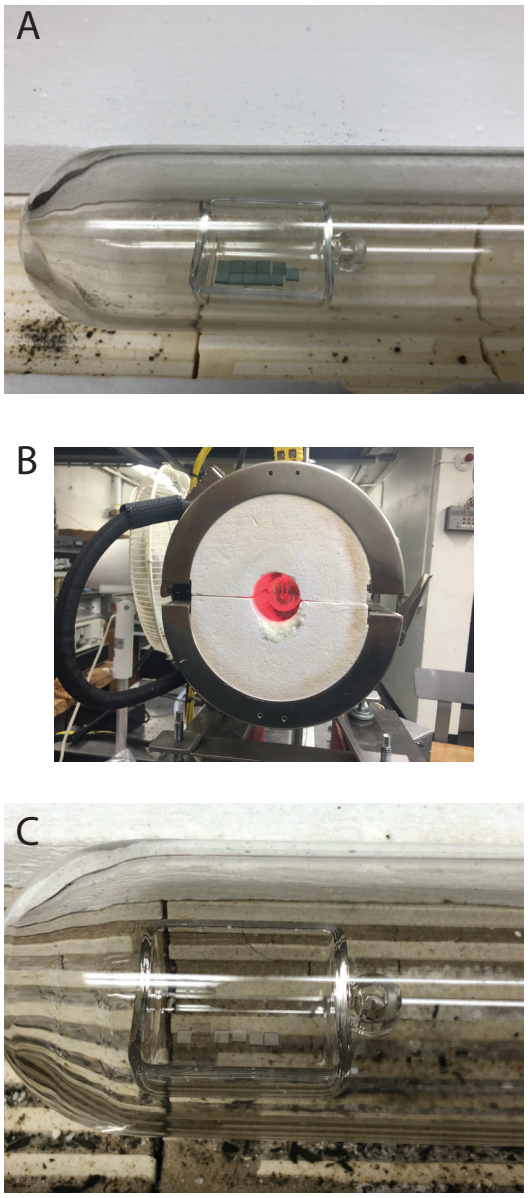

Figure D.1: (A) Diamonds following electron irradiation (hence the blue color). (B) The furnace while the diamonds are being annealed. (C) The diamonds following anneal (for layer samples they appear clear due to the large contribution of the substrate). For bulk diamonds they would appear yellow or purple depending on the Nitrogen and NV concentrations.

Appendix E

Fabrication and Engineering Methods

E.1 Fabrication of Metal Structures

For the Lock-In CW ODMR experiments and Ramsey Imaging experiments in Chapter 6, fabrication of metallic structures on various substrates is needed for microwave delivery and for the creation of phantom structures [107, 108]. Below, we will go into the protocols used for the fabrication of these structures and general considerations.

E.1.1 General Procedure for Fabrication and Assembly

The protocols described in this section utilize tools in the Harvard University Center for Nanoscale Systems (CNS) and some of the tools and specific steps are dependent on the tool used. The core methods used for metal patterning and deposition are photolithography and lift-off. The metal is deposited on a 50.8 mm diameter SiC wafer. SiC is used as the substrate due to its high thermal conductivity. There are two classes of fabricated coplanar waveguide/omega loop structures used predominantly. Large loops (>3 mm diameter), which are used for wide-field QDM measurements where Rabi homogeneity is preferred over maximum microwave strength (due to the ODMR-based sequences), and small loops (<500

μm diameter) for the Ramsey imaging experiments where large Rabi frequencies are required for fast spin manipulation ($\pi/2$ pulses).

Spin Coating

It is important to ensure the wafers/substrates being used in this process are thoroughly cleaned before being used.

1. Bring clean wafers to the spin coating station.
2. Place wafers on a hotplate at 115 $^{\circ}C$ for 1 minute to evaporate off any residual water or liquid from the wafer.
3. Spin coat HDMS onto the wafer to promote adhesion (4000 RPM).
4. Bake the wafer at 115 $^{\circ}C$ for 1 minute and then let the wafer cool to room temperature.
5. Spin coat positive photo-resist (S1813) onto the wafer (3000 RPM).
6. Bake the wafer at 115 $^{\circ}C$ for 1 minute to cure the resist.
7. Remove any residual resist on the edges of the wafer.

Direct-Write Photolithography for Exposing a Pattern

The central tool used for this work is a Heidelberg Instruments μPG501 optical direct-write lithography system. This system utilizes 390nm light and micro-mirror array to directly write patterns into the photoresist, which allows for rapid iteration in fabrication designs. The system utilizes GDSII files to write the pattern.

1. A 2D design file (such as Adobe Illustrator) is used to create a .dxf file with the pattern of interest. Open source software is utilized to convert the .dxf file to the .gdsii file the tool requires.

2. Load the .gdsii file onto the computer controlling tool and consult the relevant standard operating protocol to ensure proper procedures are being followed.

3. Load the wafer with photoresist into the tool, properly align and focus the tool with respect to the wafer. A dose matrix of total optical dose (set by exposure time) and focusing parameter is needed to optimize the achievable spatial pattern of the tool.

4. Remove the exposed wafer from the tool.

Developing the Resist

1. Bring the wafers to a proper chemical wet-bench (developing station).

2. Set aside 4 plastic cleanroom cups (with sufficient size to fit the wafer/substrate). Fill 1 cup $3/4^{th}$ of the way with Microposit MF 319 Developer. Fill 3 cups $3/4^{th}$ of the way with DI water.

3. Holding the wafer with proper tweezers, place the exposed wafer in the cup with MF319 and slowly move it around the cup for 50 seconds. If the resist was properly exposed, then some of it should start being dissolved into the solution.

4. Dump the wafer into the first cup with DI water with tweezers. Stir around for 20 seconds. Place the wafer into the second cup with DI wafer. Stir around for 20 seconds. Place the wafer into the third cup with DI water. Stir around for 20 seconds.

5. Dry the wafer with a dry air gun/nitrogen. Make sure not to use any solvents or disturb the pattern.

6. Bring the developed wafer to a microscope and evaluate the quality of the features. The bare (no resist) regions should be the places where metal is wanted.

E.1.2 Alternative to Photolithography

For applications where high resolution features are not necessary in the design a shadow mask can be used instead of photolithography to create the necessary pattern for metal evaporation.

Preparing for Metal Deposition

One important step before metal deposition is ensuring there are no defects (such as dust) on the wafer surface. These defects will result in inhomogeneities in the resultant metal structures. Given that solvents cannot be used to clean the wafer without damaging the resist and a vast majority of the possible defects are organic materials, a brief oxygen plasma etch is ideal for cleaning the top surface of the wafer.

1. An Anatech Barrel Plasma System is used for the oxygen plasma etching. Make sure to follow all the relevant standard operating procedures for the specific tool being used.

2. A power of 50W for a duration of 30 seconds is typically sufficient for cleaning the surface of the wafer without etching the resist significantly. These parameters may need to be optimized for each specific design.

3. Use a dry air gun to blow off any residual particles/dust/ash from the surface.

Metal Deposition with an Electron Evaporator

A Denton E-beam Evaporator is used for deposition of the metal onto the wafer. A wide variety of E-beam Evaporator or Thermal Evaporators could be used for the metal deposition, make sure to consult the relevant standard operating procedures for the being used.

1. Load the wafers and samples onto the holder. Clamp the wafers in place and use kapton tape (or other approved tape) to secure the wafers in place.

2. Pump down the chamber to a sufficiently low pressure ($\sim$1e^{-7} Torr), which normally takes >1 hour. A low vacuum is required to improve the quality of the metal film deposited and to minimize incorporation of defects.

3. An adhesion layer is first deposited to ensure a strong connection between the wafer and the desired metal layer. Typically the adhesion layer is 3-10 nm of either Titanium or Chromium. In these fabrication runs, chromium is used because of the wide availability of Chromium etchants.

4. For the microwave loops, 300-500 nm of gold is deposited.

5. Varying types and thicknesses of metals are used for the phantom fabricated (discussed more below) depending on the desired properties.

6. Unload the sample and remove the wafers from the holder.

Lift-off

In the final step of the process, the remaining resist is removed in a lift-off process. The wafers are placed in a solvent that reacts with and degrades the remaining resist. As the resist is dissolved, the metal on top of the resist is lifted off and only the metal where there wasn't resist remains.

1. Fill a large glass container (big enough to fit all the wafers/substrates) with Remover PG.

2. Place the wafers/substrates into the glass container with tweezers.

3. Cover the top of the container with aluminum foil (to avoid evaporation) and label the container properly.

4. Place the container on a hotplate at $80°C$ and leave overnight (>10 hours.) This duration can be reduced depending on the feature sizes and other factors about the deposition geometry.

5. Remove the wafers from the glass container and wash off the PG Remover with isopropyl alcohol, DI water, and then with dry air.

6. Evaluate the metal features under a microscope to ensure all the resist has been removed. If there is remaining resist and metal, then soft cotton swabs or other lightly abrasive tissue could be used. Be careful with these methods because they could introduce scratches in the metal surface. Putting the wafer back into PG remover or light sonication could be alternative methods to try to remove the remaining resist.

Adding Connectors

Traditionally, wirebonding the metal to another substrate or PCB is used to interface the microwave loop or phantom to a connector. However, for many biological applications where repeatability and robustness is needed and where the full mounts need to be sterilizable in an autoclave (discussed more below), wirebonding is not sufficient. In order to minimize the overall spatial profile and ensure a strong mechanical and electrical connection, planar connectors were attached to the substrate.

1. For the wafers in this work, the U.FL series of connectors were used due to their wide availability and favorable electronic properties (impedance matching, power handling, etc.).

2. The connectors are attached to the wafer with a silver epoxy (EPOTEK H20E), due to the strong mechanical properties, electrical properties, and biocompatibility.

3. A small amount of the silver epoxy is placed on the gold structures and the connectors are delicately placed on top. (Being careful not to smear the epoxy and cause shorts between the signal and the ground.)

4. The silver epoxy is cured at 120 C for 20 minutes.

5. A second round of silver epoxy is applied to improve the electrical connection. (This is done after the first round to ensure the connector is stable and does not move around.)

6. Cure at 120 $^{\circ}C$ for at least 2 hours.

7. In order to enhance the mechanical stability (especially under much use and routine sterilization in an autoclave), an additional non-conductive high strength epoxy is added to the back of the connector.

8. Either EPOTEK 353ND-T or EPOTEK OD2002 are used for this connection due to their high strength, biocompatibility, and rating for withstanding many autoclave cycles.

9. These epoxies need to be degassed before application. A small amount is added to the back of the connector.

10. Cure at 120 $^{\circ}C$ for at least 2 hours. This epoxy will come off under sulfuric acid, but not be impacted by normal solvents (acetone, isopropyl alcohol, etc.)

11. A U.FL to SMA cable is attached to the connector to allow for easy interfacing with SMAL cables used for the MW sources and amplifiers.

12. Make sure to characterize the connections with an Ohmmeter (to ensure there are no shorts) or with a Vector Network Analyzer (to check the S parameters and impedance matching.)

E.1.3 Iteration of Fabricated Phantom Design

For the Ramsey imaging results in References [107, 108], we fabricated a phantom structure that allowed for the creation of nontrivial current distributions.

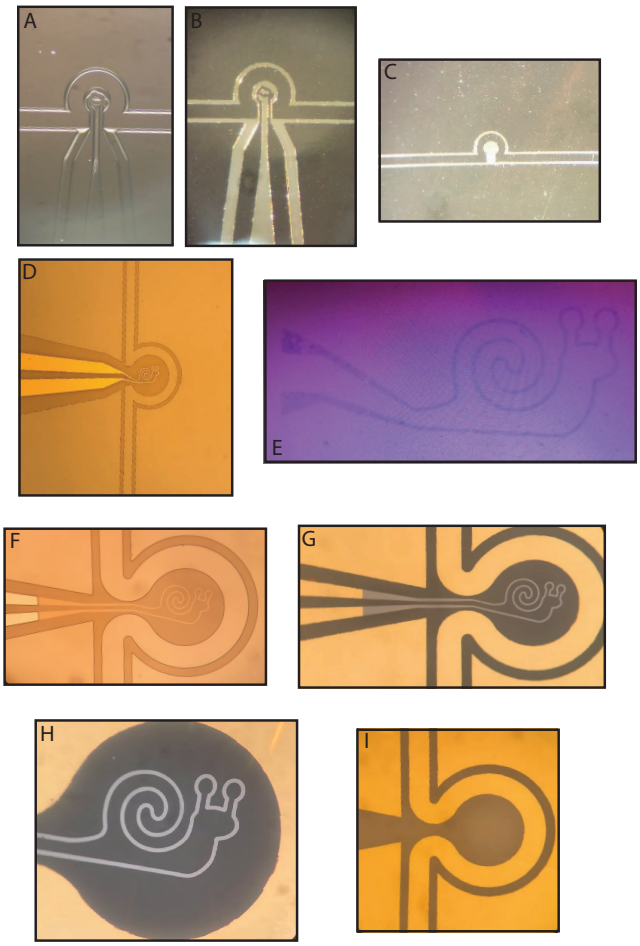

Figure E.1: (A), (B) Original phantom designs were drawn to evoke a mouse-like structure. (C) The same design but without the phantom structure to characterize the MW field from the bare loop. (D) The next iteration (to reduce microwave pickup) led to a modification of the structure to be a snail-like structure. Furthermore, the fabrication was modified to be a two-step process where the gold phantom was only 50 nm thick. (E) Use of patterned graphene was explored as an alternative to metal deposition due to the minimal microwave perturbations [145]. (F), (G), (H) The final design used (i) minimized the number of sharp corners in the MW loop and (ii) switched to a thin palladium snail structure to minimize the conductivity. (I) A MW loop was fabricated without the phantom structure to characterize the bare MW field.

As seen in Chapter 6, bringing conductive structures close to the NV layer can distort the local microwave field due to induced MW currents in the phantom structure, which constructively and destructively interferes with the MW field from the microwave loop. Due to the relatively large linear regime of sensing for Lock-In CW ODMR, the experiments were relatively robust to large fractional distortions inhomogeneities in the MW field over the sensing region. However, for the Double Quantum (DQ) Ramsey Imaging experiments presented at the end of Chapter 6 and in References [107, 108], large perturbations in the MW Rabi field degrade the fidelity of the state preparation and introduction significant perturbations to the imaging protocols. In order to overcome this two directions were pursed (i) fabricate phantom structures with lower conductivities to minimize the induced microwave currents and (ii) develop Ramsey protocols that are more robust to Rabi driving inhomogeneity. This section will focus on experimental iterations in the first direction.

E.2 Engineering of Biocompatible Mounts

E.2.1 Mount Iteration

Following the results in Chapter 3, we modified the platform for holding the biological specimens to improve robustness, enable use of mammalian cells, and fit in a standard petri-dish to enabling cell culturing. Furthermore, the mount needed to be non-magnetic, biocompatible, corrosion resistant, autoclavable, sufficient thermal and mechanical properties, compatible with the total internal reflection excitation geometry, and easy to swap components to switch diamonds or microwave delivery structures.

The initial design shown in Figure E.2(A,B), met some of the requirements above, but the significant amount of adhesives (superglue, 5-minute epoxy, and PDMS) utilized, made the device not robust and challenging to swap samples. One unfortunate design choice was

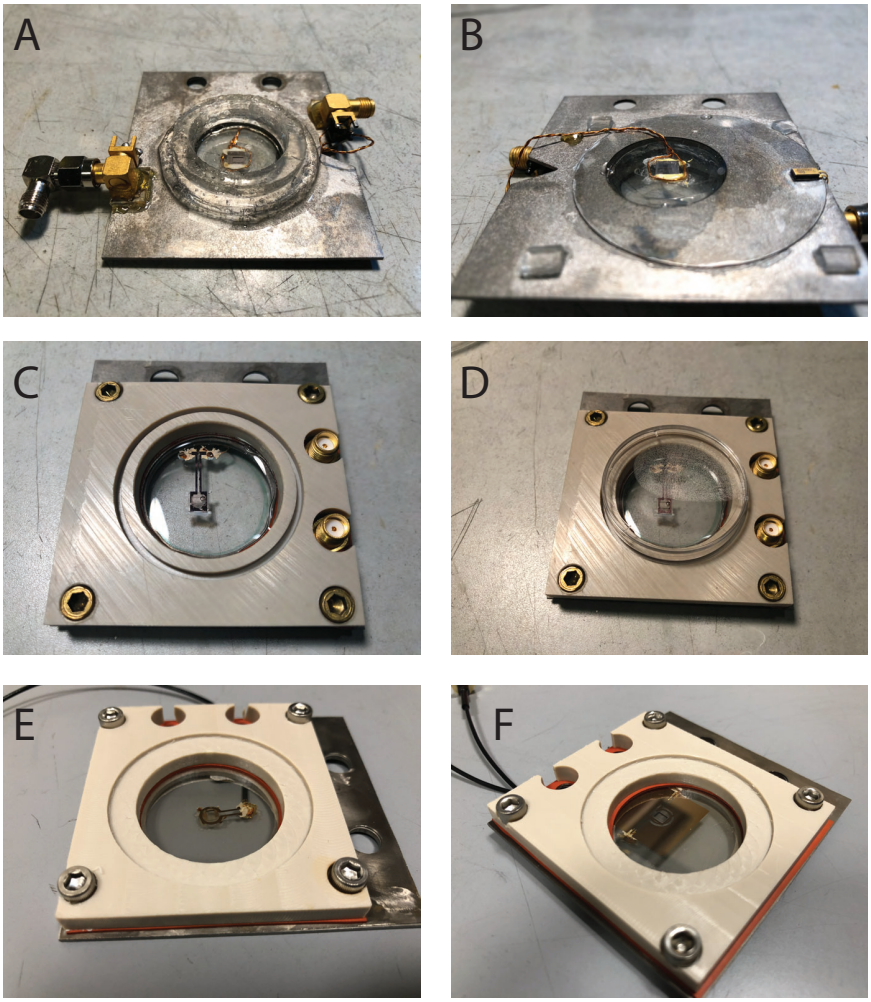

Figure E.2: (A),(B) Original designs, which utilized a tungsten plate, PDMS ring, superglue, epoxy, SMA cables, magnet wire loop for MW delivery, and PDMS pedestals (C),(D) An intermediate iteration where most of the adhesive connections were replaced with mechanical clamping. (E), (F) The final design, which swapped the tungsten mounts for non-magnetic stainless steel and replaced the magnet wire to SMA connectors with U.FL connectors.

supergluing the edges of the SiC wafer (with the diamond mounted to it) to the tungsten plate. This required a week of sitting in acetone to remove the wafer from the tungsten plate (without shattering the SiC wafer.)

In the second iteration, the primary goal was to remove as much as the adhesive as possible to improve robustness and flexibility of the diamond mount. (The only adhesive

left is the bonding of the diamond to the SiC wafer using EPOTEK 353ND-T or EPOTEK OD2002, which is done with a robust epoxy. This needs to be done carefully to ensure a water-tight connection, while not impinging optical access to the side of the diamond.) This also has the effect of making the mount more compatible with a wide range of sterilization techniques (ethanol, autoclave, bleach, etc.). We machined a PEEK plate and laser cut silicone sheets (see Figure E.3(D,E) to apply a water-tight seal. The strength of the seal was tested by two methods: (i) leaving the mount filled with water overnight and checking for leaks; and (ii) filling the mount with water and applying pressurized nitrogen gas to the seams to look for bubble formation. The other significant upgrade from this iteration was switching from an external wire loop to a fabricated structure on the SiC. The external wire loop was not repeatable and the MW properties would change each time the device was taken out and put back in the setup. The fabricated loops were connected to SMA connectors via thin magnet wire. However, the vertical profile of the device due to the SMAs made it challenging to fit the device in a standard petri-dish, motivating the next iteration.

The most recent iteration improved the MW design to have rounded loops and to have coplanar wave-guide Omega loop structures instead of the square loops. The SMA connections were also replaced by U.FL connectors to minimize the vertical profile of the device. More details about the final design are given below.

E.2.2 Details of Final Design

Figure E.3 illustrates the different major components used for the final mount used in Chapter 6. A non-magnetic stainless steel plate was used instead of the previously used tungsten sheets because of the better machine-ability, increased flatness (the tungsten was slight warped), and the improved robustness (the tungsten was brittle and would flake after

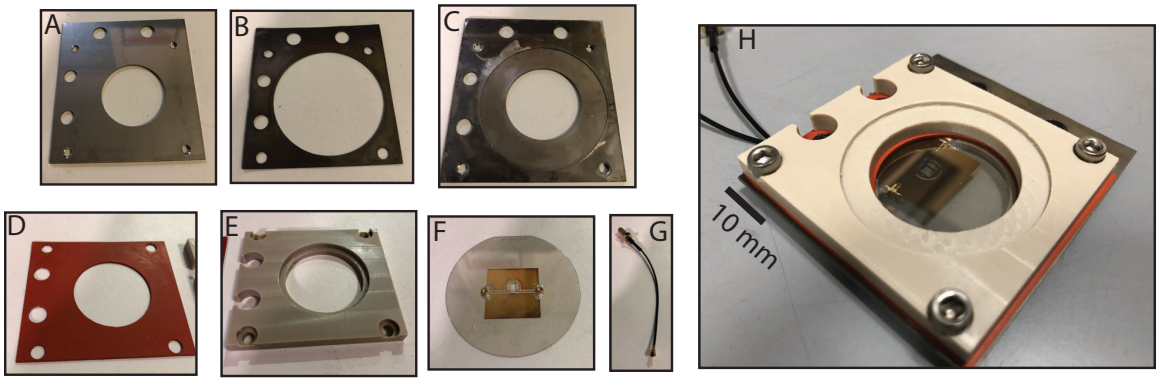

Figure E.3: Major components of the final design. (A) Waterjet cut nonmagnetic stainless steel baseplate. (B) Waterjet cut titanium shim (300 μm thick) (C) The components from (A) and (B) laser welded to one another to allow for reliable placement of the SiC wafer. (D) Silicone rubber sheet laser cut to allow for a water-tight connection. (E) Biocompatible, machined PEEK plate to apply the mechanical pressure and hold the fluid for biological measurements. (F) SiC wafer with fabricated gold structure for MW delivery. (G) U.FL connector. (H) Finalized design assembled, stainless steel or brass bolts could be used for clamping to components to the threaded holes in the baseplate in (A).

being machined/water-jet.) In order to solve another problem of ensuring the diamond would be in the same location each time the device was taken apart, a thin (300 μm) titanium shim is used to keep the wafer in place. The two components are attached via laser welding. A silicone sheet is patterned with a laser cutter, which is used to produce the water-tight seal. The PEEK plate applies the pressure (when combined with stainless steel or brass bolts) and contains volume where the liquid will be held. The SiC wafer with a 2 mm by 3 mm hole cut in the middle, gold microwave delivery structure fabricated is connectorized with a U.FL to an SMA cable and the whole structure is combined to yield the mount seen in Figure E.3(H).

Bibliography

[1] D. R. Glenn, R. R. Fu, P. Kehayias, D. Le Sage, E. A. Lima, B. P. Weiss, and R. L. Walsworth. Micrometer-scale magnetic imaging of geological samples using a quantum diamond microscope. *Geochemistry, Geophysics, Geosystems*, 18(8):3254–3267, 2017.

[2] R. Schirhagl, K. Chang, M. Loretz, and C. L. Degen. Nitrogen-vacancy centers in diamond: Nanoscale sensors for physics and biology. *Annual Review of Physical Chemistry*, 65(1):83–105, 2014.

[3] H. Weng, D. G. Beetner, and R. E. DuBroff. Prediction of radiated emissions using near-field measurements. *IEEE Transactions on Electromagnetic Compatibility*, 53(4):891–899, 2011.

[4] C. L. Degen. Scanning magnetic field microscope with a diamond single-spin sensor. *Applied Physics Letters*, 92(24):243111, 2008.

[5] L. Rondin, J.-P. Tetienne, P. Spinicelli, C. D. Savio, K. Karrai, G. Dantelle, A. Thiaville, S. Rohart, J.-F. Roch, and V. Jacques. Nanoscale magnetic field mapping with a single spin scanning probe magnetometer. *Applied Physics Letters*, 100(15):153118, 2012.

[6] P. Maletinsky, S. Hong, M. S. Grinolds, B. Hausmann, M. Lukin, R. L. Walsworth, M. Loncar, and A. Yacoby. A robust scanning diamond sensor for nanoscale imaging with single nitrogen-vacancy centres. *Nature Nanotechnology*, 7:320–324, 2012.

[7] U. Hartmann. Magnetic force microscopy. *Annual Review of Materials Science*, 29(1):53–87, 1999.

[8] L. E. Fong, J. R. Holzer, K. K. McBride, E. A. Lima, F. Baudenbacher, and M. Radparvar. High-resolution room-temperature sample scanning superconducting quantum interference device microscope configurable for geological and biomagnetic applications. *Review of Scientific Instruments*, 76(5):053703, 2005.

[9] D. Budker and M. Romalis. Optical magnetometry. *Nature Physics*, 3(4):227–234, 2007.

[10] S. Sanfilippo. Hall probes: physics and application to magnetometry. Technical report, CERN, 2011.

[11] G. Boero, M. Demierre, R. Popovic, et al. Micro-hall devices: performance, technologies and applications. *Sensors and Actuators A: Physical*, 106(1-3):314–320, 2003.

[12] D. R. Popovic, S. Dimitrijevic, M. Blagojevic, P. Kejik, E. Schurig, and R. S. Popovic. Three-axis teslameter with integrated hall probe. *IEEE Transactions on Instrumentation and Measurement*, 56(4):1396–1402, 2007.

[13] D. A. Allwood, G. Xiong, M. D. Cooke, and R. P. Cowburn. Magneto-optical kerr effect analysis of magnetic nanostructures. *Journal of Physics D: Applied Physics*, 36(18):2175–2182, 2003.

[14] Z. Q. Qiu and S. D. Bader. Surface magneto-optic kerr effect. *Review of Scientific Instruments*, 71(3):1243–1255, 2000.

[15] D. Le Sage, K. Arai, D. R. Glenn, S. J. DeVience, L. M. Pham, L. Rahn-Lee, M. D. Lukin, A. Yacoby, A. Komeili, and R. L. Walsworth. Optical magnetic imaging of living cells. *Nature*, 496:486–489, 2013.

[16] M. W. Doherty, N. B. Manson, P. Delaney, F. Jelezko, J. Wrachtrup, and L. C. L. Hollenberg. The nitrogen-vacancy colour centre in diamond. *Physics Reports*, 528(1):1 – 45, 2013.

[17] L. Rondin, J.-P. Tetienne, T. Hingant, J.-F. Roch, P. Maletinsky, and V. Jacques. Magnetometry with nitrogen-vacancy defects in diamond. *Reports on Progress in Physics*, 77(5):056503, 2014.

[18] M. L. Goldman, M. W. Doherty, A. Sipahigil, N. Y. Yao, S. D. Bennett, N. B. Manson, A. Kubanek, and M. D. Lukin. State-selective intersystem crossing in nitrogen-vacancy centers. *Phys. Rev. B*, 91:165201, 2015.

[19] J. H. N. Loubser and J. A. van Wyk. Electron spin resonance in the study of diamond. *Reports on Progress in Physics*, 41(8):1201, 1978.

[20] M. W. Doherty, F. Dolde, H. Fedder, F. Jelezko, J. Wrachtrup, N. B. Manson, and L. C. L. Hollenberg. Theory of the ground-state spin of the nv- center in diamond. *Phys. Rev. B*, 85:205203, 2012.

[21] E. Bauch, C. A. Hart, J. M. Schloss, M. J. Turner, J. F. Barry, P. Kehayias, S. Singh, and R. L. Walsworth. Ultralong dephasing times in solid-state spin ensembles via quantum control. *Phys. Rev. X*, 8:031025, 2018.

[22] C. S. Shin, M. C. Butler, H.-J. Wang, C. E. Avalos, S. J. Seltzer, R.-B. Liu, A. Pines, and V. S. Bajaj. Optically detected nuclear quadrupolar interaction of ^{14}N in nitrogen-vacancy centers in diamond. *Phys. Rev. B*, 89:205202, 2014.

[23] V. M. Acosta, E. Bauch, M. P. Ledbetter, A. Waxman, L.-S. Bouchard, and D. Budker. Temperature dependence of the nitrogen-vacancy magnetic resonance in diamond. *Phys. Rev. Lett.*, 104:070801, 2010.

[24] M. W. Doherty, V. M. Acosta, A. Jarmola, M. S. J. Barson, N. B. Manson, D. Budker, and L. C. L. Hollenberg. Temperature shifts of the resonances of the nv- center in diamond. *Phys. Rev. B*, 90:041201, 2014.

[25] V. M. Acosta, E. Bauch, M. P. Ledbetter, A. Waxman, L.-S. Bouchard, and D. Budker. Temperature dependence of the nitrogen-vacancy magnetic resonance in diamond. *Phys. Rev. Lett.*, 104:070801, 2010.

[26] S. Felton, A. M. Edmonds, M. E. Newton, P. M. Martineau, D. Fisher, D. J. Twitchen, and J. M. Baker. Hyperfine interaction in the ground state of the negatively charged nitrogen vacancy center in diamond. *Phys. Rev. B*, 79:075203, 2009.

[27] M. S. J. Barson, P. Peddibhotla, P. Ovartchaiyapong, K. Ganesan, R. L. Taylor, M. Gebert, Z. Mielens, B. Koslowski, D. A. Simpson, L. P. McGuinness, J. McCallum, S. Prawer, S. Onoda, T. Ohshima, A. C. Bleszynski Jayich, F. Jelezko, N. B. Manson, and M. W. Doherty. Nanomechanical sensing using spins in diamond. *Nano Letters*, 17(3):1496–1503, 2017.

[28] P. Udvarhelyi, V. O. Shkolnikov, A. Gali, G. Burkard, and A. Pályi. Spin-strain interaction in nitrogen-vacancy centers in diamond. *Phys. Rev. B*, 98:075201, 2018.

[29] A. Barfuss, M. Kasperczyk, J. Kölbl, and P. Maletinsky. Spin-stress and spin-strain coupling in diamond-based hybrid spin oscillator systems. *Phys. Rev. B*, 99:174102, 2019.

[30] P. Jamonneau, M. Lesik, J. P. Tetienne, I. Alvizu, L. Mayer, A. Dréau, S. Kosen, J.-F. Roch, S. Pezzagna, J. Meijer, T. Teraji, Y. Kubo, P. Bertet, J. R. Maze, and V. Jacques. Competition between electric field and magnetic field noise in the decoherence of a single spin in diamond. *Phys. Rev. B*, 93:024305, 2016.

[31] P. Kehayias, M. J. Turner, R. Trubko, J. M. Schloss, C. A. Hart, M. Wesson, D. R. Glenn, and R. L. Walsworth. Imaging crystal stress in diamond using ensembles of nitrogen-vacancy centers. *Phys. Rev. B*, 100(17):174103, 2019.

[32] L. J. Rogers, R. L. McMurtrie, M. J. Sellars, and N. B. Manson. Time-averaging within the excited state of the nitrogen-vacancy centre in diamond. *New Journal of Physics*, 11(6):063007, 2009.

[33] A. Batalov, V. Jacques, F. Kaiser, P. Siyushev, P. Neumann, L. J. Rogers, R. L. McMurtrie, N. B. Manson, F. Jelezko, and J. Wrachtrup. Low temperature studies of the excited-state structure of negatively charged nitrogen-vacancy color centers in diamond. *Phys. Rev. Lett.*, 102:195506, 2009.

[34] B. Henderson and G. F. Imbusch. *Optical Spectroscopy of Inorganic Solids.* Oxford University Press, 2006.

[35] L. Robledo, H. Bernien, T. van der Sar, and R. Hanson. Spin dynamics in the optical cycle of single nitrogen-vacancy centres in diamond. *New Journal of Physics*, 13(2):025013, 2011.

[36] J.-P. Tetienne, L. Rondin, P. Spinicelli, M. Chipaux, T. Debuisschert, J.-F. Roch, and V. Jacques. Magnetic-field-dependent photodynamics of single nv defects in diamond: an application to qualitative all-optical magnetic imaging. *New Journal of Physics*, 14(10):103033, 2012.

[37] J. Harrison, M. Sellars, and N. Manson. Measurement of the optically induced spin polarisation of n-v centres in diamond. *Diamond and Related Materials*, 15(4):586 – 588, 2006. Diamond 2005.

[38] L. J. Rogers, S. Armstrong, M. J. Sellars, and N. B. Manson. Infrared emission of the nv centre in diamond: Zeeman and uniaxial stress studies. *New Journal of Physics*, 10(10):103024, 2008.

[39] V. M. Acosta, A. Jarmola, E. Bauch, and D. Budker. Optical properties of the nitrogen-vacancy singlet levels in diamond. *Phys. Rev. B*, 82:201202, 2010.

[40] L. J. Rogers, M. W. Doherty, M. S. J. Barson, S. Onoda, T. Ohshima, and N. B. Manson. Singlet levels of the nv- centre in diamond. *New Journal of Physics*, 17(1):013048, 2015.

[41] T.-L. Wee, Y.-K. Tzeng, C.-C. Han, H.-C. Chang, W. Fann, J.-H. Hsu, K.-M. Chen, and Y.-C. Yu. Two-photon excited fluorescence of nitrogen-vacancy centers in proton-irradiated type ib diamond. *The Journal of Physical Chemistry A*, 111(38):9379–9386, 2007.

[42] R. Chapman and T. Plakhotnik. Quantitative luminescence microscopy on nitrogen-vacancy centres in diamond: Saturation effects under pulsed excitation. *Chemical Physics Letters*, 507(1-3):190 – 194, 2011.

[43] A. Dréau, M. Lesik, L. Rondin, P. Spinicelli, O. Arcizet, J.-F. Roch, and V. Jacques. Avoiding power broadening in optically detected magnetic resonance of single nv defects for enhanced dc magnetic field sensitivity. *Phys. Rev. B*, 84:195204, 2011.

[44] A. Gruber, A. Dräbenstedt, C. Tietz, L. Fleury, J. Wrachtrup, and C. v. Borczyskowski. Scanning confocal optical microscopy and magnetic resonance on single defect centers. *Science*, 276(5321):2012–2014, 1997.

[45] B. J. Roth, N. G. Sepulveda, and J. P. Wikswo. Using a magnetometer to image a two-dimensional current distribution. *Journal of Applied Physics*, 65(1):361–372, 1989.

[46] E. A. Lima and B. P. Weiss. Ultra-high sensitivity moment magnetometry of geological samples using magnetic microscopy. *Geochemistry, Geophysics, Geosystems*, 17(9):3754–3774.

[47] L. Baratchart, S. Chevillard, D. P. Hardin, J. Leblond, E. A. Lima, and J.-P. Marmorat. Magnetic moment estimation and bounded extremal problems. *Inverse Problems and Imaging* , 13(1):29, 2019.

[48] D. R. Glenn, D. B. Bucher, J. Lee, M. D. Lukin, H. Park, and R. L. Walsworth. High-resolution magnetic resonance spectroscopy using a solid-state spin sensor. *Nature*, 555, 2018.

[49] T. Mittiga, S. Hsieh, C. Zu, B. Kobrin, F. Machado, P. Bhattacharyya, N. Z. Rui, A. Jarmola, S. Choi, D. Budker, and N. Y. Yao. Imaging the local charge environment of nitrogen-vacancy centers in diamond. *Phys. Rev. Lett.*, 121:246402, 2018.

[50] F. Dolde, H. Fedder, M. W. Doherty, T. Nöbauer, F. Rempp, G. Balasubramanian, T. Wolf, F. Reinhard, L. C. L. Hollenberg, F. Jelezko, and J. Wrachtrup. Electric-field sensing using single diamond spins. *Nature Physics*, 7:459–463, 2011.

[51] E. V. Oort and M. Glasbeek. Electric-field-induced modulation of spin echoes of n-v centers in diamond. *Chemical Physics Letters*, 168(6):529 – 532, 1990.

[52] C. S. Shin, C. E. Avalos, M. C. Butler, D. R. Trease, S. J. Seltzer, J. Peter Mustonen, D. J. Kennedy, V. M. Acosta, D. Budker, A. Pines, and V. S. Bajaj. Room-temperature operation of a radiofrequency diamond magnetometer near the shot-noise limit. *J. Appl. Phys.*, 112(12):124519, 2012.

[53] D. R. Glenn, K. Lee, H. Park, R. Weissleder, A. Yacoby, M. D. Lukin, H. Lee, R. L. Walsworth, and C. B. Connolly. Single-cell magnetic imaging using a quantum diamond microscope. *Nature Methods*, 2015.

[54] J. F. Barry, M. J. Turner, J. M. Schloss, D. R. Glenn, Y. Song, M. D. Lukin, H. Park, and R. L. Walsworth. Optical magnetic detection of single-neuron action potentials using quantum defects in diamond. *Proceedings of the National Academy of Sciences*, 113(49):14133–14138, 2016.

[55] J. M. Schloss, J. F. Barry, M. J. Turner, and R. L. Walsworth. Simultaneous broadband vector magnetometry using solid-state spins. *Phys. Rev. Applied*, 10:034044, 2018.

[56] J. F. Barry, J. M. Schloss, E. Bauch, M. J. Turner, C. A. Hart, L. M. Pham, and R. L. Walsworth. Sensitivity optimization for nv-diamond magnetometry. *Rev. Mod. Phys.*, 92:015004, 2020.

[57] N. F. Ramsey. A molecular beam resonance method with separated oscillating fields. *Phys. Rev.*, 78:695–699, 1950.

[58] G. Balasubramanian, P. Neumann, D. Twitchen, M. Markham, R. Kolesov, N. Mizuochi, J. Isoya, J. Achard, J. Beck, J. Tissler, V. Jacques, P. R. Hemmer, F. Jelezko, and J. Wrachtrup. Ultralong spin coherence time in isotopically engineered diamond. *Nature Materials*, 8:383–387, 2009.

[59] J. M. Taylor, P. Cappellaro, L. Childress, L. Jiang, D. Budker, P. R. Hemmer, A. Yacoby, R. Walsworth, and M. D. Lukin. High-sensitivity diamond magnetometer with nanoscale resolution. *Nature Phys*, 4(10):810–816, 2008.

[60] G. de Lange, Z. H. Wang, D. Ristè, V. V. Dobrovitski, and R. Hanson. Universal dynamical decoupling of a single solid-state spin from a spin bath. *Science*, 330(6000):60–63, 2010.

[61] E. Bauch, S. Singh, J. Lee, C. A. Hart, J. M. Schloss, M. J. Turner, J. F. Barry, L. Pham, N. Bar-Gill, S. F. Yelin, et al. Decoherence of dipolar spin ensembles in diamond. *arXiv preprint, arXiv:1904.08763*, 2019.

[62] L. Cywiński, R. M. Lutchyn, C. P. Nave, and S. Das Sarma. How to enhance dephasing time in superconducting qubits. *Phys. Rev. B*, 77:174509, 2008.

[63] L. M. Pham, N. Bar-Gill, C. Belthangady, D. Le Sage, P. Cappellaro, M. D. Lukin, A. Yacoby, and R. L. Walsworth. Enhanced solid-state multispin metrology using dynamical decoupling. *Phys. Rev. B*, 86:045214, 2012.

[64] R. de Sousa. Electron Spin as a Spectrometer of Nuclear-Spin Noise and Other Fluctuations. In M. Fanciulli, editor, *Electron Spin Resonance and Related Phenomena in Low-Dimensional Structures*, volume 115 of *Topics in Applied Physics*, pages 183–220. Springer, 2009.

[65] P. Szańkowski, G. Ramon, J. Krzywda, D. Kwiatkowski, et al. Environmental noise spectroscopy with qubits subjected to dynamical decoupling. *Journal of Physics: Condensed Matter*, 29(33):333001, 2017.

[66] L. Shao, R. Liu, M. Zhang, A. V. Shneidman, X. Audier, M. Markham, H. Dhillon, D. J. Twitchen, Y.-F. Xiao, and M. Lončar. Wide-field optical microscopy of microwave fields using nitrogen-vacancy centers in diamonds. *Advanced Optical Materials*, 4(7):1075–1080, 2016.

[67] A. Horsley, P. Appel, J. Wolters, J. Achard, A. Tallaire, P. Maletinsky, and P. Treutlein. Microwave device characterization using a widefield diamond microscope. *Phys. Rev. Applied*, 10:044039, 2018.

[68] S. Steinert, F. Ziem, L. T. Hall, A. Zappe, M. Schweikert, N. Götz, A. Aird, G. Balasubramanian, L. Hollenberg, and J. Wrachtrup. Magnetic spin imaging under ambient conditions with sub-cellular resolution. *Nature Communications*, 4, 2013.

[69] B. Naydenov, F. Dolde, L. T. Hall, C. Shin, H. Fedder, L. C. L. Hollenberg, F. Jelezko, and J. Wrachtrup. Dynamical decoupling of a single-electron spin at room temperature. *Phys. Rev. B*, 83:081201, 2011.

[70] S. Steinert, F. Dolde, P. Neumann, A. Aird, B. Naydenov, G. Balasubramanian, F. Jelezko, and J. Wrachtrup. High sensitivity magnetic imaging using an array of spins in diamond. *Rev. Sci. Instrum.*, 81:043705, 2010.

[71] B. Naydenov, F. Reinhard, A. Lämmle, V. Richter, R. Kalish, U. F. S. D'Haenens-Johansson, M. Newton, F. Jelezko, and J. Wrachtrup. Increasing the coherence time of single electron spins in diamond by high temperature annealing. *Applied Physics Letters*, 97(24):242511, 2010.

[72] S. Pezzagna, B. Naydenov, F. Jelezko, J. Wrachtrup, and J. Meijer. Creation efficiency of nitrogen-vacancy centres in diamond. *New Journal of Physics*, 12(6):065017, 2010.

[73] D. M. Toyli, C. D. Weis, G. D. Fuchs, T. Schenkel, and D. D. Awschalom. Chip-scale nanofabrication of single spins and spin arrays in diamond. *Nano Letters*, 10(8):3168–3172, 2010.

[74] H. Ozawa, K. Tahara, H. Ishiwata, M. Hatano, and T. Iwasaki. Formation of perfectly aligned nitrogen-vacancy-center enarembles in chemical-vapor-deposition-grown diamond (111). *Applied Physics Express*, 10(4):045501, 2017.

[75] K. Ohno, F. J. Heremans, L. C. Bassett, B. A. Myers, D. M. Toyli, A. C. B. Jayich, C. J. Palmstrom, and D. D. Awschalom. Engineering shallow spins in diamond with nitrogen delta-doping. *Applied Physics Letters*, 101(8):082413, 2012.

[76] M. Loretz, S. Pezzagna, J. Meijer, and C. L. Degen. Nanoscale nuclear magnetic resonance with a 1.9-nm-deep nitrogen-vacancy sensor. *Applied Physics Letters*, 104(3):–, 2014.

[77] V. M. Acosta, E. Bauch, M. P. Ledbetter, C. Santori, K.-M. C. Fu, P. E. Barclay, R. G. Beausoleil, H. Linget, J. F. Roch, F. Treussart, S. Chemerisov, W. Gawlik, and D. Budker. Diamonds with a high density of nitrogen-vacancy centers for magnetometry applications. *Phys. Rev. B*, 80:115202, 2009.

[78] J. Smits, J. T. Damron, P. Kehayias, A. F. McDowell, N. Mosavian, I. Fescenko, N. Ristoff, A. Laraoui, A. Jarmola, and V. M. Acosta. Two-dimensional nuclear magnetic resonance spectroscopy with a microfluidic diamond quantum sensor. *Science advances*, 5(7), 2019.

[79] E. E. Kleinsasser, M. M. Stanfield, J. K. Q. Banks, Z. Zhu, W.-D. Li, V. M. Acosta, H. Watanabe, K. M. Itoh, and K.-M. C. Fu. High density nitrogen-vacancy sensing surface created via he+ ion implantation of 12c diamond. *Applied Physics Letters*, 108(20), 2016.

[80] D. Aude Craik, P. Kehayias, A. Greenspon, X. Zhang, M. Turner, J. Schloss, E. Bauch, C. Hart, E. Hu, and R. Walsworth. Microwave-assisted spectroscopy technique for studying charge state in nitrogen-vacancy ensembles in diamond. *Phys. Rev. Applied*, 14:014009, 2020.

[81] M. S. Grinolds, M. Warner, K. D. Greve, Y. Dovzhenko, L. Thiel, R. L. Walsworth, S. Hong, P. Maletinsky, and A. Yacoby. Subnanometre resolution in three-dimensional magnetic resonance imaging of individual dark spins. *Nature Nanotechnology*, 9:279–284, 2014.

[82] T. Rosskopf, A. Dussaux, K. Ohashi, M. Loretz, R. Schirhagl, H. Watanabe, S. Shikata, M. Itoh, K. and L. Degen, C.˙Investigation of surface magnetic noise by shallow spins in diamond. *Phys. Rev. Lett.*, 112:147602, 2014.

[83] S. Kilin, A. Nizovtsev, T. Maevskaya, A. Dräbenstedt, and J. Wrachtrup. Spectroscopy on single n-v defect centers in diamond: tunneling of nitrogen atoms into vacancies and fluorescence spectra. *Journal of Luminescence*, 86:201 – 206, 2000.

[84] N. Aslam, G. Waldherr, P. Neumann, F. Jelezko, and J. Wrachtrup. Photo-induced ionization dynamics of the nitrogen vacancy defect in diamond investigated by single-shot charge state detection. *New Journal of Physics*, 15(1):013064, 2013.

[85] E. Bauch. Nitrogen-vacancy defects in diamond for sub-millimeter magnetometry. Master's thesis, TU Berlin, 2010.

[86] F. M. Storner, A. Brenneis, J. Kassel, U. Wostradowski, R. Rolver, T. Fuchs, K. Nakamura, H. Sumiya, S. Onoda, J. Isoya, and F. Jelezko. Compact integrated magnetometer based on nitrogen-vacancy centres in diamond. *Diamond and Related Materials*, 93:59 – 65, 2019.

[87] K. Beha, A. Batalov, N. B. Manson, R. Bratschitsch, and A. Leitenstorfer. Optimum photoluminescence excitation and recharging cycle of single nitrogen-vacancy centers in ultrapure diamond. *Phys. Rev. Lett.*, 109:097404, 2012.

[88] A. M. Wojciechowski, M. Karadas, A. Huck, C. Osterkamp, S. Jankuhn, J. Meijer, F. Jelezko, and U. L. Andersen. Contributed review: Camera-limits for wide-field magnetic resonance imaging with a nitrogen-vacancy spin sensor. *Review of Scientific Instruments*, 89(3):031501, 2018.

[89] L. T. Hall, P. Kehayias, D. A. Simpson, A. Jarmola, A. Stacey, D. Budker, and L. C. L. Hollenberg. Detection of nanoscale electron spin resonance spectra demonstrated using nitrogen-vacancy centre probes in diamond. *Nature Communications*, 7:10211, 2016.

[90] I. Fescenko, A. Laraoui, J. Smits, N. Mosavian, P. Kehayias, J. Seto, L. Bougas, A. Jarmola, and V. M. Acosta. Diamond magnetic microscopy of malarial hemozoin nanocrystals. *Phys. Rev. Applied*, 11:034029, 2019.

[91] R. Fischer, A. Jarmola, P. Kehayias, and D. Budker. Optical polarization of nuclear ensembles in diamond. *Phys. Rev. B*, 87:125207, 2013.

[92] M. Steiner, P. Neumann, J. Beck, F. Jelezko, and J. Wrachtrup. Universal enhancement of the optical readout fidelity of single electron spins at nitrogen-vacancy centers in diamond. *Phys. Rev. B*, 81:035205, 2010.

[93] M. P. Backlund, P. Kehayias, and R. L. Walsworth. Diamond-based magnetic imaging with fourier optical processing. *Phys. Rev. Applied*, 8:054003, 2017.

[94] K. Bayat, J. Choy, M. Farrokh Baroughi, S. Meesala, and M. Loncar. Efficient, uniform, and large area microwave magnetic coupling to nv centers in diamond using double split-ring resonators. *Nano Letters*, 14(3):1208–1213, 2014.

[95] N. Zhang, C. Zhang, L. Xu, M. Ding, W. Quan, Z. Tang, and H. Yuan. Microwave magnetic field coupling with nitrogen-vacancy center ensembles in diamond with high homogeneity. *Applied Magnetic Resonance*, pages 1–11, 2016.

[96] D. Labanowski, V. P. Bhallamudi, Q. Guo, C. M. Purser, B. A. McCullian, P. C. Hammel, and S. Salahuddin. Voltage-driven, local, and efficient excitation of nitrogen-vacancy centers in diamond. *Science Advances*, 4(9), 2018.

[97] W. Jia, Z. Shi, X. Qin, X. Rong, and J. Du. Ultra-broadband coplanar waveguide for optically detected magnetic resonance of nitrogen-vacancy centers in diamond. *Review of Scientific Instruments*, 89(6):064705, 2018.

[98] K. Sasaki, Y. Monnai, S. Saijo, R. Fujita, H. Watanabe, J. Ishi-Hayase, K. M. Itoh, and E. Abe. Broadband, large-area microwave antenna for optically detected magnetic resonance of nitrogen-vacancy centers in diamond. *Review of Scientific Instruments*, 87(5):053904, 2016.

[99] E. R. Eisenach, J. F. Barry, L. M. Pham, R. G. Rojas, D. R. Englund, and D. A. Braje. Broadband loop gap resonator for nitrogen vacancy centers in diamond. *Review of Scientific Instruments*, 89(9):094705, 2018.

[100] M. Mrózek, J. Mlynarczyk, D. S. Rudnicki, and W. Gawlik. Circularly polarized microwaves for magnetic resonance study in the ghz range: Application to nitrogen-vacancy in diamonds. *Applied Physics Letters*, 107(1):013505, 2015.

[101] T. P. M. Alegre, C. Santori, G. Medeiros-Ribeiro, and R. G. Beausoleil. Polarization-selective excitation of nitrogen vacancy centers in diamond. *Phys. Rev. B*, 76:165205, 2007.

[102] E. Farchi, Y. Ebert, D. Farfurnik, G. Haim, R. Shaar, and N. Bar-Gill. Quantitative vectorial magnetic imaging of multi-domain rock forming minerals using nitrogen-vacancy centers in diamond. *SPIN*, 07(03):1740015, 2017.

[103] J. C. Allred, R. N. Lyman, T. W. Kornack, and M. V. Romalis. High-sensitivity atomic magnetometer unaffected by spin-exchange relaxation. *Phys. Rev. Lett.*, 89:130801, 2002.

[104] V. V. Dobrovitski, A. E. Feiguin, D. D. Awschalom, and R. Hanson. Decoherence dynamics of a single spin versus spin ensemble. *Phys. Rev. B*, 77:245212, 2008.

[105] L. T. Hall, J. H. Cole, and L. C. L. Hollenberg. Analytic solutions to the central-spin problem for nitrogen-vacancy centers in diamond. *Phys. Rev. B*, 90:075201, 2014.

[106] E. Bauch. *Optimizing Solid-State Spins in Diamond for Nano-to Millimeter-Scale Magnetic Field Sensing*. PhD thesis, Harvard University, 2018.

[107] J. Schloss. *Optimizing Nitrogen-Vacancy Diamond Magnetic Sensors and Imagers for Broadband Sensitivity*. PhD thesis, Massachusetts Institute of Technology, 2019.

[108] C. Hart. *Experimental Realization of Improved Magnetic Sensing and Imaging in Ensembles of Nitrogen Vacancy Centers in Diamond*. PhD thesis, Harvard University, 2020.

[109] M. Hämäläinen, R. Hari, R. J. Ilmoniemi, J. Knuutila, and O. V. Lounasmaa. Magnetoencephalography—theory, instrumentation, and applications to noninvasive studies of the working human brain. *Rev. Mod. Phys.*, 65:413–497, 1993.

[110] E. A. Lima and B. P. Weiss. Obtaining vector magnetic field maps from single-component measurements of geological samples. *Journal of Geophysical Research: Solid Earth*, 114(B6), 2009.

[111] U. Ribary, A. A. Ioannides, K. D. Singh, R. Hasson, J. P. Bolton, F. Lado, A. Mogilner, and R. Llinás. Magnetic field tomography of coherent thalamocortical 40-hz oscillations in humans. *Proceedings of the National Academy of Sciences*, 88(24):11037–11041, 1991.

[112] R. S. Gonnelli and M. Agnello. Inverse problem solution in cardiomagnetism using a current multipole expansion of the primary sources. *Physics in Medicine and Biology*, 32(1):133–142, 1987.

[113] J. T. Nenonen. Solving the inverse problem in magnetocardiography. *IEEE Engineering in Medicine and Biology Magazine*, 13(4):487–496, 1994.

[114] O. Dössel. Inverse problem of electro-and magnetocardiography: Review and recent progress. *International Journal of Bioelectromagnetism*, 2(2):22, 2000.

[115] R. Model and L. Trahms. An inverse problem of magnetic source localization. *Numerical algorithms*, 5(12):603–610, 1993.

[116] L. De Rochefort, R. Brown, M. R. Prince, and Y. Wang. Quantitative mr susceptibility mapping using piece-wise constant regularized inversion of the magnetic field. *Magnetic Resonance in Medicine: An Official Journal of the International Society for Magnetic Resonance in Medicine*, 60(4):1003–1009, 2008.

[117] A. Jeffers. *3D Magnetic Imaging using SQUIDs and Spin-valve Sensors*. PhD thesis, University of Maryland: College Park, 2016.

[118] F. Casola, T. van der Sar, and A. Yacoby. Probing condensed matter physics with magnetometry based on nitrogen-vacancy centres in diamond. *Nature Reviews Materials*, 3(1):1–13, 2018.

[119] I. Mayergoyz, M. Dimian, G. Bertotti, and C. Serpico. Inverse problem approach to the design of magnetic field pulses for precessional switching. *Journal of Applied Physics*, 95(11):7004–7006, 2004.

[120] J. W. Zuber, F. S. Wells, S. A. Fedoseev, T. H. Johansen, A. B. Rosenfeld, and A. V. Pan. A new approach to the inverse problem for current mapping in thin-film superconductors. *Journal of Applied Physics*, 123(12):123906, 2018.

[121] T. Johansen, M. Baziljevich, H. Bratsberg, Y. Galperin, P. Lindelof, Y. Shen, and P. Vase. Direct observation of the current distribution in thin superconducting strips using magneto-optic imaging. *Phys. Rev. B*, 54(22):16264, 1996.

[122] M. Carrera, J. Amorós, X. Granados, R. Maynou, T. Puig, and X. Obradors. Computation of current distribution in ybco tapes with defects obtained from hall magnetic mapping by inverse problem solution. *IEEE transactions on applied superconductivity*, 21(3):3408–3412, 2010.

[123] R. Merwa, K. Hollaus, P. Brunner, and H. Scharfetter. Solution of the inverse problem of magnetic induction tomography (MIT). *Physiological Measurement*, 26(2):S241–S250, 2005.

[124] M. Ziolkowski, S. Gratkowski, and R. Palka. Solution of three dimensional inverse problem of magnetic induction tomography using tikhonov regularization method. *International Journal of Applied Electromagnetics and Mechanics*, 30(3-4):245–253, 2009.

[125] J. Wikswo. The magnetic inverse problem for nde. In *SQUID sensors: fundamentals, fabrication and applications*, pages 629–695. Springer, 1996.

[126] Y. P. Ma and J. P. Wikswo. Techniques for depth-selective, low-frequency eddy current analysis for squid-based nondestructive testing. *Journal of nondestructive evaluation*, 14(3):149–167, 1995.

[127] V. P. Bui, O. Chadebec, L. . Rouve, and J. . Coulomb. Noninvasive fault monitoring of electrical machines by solving the steady-state magnetic inverse problem. *IEEE Transactions on Magnetics*, 44(6):1050–1053, 2008.

[128] S. Russenschuck, T. Tortschanoff, A. Ijspeert, R. Perin, and N. Siegel. Tracing back measured magnetic field imperfections in lhc magnets by means of the inverse problem approach. *IEEE transactions on magnetics*, 30(4):1797–1800, 1994.

[129] O. Chadebec, J. . Coulomb, J. . Bongiraud, G. Cauffet, and P. Le Thiec. Recent improvements for solving inverse magnetostatic problem applied to thin shells. *IEEE Transactions on Magnetics*, 38(2):1005–1008, 2002.

[130] M. McIver. An Inverse Problem in Electromagnetic Crack Detection. *IMA Journal of Applied Mathematics*, 47(2):127–145, 1991.

[131] T. Katou, Y. Gotoh, N. Takahashi, and M. Izumi. Measurement technique of distribution of power generation current using static magnetic field around polymer electrolyte fuel cell by 3d inverse problem fem. *Materials Transactions*, 53(2):279–284, 2012.

[132] J. Sarvas. Basic mathematical and electromagnetic concepts of the biomagnetic inverse problem. *Phys. Med. Biol.*, 32(1):11, 1987.

[133] R. Kress, L. Kuhn, and R. Potthast. Reconstruction of a current distribution from its magnetic field. *Inverse Problems*, 18(4):1127–1146, 2002.

[134] S. Tan, B. J. Roth, and J. P. Wikswo. The magnetic field of cortical current sources: the application of a spatial filtering model to the forward and inverse problems. *Electroencephalography and Clinical Neurophysiology*, 76(1):73 – 85, 1990.

[135] M. S. Hämäläinen and R. J. Ilmoniemi. Interpreting magnetic fields of the brain: minimum norm estimates. *Medical & biological engineering & computing*, 32(1):35–42, 1994.

[136] R. Greenblatt. Probabilistic reconstruction of multiple sources in the bioelectromagnetic inverse problem. *Inverse problems*, 9(2):271, 1993.

[137] T. Auranen, A. Nummenmaa, M. S. Hämäläinen, I. P. Jääskeläinen, J. Lampinen, A. Vehtari, and M. Sams. Bayesian analysis of the neuromagnetic inverse problem with p-norm priors. *NeuroImage*, 26(3):870–884, 2005.

[138] D. Netter and A. Rezzoug. Genetic algorithm to treat a superconducting magnet calculation as a magnetostatic inverse problem. *IEE Proceedings-Science, Measurement and Technology*, 148(6):253–256, 2001.

[139] J. Zuber, F. S. Wells, S. A. Fedoseev, T. H. Johansen, A. B. Rosenfeld, and A. V. Pan. A new approach to the inverse problem for current mapping in thin-film superconductors. *Journal of Applied Physics*, 123(12):123906, 2018.

[140] C. Jooss, R. Warthmann, A. Forkl, and H. Kronmüller. High-resolution magneto-optical imaging of critical currents in yba2cu3o7- δ thin films. *Physica C: Superconductivity*, 299(3-4):215–230, 1998.

[141] A. A. Ioannides, J. P. R. Bolton, and C. J. S. Clarke. Continuous probabilistic solutions to the biomagnetic inverse problem. *Inverse Problems*, 6(4):523–542, 1990.

[142] I. Gradshteyn and I. Ryzhik. *Table of Integrals, Series, and Products*. Elsevier Science, 2014.

[143] B. J. Roth and J. P. Wikswo. The magnetic field of a single axon. a comparison of theory and experiment. *Biophys. J.*, 48(1):93–109, 1985.

[144] The Mathworks, Inc., Natick, Massachusetts. *MATLAB version 9.7.0.1261785 (R2019b) Update 3*, 2019.

[145] M. J. H. Ku, T. X. Zhou, Q. Li, Y. J. Shin, J. K. Shi, C. Burch, L. E. Anderson, A. T. Pierce, Y. Xie, A. Hamo, U. Vool, H. Zhang, F. Casola, T. Taniguchi, K. Watanabe, M. M. Fogler, P. Kim, A. Yacoby, and R. L. Walsworth. Imaging viscous flow of the dirac fluid in graphene. *Nature*, 583(7817):537–541, 2020.

[146] M. J. Turner, N. Langellier, R. Bainbridge, D. Walters, S. Meesala, T. M. Babinec, P. Kehayias, A. Yacoby, E. Hu, M. Lončar, R. L. Walsworth, and E. V. Levine. Magnetic field fingerprinting of integrated-circuit activity with a quantum diamond microscope. *Phys. Rev. Applied*, 14:014097, 2020.

[147] J. D. Jackson. *Classical electrodynamics*. Wiley, New York, NY, 3rd ed. edition.

[148] R. Stolz, V. Zakosarenko, M. Schulz, A. Chwala, L. Fritzsch, H.-G. Meyer, and E. Köstlin. Magnetic full-tensor squid gradiometer system for geophysical applications. *The Leading Edge*, 25(2):178–180, 2006.

[149] J. Zimmerman and N. V. Frederick. Miniature ultrasensitive superconducting magnetic gradiometer and its use in cardiography and other applications. *Applied Physics Letters*, 19(1):16–19, 1971.

[150] W. Wynn, C. Frahm, P. Carroll, R. Clark, J. Wellhoner, and M. Wynn. Advanced superconducting gradiometer/magnetometer arrays and a novel signal processing technique. *IEEE Transactions on Magnetics*, 11(2):701–707, 1975.

[151] P. Schmidt, D. Clark, K. Leslie, M. Bick, D. Tilbrook, and C. Foley. Getmag–a squid magnetic tensor gradiometer for mineral and oil exploration. *Exploration Geophysics*, 35(4):297–305, 2004.

[152] P. W. Schmidt and D. A. Clark. The magnetic gradient tensor: Its properties and uses in source characterization. *The Leading Edge*, 25(1):75–78, 2006.

[153] M. Beiki, D. A. Clark, J. R. Austin, and C. A. Foss. Estimating source location using normalized magnetic source strength calculated from magnetic gradient tensor datanormalized source strength. *Geophysics*, 77(6):J23–J37, 2012.

[154] W. M. Wynn. Magnetic dipole localization using the gradient rate tensor measured by a five-axis magnetic gradiometer with known velocity. In *Detection Technologies for Mines and Minelike Targets*, volume 2496, pages 357–367. International Society for Optics and Photonics, 1995.

[155] A. Bruno, P. Costa Ribeiro, J. von der Weid, and O. Symko. Discrete spatial filtering with squid gradiometers in biomagnetism. *Journal of applied physics*, 59(7):2584–2589, 1986.

[156] A. Bruno and P. C. Ribeiro. Spatial deconvolution algorithm for superconducting planar gradiometer arrays. *IEEE Transactions on Magnetics*, 25(2):1219–1222, 1989.

[157] T. Ogawa, Y. Kosugi, and H. Kanada. Neural network based solution to inverse problems. In *1998 IEEE International Joint Conference on Neural Networks Proceedings. IEEE World Congress on Computational Intelligence (Cat. No. 98CH36227)*, volume 3, pages 2471–2476. IEEE, 1998.

[158] J. Adler and O. Öktem. Solving ill-posed inverse problems using iterative deep neural networks. *Inverse Problems*, 33(12):124007, 2017.

[159] R. Yamashita, M. Nishio, R. K. G. Do, and K. Togashi. Convolutional neural networks: an overview and application in radiology. *Insights into imaging*, 9(4):611–629, 2018.

[160] B. Zhu, J. Z. Liu, S. F. Cauley, B. R. Rosen, and M. S. Rosen. Image reconstruction by domain-transform manifold learning. *Nature*, 555(7697):487–492, 2018.

[161] Y. Rivenson, Z. Göröcs, H. Günaydin, Y. Zhang, H. Wang, and A. Ozcan. Deep learning microscopy. *Optica*, 4(11):1437–1443, 2017.

[162] E. Nehme, L. E. Weiss, T. Michaeli, and Y. Shechtman. Deep-storm: super-resolution single-molecule microscopy by deep learning. *Optica*, 5(4):458–464, 2018.

[163] W. Ouyang, A. Aristov, M. Lelek, X. Hao, and C. Zimmer. Deep learning massively accelerates super-resolution localization microscopy. *Nature biotechnology*, 36(5):460–468, 2018.

[164] K. H. Jin, M. T. McCann, E. Froustey, and M. Unser. Deep convolutional neural network for inverse problems in imaging. *IEEE Transactions on Image Processing*, 26(9):4509–4522, 2017.

[165] P. Ramuhalli, L. Udpa, and S. S. Udpa. Neural network-based inversion algorithms in magnetic flux leakage nondestructive evaluation. *Journal of applied physics*, 93(10):8274–8276, 2003.

[166] E. Coccorese, R. Martone, and F. C. Morabito. A neural network approach for the solution of electric and magnetic inverse problems. *IEEE transactions on magnetics*, 30(5):2829–2839, 1994.

[167] C. S. Koh, O. A. Mohammed, and S.-Y. Hahn. Detection of magnetic body using artificial neural network with modified simulated annealing. *IEEE transactions on magnetics*, 30(5):3644–3647, 1994.

[168] T. Tieleman and G. Hinton. Lecture 6.5—RmsProp: Divide the gradient by a running average of its recent magnitude. COURSERA: Neural Networks for Machine Learning, 2012.

[169] J. K. Woosley, B. J. Roth, and J. P. Wikswo. The magnetic field of a single axon: A volume conductor model. *Math. Biosci.*, 76(1):1 – 36, 1985.

[170] K. R. Swinney and J. Wikswo, J P. A calculation of the magnetic field of a nerve action potential. *Biophysical journal*, 32(2):719–731, 1980.

[171] J. A. C. Nicol. The giant nerve-fibres in the central nervous system of Myxicola (Polychaeta, Sabellidae). *Q. J. Microsc. Sci.*, 89(1):1–45, 1948.

[172] B. Rudy. Inactivation in myxicola giant axons responsible for slow and accumulative adaptation phenomena. *The Journal of Physiology*, 312(1):531–549, 1981.

[173] L. Binstock and L. Goldman. Current- and Voltage-Clamped Studies on Myxicola Giant Axons : Effect of tetrodotoxin . *Journal of General Physiology*, 54(6):730–740, 1969.

[174] J. Fish and S. Fish. *A Student's Guide to the Seashore*. Cambridge University Press, 1996.

[175] M. B. V. Roberts. The rapid response of *Myxicola infundibulum*. *J. Mar. Biol. Assoc. U K*, 42(3):527–539, 1962.

[176] Y. Song and S. T. Brady. Analysis of microtubules in isolated axoplasm from the squid giant axon. *Methods Cell Biol.*, 115:125–137, 2013.

[177] J. A. C. Nicol. The giant axons of annelids. *Q. Rev. Biol.*, 23(4):291–323, 1948.

[178] T. Wolf, P. Neumann, K. Nakamura, H. Sumiya, T. Ohshima, J. Isoya, and J. Wrachtrup. Subpicotesla diamond magnetometry. *Phys. Rev. X*, 5:041001, 2015.

[179] R. S. Schoenfeld and W. Harneit. Real time magnetic field sensing and imaging using a single spin in diamond. *Phys. Rev. Lett.*, 106(3):030802–, 2011.

[180] K. Jensen, N. Leefer, A. Jarmola, Y. Dumeige, V. M. Acosta, P. Kehayias, B. Patton, and D. Budker. Cavity-enhanced room-temperature magnetometry using absorption by nitrogen-vacancy centers in diamond. *Phys. Rev. Lett.*, 112(16):160802, 2014.

[181] I. Popa, T. Gaebel, M. Domhan, C. Wittmann, F. Jelezko, and J. Wrachtrup. Energy levels and decoherence properties of single electron and nuclear spins in a defect center in diamond. *Phys. Rev. B*, 70(20):201203–, 2004.

[182] V. M. Acosta, A. Jarmola, E. Bauch, and D. Budker. Optical properties of the nitrogen-vacancy singlet levels in diamond. *Phys. Rev. B*, 82(20):201202, 2010.

[183] J. P. Wikswo and B. J. Roth. Magnetic determination of the spatial extent of a single cortical current source: a theoretical analysis. *Electroencephalography and Clinical Neurophysiology*, 69(3):266 – 276, 1988.

[184] D. Carpenter, M. Hovey, and A. Bak. Resistivity of axoplasm. ii. internal resistivity of giant axons of squid and myxicola. *J. Gen. Physiol.*, 66(2):139–148, 1975.

[185] F. Ramon, R. Joyner, and J. Moore. Propagation of action potentials in inhomogeneous axon regions. In *Membranes, Ions, and Impulses*, pages 85–100. Springer, 1975.

[186] S. S. Goldstein and W. Rall. Changes of action potential shape and velocity for changing core conductor geometry. *Biophys. J.*, 14(10):731–757, 1974.

[187] M. L. Hines and N. T. Carnevale. The neuron simulation environment. *Neural Comput.*, 9(6):1179–1209, 1997.

[188] D. Hellerstein. Passive membrane potentials: a generalization of the theory of electrotonus. *Biophysical journal*, 8(3):358–379, 1968.

[189] X. Zhang, S. Zhu, and B. He. Imaging electric properties of biological tissues by rf field mapping in mri. *IEEE Transactions on medical Imaging*, 29(2):474–481, 2010.

[190] J. Jack, D. Noble, and R. Tsien. *Electric Current Flow in Excitable Cells*. Oxford science publications. Clarendon Press, 1983.

[191] D. R. Hochbaum, Y. Zhao, S. L. Farhi, N. Klapoetke, C. A. Werley, V. Kapoor, P. Zou, J. M. Kralj, D. Maclaurin, N. Smedemark-Margulies, J. L. Saulnier, G. L. Boulting, C. Straub, Y. K. Cho, M. Melkonian, G. K.-S. Wong, D. J. Harrison, V. N. Murthy, B. L. Sabatini, E. S. Boyden, R. E. Campbell, and A. E. Cohen. All-optical electrophysiology in mammalian neurons using engineered microbial rhodopsins. *Nature Methods*, 11(8):825–833, 2014.

[192] R. L. Parker. Understanding inverse theory. *Annual Review of Earth and Planetary Sciences*, 5(1):35–64, 1977.

[193] R. S. Eisenberg and E. A. Johnson. Three-dimensional electrical field problems in physiology. *Progress in Biophysics and Molecular Biology*, 20:1–65, 1970.

[194] W. F. Pickard. The spatial variation of plasmalemma potential in a spherical cell polarized by a small current source. *Mathematical Biosciences*, 10(3-4):307–328, 1971.

[195] R. Eisenberg and E. Engel. The spatial variation of membrane potential near a small source of current in a spherical cell. *The Journal of general physiology*, 55(6):736–757, 1970.

[196] D. A. Wollner and W. A. Catterall. Localization of sodium channels in axon hillocks and initial segments of retinal ganglion cells. *Proceedings of the National Academy of Sciences*, 83(21):8424–8428, 1986.

[197] S. Sakatani and A. Hirose. The influence of neuron shape changes on the firing characteristics. *Neurocomputing*, 52:355–362, 2003.

[198] B. D. Clark, E. M. Goldberg, and B. Rudy. Electrogenic tuning of the axon initial segment. *The Neuroscientist*, 15(6):651–668, 2009.

[199] A. Marblestone, B. Zamft, Y. Maguire, M. Shapiro, T. Cybulski, J. Glaser, D. Amodei, P. B. Stranges, R. Kalhor, D. Dalrymple, D. Seo, E. Alon, M. Maharbiz, J. Carmena, J. Rabaey, E. Boyden, G. Church, and K. Kording. Physical principles for scalable neural recording. *Front. Comput. Neurosci.*, 7:137, 2013.

[200] E. V. Levine, M. J. Turner, P. Kehayias, C. A. Hart, N. Langellier, R. Trubko, D. R. Glenn, R. R. Fu, and R. L. Walsworth. Principles and techniques of the quantum diamond microscope. *Nanophotonics*, 8(11):1945–1973, 2019.

[201] A. M. Edmonds, C. A. Hart, M. J. Turner, P.-O. Colard, J. M. Schloss, K. Olsson, R. Trubko, M. L. Markham, A. Rathmill, B. Horne-Smith, et al. Generation of nitrogen-vacancy ensembles in diamond for quantum sensors: Optimization and scalability of cvd processes. *arXiv preprint, arXiv:2004.01746*, 2020.

[202] N. Manson and J. Harrison. Photo-ionization of the nitrogen-vacancy center in diamond. *Diamond and Related Materials*, 14(10):1705 – 1710, 2005.

[203] S. Rajendran, N. Zobrist, A. O. Sushkov, R. Walsworth, and M. Lukin. A method for directional detection of dark matter using spectroscopy of crystal defects. *Phys. Rev. D*, 96:035009, 2017.

[204] K. E. Spear and J. P. Dismukes. *Synthetic Diamond: Emerging CVD Science and Technology*. Wiley, 1994.

[205] H. C. Davis, P. Ramesh, A. Bhatnagar, A. Lee-Gosselin, J. F. Barry, D. R. Glenn, R. L. Walsworth, and M. G. Shapiro. Mapping the microscale origins of mri contrast with subcellular nv diamond magnetometry. *Nature Communications*, 9:131, 2018.

[206] I. Friel, S. Clewes, H. Dhillon, N. Perkins, D. Twitchen, and G. Scarsbrook. Control of surface and bulk crystalline quality in single crystal diamond grown by chemical vapour deposition. *Diamond and Related Materials*, 18(5):808 – 815, 2009.

[207] A. Crisci, F. Baillet, M. Mermoux, G. Bogdan, M. Nesládek, and K. Haenen. Residual strain around grown-in defects in cvd diamond single crystals: A 2d and 3d raman imaging study. *physica status solidi (a)*, 208(9):2038–2044, 2011.

[208] P. L. Hanley, I. Kiflawi, and A. R. Lang. On topographically identifiable sources of cathodoluminescence in natural diamonds. *Proceedings of the Royal Society of London. Series A, Mathematical and Physical Sciences*, 284(1324):329–368, 1977.

[209] D. A. Broadway, B. C. Johnson, M. S. J. Barson, S. E. Lillie, N. Dontschuk, D. J. McCloskey, A. Tsai, T. Teraji, D. A. Simpson, A. Stacey, J. C. McCallum, J. E. Bradby, M. W. Doherty, L. C. L. Hollenberg, and J. P. Tetienne. Microscopic imaging of the stress tensor in diamond using in situ quantum sensors. *Nano Letters*, 19(7):4543–4550, 2019.

[210] L. T. M. Hoa, T. Ouisse, D. Chaussende, M. Naamoun, A. Tallaire, and J. Achard. Birefringence microscopy of unit dislocations in diamond. *Crystal Growth & Design*, 14(11):5761–5766, 2014.

[211] A. M. Glazer, J. G. Lewis, and W. Kaminsky. An automatic optical imaging system for birefringent media. *Proceedings of the Royal Society of London A: Mathematical, Physical and Engineering Sciences*, 452(1955):2751–2765, 1996.

[212] W. Kaminsky, E. Gunn, R. Sours, and B. Kahr. Simultaneous false-colour imaging of birefringence, extinction and transmittance at camera speed. *Journal of Microscopy*, 228(2):153–164, 2007.

[213] D. Howell. Strain-induced birefringence in natural diamond: a review. *European Journal of Mineralogy*, 24(4):575, 2012.

[214] D. Howell, I. G. Wood, F. Nestola, P. Nimis, and L. Nasdala. Inclusions under remnant pressure in diamond: a multi-technique approach. *European Journal of Mineralogy*, 24(4):563–573, 2012.

[215] D. Howell, I. G. Wood, D. P. Dobson, A. P. Jones, L. Nasdala, and J. W. Harris. Quantifying strain birefringence halos around inclusions in diamond. *Contributions to Mineralogy and Petrology*, 160(5):705–717, 2010.

[216] A. Zaitsev. *Optical Properties of Diamond: A Data Handbook*. Springer, 2001.

[217] Geday, Kaminsky, Lewis, and Glazer. Images of absolute retardance l.n, using the rotating polariser method. *Journal of Microscopy*, 198(1):1–9, 2000.

[218] H. Pinto and R. Jones. Theory of the birefringence due to dislocations in single crystal cvd diamond. *Journal of Physics: Condensed Matter*, 21(36):364220, 2009.

[219] J. F. Nye. *Physical Properties of Crystals*. Oxford University Press, 1957.

[220] G. N. Ramachandran. Birefringence of crystals and its temperature-variation. *Proceedings of the Indian Academy of Sciences - Section A*, 26(1):77, 1947.

[221] L. S. Hounsome, R. Jones, M. J. Shaw, and P. R. Briddon. Photoelastic constants in diamond and silicon. *physica status solidi (a)*, 203(12):3088–3093, 2006.

[222] H. Jasbeer, R. J. Williams, O. Kitzler, A. McKay, S. Sarang, J. Lin, and R. P. Mildren. Birefringence and piezo-raman analysis of single crystal cvd diamond and effects on raman laser performance. *J. Opt. Soc. Am. B*, 33(3):B56–B64, 2016.

[223] M. W. Doherty, V. V. Struzhkin, D. A. Simpson, L. P. McGuinness, Y. Meng, A. Stacey, T. J. Karle, R. J. Hemley, N. B. Manson, L. C. L. Hollenberg, and S. Prawer. Electronic properties and metrology applications of the diamond nv center under pressure. *Phys. Rev. Lett.*, 112:047601, 2014.

[224] H. Pinto, R. Jones, J. P. Goss, and P. R. Briddon. Point and extended defects in chemical vapour deposited diamond. *J. Phys.: Conf. Ser.*, 281:012023, 2011.

[225] M. Gaukroger, P. Martineau, M. Crowder, I. Friel, S. Williams, and D. Twitchen. X-ray topography studies of dislocations in single crystal cvd diamond. *Diamond and Related Materials*, 17(3):262 – 269, 2008.

[226] N. Tsubouchi, Y. Mokuno, H. Yamaguchi, N. Tatsumi, A. Chayahara, and S. Shikata. Characterization of crystallinity of a large self-standing homoepitaxial diamond film. *Diamond and Related Materials*, 18(2):216 – 219, 2009. Proceedings of the International Conference on New Diamond and Nano Carbons 2008.

[227] P. M. Martineau, S. C. Lawson, A. J. Taylor, S. J. Quinn, D. J. F. Evans, and M. J. Crowder. Identification of synthetic diamond grown using chemical vapor deposition (cvd). *Gems & Gemology*, 40:2–25, 2004.

[228] D. Hull and D. J. Bacon. *Introduction to dislocations*, volume 37. Elsevier, 2011.

[229] Y. Mita. Change of absorption spectra in type-ib diamond with heavy neutron irradiation. *Phys. Rev. B*, 53:11360–11364, 1996.

[230] K. Groot-Berning, N. Raatz, I. Dobrinets, M. Lesik, P. Spinicelli, A. Tallaire, J. Achard, V. Jacques, J.-F. Roch, A. M. Zaitsev, J. Meijer, and S. Pezzagna. Passive charge state control of nitrogen-vacancy centres in diamond using phosphorous and boron doping. *physica status solidi (a)*, 211(10):2268–2273, 2014.

[231] H. Jayakumar, J. Henshaw, S. Dhomkar, D. Pagliero, A. Laraoui, N. B. Manson, R. Albu, M. W. Doherty, and C. A. Meriles. Optical patterning of trapped charge in nitrogen-doped diamond. *Nature Communications*, 7(1):12660, 2016.

[232] S. Dhomkar, P. R. Zangara, J. Henshaw, and C. A. Meriles. On-demand generation of neutral and negatively charged silicon-vacancy centers in diamond. *Phys. Rev. Lett.*, 120:117401, 2018.

[233] H. Jayakumar, A. Lozovoi, D. Daw, and C. A. Meriles. Long-term spin state storage using ancilla charge memories. *arXiv preprint, arXiv:2003.13148*, 2020.

[234] P. Ji and M. V. G. Dutt. Charge state dynamics of the nitrogen vacancy center in diamond under 1064-nm laser excitation. *Phys. Rev. B*, 94:024101, 2016.

[235] Y. Doi, T. Fukui, H. Kato, T. Makino, S. Yamasaki, T. Tashima, H. Morishita, S. Miwa, F. Jelezko, Y. Suzuki, and N. Mizuochi. Pure negatively charged state of the nv center in n-type diamond. *Phys. Rev. B*, 93:081203, 2016.

[236] N. B. Manson, M. Hedges, M. S. Barson, R. Ahlefeldt, M. W. Doherty, H. Abe, T. Ohshima, and M. J. Sellars. Nv—n+ pair centre in 1b diamond. *New Journal of Physics*, 20(11):113037, 2018.

[237] M. Drake, E. Scott, and J. Reimer. Influence of magnetic field alignment and defect concentration on nitrogen-vacancy polarization in diamond. *New Journal of Physics*, 18(1):013011, 2015.

[238] S. Charles, J. Butler, B. Feygelson, M. Newton, D. Carroll, J. Steeds, H. Darwish, C.-S. Yan, H. Mao, and R. Hemley. Characterization of nitrogen doped chemical vapor deposited single crystal diamond before and after high pressure, high temperature annealing. *physica status solidi (a)*, 201(11):2473–2485, 2004.

[239] X.-D. Chen, C.-H. Dong, F.-W. Sun, C.-L. Zou, J.-M. Cui, Z.-F. Han, and G.-C. Guo. Temperature dependent energy level shifts of nitrogen-vacancy centers in diamond. *Applied Physics Letters*, 99(16):161903, 2011.

[240] T. L. McCormick, W. E. Jackson, and R. J. Nemanich. The characterization of strain, impurity content, and crush strength of synthetic diamond crystals. *Journal of Materials Research*, 12(1):253–263, 1997.

[241] E. Fraczek, V. G. Savitski, M. Dale, B. G. Breeze, P. Diggle, M. Markham, A. Bennett, H. Dhillon, M. E. Newton, and A. J. Kemp. Laser spectroscopy of nv- and nv0 colour centres in synthetic diamond. *Opt. Mater. Express*, 7(7):2571–2585, 2017.

[242] J. Storteboom, P. Dolan, S. Castelletto, X. Li, and M. Gu. Lifetime investigation of single nitrogen vacancy centres in nanodiamonds. *Opt. Express*, 23(9):11327–11333, 2015.

[243] S. Hell, G. Reiner, C. Cremer, and E. H. Stelzer. Aberrations in confocal fluorescence microscopy induced by mismatches in refractive index. *Journal of microscopy*, 169(3):391–405, 1993.

[244] M. P. Backlund, P. Kehayias, and R. L. Walsworth. Diamond-based magnetic imaging with fourier optical processing. *Phys. Rev. Applied*, 8(5):054003, 2017.

[245] M. Rostami, F. Koushanfar, and R. Karri. A primer on hardware security: Models, methods, and metrics. *Proceedings of the IEEE*, 102(8):1283–1295, 2014.

[246] M. Tehranipoor, H. Salmani, X. Zhang, M. Wang, R. Karri, J. Rajendran, and K. Rosenfeld. Trustworthy hardware: Trojan detection and design-for-trust challenges. *Computer*, 44(7):66–74, 2010.

[247] Semiconductor Industry Association. Winning the battle against counterfeit semiconductor products. *SIA Whitepaper, Washington DC*, 2013.

[248] P. Hoeper and J. Manferdelli. Dsb task force on cyber supply chain. *Defense Science Board Washington DC USA*, 2017.

[249] U. Guin, K. Huang, D. DiMase, J. M. Carulli, M. Tehranipoor, and Y. Makris. Counterfeit integrated circuits: A rising threat in the global semiconductor supply chain. *Proceedings of the IEEE*, 102(8):1207–1228, 2014.

[250] J. Balasch, B. Gierlichs, and I. Verbauwhede. Electromagnetic circuit fingerprints for hardware trojan detection. *2015 IEEE International Symposium on Electromagnetic Compatibility (EMC)*, pages 246–251, 2015.

[251] J. Gaudestad and A. Orozco. Magnetic field imaging for non destructive 3d IC testing. *Microelectronics Reliability*, 54(9-10):2093–2098, 2014.

[252] Y. Tagro, J. J. Yan, D. F. Kimball, H. Ghajari, and D. F. Sievenpiper. Innovative magnetic-field array probe for trust integrated circuits. In *GOMACTech*, 2017.

[253] A. Orozco. Magnetic field imaging for electrical fault isolation. *Microelectronics Failure Analysis Desk Reference*, page 111, 2019.

[254] A. N. Campbell, E. Cole, B. A. Dodd, and R. E. Anderson. Internal current probing of integrated circuits using magnetic force microscopy. *31st Annual Proceedings Reliability Physics 1993*, pages 168–177, 1993.

[255] H. H. Huston and C. P. Clarke. Reliability defect detection and screening during processing-theory and implementation. *30th Annual Proceedings Reliability Physics 1992*, pages 268–275, 1992.

[256] Semiconductor Industry Association. Semiconductor research opportunities. 2017.

[257] J. Taylor, P. Cappellaro, L. Childress, L. Jiang, D. Budker, P. Hemmer, A. Yacoby, R. Walsworth, and M. Lukin. High-sensitivity diamond magnetometer with nanoscale resolution. *Nature Physics*, 4(10):810, 2008.

[258] A. Gruber, A. Dräbenstedt, C. Tietz, L. Fleury, J. Wrachtrup, and C. v. Borczyskowski. Scanning confocal optical microscopy and magnetic resonance on single defect centers. *Science*, 276(5321):2012–2014, 1997.

[259] J. R. Maze, P. L. Stanwix, J. S. Hodges, S. Hong, J. M. Taylor, P. Cappellaro, L. Jiang, M. V. G. Dutt, E. Togan, A. S. Zibrov, A. Yacoby, R. L. Walsworth, and M. D. Lukin. Nanoscale magnetic sensing with an individual electronic spin in diamond. *Nature*, 455(7213):644–647, 2008.

[260] G. Balasubramanian, I. Y. Chan, R. Kolesov, M. Al-Hmoud, J. Tisler, C. Shin, C. Kim, A. Wojcik, P. R. Hemmer, A. Krueger, T. Hanke, A. Leitenstorfer, R. Bratschitsch, F. Jelezko, and J. Wrachtrup. Nanoscale imaging magnetometry with diamond spins under ambient conditions. *Nature*, 455(7213):648–651, 2008.

[261] L. M. Pham, D. Le Sage, P. L. Stanwix, T. K. Yeung, D. Glenn, A. Trifonov, P. Cappellaro, P. R. Hemmer, M. D. Lukin, H. Park, A. Yacoby, and R. L. Walsworth. Magnetic field imaging with nitrogen-vacancy ensembles. *New Journal of Physics*, 13(4):045021, 2011.

[262] A. Nowodzinski, M. Chipaux, L. Toraille, V. Jacques, J.-F. Roch, and T. Debuisschert. Nitrogen-vacancy centers in diamond for current imaging at the redistributive layer level of integrated circuits. *Microelectronics Reliability*, 55(9):1549 – 1553, 2015.

[263] D. A. Simpson, J.-P. Tetienne, J. McCoey, K. Ganesan, L. T. Hall, S. Petrou, R. E. Scholten, and L. C. L. Hollenberg. Magneto-optical imaging of thin magnetic films using spins in diamond. *Scientific Reports*, 6:22797, 2016.

[264] R. R. Fu, B. P. Weiss, E. A. Lima, R. J. Harrison, X.-N. Bai, S. J. Desch, D. S. Ebel, C. Suavet, H. Wang, D. Glenn, D. Le Sage, T. Kasama, R. L. Walsworth, and A. T. Kuan. Solar nebula magnetic fields recorded in the semarkona meteorite. *Science*, 346(6213):1089–1092, 2014.

[265] E. De Mulder. *Electromagnetic techniques and probes for side-channel analysis on cryptographic devices*. PhD thesis, Katholieke Universiteit Leuven, 2010.

[266] L. Sauvage, S. Guilley, and Y. Mathieu. Electromagnetic radiations of FPGAs: High spatial resolution cartography and attack on a cryptographic module. *ACM Transactions on Reconfigurable Technology and Systems (TRETS)*, 2(1):4, 2009.

[267] A. Horsley, G.-X. Du, and P. Treutlein. Widefield microwave imaging in alkali vapor cells with sub-100 μm resolution. *New Journal of Physics*, 17(11):112002, 2015.

[268] X. Zhang and M. Tehranipoor. RON: An on-chip ring oscillator network for hardware trojan detection. *2011 Design, Automation & Test in Europe*, pages 1–6, 2011.

[269] M. Mandal and B. C. Sarkar. Ring oscillators: Characteristics and applications. *Indian Journal of Pure and Applied Physics*, 48:136–145, 2010.

[270] F. Dolde, H. Fedder, M. W. Doherty, T. Nöbauer, F. Rempp, G. Balasubramanian, T. Wolf, F. Reinhard, L. C. Hollenberg, F. Jelezko, et al. Electric-field sensing using single diamond spins. *Nature Physics*, 7(6):459–463, 2011.

[271] A. Przybylski, B. Thiel, J. Keller-Findeisen, B. Stock, and M. Bates. Gpufit: An open-source toolkit for gpu-accelerated curve fitting. *Scientific Reports*, 7(1), 2017.

[272] C. A. Werley, M.-P. Chien, and A. E. Cohen. Ultrawidefield microscope for high-speed fluorescence imaging and targeted optogenetic stimulation. *Biomed. Opt. Express*, 8(12):5794–5813, 2017.

[273] D. Le Sage, L. M. Pham, N. Bar-Gill, C. Belthangady, M. D. Lukin, A. Yacoby, and R. L. Walsworth. Efficient photon detection from color centers in a diamond optical waveguide. *Phys. Rev. B*, 85:121202, 2012.

[274] A. M. Wojciechowski, M. Karadas, A. Huck, C. Osterkamp, S. Jankuhn, J. Meijer, F. Jelezko, and U. L. Andersen. Contributed review: Camera-limits for wide-field magnetic resonance imaging with a nitrogen-vacancy spin sensor. *Review of Scientific Instruments*, 89(3):031501, 2018.

[275] G. van Rossum. Python tutorial. Technical Report CS-R9526, Centrum voor Wiskunde en Informatica (CWI), Amsterdam, 1995.

[276] F. Pedregosa, G. Varoquaux, A. Gramfort, V. Michel, B. Thirion, O. Grisel, M. Blondel, P. Prettenhofer, R. Weiss, V. Dubourg, J. Vanderplas, A. Passos, D. Cournapeau, M. Brucher, M. Perrot, and E. Duchesnay. Scikit-learn: Machine learning in Python. *Journal of Machine Learning Research*, 12:2825–2830, 2011.

[277] K. P. F.R.S. On lines and planes of closest fit to systems of points in space. *The London, Edinburgh, and Dublin Philosophical Magazine and Journal of Science*, 2(11):559–572, 1901.

[278] H. Hotelling. Relations between two sets of variates. *Biometrika*, 28(3/4):321–377, 1936.

[279] C. Cortes and V. Vapnik. Support-vector networks. *Machine Learning*, 20:273–297, 1995.

[280] P. Kocher, J. Jaffe, and B. Jun. Differential power analysis. In M. Wiener, editor, *Advances in Cryptology — CRYPTO' 99*, pages 388–397, Berlin, Heidelberg, 1999. Springer Berlin Heidelberg.

[281] S. B. Örs, E. Oswald, and B. Preneel. Power-analysis attacks on an fpga – first experimental results. In C. D. Walter, Ç. K. Koç, and C. Paar, editors, *Cryptographic Hardware and Embedded Systems*, pages 35–50, Berlin, Heidelberg, 2003. Springer Berlin Heidelberg.

[282] U. Rührmair, X. Xu, J. Sölter, A. Mahmoud, M. Majzoobi, F. Koushanfar, and W. Burleson. Efficient power and timing side channels for physical unclonable functions. In L. Batina and M. Robshaw, editors, *Cryptographic Hardware and Embedded Systems*, pages 476–492, Berlin, Heidelberg, 2014. Springer Berlin Heidelberg.

[283] S. Rohr. Role of gap junctions in the propagation of the cardiac action potential. *Cardiovascular research*, 62(2):309–322, 2004.

[284] C.-h. Luo and Y. Rudy. A model of the ventricular cardiac action potential. depolarization, repolarization, and their interaction. *Circulation research*, 68(6):1501–1526, 1991.

[285] M. Rook, B. De Jonge, H. Jongsma, and M. Masson-Pevet. Gap junction formation and functional interaction between neonatal rat cardiocytes in culture: a correlative physiological and ultrastructural study. *The Journal of membrane biology*, 118(2):179–192, 1990.

[286] M. Oyamada, H. Kimura, Y. Oyamada, A. Miyamoto, H. Ohshika, and M. Mori. The expression, phosphorylation, and localization of connexin 43 and gap-junctional intercellular communication during the establishment of a synchronized contraction of cultured neonatal rat cardiac myocytes. *Experimental cell research*, 212(2):351–358, 1994.

[287] C.-W. Hsiao, M.-Y. Bai, Y. Chang, M.-F. Chung, T.-Y. Lee, C.-T. Wu, B. Maiti, Z.-X. Liao, R.-K. Li, and H.-W. Sung. Electrical coupling of isolated cardiomyocyte clusters grown on aligned conductive nanofibrous meshes for their synchronized beating. *Biomaterials*, 34(4):1063–1072, 2013.

[288] Y. Haraguchi, T. Shimizu, M. Yamato, A. Kikuchi, and T. Okano. Electrical coupling of cardiomyocyte sheets occurs rapidly via functional gap junction formation. *Biomaterials*, 27(27):4765–4774, 2006.

[289] S. D. Girouard, K. R. L. Ph. D, and D. S. Rosenbaum. Unique properties of cardiac action potentials recorded with voltage-sensitive dyes. *Journal of cardiovascular electrophysiology*, 7(11):1024–1038, 1996.

[290] J. P. Barach and J. Wikswo. Magnetic fields from simulated cardiac action currents. *IEEE transactions on biomedical engineering*, 41(10):969–974, 1994.

[291] B. J. Roth and J. P. Wikswo. A bidomain model for the extracellular potential and magnetic field of cardiac tissue. *IEEE Transactions on Biomedical Engineering*, (4):467–469, 1986.

[292] J. R. Holzer, L. E. Fong, V. Y. Sidorov, J. P. Wikswo Jr, and F. Baudenbacher. High resolution magnetic images of planar wave fronts reveal bidomain properties of cardiac tissue. *Biophysical journal*, 87(6):4326–4332, 2004.

[293] D. J. Staton. *Magnetic imaging of applied and propagating action currents in cardiac tissue slices: determination of anisotropic electrical conductivities in a two-dimensional bidomain.* PhD thesis, Vanderbilt University, 1994.

[294] M. Valderrábano. Influence of anisotropic conduction properties in the propagation of the cardiac action potential. *Progress in biophysics and molecular biology*, 94(1-2):144–168, 2007.

[295] S. Dhein, T. Seidel, A. Salameh, J. Jozwiak, A. Hagen, M. Kostelka, G. Hindricks, and F.-W. Mohr. Remodeling of cardiac passive electrical properties and susceptibility to ventricular and atrial arrhythmias. *Frontiers in physiology*, 5:424, 2014.

[296] H. M. van der Velden and H. J. Jongsma. Cardiac gap junctions and connexins: their role in atrial fibrillation and potential as therapeutic targets. *Cardiovascular research*, 54(2):270–279, 2002.

[297] N. J. Severs, S. R. Coppen, E. Dupont, H.-I. Yeh, Y.-S. Ko, and T. Matsushita. Gap junction alterations in human cardiac disease. *Cardiovascular research*, 62(2):368–377, 2004.

[298] S. Dhein, A. Hagen, J. Jozwiak, A. Dietze, J. Garbade, M. Barten, M. Kostelka, and F.-W. Mohr. Improving cardiac gap junction communication as a new antiarrhythmic mechanism: the action of antiarrhythmic peptides. *Naunyn-Schmiedeberg's archives of pharmacology*, 381(3):221–234, 2010.

[299] W. Rall. Electrophysiology of a dendritic neuron model. *Biophysical journal*, 2(2):145–167, 1962.

[300] S. Landry, P. L. McGhee, R. J. Girardin, and W. J. Keeler. Monitoring live cell viability: Comparative study of fluorescence, oblique incidence reflection and phase contrast microscopy imaging techniques. *Opt. Express*, 12(23):5754–5759, 2004.

[301] L. A. MacQueen, S. P. Sheehy, C. O. Chantre, J. F. Zimmerman, F. S. Pasqualini, X. Liu, J. A. Goss, P. H. Campbell, G. M. Gonzalez, S.-J. Park, et al. A tissue-engineered scale model of the heart ventricle. *Nature biomedical engineering*, 2(12):930–941, 2018.

[302] N. Zhou, C. Liu, J. A. Lewis, and D. Ham. Gigahertz electromagnetic structures via direct ink writing for radio-frequency oscillator and transmitter applications. *Advanced Materials*, 29(15):1605198, 2017.

[303] A. Grosberg, P. W. Alford, M. L. McCain, and K. K. Parker. Ensembles of engineered cardiac tissues for physiological and pharmacological study: heart on a chip. *Lab on a chip*, 11(24):4165–4173, 2011.

[304] L. M. Pham, N. Bar-Gill, D. Le Sage, C. Belthangady, A. Stacey, M. Markham, D. Twitchen, M. D. Lukin, and R. L. Walsworth. Enhanced metrology using preferential orientation of nitrogen-vacancy centers in diamond. *Phys. Rev. B*, 86(12):121202, 2012.

[305] V. T. Hoang, G. Stępniewski, K. H. Czarnecka, R. Kasztelanic, V. C. Long, K. D. Xuan, L. Shao, M. Śmietana, R. Buczyński, et al. Optical properties of buffers and cell culture media for optofluidic and sensing applications. *Applied Sciences*, 9(6):1145, 2019.

[306] K. Fang, V. M. Acosta, C. Santori, Z. Huang, K. M. Itoh, H. Watanabe, S. Shikata, and R. G. Beausoleil. High-sensitivity magnetometry based on quantum beats in diamond nitrogen-vacancy centers. *Phys. Rev. Lett.*, 110:130802, 2013.

[307] H. J. Mamin, M. H. Sherwood, M. Kim, C. T. Rettner, K. Ohno, D. D. Awschalom, and D. Rugar. Multipulse double-quantum magnetometry with near-surface nitrogen-vacancy centers. *Phys. Rev. Letters*, 113(3):1–5, 2014.

[308] H. M. McNamara, S. Dodson, Y.-L. Huang, E. W. Miller, B. Sandstede, and A. E. Cohen. Geometry-dependent arrhythmias in electrically excitable tissues. *Cell systems*, 7(4):359–370, 2018.

[309] D. Qin, Y. Xia, and G. M. Whitesides. Soft lithography for micro-and nanoscale patterning. *Nature protocols*, 5(3):491–502, 2010.

[310] J. Choi, H. Zhou, H. S. Knowles, R. Landig, S. Choi, and M. D. Lukin. Robust dynamic hamiltonian engineering of many-body spin systems. *Phys. Rev. X*, 10:031002, 2020.

[311] H. Zhou, J. Choi, S. Choi, R. Landig, A. M. Douglas, J. Isoya, F. Jelezko, S. Onoda, H. Sumiya, P. Cappellaro, H. S. Knowles, H. Park, and M. D. Lukin. Quantum metrology with strongly interacting spin systems. *Phys. Rev. X*, 10:031003, 2020.

[312] M. F. O'Keeffe, L. Horesh, J. F. Barry, D. A. Braje, and I. L. Chuang. Hamiltonian engineering with constrained optimization for quantum sensing and control. *New Journal of Physics*, 21(2):023015, 2019.

[313] I. Fescenko, A. Jarmola, I. Savukov, P. Kehayias, J. Smits, J. Damron, N. Ristoff, N. Mosavian, and V. M. Acosta. Diamond magnetometer enhanced by ferrite flux concentrators. *Phys. Rev. Research*, 2:023394, 2020.

[314] K. S. Cole and J. W. Moore. Ionic current measurements in the squid giant axon membrane. *The Journal of general physiology*, 44(1):123–167, 1960.

[315] J. D. Clements and S. J. Redman. Cable properties of cat spinal motoneurones measured by combining voltage clamp, current clamp and intracellular staining. *The Journal of Physiology*, 409(1):63–87, 1989.

[316] K. L. Perkins. Cell-attached voltage-clamp and current-clamp recording and stimulation techniques in brain slices. *Journal of neuroscience methods*, 154(1-2):1–18, 2006.

[317] D. Jaeger and J. M. Bower. Synaptic control of spiking in cerebellar purkinje cells: dynamic current clamp based on model conductances. *Journal of Neuroscience*, 19(14):6090–6101, 1999.

[318] E. C. Beyer, D. L. Paul, and D. A. Goodenough. Connexin43: a protein from rat heart homologous to a gap junction protein from liver. *The Journal of cell biology*, 105(6):2621–2629, 1987.

[319] M. Abbaci, M. Barberi-Heyob, W. Blondel, F. Guillemin, and J. Didelon. Advantages and limitations of commonly used methods to assay the molecular permeability of gap junctional intercellular communication. *Biotechniques*, 45(1):33–62, 2008.

[320] E. C. Beyer, D. L. Paul, and D. A. Goodenough. Connexin family of gap junction proteins. *The Journal of membrane biology*, 116(3):187–194, 1990.

[321] N. M. Kumar and N. B. Gilula. The gap junction communication channel. *Cell*, 84(3):381–388, 1996.

[322] R. J. Thompson, N. Zhou, and B. A. MacVicar. Ischemia opens neuronal gap junction hemichannels. *Science*, 312(5775):924–927, 2006.

[323] J. H. Lin, H. Weigel, M. L. Cotrina, S. Liu, E. Bueno, A. J. Hansen, T. W. Hansen, S. Goldman, and M. Nedergaard. Gap-junction-mediated propagation and amplification of cell injury. *Nature neuroscience*, 1(6):494–500, 1998.

[324] J. Neijssen, B. Pang, and J. Neefjes. Gap junction-mediated intercellular communication in the immune system. *Progress in biophysics and molecular biology*, 94(1-2):207–218, 2007.

[325] P. A. Weber, H.-C. Chang, K. E. Spaeth, J. M. Nitsche, and B. J. Nicholson. The permeability of gap junction channels to probes of different size is dependent on connexin composition and permeant-pore affinities. *Biophysical journal*, 87(2):958–973, 2004.

[326] W. H. Evans, E. De Vuyst, and L. Leybaert. The gap junction cellular internet: connexin hemichannels enter the signalling limelight. *Biochemical Journal*, 397(1):1–14, 2006.

[327] J. L. Orthmann-Murphy, C. K. Abrams, and S. S. Scherer. Gap junctions couple astrocytes and oligodendrocytes. *Journal of Molecular Neuroscience*, 35(1):101–116, 2008.

[328] G. T. Cottrell and J. M. Burt. Functional consequences of heterogeneous gap junction channel formation and its influence in health and disease. *Biochimica et Biophysica Acta (BBA)-Biomembranes*, 1711(2):126–141, 2005.

[329] S. B. Danik, F. Liu, J. Zhang, H. J. Suk, G. E. Morley, G. I. Fishman, and D. E. Gutstein. Modulation of cardiac gap junction expression and arrhythmic susceptibility. *Circulation research*, 95(10):1035–1041, 2004.

[330] J. E. Saffitz, R. B. Schuessler, and K. A. Yamada. Mechanisms of remodeling of gap junction distributions and the development of anatomic substrates of arrhythmias. *Cardiovascular research*, 42(2):309–317, 1999.

[331] P. Sundaram, A. Nummenmaa, W. Wells, D. Orbach, D. Orringer, R. Mulkern, and Y. Okada. Direct neural current imaging in an intact cerebellum with magnetic resonance imaging. *Neuroimage*, 132:477–490, 2016.

[332] D. B. Bucher, D. P. L. Aude Craik, M. P. Backlund, M. J. Turner, O. Ben Dor, D. R. Glenn, and R. L. Walsworth. Quantum diamond spectrometer for nanoscale NMR and ESR spectroscopy. *Nature Protocols*, 14(9):2707–2747, 2019.

[333] D. B. Bucher, D. R. Glenn, H. Park, M. D. Lukin, and R. L. Walsworth. Hyperpolarization-Enhanced NMR Spectroscopy with Femtomole Sensitivity Using Quantum Defects in Diamond. *Phys. Rev. X*, 10(2):021053, 2020.

[334] N. Arunkumar, D. B. Bucher, M. J. Turner, P. TomHon, D. Glenn, S. Lehmkuhl, M. D. Lukin, H. Park, M. S. Rosen, T. Theis, et al. Micron-scale sabre-enhanced nv-nmr spectroscopy. *arXiv preprint, arXiv:2006.03910*, 2020.

[335] X.-H. Zhu, M. Lu, B.-Y. Lee, K. Ugurbil, and W. Chen. In vivo nad assay reveals the intracellular nad contents and redox state in healthy human brain and their age dependences. *Proceedings of the National Academy of Sciences*, 112(9):2876–2881, 2015.

[336] R. A. de Graaf and K. L. Behar. Detection of cerebral nad+ by in vivo 1h nmr spectroscopy. *NMR in biomedicine*, 27(7):802–809, 2014.

[337] J. L. Markley, R. Brüschweiler, A. S. Edison, H. R. Eghbalnia, R. Powers, D. Raftery, and D. S. Wishart. The future of nmr-based metabolomics. *Current opinion in biotechnology*, 43:34–40, 2017.

[338] M. C. Marshall, M. J. Turner, M. J. Ku, D. F. Phillips, and R. L. Walsworth. Directional detection of dark matter with diamond. *arXiv preprint, arXiv:2009.01028*, 2020.

[339] T. J. Karras. Equivalent noise bandwidth analysis from transfer functions. Technical report, 1965.

[340] M. G. Shapiro, M. F. Priest, P. H. Siegel, and F. Bezanilla. Thermal mechanisms of millimeter wave stimulation of excitable cells. *Biophysical journal*, 104(12):2622–2628, 2013.

[341] J. P. Wikswo and J. P. Barach. An estimate of the steady magnetic field strength required to influence nerve conduction. *IEEE Transactions on Biomedical Engineering*, BME-27(12):722–723, 1980.

[342] S. Chakravarthi, C. Moore, A. Opsvig, C. Pederson, E. Hunt, A. Ivanov, I. Christen, S. Dunham, and K.-M. C. Fu. Window into nv center kinetics via repeated annealing and spatial tracking of thousands of individual nv centers. *Phys. Rev. Materials*, 4:023402, 2020.